**UNIVERSITÉ D'AIX MARSEILLE**

Faculté des Sciences de la vie et de la santé
Institut de Neurosciences de la Timone
UMR 7289 CNRS & AMU

Thèse présentée pour obtenir le grade universitaire de Docteur
Discipline : Neurosciences

Présentée publiquement par

**Nina JURČIĆ**

# $GABA_B$ RECEPTORS AND CALCIUM HOMEOSTASIS IN MEDULLO-SPINAL CSF-CONTACTING NEURONS

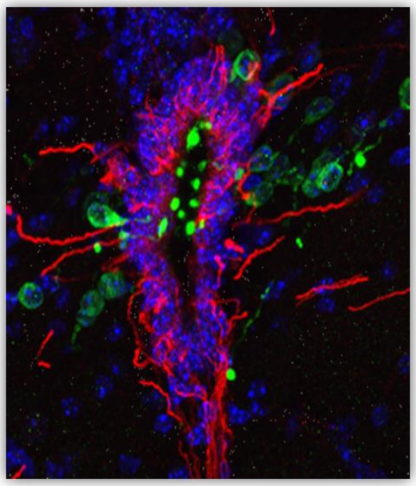

Soutenue le 20/05/2019 devant le jury :

| | |
|---|---|
| **Dr. Matilde CORDERO-ERAUSQUIN**, CNRS, Strasbourg | Rapporteur |
| **Prof. Regis LAMBERT**, CNRS, INSERM, Paris | Rapporteur |
| **Dr. Corinne BEURRIER**, IBDM, Marseille | Examinateur |
| **Prof. Jérôme TROUSLARD**, AMU, INT, Marseille | Directeur de Thèse |

co-Directeur de Thèse, **Dr. Nicolas WANAVERBECQ,** AMU, INT, Marseille

# TABLE OF CONTENTS

# LIST OF ABBREVATIONS

**ABP:** AID-binding pocket

**AC-αTub:** acetylated α tubuline

**AC3:** adenylate cyclase 3

**ACE:** angiotensin converting enzyme

**ACh:** acetylcholine

**AID:** α interaction domain

**ANP:** atrial natriuretic peptide

**AP:** action potential

**ASIC:** acid-sensing ion channel

**ATP:** adenosine triphosphate

**BBB:** blood-brain barrier

**CaBP:** $Ca^{2+}$-binding protein 1

**CA:** carbonic anhydrase enzyme

**CAE:** childhood absence epilepsy

**CaM:** calmodulin

**cAMP:** cyclic adenosine monophosphate

**CaP:** caudal primary motoneurons

**$Ca_v$:** voltage-dependent $Ca^{2+}$ channel

**CBD:** CaM-bindng domain

**CC:** central canal

**CDI:** $Ca^{2+}$-dependent inactivation

**ChAT:** choline acetyltransferase

**ChR2:** channelrhodopsin-2

**CICR:** $Ca^{2+}$-induced $Ca^{2+}$ release

**CNO:** clozapine-*N*-oxide

**CNS:** central nervous system

**CoPA:** commissural primary ascending interneurons

**CPG:** central pattern generator

**CSF:** cerebrospinal fluid

**CSF-cN:** CSF-contacting neuron

**DAG:** 1,1,-Diacylglycerol

**DCX:** doublecortin

**DHP:** dihydropyridine

**DNQX:** 6,7-dinitroquinoxaline-2,3-dione disodium salt

**DREADD:** Designer Receptors Exclusively Activated by Designer Drug

**DRG:** dorsal root ganglion

**DTT:** dithiothreitol

**EC:** excitation-contraction coupling

**ER:** endoplasmic reticulum

**EX:** embryonic day X

**EYFP:** enhanced yellow fluorescent protein

**$GABA_BR$:** $GABA_B$ receptor

**GAD:** glutamic acid decarboxylase

**GDP:** guanosine diphosphate

**GFP:** green fluorescent protein

**GIRK:** inwardly rectifying $K^+$ channel

**GK:** guanlylate kinase

**GPCR:** G protein coupled receptor

**GPI:** glycophosphatidylinositol anchor

**GRK:** G protein coupled receptor kinase

**GTP:** guanosine triphosphate

**HEK293:** human embryonic kidney 293 cell

**hMX:** human muscarinic X receptor

**HuC/D:** human neuronal protein HuC/HuD

**HVA:** high-voltage activated

**IBC:** $IP_3$-binding core

**$IP_3R$:** inositol 1,4,5-trisphosphate receptor

**KA:** Kolmar-Agduhr

**LTP:** long-term potentiation

**LVA:** low-voltage activated

***m*-3M3FBS:** 2,4,6-trimethyl-*N*-(*meta*-3-trifluormethyl-phenyl)-benzosulfonamide

**mAChR:** muscarinic acetylcholine receptors

**MAP2:** microtubule-associated protein 2

**MIDAS:** metal ion-dependent adhesion site

**MPS:** methyl-phenyl-succinimide

**nAChR:** nicotinic acetylcholine receptors

**NCX:** $Na^{2+}/Ca^{2+}$ exchange

**NeuN:** neuronal nuclei

**NF-160:** Neurofilament-160 kDa

**NKKC1:** $Na^{+}$-$K^{+}$-$2Cl^{-}$ cotransporter 1

**$NP_o$:** open probability

**NREM:** non-rapid eye movement

**NSE:** neuron specific enolase

**$P_{Co2}$:** carbon dioxide partial pressure

**PcTx1:** *Psalmopoeus cambridgei* toxin 1

**$PIP_2$:** phosphatidylinositol 4,5-bisphosphate

**PKC:** protein kinase C

**PKD2L1:** polycystin kidney disease 2-like 1 protein

**PLC:** phospholipase C

**PMCA:** $Ca^{2+}$-ATPse pump

**PP1:** protein phosphatase 1

**PP2B:** protein phosphatase calcineurin

**PX:** postnatal day X

**RMP:** resting membrane potential

**ROI:** region of interest

**RyR:** ryanodine receptor

**sAHP:** slow after-hyperpolarization

**SAN:** sinoatrial node

**SERCA:** sarco(endo)plasmic reticulum pump

**SH3:** SRC homology 3

**s-ICAM:** soluble intracellular adhesion molecule

**SNAP-25:** 25K synaptosome-associated protein

**SR:** sarcoplasmic reticulum

**TARP:** transmembrane AMPA receptor regulatory protein

**TEM:** transmission electron microscopy

**TP:** threshold potential

**TRP:** transient receptor potential

**TTX:** tetrodotoxine

**VAMP:** vesicle-associated membrane protein

**VGAT:** vesicular GABA transporter

**VGCC:** volatage-gated $Ca^{2+}$ channel

**VIP:** vasoactive intestinal polypeptide

**VWA:** Willebrand factor type A domain

**YFP:** yellow fluorescent protein

# LIST OF FIGURES

# LIST OF TABLES

# ABSTRACT

Neurons in contact with the cerebrospinal fluid (CSF-cNs) are located in the ependymal region around the central canal (CC) in the brainstem and the spinal cord and are conserved in all vertebrates. These GABAergic neurons exhibit a unique morphology with a single dendrite that projects to the CSF and ends with a large protrusion. They selectively express the polycystin isoform (PKD2L1) of "Transient Receptor Potential" (TRP) channels suggested to act as chemo- and mechanoreceptor. Considering their localization, morphology and selective expression of PKD2L1 channel, CSF-cNs would represent a novel population of sensory neurons within the CNS. It was shown that CSF-cNs express functional ionotropic receptors for GABA, glutamate, acetylcholine and glycine, and it is indicated that CSF-cNs are inserted in a neuronal network and that their activity may be regulated by synaptic partners which remain to be identified. Recent studies carried out in lower vertebrates demonstrated that these neurons actively modulate motor activities and swimming behavior *in vivo*. So far, little information is available regarding the role of CSF-cNs in mammalian CNS.

To better understand the role of CSF-cNs in mammals, it is necessary to describe the physiological properties and modulation of CFS-cNs. In the present study, using electrophysiological recordings in spinal cord and brainstem acute slices together with $Ca^{2+}$ imaging, I describe $Ca^{2+}$ signaling mechanisms in mouse medullo-spinal CSF-cNs. I report that CSF-cNs express mainly high-voltage activated (HVA) $Ca^{2+}$ channels ($Ca_v$s) that are modulated by metabotropic $GABA_B$ and muscarinic acetylcholine receptors. I also describe $Ca^{2+}$ homeostasis and show the involvement of intracellular $Ca^{2+}$ stores in the regulation of intracellular $Ca^{2+}$. Next, using paired recordings from CSF-cN protrusion and soma, I demonstrate their functional relationship and indicate that the protrusion would be devoid of active ionic conductance.

At the network level, CSF-cNs were shown to receive synaptic entries. Here we show that they are synaptically connected with GABAergic and glutamatergic neurons and that $GABA_B$ receptors modulate neurotransmission from both neuronal population whose localization remains to be determined.

Finally, one crucial question about CSF-cNs in mammals concerns their role in CNS activity and in particular within the spinal motor network. To address this question, we developed chemogenetic (DREADDs) and optogenetic (channelrhodopsin) mice models to be

able to selectively manipulate CSF-cN activity and demonstrate their function in more integrated model. To date, I validated these models *in vitro* and showed that optogenetic approach provides a way forward to manipulate CSF-cN activity to assess their role *in vivo*.

Altogether, the results of my PhD study contribute to better understanding mammalian medullo-spinal CSF-cNs by providing valuable information on their physiology and modulation. They also set ground for further studies carried out in *ex-vivo* preparation or *in vivo* models to demonstrate their role in the regulation of CNS activity.

**Keywords:** CSF-contacting neurons, PKD2L1 channel, calcium, $GABA_B$ receptor, mouse, spinal cord

# RÉSUMÉ

Les neurones en contact avec le liquide céphalorachidien (Nc-LCR) sont situés dans la région épendymaire autour du canal central (CC) dans le tronc cérébral et la moelle épinière et sont conservés chez tous les vertébrés. Ces neurones GABAergiques présentent une morphologie unique avec une seule dendrite qui se projette dans le LCR et se termine par une grande protrusion. Ils expriment sélectivement l'isoforme de polycystine (PKD2L1) des canaux du " Transient Receptor Potential" (TRP), suggérés pour agir comme chimio-récepteur et mécanorécepteur. Compte tenu de leur localisation, de leur morphologie et de l'expression sélective du canal PKD2L1, les Nc-LCR représenteraient une nouvelle population de neurones sensoriels dans le système nerveux central (SNC). Il a été démontré que les Nc-LCR expriment des récepteurs ionotropiques fonctionnels pour le GABA, le glutamate, l'acétylcholine et la glycine, et il est indiqué que les Nc-LCR sont insérés dans un réseau neuronal et que leur activité peut être régulée par des partenaires synaptiques qui restent à identifier. Des études récentes menées chez des vertébrés inférieurs ont démontré que ces neurones modulent activement les activités motrices et le comportement de nage *in vivo*. Jusqu'à présent, peu d'informations sont disponibles sur le rôle des Nc-LCR dans le SNC des mammifères.

Pour mieux comprendre le rôle des Nc-LCR chez les mammifères, il est nécessaire de décrire les propriétés physiologiques et la modulation des Nc-LCR. Dans la présente étude, en utilisant des enregistrements électrophysiologiques dans des coupes aiguës de la moelle épinière et du tronc cérébral ainsi que l'imagerie $Ca^{2+}$, je décris les mécanismes de signalisation du $Ca^{2+}$ dans les Nc-LCR médullo-spinaux de souris. Je rapporte que les Nc-LCR expriment principalement des canaux $Ca^{2+}$ ($Ca_v$s) activés à haute tension (HVA) qui sont modulés par les récepteurs métabolotropiques $GABA_B$ et muscariniques d'acétylcholine. Je décris également l'homéostasie du $Ca^{2+}$ et montre l'implication des réserves intracellulaires calcique dans la régulation du $Ca^{2+}$ intracellulaire. Ensuite, à l'aide d'enregistrements simultanés de la protrusion et du soma Nc-LCR, je démontre leur relation fonctionnelle et indique que la protrusion serait dépourvue de conductance ionique active.

Au niveau du réseau, il a été démontré que les Nc-LCR reçoivent des entrées synaptiques. Nous montrons ici qu'ils sont liés synaptiquement aux neurones GABAergic et glutamatergiques et que les récepteurs $GABA_B$ modulent la neurotransmission des deux populations neuronales dont la localisation reste à déterminer.

Enfin, une question cruciale sur les Nc-LCR chez les mammifères concerne leur rôle dans l'activité du SNC et en particulier dans le réseau moteur spinal. Pour répondre à cette question, nous avons développé des modèles de souris chimiogénétiques (DREADD) et optogénétiques (channelrhodopsin) afin de pouvoir manipuler sélectivement l'activité des Nc-LCR et démontrer leur fonction dans un modèle plus intégré. A ce jour, j'ai validé ces modèles *in vitro* et montré que l'approche optogénétique permet de manipuler l'activité des Nc-LCR pour évaluer leur rôle *in vivo*.

Dans l'ensemble, les résultats de mon étude de doctorat contribuent à mieux comprendre les Nc-LCR médullo-spinaux des mammifères en fournissant des informations précieuses sur leur physiologie et leur modulation. Ceci ont également ouvert la voie à d'autres études menées dans le cadre d'une préparation *ex vivo* ou de modèles *in vivo* pour démontrer leur rôle dans la régulation de l'activité du SNC.

**Mots clés :** neurones au contact du LCR, PKD2L1 canal, calcium, récepteur $GABA_B$, souris, moelle épinière

# THE AIM OF THESIS

My PhD thesis focuses on peculiar neurons in contact with the cerebrospinal fluid (CSF). These CSF-contacting neurons (CSF-cNs) located in the ependymal region around the central canal (CC) in the spinal cord and the brainstem present characteristic enlargement or "bud" at the end of dendritic process that directly contacts the CSF (Orts-Del'Immagine *et al.*, 2012; Marichal *et al.*, 2009; Djenoune *et al.*, 2014; Vigh-Teichmann & Vigh *et al.*, 1989). Although these neurons are well described at the histological level, their function in mammalian central nervous system (CNS) remains largely unknown. Several groups, including the laboratory that I am enrolled in, demonstrated that medullo-spinal CSF-cNs represent GABAergic neurons which selectively express the Polycystin Kidney Disease 2-Like 1 (PKD2L1) channel, a member of "Transient Receptor Potential" (TRP) superfamily that acts as chemosensor or mechanosensor. As shown by my team, PKD2L1 presents spontaneous activity at the level of the unitary current and it is capable of modulating the excitability of CSF-cNs (Orts-Del'Immagine *et al.*, 2012, 2015). Regarding the localization of CSF-cNs between the CSF and parenchyma, their characteristic morphology and selective expression of PKD2L1 channel strongly suggest that CSF-cNs might represent a novel population of sensory neurons within the CNS, capable of regulating their activity in response to changes in CSF composition or flow. Finally, my team demonstrated that CSF-cNs express functional ionotropic receptors for GABA, glutamate, acetylcholine and glycine (Orts-Del'Immagine *et al.*, 2012, 2015). However, only GABAergic, glutamatergic and glycinergic receptors were shown to be involved in synaptic transmission. These results indicate that CSF-cNs are inserted in a neuronal network and that their activity may be regulated by synaptic partners which remain to be identified. However, whether metabotropic receptors also participate in synaptic transmission in medullo-spinal CSF-cNs remains unknown.

So far, little information is available regarding the role of CSF-cNs in mammalian CNS. Recent studies carried out in lower vertebrates (lamprey, zebrafish) demonstrated that these neurons actively modulate motor activities and swimming behavior *in vivo* (Wyart *et al.*, 2009; Fidelin *et al.*, 2015; Böhm *et al.*, 2016; Jalalvand *et al.*, 2016b). Nevertheless, similar role of CSF-cNs in mammalian CNS needs to be established. Therefore, my study was divided in two lines of research. My first aim was to describe the properties of CSF-cNs at the cellular level, and in the second axe of my study I aimed to investigate the role of CSF-cNs in

more integrated systems. Thus, to understand better the role of CSF-cNs in mammals, it is necessary to describe the physiological properties and modulation of CSF-cNs at the cellular level. In the first part of my study I focused on voltage-dependent $Ca^{2+}$ channels ($Ca_v$s) known to undergo the modulation by metabotropic receptors. As we recently demonstrated, CSF-cNs express metabotropic receptors for GABA, $GABA_B$ (Jurčić *et al*., 2019). Here, I looked for expression of $Ca_v$s and their modulation by metabotropic receptors. Next, I focused on regulation of $Ca^{2+}$ signaling in CSF-cNs with the aim to describe the mechanisms involved in regulation of intracellular $Ca^{2+}$ concentration in mouse medullo-spinal CSF-cNs, and the obtained results were expected to better understand the physiology of CSF-cNs.

As previously mentioned, the 'bud' of CSF-cNs directly contacts the CSF, suggesting that it could act as receptor pole of CSF-cNs able to receive the information that diffuse in the CSF, and to transmit them towards the parenchyma and postsynaptic partners of CSF-cNs in mouse, which are still unknown. It could further act as a secretory pole of CSF-cNs able to release the information directly into the CSF. To reveal the function of the 'bud', I focused on describing its properties and its relationship with soma, which are still unknown.

Finally, to understand the role of CSF-cNs in the CNS, it is important to describe the projectory path of their axons and their postsynaptic partners. In the last part of my thesis, I developed two transgenic mouse models. One of them is chemogenetic model, in which CSF-cNs express DREADDs, mutated human muscarinic receptors that can inhibit the neuronal excitability. Another model is optogenetic model, where the excitability of CSF-cNs expressing light-gated channel, channelrhodopisn-2, could be elicited by the light. These models are expected to understand better the role of CSF-cNs in more integrated systems.

# ACKNOWLEDGEMENTS

*At the end of this important chapter of my life, I would like to thank everybody who helped me enormously to come to this point, at the end of my PhD, by giving me a lot of support and many valuable advices which finally gave me the strength to accomplish one of my dreams.*

*Huge thanks to my supervisors, Pr. Jérôme Trouslard and Dr. Nicolas Wanaverbecq, who enabled me to explore the magnificent world of neuroscience and who turned my initial fear of electrophysiology into a passion. Thank for sharing your knowledge with me, I appreciate a lot your help and advices, you motivated me to accomplish more than I was thinking I was able. Thank you for giving me the chance when you accepted me to be a part of your team. From the first day, I enjoyed every moment spent in the lab. Surrounded by such a positive energy and huge support, you gave me the strength to give my best, every day.*

*Thank to the members of the jury for accepting to participate in my thesis defense but also for reading and evaluating my work.*

*Thank to other members of the team, Riad, Anne and Caroline for your advices, conversations and support. It was a pleasure to be a part of such an experienced team. Another thanks to former team members, Ghizlane, Lourdes, and Coraline, you made me laugh a lot with you. Thank to everybody that I was working with while our lab was still at the faculty of St Jerôme. Christine, Florent, Sandrine, Caroline, Adel, and the members of Biomeostasis, thank you for accepting me from the very beginning when I didn't know a single french word. After our morning coffees, my days were starting with joy.*

*A huge thank to my parents for believing in me, supporting me, and for standing by my side. With our conversation, you gave me back the confidence when I missed it. Thank you for all your help and your advices, and for going with me through this important path of my life.*

*Thank to my sister for our conversations and all small talks. Thank you for being here for me, while still being so far away, and for being a part of this adventure of my life. Danijel, thank you for your support and for organizing such relaxing vacations, especially summer ones!*

*My dear Ema, thank you for your laughs. You are the best thing that ever happened to me (and all of us). Thank you for bringing a lot of joy in our lives, you know the best how to brighten every day.*

*Thanks to my friends, wherever you are. Even if some of you are far away, you're always by my side. Romain, thank you for being here for (and with) me and for supporting me during the great part of my thesis. Thank you for everything you did for me, for all the conversations we had when I needed it most, and for all our laughs and moments we spent together. Kévin, thank you for your friendship and for making my first days in France easier.*

*Thank you for your positive energy, for your laughs and conversations and for our cake baking competition. You're the best karaoke singer I know.*

*Thanks to my friends and colleagues, Nejada, Marcel and Irene, for your advices, whether about the life or the science. You helped me to stay motivated while writing my thesis, and to maintain my daily energy level with our coffees.*

*Thanks to the students that spent their traineeship in our lab, Claudia, Edith, Priscile, Jean-Charles. It was a pleasure and joy to work with you! Thank you for your support during and at the end of my thesis. I am grateful for being your colleague.*

*Another big thank to my friends back in Croatia, who have been there for me since a long time. Ana, Iva, Antonela, thank you for all our coffees, and laughs. Thank you for helping me when I needed it. We went through so many things together, and I hope there are still many years to come to enjoy each other company and friendship.*

*Thank to Ana and Džejla. You helped me to realize that life gives us lessons every day, and that we should be strong and always choose the way which will enable us to enjoy every single moment.*

*Thank to Carola in Germany, for being the best roommate I could wish for. Thank you a lot for your support and for fun times together!*

*There are a lot of thanks, but there are still not enough words to express my gratitude to everybody that I was surrounded with during my PhD, but also before. With your help, faith, and friendship, you made my journey through the PhD easier. I have learnt a lot from this experience, and I enjoyed the challenge.*

# I. INTRODUCTION

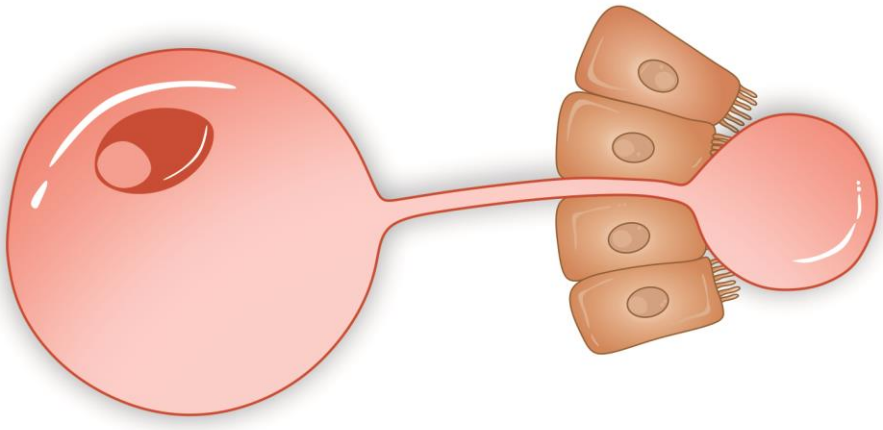

# I. INTRODUCTION

## A) CEREBROSPINAL FLUID

Cerebrospinal fluid (CSF) is a clear fluid which fills the ventricles and subarachnoid space in the brain and central canal (CC) of the brainstem and the spinal cord. It is mainly secreted by the choroid plexuses in the brain and it has an important role in maintaining of the brain homeostasis (Redzic & Segal, 2004; Oresković & Klarica, 2010). In humans, CSF is renewed up to four times per day, accounting for a total of about 600 ml of CSF which is secreted by choroid plexuses. In the average, about 140 ml of the CSF is circulating in the central nervous system (CNS) between the exchanges (Redzic & Segal, 2004). In mice, the total CSF volume of 40 µl is replaced 12 to 13 times per day (Rudick *et al.*, 1982; Oshio *et al.*, 2005; Simon & Iliff, 2016). Classically, CSF provides mechanical support to the brain and it reduces its weight for about 25% (Redzic & Segal, 2004). In addition, it removes the toxic waste from the CNS, and it also participates in the communication between the CNS (Di Terlizzi & Platt, 2006; Iliff *et al.*, 2012). Any changes in the production, secretion or absorption of the CSF lead to development of various pathologies. Therefore, regarding the importance of CSF in the CNS, its main properties are going to be further described.

### 1. CHOROID PLEXUSES ARE THE MAIN SOURCE OF THE CEREBROSPINAL FLUID

CSF represents the main extracellular fluid that fills the ventricles of the brain, subarachnoid space around the brain and CC in the spinal cord. It is separated from surrounding tissues by ependymal cells lying the ventricles and canal, and pia that is lying over the surface of the brain (Wright, 1978; Brown *et al.*, 2004). CSF is a complex solution which is continuously produced and secreted by epithelial cells of four choroid plexuses located in the brain (Brown *et al.*, 2004). Two of them are found in lateral ventricles, one in the 3$^{rd}$ ventricle and one in the 4$^{th}$ ventricle (Sakka *et al.*, 2011). At the microscopic level, choroid plexuses are branched, leaf-like structures that are formed of villi projecting into the ventricles of the brain (Figure 1.). Each choroid plexus contains numerous large blood capillaries that are covered by only one layer of ependymal cells. These capillaries have

fenestrations which permit the passage of small hydrophilic molecules into the interstitial fluid of choroid plexus (Brown *et al.*, 2004; Redzic & Segal, 2004). The epithelial cells of choroid plexuses are connected with tight junctions (zonula occludens; Brown *et al.*, 2004) which are short and located close to the apical side of the tissue that is in contact with the CSF. These connections restrict the movement of different ions and molecules from the blood into the CSF since there is no extracellular space between the ependymal cells. Because of such tight connections between the epithelial cells, tight junctions form the blood-CSF barrier. Moreover, choroid plexuses contain mitochondria and endoplasmic reticulum (ER) and have larger surface due to folded basolateral membrane, which are common features of secretory cells (Brown *et al.*, 2004). The larger surface of the cells provides larger area available for both exchange of molecules between the cells and the CSF, and their absorption. Although the highly vascularized choroid plexuses represent the main production site for the CSF, it can also be derived from interstitial (extracellular) fluid originating from the brain cells and cerebral capillaries where CSF can be produced by the ultrafiltration across the microvessels (Redzic & Segal, 2004; Sakka *et al.*, 2011).

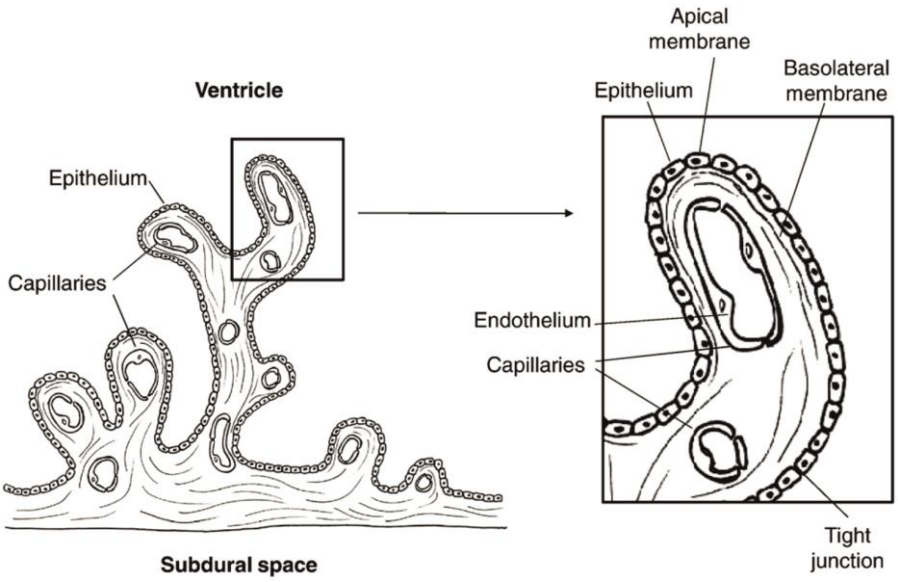


**Figure 1. Schematic illustation of choroid plexus structure.**

Choroid plexus is a branched structure with the villi that project into the brain ventricles. Each choroid plexus contains blood capillaries covered by one layer of ependymal cells. Adjacent ependymal cells are connected with tight junctions (inset). Drawing from Oreskovic & Klarica, 2010.

Choroid plexuses constantly produce the CSF in order to maintain the metabolic balance in the CNS, and in humans the volume of CSF is about 140 ml. Nevertheless, this relatively

small amount of the CSF is produced fast at a rate of 0.2 ml/min per gram of plexuses whose mass in humans is about 2 g (Sakka *et al.*, 2011). CSF is replaced four times per day, leading to a total amount of 600 ml of CSF produced in humans per day (Redzic & Segal, 2004). In mice, CSF is produced at a rate of 0.38 µl/min, and total CSF volume of 40 µl is renewed up to 13 times per day (Rudick *et al.*, 1982; Oshio *et al.*, 2005; Johanson *et al.*, 2008; Simon & Iliff, 2016). Fast rate of CSF production is possible due to high vascularization of choroid plexuses and rich blood supply, the presence of fenestrated capillaries which allow the passage of small molecules, and large surface area of choroid plexuses as a consequence of numerous microvilli that are present on the apical membrane and folded basolateral membrane (Redzic & Segal, 2004). Once produced, CSF is distributed around the CNS, and it can be found mostly in cranial and spinal subarachnoid space, while only small amount is found in the ventricles (Redzic & Segal, 2004; Sakka *et al.*, 2011).

## 2. THE MECHANISM OF CSF SECRETION BY CHOROID PLEXUSES

Secretion of CSF by choroid plexuses depends on active, unidirectional transport of ions from the blood into the ventricles of the brain. The production of CSF in choroid plexus begins with filtration of plasma from permeable choroid capillaries to choroid interstitial space, followed by active transport of ions across the apical membrane of choroid epithelial cells into the ventricles (Johanson *et al.*, 2008; Sakka *et al.*, 2011). This flux of the ions creates an osmotic gradient that is followed by the movement of water and it involves the transporter proteins and ion channels that are expressed on the apical and basolateral membranes of choroid plexuses (Brown *et al.*, 2004; Redzic & Segal, 2004).

Important step in CSF formation is dissociation of carbonic acid into $HCO_3^-$ and $H^+$ ions, reaction catalyzed by enzyme carbonic anhydrase (CA) in the cytoplasm of choroid plexus epithelial cells. Both $HCO_3^-$ and $H^+$ ions are exchanged for $Cl^-$ and $Na^+$, respectively, a transport that is facilitated by ion exchangers or carrier proteins at the basolateral membrane of the epithelial monolayer (Redzic & Segal, 2004; Johanson *et al.*, 2008; Sakka *et al.*, 2011). Therefore, as a consequence of CA activity, $Na^+$-$H^+$ exchanger transports $H^+$ ions out of the cell and it translocates $Na^+$ ions into the cell, while $Cl^-$-$HCO_3^-$ exchanger secrets $HCO_3^-$ out of the cell and transfers $Cl^-$ into the cell, leading to intracellular accumulation of $Na^+$ and $Cl^-$ ions (Figure 2.) (Speake *et al.*, 2001; Redzic & Segal, 2004; Johanson *et al.*, 2008).

At the apical membrane of choroid plexuses, CSF secretion is regulated by ATP-dependent ion pumps that secrets accumulated $Na^+$ and $Cl^-$ ions, but also $HCO_3^-$ and $K^+$ ions, into the ventricular lumen (Figure 2.). $Na^+$ ions accumulated in the intracellular space are extruded into the ventricular lumen by the activity of $Na^+$-$K^+$ ATPase pump which extrudes $3Na^+$ out of the cell at the expense of ATP in exchange for $2K^+$ in the cell (Sakka *et al.*, 2011; Damkier *et al.*, 2013). Generated $Na^+$ gradient activates $Na^+$-$K^+$-$2Cl^-$ cotransporter 1 (NKCC1) that enables bidirectional movement of the ions across the apical membrane of choroid plexus and transport of $Na^+$ back into the cell (Johanson *et al.*, 2008; Damkier *et al.*, 2013). In addition to $Na^+$ ions, $Cl^-$ ions accumulated upon the exchange for $HCO_3^-$ at the apical side and generated $Cl^-$ gradient contributes to activity of NKCC1. With diffusion of $Na^+$ ions in the cell, there is a simultaneous movement of $2Cl^-$ and $K^+$ out of the cell. This extrusion of $K^+$ ions through NKCC1 and potassium ($K^+$) channels present at the apical membrane prevent intracellular accumulation of $K^+$ and control of cellular volume (Redzic & Segal, 2004; Damkier *et al.*, 2013). Finally, the movement of ions from basolateral to apical side generates an osmotic gradient across the membrane of the epithelial cells and movement of the water facilitated by type 1 of aquaporins (aquaporin-1) (Brown *et al.*, 2004; Redzic & Segal, 2004; Damkier *et al.*, 2013).

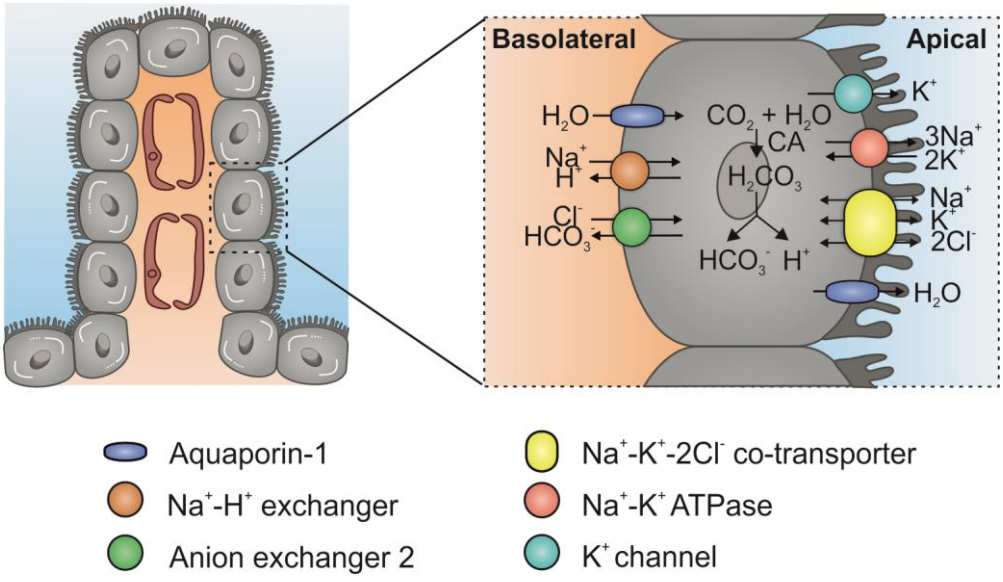


**Figure 2. Schematic illustration of CSF secretion in choroid plexus.**

Inset on the left shows distribution of channels, ion exchangers and co-transporters on basolateral side of choroid plexus that contacts the blood, and on apical side that is in direct contact with the CSF. $Na^+$-$H^+$ exchanger, and $Cl^-$-$HCO_3^+$ exchanger are located on the basolateral membrane, while $Na^+$-$K^+$ ATPase, and $Na^+$-$K^+$-$2Cl^-$ co-transporter are located exclusively on the apical (luminal) side. Potassium channels ($K^+$ channels) and aquaporin-1 are located on both basolateral and apical sides of the choroid plexus. Drawings are adapted from Redzic & Segal, 2004; Oresković & Klarica, 2010.

## 3. CIRCULATION OF THE CSF AND ITS ABSORPTION

Once CSF is produced, arterio-venous pressure gradient represents a driving force for the CSF circulation throughout the CNS. The CSF that is secreted by choroid plexuses in the lateral ventricles flows through two intraventricular foramina of Munro into the third ventricle (Figure 3.). Passing through the cerebral aqueduct of Sylvius, CSF reaches the fourth ventricle and finally the medullo-spinal CC (Sakka *et al.*, 2011). From the fourth ventricle, CSF exits through the paired foramina of Luschka and single foramina of Magendie, to enter the cranial subarachnoid space. Once CSF is in the subarachnoid space, it is absorbed into the blood of the superior sagittal sinus (dural sinus) *via* arachnoid villi or granulations (Wright, 1978; Brown *et al.*, 2004; Redzic & Segal, 2004; Sakka *et al.*, 2011). This main pathway for CSF circulation is called the "third circulation", with the first and second circulation being blood and lymph circulation, respectively (Spector *et al.*, 2015).

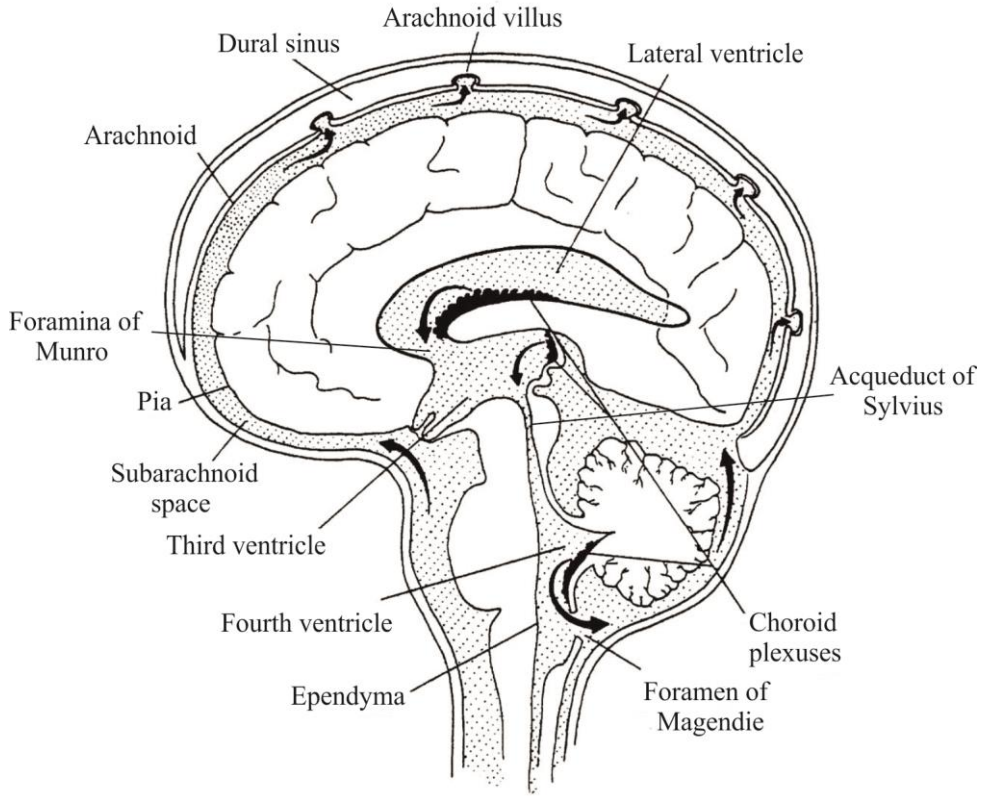


**Figure 3. Schematic illustration of CSF circulation throughout the brain.**

CSF (represented with dots) is produced in choroid plexuses (black structures) and it flows through the brain ventricles in direction represented by black arrows. CSF is absorbed into the arachnoid space via arachnoid villi of the dural sinuses (small black arrows). Drawing is adapted from Brown *et al.*, 2004.

Arachnoid villi are suggested to be the main structures responsible for CSF absorption from the subarachnoid space to the venous blood of the superior sagittal sinus (Oresković & Klarica, 2010). They are invaginations of the arachnoid lined with the endothelium that protrude into the cranial venous sinuses of the brain (Figure 4.). In the spinal cord, arachnoid villi are in contact with venous plexus, but they are also present in the meningeal sheath of spinal nerve roots. Regardless of their localization in the brain or in the spinal cord, the absorption of the CSF by arachnoid villi depends on the CSF pressure. With increased pressure of the CSF, arachnoid villi tend to increase their surface, therefore increasing the area for the CSF absorption (Sakka *et al.*, 2011).

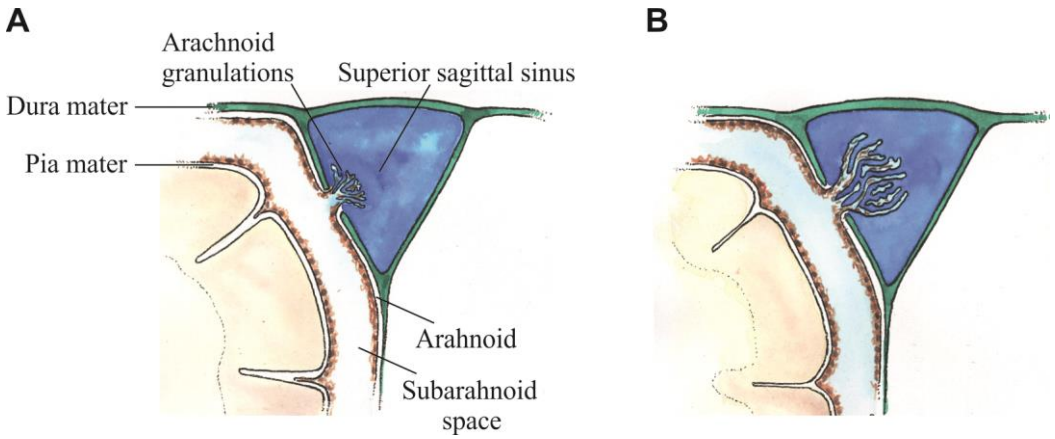


**Figure 4. Arachnoid villi allow the absorption of the CSF.**

**A.** Arachnoid granulations are protrusions of arachnoid into superior sagittal sinuses through dura mater. **B.** The surface of arachnoid villi increases with increased CSF pressure, which enables larger surface for CSF absorption. Drawings are adapted from Sakka *et al.*, 2011.

Along the classical CSF absorption pathway, the fluid diffuses from the subarachnoid space to the lymphatic system (Oresković & Klarica, 2010) through two pathways (Sakka *et al.*, 2011; Khasawneh *et al.*, 2018). One of the pathways involves absorption of the CSF by cranial and spinal nerves in the subarachnoid space which represents a direct route for CSF transport to the lymphatic system. Another extra-arachnoid pathway includes Virchow-Robin perivascular spaces located around the arteries and veins that penetrate the brain parenchyma. When the CSF enters the Virchow-Robin spaces, it can re-enter the subarachnoid space or be reabsorbed by cervical lymphatics (Khasawneh *et al.*, 2018).

## 4. COMPOSITION OF THE CSF

CSF is a fluid which contains numerous proteins, ions, vitamins and neurotransmitters. In general, the composition of the CSF, including concentrations of major cations and anions, pH and osmolality, closely resambles to that of the plasma. With an overall composition and a high salt content (> 150 mmol/L) similar to that observed in the plasma (Bjorefeldt et al., 2018), CSF is often presented as a simple ultrafiltrate of blood plasma. However, more recent measurements have shown that concentrations of sodium, chloride and magnesium ions are higher in CSF than in plasma, while concentrations of potassium and calcium ions are lower (Table 1.) (Sakka et al., 2011). This led to the hypothesis that CSF is the result of active secretion from choroid plexuses. One of the evidences is the careful and precise regulation of CSF composition with maintained CSF ionic concentrations even when the plasma concentrations of the same ions variate (Wright, 1978; Redzic & Segal, 2004; Sakka et al., 2011). Another evidence for CSF specificity is its higher osmolarity compared to the plasma; this would not be the case if CSF was originating from plasma (Speake et al., 2001). Finally, the major difference between CSF and plasma is seen in the protein concentration. In the CSF, protein content is around 25 mg/100 mL, while it is more than 200-fold higher in plasma, and it measures 6 500 mg/100 mL (Wright, 1978; Brown et al., 2004; Spector et al., 2015).

The large fraction of CSF ***proteins*** mainly originates from the blood, while a smaller fraction of proteins is derived from the brain itself (Table 2.). These brain-derived proteins originate exclusively from brain cells (neurons and glial cells) or leptomeningeal cells, however there are proteins with a small, negligleable contribution of blood-derived fraction, that originate from both brain and blood (Reiber, 2001, 2003). It is interesting to note that about 90% of the protein transthyretin, a carrier protein for thyroxine and vitamin A, originate from choroid plexus. Other brain-derived proteins are Tau proteins, S-100 and Neuron Specific Enolase (NSE) that originate from neurons and glial cells. β-trace protein and cystatin C originating from leptomeninges, and angiotensin converting enzyme (ACE) and soluble intracellular adhesion molecule (s-ICAM) which are mostly derived from the blood (Reiber, 2001). Moreover, brain-derived proteins can be distinguished from blood-derived ones as they are present in higher concentrations in the CSF than in plasma (Reiber, 2003).

| | Concentration (mM) | |
|---|---|---|
| | **CSF** | **Plasma** |
| **$Na^+$** | 151 | 155 |
| **$K^+$** | 3.0 | 4.6 |
| **$Mg^{2+}$** | 1.0 | 0.7 |
| **$Ca^{2+}$** | 1.4 | 2.9 |
| **$Cl^-$** | 133 | 121 |
| **$HCO_3^-$** | 25.8 | 26.2 |
| **Glucose** | 4.2 | 6.3 |
| **Amino acids** | 0.8 | 2.3 |
| **pH[a]** | 7.31 | 7.40 |
| **Osmolality (mosmol.Kg/H2O)[b]** | 305 | 299 |
| **Proteins (mg/100 g)[c]** | 25 | 6500 |

**Table 1. The concentrations of main ions, osmolality and pH in CSF and plasma from dog.**

The distribution of main ions described for CSF and plasma determined in dog. Adapted from (Brown *et al.*, 2004). [a]Value is adapted from Wright, 1978. [b]Value is adapted from Damkier *et al.*, 2013. [c]Values are obtained from rabbit and are adapted from Davson *et al.*, 1988.

As already mentioned, most of the proteins found in the CSF originate from blood. The most abundant blood-derived protein in the CSF is albumin, exclusively synthesized in the liver, which accounts for 35 - 80% of total protein concentration in the CSF (Reiber, 2003; Di Terlizzi & Platt, 2006). Because the concentration of the albumin is higher in the blood, any damage of the blood-brain barrier (BBB) causes an increase in concentration of this protein in the CSF as BBB is no longer selective for molecules of different size. Therefore, albumin represents an important marker for BBB permeability which can ease the diagnosis of neurological diseases (Reiber, 2003). In contrast to albumin, γ-globulin constitutes only a minority of total protein concentration (5-12%) (Di Terlizzi & Platt, 2006). The concentration of γ-globulin in the CSF can be used as an indicatior for immunoglobuline production such as immunoglobulin G (IgG) and it is a reliable marker for multiple sclerosis (Paterson *et al.*, 1971).

| Protein | MW (kDa) | CSF concentration (mg/mL) | CSF/serum ratio |
|---|---|---|---|
| Brain-derived proteins | | | |
| S-100B | 21 | 0.0015 | 18:1 |
| Tau Protein | 55 - 74 | 0.0020 | 10:1 |
| β-trace Protein | 25 | 16.6 | 34:1 |
| Cystatin C | 13.3 | 3.1 | 5:1 |
| Transthyretin | 55 | 17 | 1:18 |
| s-ICAM | 90 | 0.0015 | 1:190 |
| NSE | 78 | 8 | 1:1 |
| ACE | 150 | / | 1:100 |
| Blood-derived proteins | | | |
| Albumin | 67 | 245 | 1:205 |
| IgG | 150 | 25 | 1:400 |
| IgA | 170 | 1 | 1:800 |
| IgM | 900 | 0.2 | 1:3400 |

**Table 2. Proteins found in the CSF.**

Concentrations of main brain- and blood-derived proteins found in human CSF are listed in the table. Adapted from Reiber, 2001.

Numerous ***neuromodulators***, including neurotransmitters and neuropeptides, are found in the CSF (Table 3.). CNS resident cells represent the main source of neuromodulators, although the contribution of distinct CNS compartments is still elusive. Such sources are suggested to include subcortical monoaminergic and cholinergic nuclei, hypothalamic neurons but also CSF-contacting neurons which send varicose terminal into the CSF (Vígh *et al.*, 2004; Bjorefeldt *et al.*, 2018). In addition to CNS-derived neuromodulators, diverse blood-derived neuromodulators, such as leptin, can be secreted into the CSF (Bjorefeldt *et al.*, 2018).

Regarding neurotransmitter and neuromodulator concentration, the CSF serves again as readout for pathological state of the CNS. Indeed, during neurological disorders, the

concentrations of the main neuromodulators found in the CSF are prone to change and the most investigated signals are GABA, dopamine or glutamate (Kuroda *et al.*, 1982; Di Terlizzi & Platt, 2006; Bjorefeldt *et al.*, 2018). In humans, levels of GABA, the main inhibitory neurotransmitter in the CNS, are disrupted in several neurological disorders (Kuroda *et al.*, 1982; Orhan *et al.*, 2018). For example, in patients with the cerebellar atrophy, GABA concentration is strongly reduced from 143 pmol/mL (physiological concentration) to 65 pmol/mL (Kuroda *et al.*, 1982) and similar decrease is observed in patients suffering from schizophrenia (Orhan *et al.*, 2018). In contrast, increased levels of GABA are measured in patients with meningitis (309 pmol/mL) (Kuroda *et al.*, 1982). Therefore, variation in CSF GABA content serves as a marker for the diagnosis of the severity in neuronal disorders. In addition, Parkinson's disease is characterized with a loss of dopaminergic neurons in the striatum and of dopamine. Dopamine represents another neurotransmitter found in the CSF composition and changes in its concentrations are also observed (Kuroda *et al.*, 1982; Bjorefeldt *et al.*, 2018; Orhan *et al.*, 2018). However, to date, measurements of the dopamine concentrations in CSF are not reliable diagnostic test for Parkinson's disease (Bjorefeldt *et al.*, 2018).

| | **CSF concentration (mM)** | **Reference** |
|---|---|---|
| **GABA** | $84x10^{-6}$ | (Kvamme, 1988) |
| **Glutamate** | $4.73x10^{-3}$ | (Hashimoto *et al.*, 2005) |
| **Glycine** | 13 | (van der Knaap *et al.*, 1999) |
| **Acetylcholine** | $7x10^{-5}$ | (Welch *et al.*, 1976) |
| **Dopamine** | $39.5x10^{-6}$ | (Strittmatter *et al.*, 1997) |
| **Somatostatin** | $36.2x10^{-9}$ | (Strittmatter *et al.*, 1997) |
| **VIP** | $7x10^{-6}$ | (Juul *et al.*, 1995) |
| **Neuropeptide Y** | $0.2x10^{-7}$ | (Heilig *et al.*, 2004) |
| **Substance P** | $34.2x10^{-9}$ | (Strittmatter *et al.*, 1997) |

**Table 3. Examples of neurotransmitters and neuropeptides present in human CSF.**

## 5. REGULATION OF pH, OSMOLARITY AND PRESSURE OF THE CSF

To maintain brain homeostasis and avoid development of neurological trauma, it is of great importance to preserve stable pH, osmolarity and pressure of the CSF. Regarding the ***pH regulation***, the main determinants of the CSF acid-base balance are carbon dioxide partial pressure ($P_{Co2}$) and the bicarbonate ($HCO_3^-$) concentration. In humans, normal pH and $P_{Co2}$ of the CSF at 37°C are 7.33 and 45 mmHg, respectively (Siesjö, 1972). Several studies have demonstrated that the acid-base balance can differ between cisternal ($4^{th}$ ventricle) and lumbar CSF (van Heijst *et al.*, 1966). The pH of cisternal CSF is around 7.345, and it is slightly elevated compared to pH of lumbar CSF, which is around 7.325 (Siesjö, 1972). Moreover, acid-base balance also varies between cisternal/lumbar CSF, and arterial blood where lower $P_{Co2}$ compared to $P_{Co2}$ of CSF is observed, and it measures around 38 mmHg (Siesjö, 1972; Andrews *et al.*, 1994). In contrast, pH of cisternal and lumbar CSF is reduced by 0.02-0.10 units compared to pH of arterial blood that is around 7.41 (van Heijst *et al.*, 1966; Siesjö, 1972; Andrews *et al.*, 1994).

The main mechanisms involved in regulation of CSF pH are pulmonary ventilation and renal reabsorption of bicarbonate ($HCO_3^-$) that control $P_{Co2}$ and plasma concentration of $HCO_3^-$ respectively. Any changes in arterial $P_{Co2}$ can be transmitted to the CSF that lacks protein buffers and that is highly permeable to $CO_2$ (Siesjö, 1972). Acid-base balance of CSF is maintained by transport proteins on the membrane of choroid plexus epithelial cells, involved in movement of acid-base equivalents, $H^+$ and $HCO_3^-$, between the blood and the CSF (Damkier *et al.*, 2013). At the apical membrane, important role in transport of base has $Na^+$- $HCO_3^-$ cotransporter, NBCe2 (Bouzinova *et al.*, 2005), that mediates the efflux of $Na^+$ and $HCO_3^-$ ions from the choroid plexus into the CSF (Millar & Brown, 2008) and it is most certainly involved in regulation of CSF pH. Furthermore, the significant role of $HCO_3^-$ in CSF pH regulation is seen during prolonged respiratory and metabolic acidosis and alkalosis, as $HCO_3^-$ aims to restore physiological pH value of the CSF within short period of time (Messeter & Siesjö, 1971; Christensen, 1974). The regulation of CSF pH by $HCO_3^-$ is described for sustained respiratory acidosis, a condition in which accumulation of $HCO_3^-$ stabilizes the pH, indicating that such condition generates electrochemical gradient that drives the movement of $HCO_3^-$ from plasma towards the CSF (Messeter & Siesjö, 1971). However, the regulation of CSF pH is complex and it includes mechanisms which should still be described.

***Osmolarity*** of the CSF is another important factor which is constantly controlled in the CSF. In humans, CSF osmolarity at 37°C is around 281 mOsm/kg, although the actual values vary between 269 and 304 mOsm/kg (Goldberg *et al.*, 1965). CSF osmolarity is close to that of plasma, which ranges between 286 and 291 mOsm/kg (Hendry, 1961). Similar values for CSF osmolality were measured in other species, including the dogs (Brown *et al.*, 2004; Redzic & Segal, 2004) and rabbits (Redzic & Segal, 2004). The main ions involved in determination of the CSF osmolality are sodium and chloride ions, the most abundant ions in the CSF (Hendry, 1961; Brown *et al.*, 2004; Di Terlizzi & Platt, 2006). The movements of these ions across the apical membrane of choroid plexus creates an osmotic gradient and movement of water into the CSF mainly through the aquaporin-1 water channel (Speake *et al.*, 2001). Therefore, the levels of sodium and chloride ions should be carefully regulated to ensure normal functioning of the physiological processes.

The regulation of CSF osmolality involves the regulation of salt and water intake and excretion. The brain expresses both sensors for $Na^+$ level and osmosensors which take part in this regulation. Non-specific sodium channels, $Na_x$, are considered as $Na^+$-level sensors in circumventricular organs and appear involved in the control of salt intake. These channels open in response to increased extracellular $Na^+$ concentration. Due to influx, $Na^+$ is accumulated in the cell, leading to the activation of $Na^+$-$K^+$ ATPase pump, extrusion of $Na^+$ out of the cell and activation of anaerobic glycolysis with lactate production. Lactate, as a final product of the reaction, activates GABAergic neurons which in turn regulate neurons involved in the regulation of salt intake (Noda & Sakuta, 2013). In addition to $Na^+$-level sensors, transient receptor potential (TRP) channels represent osmosensors of the brain that are involved in the regulation of water intake. These channels can sense the changes in the cell volume due to changes in extracellular osmolality. In the condition of extracellular hypo-osmolality when the cells volume is reduced, opening of the TRP channels induce $Ca^{2+}$ influx and cell depolarization, leading to increased water uptake (Noda & Sakuta, 2013).

Finally, ***pressure*** of the CSF, or intracranial pressure, is regulated by secretion of the CSF, its absorption by arachnoid villi and resistance to flow. Normal values of CSF pressure are prone to vary between individuals. In adults, the pressure is between 10 – 15 mmHg, and in infants, it is between 3 – 4 mmHg. CSF pressure can change with the systolic pulse wave, respiratory cycle or physical activity (Sakka *et al.*, 2011). In some cases, increased pressure is a consequence of disrupted activity of arachnoid villi due to block by atmospheric aerosol particles, fibrosis, or elevated plasma protein molecules. Such states include cerebral edema,

meningoencephalitis or vitamin A deficiency due to low absorption of CSF by villi (Di Terlizzi & Platt, 2006). In addition, pressure can be regulated by atrial natriuretic peptide (ANP) (Yamasaki *et al.*, 1997; Johanson *et al.*, 2006; Sakka *et al.*, 2011). ANP is known to bind its receptors located on the epithelial cells of the choroid plexus which leads to reduced production of CSF and consequential reduction in CSF pressure. Such regulation of the pressure is described in the patients with intracranial hypertension, in which the increased concentration of ANP correlates with increased CSF pressure (Yamasaki *et al.*, 1997).

## 6. IMPORTANT ROLES OF THE CSF

CSF produced by choroid plexuses fills the ventricles and CC of the CNS, and subarachnoid spaces of the brain and the spinal cord, providing the nutrients and protective effect to the CNS. Several important roles have been attributed to the CSF (Redzic & Segal, 2004; Di Terlizzi & Platt, 2006), including mechanical protection of the brain. Such protection is possible as CSF provides buoyancy to the brain, which is submerged in the CSF. The weight of the brain "floating" in the CSF is reduced for about 65% (from 1500 g to around 50 g) due to the difference in the gravities between the brain and the CSF (Telano & Baker, 2019; Wood, 2013). Furthermore, buoyancy prevents the mechanical injury to the brain parenchyma and cerebral vessels (Telano & Baker, 2019).

One of the active roles of the CSF is to maintain the intracranial pressure, which may vary following changes in posture or respiration. For example, during normal respiratory activity, CSF pressure drops during inspiration, and rises back following expiration. Fluctuations in pressure changes are between 2 and 5 mmHg, or higher upon deep breathing. By displacing the CSF, together with the blood, intracranial volume and pressure remain constant (Di Terlizzi & Platt, 2006).

Another important role for CSF is the removal of toxic waste from the CNS and of cerebral metabolism catabolites with the aim of preserving the constant fluids composition. Since the lymphatic system is not present in the brain, the "waste" is leaving the brain through the perivascular system or through the subarachnoid space into the CSF, where it can be absorbed into the cerebral veins by arachnoid villi (Di Terlizzi & Platt, 2006). Indeed, CSF possesses an alternative pathway for waste removal known as "glymphatic" pathway (Iliff *et al.*, 2012). CSF from subarachnoid space enters the parenchyma via perivascular space

(Virchow-Robin space) that surrounds brain penetrating artery. The outer wall of this perivascular space is lined by astrocytes vascular end-feet which express aquaporin-4, water channels facilitating CSF transport towards the parenchyma. Once CSF reaches the parenchyma, it mixes with interstitial fluid and facilitates waste removal (Iliff *et al.*, 2012; Jessen *et al.*, 2015).

Finally, CSF is involved in communication between distal parts of the CNS by enabling the circulation and transport of active molecules and nutrients, including neurotransmitters or neuropeptides. For that reason, CSF is suggested to represent a way or “active vessel” for transport and distribution of neuromodulators within the brain. In addition, CSF may uptake neuromodulators from the parenchyma that can diffuse from their releasing site along their concentration gradient (Bjorefeldt *et al.*, 2018).

## B) CEREBROSPINAL FLUID - CONTACTING NEURONS

Epithelial cells in the CNS constitue an interface between the CSF and the brain and spinal cord parenchyma. This interface is mainly constituted of cuboidal ependymal cells lining the ventricular cavities and the CC in the brain and spinal cord (Moore, 2016). Ependymal cells extend cilia that direct the CSF flow by beating coordinately in the same direction (Breunig *et al.*, 2010). These cells are closely connected with tight junctions and desmosomes which form a single layer of epithelium (Haemmerle *et al.*, 2015). Tight junctions of ependymal cells of the choroid plexuses found in brain ventricles form blood-CSF barrier (Brown *et al.*, 2004). Among the ependymal cells that form CC lining, there are three main types of the cells that contribute to the complexity of the region around the CC. These cells can be located in close proximity to the CC or in subependymal layer distal from the CC. The most numerous cells forming the lining of the CC are ependymocytes that provide the structural support to the CC in the brainstem and spinal cord. Tanycytes are less numerous cells which extend their basal process towards the blood vessels surrounding the CC and provide physical contact between the CSF and blood vessels (Hugnot & Franzen, 2011; Moore, 2016). Neuronal stem and progenitor cells are also found in this heterogeneous region in the spinal cord (Hamilton *et al.*, 2009; Hugnot & Franzen, 2011). Finally, a peculiar neuronal-like population of cells discovered centuries ago contributes to heterogeneity of the ependymal layer around the CC. These are ***cerebrospinal fluid – contacting neurons (CSF-cNs)*** which send a single dendrite towards the CC where it ends with a ciliated enlargement (Vigh & Vigh-Teichmann, 1998; Böhm *et al.*, 2016). They were first described by Landolt in 1871 (Vígh *et al.*, 2004). Using silver impregnation technique, Landolt showed that bipolar neurons in the retina of amphibians extend processes ending with enlargements called "Landolt's club" (Vígh *et al.*, 2004). Neurons with similar morphology were extensively described by Kolmer in 1921 and Agduhr in 1922 (Vigh & Vigh-Teichmann, 1998) in many vertebrate species. Based on the peculiar location of these intriguing neurons between CSF and parenchyma, Vigh and colleagues named them CSF-cNs (Vigh & Vigh-Teichmann, 1998). Later on, Dale named CSF-cNs neurons as Kolmar-Agduhr (KA) cells to distinguish them from other ciliated ependymal cells (Dale *et al.*, 1987). Except for their characteristic morphology, CSF-cNs selectively express polycystin kidney disease 2-like 1 (PKD2L1) channel which is a member of transient receptor potential (TRP) superfamily, and represents another specific hallmark of these neurons (Huang *et al.*, 2006; Orts-Del'Immagine *et al.*, 2012; Djenoune *et al.*, 2014).

Since their discovery, most studies concentrated on CSF-cN morphology or phenotype, however only recently reasrchers started to investigate their properties and function in the CNS. CSF-cNs are found along the ventricular system and around the CC of all the vertebrates studied so far. They show specific morphology and represent a conserved neuronal type among the species (Vígh *et al.*, 2004). Nevertheless, their role is still poorly described, especially in humans. Based on their localization and morphology, already in the early years of their characterization by Kolmer and Agduhr suggested that they might represent sensory neurons with receptor function (mechanoreceptors and chemoreceptors) that depends on their localization around the ventricular/CC system. This assumption was further supported by their selective expression of chemo-/mechanosensitive PKD2L1 channels. In recent years (see below), several studies mainly carried out in lower vertebrate started to provide insights on their potential role in the CNS (Fidelin *et al.*, 2015; Böhm *et al.*, 2016; Jalalvand *et al.*, 2016*b*). These recent advances in the understanding of medullo-spinal CSF-cNs were largely possible due to development of sophisticated technologies and novel animal models.

## 1. MORPHOLOGY AND DISTRIBUTION OF CSF-cNs

The presence of CSF-cNs was shown in many vertebrates studied so far (Vígh *et al.*, 2004). These neurons were studied extensively by Kolmer and Agduhr, who identified the presence of CSF-cNs in more than 200 vertebrates (Djenoune *et al.*, 2014). Among all the species investigated, CSF-cNs show similar morphology and organization. They are located in the periventricular regions of the brain (Vígh *et al.*, 2004) and in (sub)ependymal layer around the CC in the brainstem (Orts-Del'Immagine *et al.*, 2012, 2014) and the spinal cord (Stoeckel *et al.*, 2003; Marichal *et al.*, 2009; Kútna *et al.*, 2013; Djenoune *et al.*, 2014). CSF-cNs extend short dendritic process towards the CC where it ends with ciliated enlargement that contacts the CSF (Vigh-Teichmann & Vigh, 1989). In lamprey spinal cord, such type of CSF-cNs is referred as *type 1*, while another subpopulation of cells, referred as *type 2*, have smaller soma located away from the CC and long dendrite that extends towards the edge of the lumen (Jalalvand *et al.*, 2014). In mouse brainstem (Orts-Del'Immagine *et al.*, 2014) and zebrafish spinal cord (Djenoune *et al.*, 2014), neurons with similar morphology as CSF-cNs were observed away from the CC, although these neurons lack typical dendritic projection towards the CC. In this chapter, special attention is going to be given on morphology and distribution of the CSF-cNs that are in contact with the CSF (*type 1*).

### 1.1. Morphology and ultrastructure of medullo-spinal CSF-cNs

In most vertebrates, medullo-spinal CSF-cNs are polarized cells whose soma is inserted in subependymal (LaMotte, 1987; Djenoune *et al.*, 2014; Orts-Del'Immagine *et al.*, 2014) or ependymal layer (LaMotte, 1987; Djenoune *et al.*, 2014) around the CC (Figure 5. A). They send a thick neurite arising from the soma towards the CC where it ends with an enlargement, or bud, in contact with the CSF (Figure 5. A) (Djenoune *et al.*, 2014). This neurite was shown to be immunoreactive against the dendritic specific marker (MAP2) in CSF-cNs of mouse brainstem (Figure 5. B, $C_1$) (Orts-Del'Immagine *et al.*, 2014) and therefore of dendritic nature. On the other side, CSF-cNs send a thin process, presumably the axon, towards the parenchyma to yet unknown destination. This process lacks the expression of selective axonal marker NF-160 (Orts-Del'Immagine *et al.*, 2014), and it is also MAP2 negative (Figure 5. C). The authors referred this structure as axon-like projection since its axonal nature could not be confirmed.

***Soma*** of CSF-cNs is a small structure of several micrometers whose shape and diameter can vary between and within the species. Inserted in ependymal or subependymal layer around the CC of the brainstem and the spinal cord, soma can be a rounded structure with an average diameter between 8 and 12 µm (Barber *et al.*, 1982; LaMotte, 1987; Orts-Del'Immagine *et al.*, 2014; Djenoune *et al.*, 2017), or oval, polygonal or rod-shaped with a diameter between 13 and 28 µm (Shimosegawa *et al.*, 1986; Dale *et al.*, 1987). In rat spinal cord, spindle-shaped CSF-cNs were measured to be 22 µm long and 5.3 – 9 µm wide (Barber *et al.*, 1982; Stoeckel *et al.*, 2003). Two types of CSF-cNs, type I and type II, are described in lamprey spinal cord, as soma of type I CSF-cNs is located closer to the CC and it can be distinguished from type II CSF-cNs based on its larger size (and electrophysiological properties, see below) (Jalalvand *et al.*, 2014). Shimosegawa and colleagues (1986) observed different somatic shape of rat spinal CSF-cNs, which was the basis for CSF-cNs classification into three groups (Figure 6.). Type I and Type II groups consist of CSF-cNs that have perikarya of oval or polygonal shape, while group III includes perikarya of rod-like shape which are attached to the ependymal layer (Shimosegawa *et al.*, 1986). This classification also considers the localization or arising site of the axon (see below).

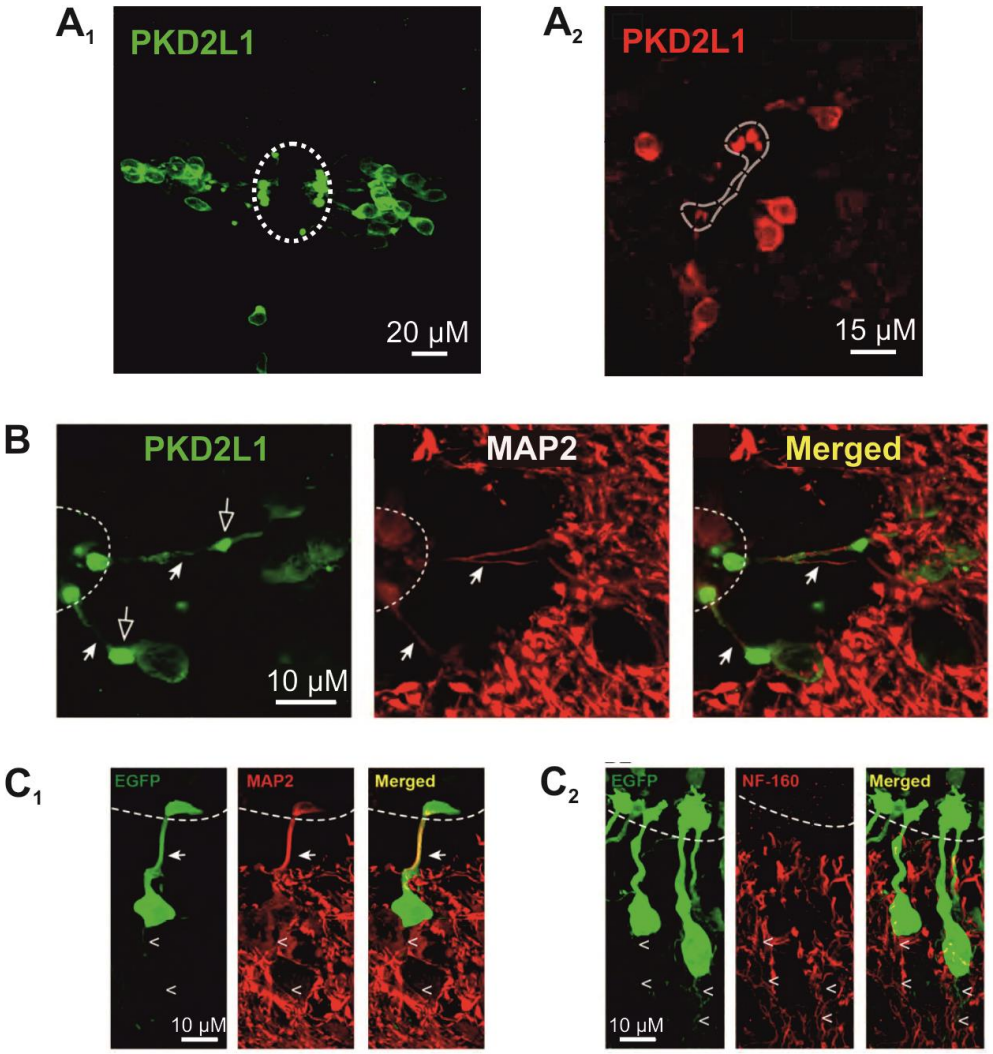


**Figure 5. Morphology of CSF-cNs located around the central canal in the brainstem and the spinal cord.**

**A.** CSF-cNs immunostained against PKD2L1 in murine acute brainstem (**$A_1$**) and spinal cord (**$A_2$**) slices have small, rounded soma and single dendrite that extends towards the CC. Terminal protrusions contact the CSF. **B**. Neurite arising from soma (arrows) has cytoplasmic enlargement (open arrows) and it is immunolabeled against both PKD2L1 and MAP2, indicating that CSF-cNs possess neurite of dendritic nature. **C.** Brainstem sections from PKD2L1:EGFP$^+$ mice are labeled against GFP and MAP2 (**$C_1$**) or GFP and NF-160 (**$C_2$**). MAP2$^+$ neurite (**$C_1$**) is not labeled with NF-160 antibody (**$C_2$**), which confirms its dendritic nature. In contrast, GFP$^+$ processes extending from the soma towards the parenchyma (open arrows) are not labeled with MAP2 (**$C_1$**) nor NF-160 antibodies (**$C_2$**). Figures in $A_1$, B, and C are adapted from Orts-Del'Immagine *et al.*, 2014. Figure $A_2$ is adapted from Djenoune *et al.*, 2014.

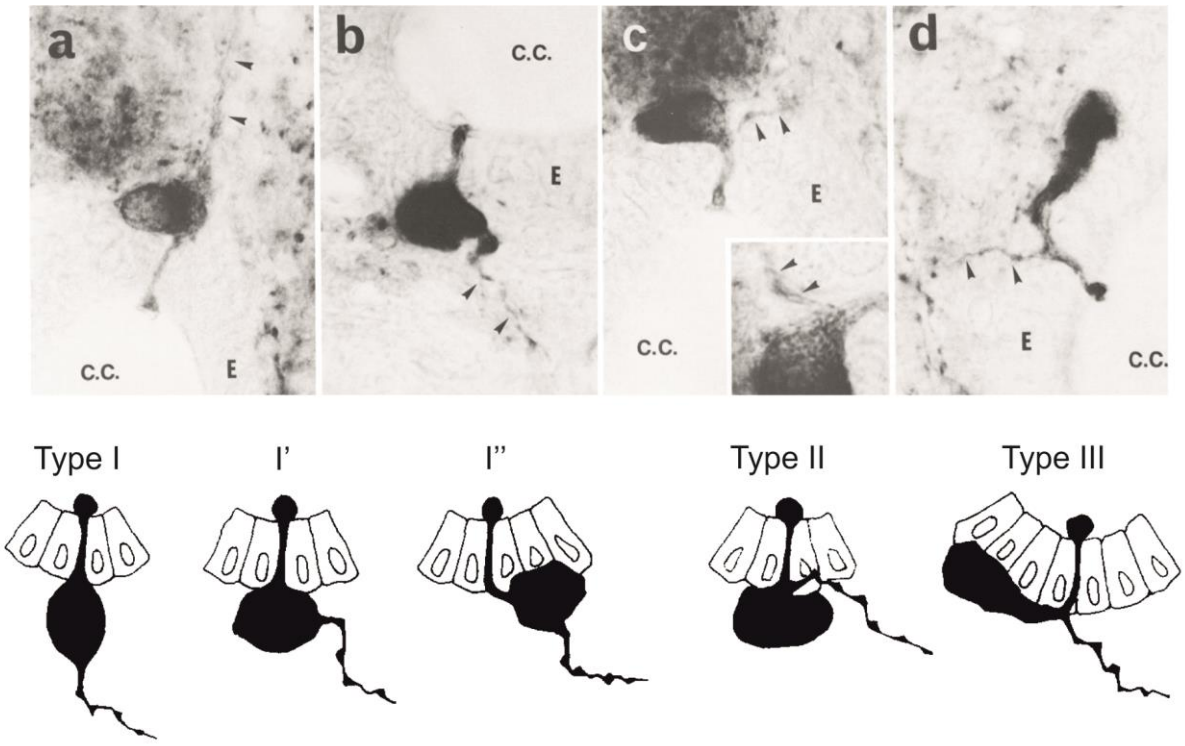


**Figure 6. Representation of different types of CSF-cNs.**

Type I CSF-cNs have oval soma and axon arising from basal (a) or lateral (b) surface of the soma. CSF-cNs with polygonal shaped soma (type II) have an axon arising from dendritic root (c), while type III CSF-cNs are attached to the ependymal layer and possess an axon extending from middle part of dendrite (d). Adapted from Shimosegawa *et al.*, 1986.

Analyzing the ultrastructure of CSF-cNs, Marichal and colleagues (2009) described rounded nucleus of the CSF-cNs that was in contrast to elongated nuclei of surrounding ependymal cells (Figure 7. A). The spherical-shaped nucleus of CSF-cNs was described by Barber and colleagues (1982), that also contrasted with the nucleus shape of adjacent cells, although they shared similar patterns of chromatin (Barber *et al.*, 1982). The perikaryon of CSF-cNs has dense cytoplasm that contains many free ribosomes (Barber *et al.*, 1982; Marichal *et al.*, 2009), rough ER, rounded mitochondria (Barber *et al.*, 1982; Fujita *et al.*, 2012), and Golgi complex (Fujita *et al.*, 2012). In addition, perikarya of medullo-spinal CSF-cNs (Vigh *et al.*, 1983), but also neurons of hypothalamic magnocellular nuclei (Vigh-Teichmann & Vigh, 1989) contain granular vesicles whose diameter is about 130 nm (Vigh-Teichmann & Vigh, 1989).

By performing electron microscopic studies on spinal cord slices from several species, such as rat, opossum, mouse or zebrafish, it was shown that CSF-cNs receive axosomatic synapses originating from unknown synaptic partners (Barber *et al.*, 1982; Vigh *et al.*, 1983; Orts-Del'Immagine *et al.*, 2014; Djenoune *et al.*, 2017) shown to contain granular or synaptic vesicles, which are different from those found in soma of CSF-cNs (Barber *et al.*, 1982; Vigh *et al.*, 1983; Vígh *et al.*, 2004). These synaptic contacts on CSF-cNs were found to contain up to 100 nm large granular vesicles with dense core and were suggested to be of distal projection fibers with hypothalamic origin that may release different bioactive agents, such as oxytocin or neurophysin (Barber *et al.*, 1982; Vigh *et al.*, 1983). Moreover, synaptic terminals onto CSF-cNs may contain small, clear synaptic vesicles suggested to originate from GABAergic neurons located in close proximity of CSF-cNs (Barber *et al.*, 1982). This is in agreement with a recent study which showed that a great number of dot-like structures expressing glutamate decarboxylase enzyme (GAD67) are found around the CC and the surrounding parenchyma, and in close contact with the CSF-cN soma (Orts-Del'Immagine *et al.*, 2014). In addition, the presence of functional GABAergic synapses onto CSF-cNs was confirmed using electrophysiological recordings (Orts-Del'Immagine *et al.*, 2012). Other synaptic inputs, including glycinergic and glutamatergic synaptic entries onto CSF-cNs were observed in the lamprey and mouse spinal cord (Jalalvand *et al.*, 2014; Orts Del'Immagine *et al.*, 2015; Orts-Del'Immagine *et al.*, 2017; Jurčić *et al.*, 2019). In the mouse, serotoninergic, catecholaminergic and cholinergic fibers were also shown to come in the vicinity with CSF-cNs, indicating that different neurotransmitters may be involved in the modulation of CSF-cNs activity (Orts-Del'Immagine *et al.*, 2012). Further, some of nerve terminals onto CSF-cNs showed strong immunoreactivity against Met-Enk-Arg-Gly-Leu and it was suggested that they might affect the activity of CSF-cNs, but their origin remained unknown (Shimosegawa *et al.*, 1986). Taken together, these data indicate that medullo-spinal CSF-cNs are integrated in a synaptic network. Nevertheless, the localization, nature and function of these presynaptic contacts remain to be demonstrated.

A thick process of CSF-cNs, or ***dendrite***, which protrudes into the CC where it forms an enlargement, represents one of the characteristic features of these neurons. Its diameter is measured to vary between 1.4 and 2.9 µm (Shimosegawa *et al.*, 1986), although enlargements on the dendrites of CSF-cNs can often be observed (Orts-Del'Immagine *et al.*, 2014). In mouse, the dendritic length has been reported to vary among CSF-cNs depending on their localization along the medullo-spinal axis as well as around the CC. Thus, ventral CSF-cNs of

the cervical spinal cord have dendrite about 32 µm long, while those located laterally or dorsally present shorter dendrite (about 20 µm long). When moving to more rostral region, the dendrite of ventral CSF-cNs becomes shorter, while that of dorso-lateral CSF-cNs increases (Orts-Del'Immagine *et al.*, 2014). A similar observation was made for CSF-cNs in the zebrafish spinal cord (Djenoune *et al.*, 2017). There, ventral CSF-cNs have shorter and more compact dendrites, while dorsal CSF-cNs have dendrites that extend following the border of the CC (Djenoune *et al.*, 2017). Altogether, these data suggest that CSF-cNs are a heterogenous population of at least two distinct types (ventral and dorso-lateral). Indeed, two distinct types of CSF-cNs with distinct properties and localization around the CC are recently described in mouse (Petracca *et al.*, 2016) and are going to be described later.

Formed by dendritic extension into the CC, the ***bud*** of CSF-cNs is a globular-shaped structure in contact with the CSF whose average diameter is between 1.4 and 5 µm (Barber *et al.*, 1982; Shimosegawa *et al.*, 1986; Orts-Del'Immagine *et al.*, 2014). The bud appears to be tightly connected to neighbouring ependymal cells through tight junction (Stoeckel *et al.*, 2003). Similarly to the soma ultrastructure, bud also contains large granular vesicles (Vigh *et al.*, 1983; Djenoune *et al.*, 2017), the cytoplasm displays mitochondria (Vigh *et al.*, 1983; Fujita *et al.*, 2012), and both rough and smooth ER (Fujita *et al.*, 2012). These features would suggest a secretory function for the bud. However, these assumptions are only based on histological data, but no functional evidences are available.

In all species analyzed, bud presents numerous microvili that can be distinguished from ciliated ependymal cells as they appear longer and thicker (Vigh *et al.*, 1977). The number of stereocilia on CSF-cN enlargement can vary between different species. In opossum, they are more numerous than in guinea pig, while in mouse, only few stereocilia are present (Vigh *et al.*, 1983). The expression of numerous stereocilia on terminal enlargements of CSF-cNs, as seen in mechanoreceptor cells, led to the assumption that these neurons act as neurosensory cells with regulatory function that remains to be determined (Vigh *et al.*, 1977, 1983). Further, bud of CSF-cNs bears a cilium of different types (Dale *et al.*, 1987; Vigh-Teichmann & Vigh, 1989; Orts-Del'Immagine *et al.*, 2014). Immunohistochemical studies carried out in mouse (Orts-Del'Immagine *et al.*, 2014) and lamprey (Jalalvand *et al.*, 2016*b*) CSF-cNs showed that bud is immunoreactive against marker for microtubule-based cilia, acetylated α tubuline (Ac-αTub). Bud of medullo-spinal CSF-cNs of turtle (Vígh *et al.*, 2004) and zebrafish (Djenoune *et al.*, 2017) bears a longer cilium formed by microtubules in the 9 x 2 + 2 arrangement

(Figure 7. B, C) where 9 pairs of microtubule doublets surround a central pair of microtubules, which is characteristic for motile kinocilia. In contrast, 9 x 2 + 0 patterns are seen in hypothalamic CSF-cNs (Vigh-Teichmann & Vigh, 1989; Fujita *et al.*, 2012), a microtubular organization typical of non-motile or primary cilia that have 9 pairs of microtubule doublets, but lack the central pair of microtubules. Similar results were obtained in rat by Marichal and Stoeckel and their colleagues, and the cilium was suggested to be of primary type, with adenylate cyclase 3 (AC3) being a characteristic marker (Stoeckel *et al.*, 2003; Bishop *et al.*, 2007; Marichal *et al.*, 2009). In mouse, immunohistochemical studies were carried out to demonstrate the presence of a primary cilium on the bud (Orts-Del'Immagine *et al.*, 2014). However, to date, such cilium was not observed on the bud but on the perikarya of CSF-cNs.

In addition to dendrite projecting to the CC, CSF-cNs extend the ***axon*** arising from the soma towards the parenchyma. Considering the portion of the soma where the axon is arising from, CSF-cNs were classified into three groups corresponding to those described based on the somatic shape (Figure 6.). Type I neurons are subdivided into two groups as they have axons that are emitted from basal or lateral surface of the soma. Axons that arise from soma at dendritic root form the second group of neurons or Type II. In some cases, axon can be emitted from the middle portion of the dendrite, therefore giving rise to Type III CSF-cNs (Shimosegawa *et al.*, 1986).

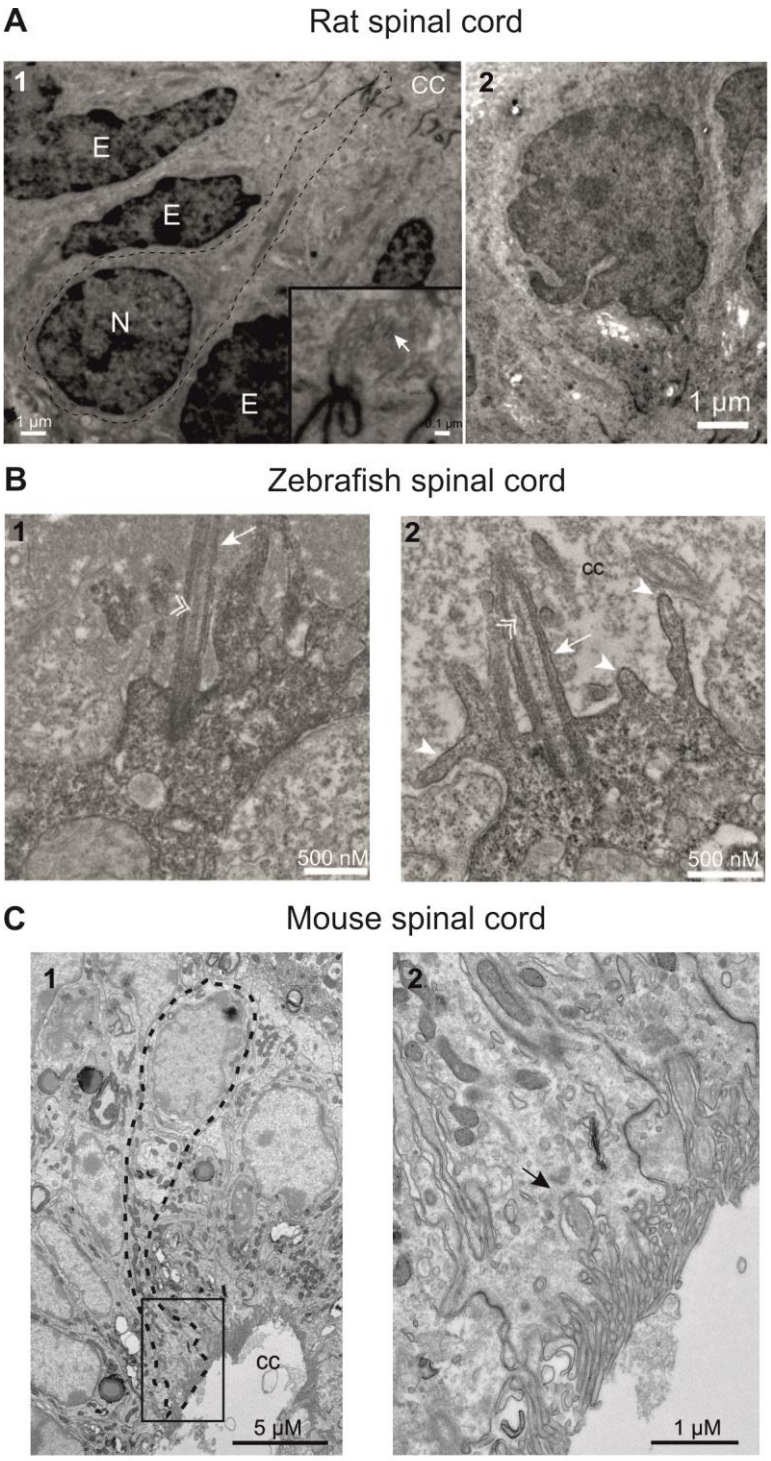


**Figure 7. Ultrastructural properties of CSF-cNs in spinal cord from different species.**

**$A_1$**. Micrograph of CSF-cN (dotted line) obtained with transmission electron microscopy (TEM) in spinal cord slice from neonatal rat. Rounded nucleus of CSF-cN (N) contrasts elongated nuclei of surrounding ependymal cells (E). Inset shows single cilium (arrow) extending from the bud. **$A_2$**. Cytoplasm of CSF-cN contains free ribosomes. **B.** TEM was also used to image dendritic terminals of ventral (**$B_1$**) and dorsal (**$B_2$**) CSF-cNs in zebrafish larva spinal cord. The arrow indicates single cilium with central pair of microtubules (double arrowhead) along the axoneme that is surrounded by microvilli (arrowhead in **$B_2$**). **$C_1$.** Micrograph of CSF-cN (dotted line) obtained with TEM in mouse spinal cord slice that contacts the central canal (cc). Square indicates dendritic terminal in (**$C_2$**) which

bears a single cilium (arrow) presumably without the central pair of microtubules. Figures in A are adapted from Marichal *et al.*, 2009, figures in B are adapted from Djenoune *et al.*, 2017, while figures in C are from personal dataset.

### 1.2. Axonal projections of CSF-cNs and their synaptic partners

In many studies, the axonal projections of CSF-cNs were traced with the aim to target their synaptic partners. Early study carried out in the spinal cord of turtle described CSF-cN projections along the whole projection path (Vigh *et al.*, 1977). Arising at the basal surface of the soma, axons of CSF-cNs converge on lateral sides of the CC where they form thin, unmyelinated tracts at the borderline of the central grey matter. There, they turn ventrolaterally towards the end of ventral column where they separate and enter the white matter. Finally, these tracts end with small enlargements at the ventrolateral surface of the spinal cord, where they come in contact with the external basal lamina (Figure 8. A) (Vigh *et al.*, 1977). The axonal terminals contain granular and synaptic vesicles of different sizes (Vigh *et al.*, 1983). They can vary from small vesicles with an average diameter of 800 Å to larger vesicles with an average diameter of 1400 Å (Vigh *et al.*, 1977). The terminals are connected to the basal lamina with hemidesmosome-like structure and these sites represent an accumulation site for synaptic vesicles, called “synaptic hemidesmosome” (Vigh *et al.*, 1977).

In zebrafish, axons were shown to be ipsilateral (Wyart *et al.*, 2009; Fidelin *et al.*, 2015; Djenoune *et al.*, 2017) and ascending (Fidelin *et al.*, 2015; Djenoune *et al.*, 2017), and to extend collaterals over two to six spinal cord segments (Wyart *et al.*, 2009). As seen for dendrites, axonal projections between ventral and dorsal CSF-cNs differ in the length of the axons, their arborizations and number of axonal branches, which are shown to be larger in ventral CSF-cNs (Figure 8. $B_1$). Axonal projections of ventral cells also cover more ventral regions of the spinal cord (Fidelin *et al.*, 2015; Djenoune *et al.*, 2017). Interestingly, ventral and dorsal CSF-cNs in zebrafish larvae were shown to target distinct projection partners. Djenoune and colleagues (2017) showed that only ventral CSF-cNs (Figure 8. $B_2$, a) contact caudal primary (CaP) motoneurons by forming basket-like structures around their soma. In contrast, only dorsal CSF-cNs (Figure 8. $B_2$, b) project onto ventrolateral glutamatergic (V0-v) interneurons (Djenoune *et al.*, 2017) which were previously reported to receive inhibitory GABAergic inputs from CSF-cNs (Fidelin *et al.*, 2015). However, commissural primary

ascending (CoPA) sensory interneuron represents a neuronal target for both ventral and dorsal CSF-cNs (Djenoune *et al.*, 2017).

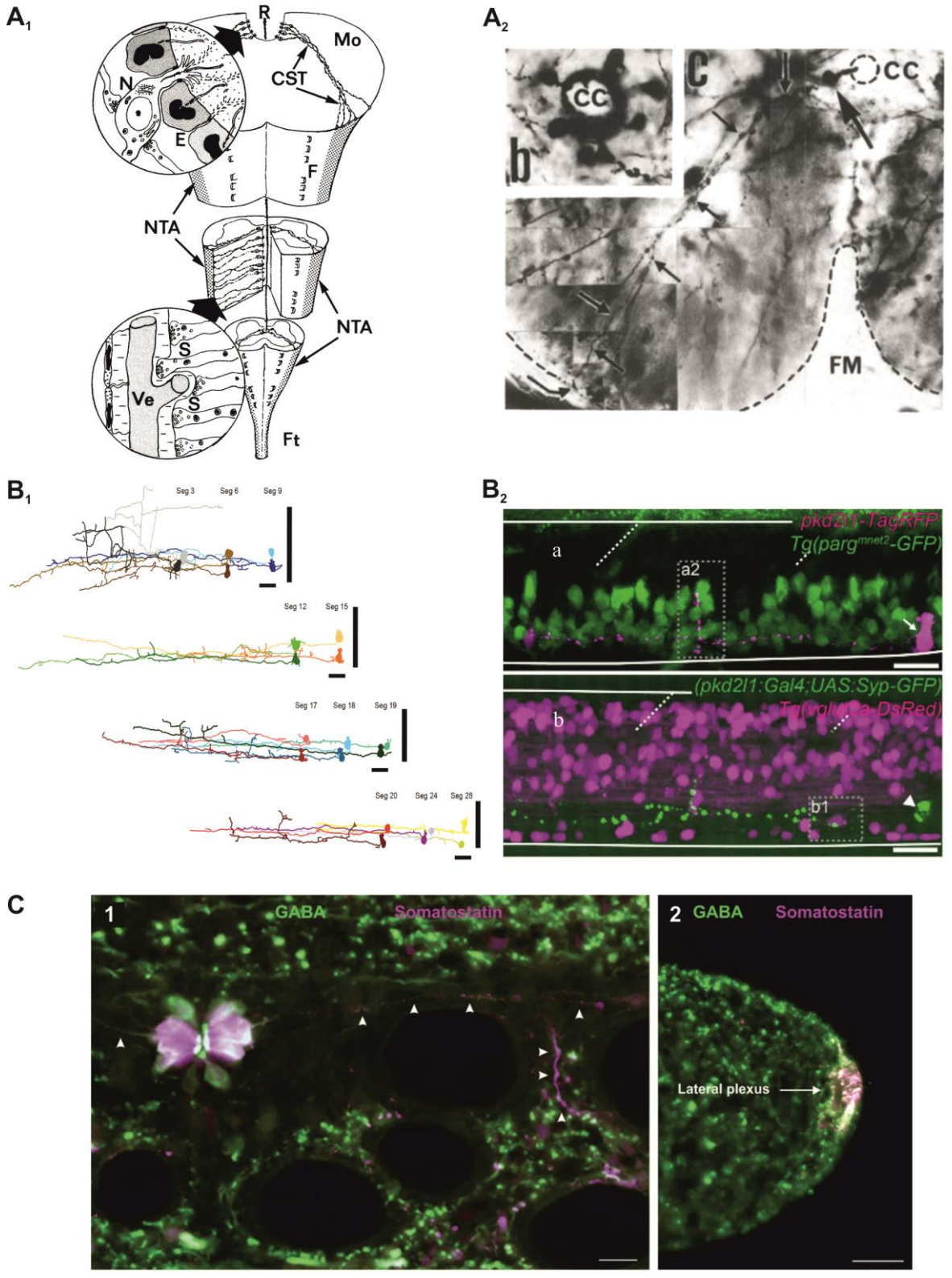


**Figure 8. Axonal projections of CSF-cNs described in various species.**

**Figure 8. Axonal projections of CSF-cNs described in various species. A.** Schematic representation of spinal CSF-cNs organization. **$A_1$.** CSF-cNs form thin tract of axons in the grey matter of the spinal cord. The axons run ventrolaterally towards the end of ventral column where they enter the white matter and form the terminal at the surface of the spinal cord. CSF-cNs also receive synaptic inputs on their soma from unknown partners. **$A_2$.** In turtle spinal cord, CSF-cNs are arranged around the CC (inset) and extend the axon towards the ventrolateral surface of the spinal cord. **$B_1$**. Reconstruction of ventral and dorsal CSF-cNs from different segments in spinal cord of zebrafish larva. There is diversity in axonal projections of ventral and dorsal CSF-cNs. **$B_2$.** In zebrafish larva spinal cord, ventral CSF-cNs (**a**, magenta, arrow) contact CaP motoneurons (green, dotted square, a2). Dorsal CSF-cNs (**b**, green, arrowhead) contact V0-v interneurons (magenta, dotted square, b1). **C.** Micrograph on left (1) showing CSF-cNs in the lamprey spinal cord located laterally around the CC and immunoreactive to GABA (green) and somatostatin (magenta). They extend fibers bearing varicosities (arrowheads). Micrograph on right (2) shows co-localization of GABA and somatostatin in the lateral plexus at the margin of the lamprey spinal cord. Figures in A are adapted from Vigh *et al.*, 1977, figures in B from Djenoune *et al.*, 2017, and figures in C from Jalalvand *et al.*, 2014. cc: central canal; CST: centrosuperficial tract formed by CSF-cNs axons; E: ependymal cells; F: fila radicularia motorica; FM: anterior median fissure; Ft: terminal filum; Mo: medulla oblongata; N: CSF-cN; NTA: nerve terminal area formed by CSF-cNs axons; R: Reissner's fiber; S: different types of synaptic hemidesmosomes on the basal lamina of the surface of the spinal cord; Ve: meningeal vessel. Scale bars = 20 µm in $B_2$, $C_1$; 50 µm in $C_2$.

CSF-cNs of type 1 located in the lateral quadrants around the CC are immunoreactive to GABA and somatostatin (Figure 8. $C_1$). They were shown to project laterally the varicose axons towards the dendrites of mechanosensor cells known as edge cells in the lamprey spinal cord (Jalalvand *et al.*, 2014). These axons ramify ventrolaterally before they reach the lateral plexus at the margin of the spinal cord (Figure 8. $C_2$). In contrast, type 2 CSF-cNs lack the expression of GABA and somatostatin, extend their smooth processes towards the lateral margin of the spinal cord, but do not ramify (Jalalvand et al., 2014).

Unlike in reptiles and lower vertebrates, the projection paths for axons of CSF-cNs in mammals are poorly described. In the rat spinal cord, it was shown that axonal processes run dorsally before they turned ventrolaterally, but it could not be followed for longer than 150 µm. Therefore, its terminals could not be determined (Shimosegawa *et al.*, 1986). Further, in the region between low thoracic and lumbar segments of the rat spinal cord, $P2X_2$ positive small patches were observed in the dorsal regions of the corticospinal tract. $P2X_2$ positive structures were also seen apposed against the dorsolateral walls of the ventral median fissure (Figure 9.) (Stoeckel *et al.*, 2003). These structures were immunolabeled against GABA, GAD (Figure 9.) and synaptotagmin, and therefore suggested to represent CSF-cN axons forming bundles distributed irregularly around the CC (Stoeckel *et al.*, 2003). Similar

projection pathway was observed in the cat, where CSF-cNs form small bundles of varicose fibers that were traced longitudinally along the CC (LaMotte, 1987). In mouse, to date, there is no evidence for the projection path of CSF-cNs. Using specific transgenic mouse model where CSF-cNs selectively express eGFP, their axons could be observed projecting laterally in coronal slice preparations (Orts-Del'Immagine *et al.*, 2012). However, they could only be followed over short distances, most probably because they would rapidly turn to the ventral regions to form the longitudinal fiber tracts observed in rat.

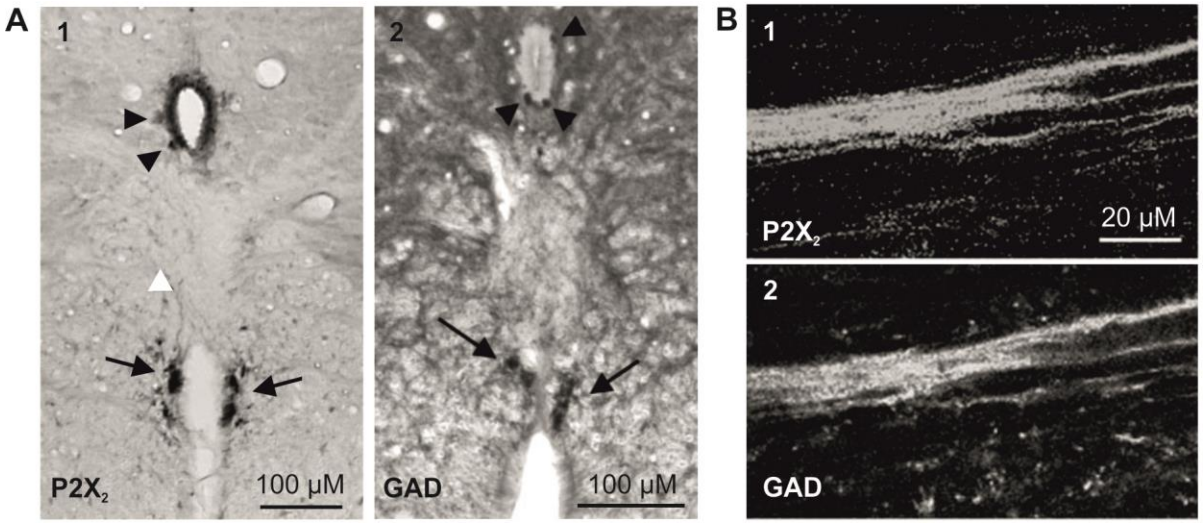


**Figure 9. Projections of CSF-cNs in rat spinal cord.**

**A.** In transverse spinal cord slices, $P2X_2$ (**$A_1$**) and GAD (**$A_2$**) label CSF-cNs cellular bodies (arrowhead), fibers extending from the CSF-cNs (**$A_1$**, white arrowhead), and patches apposed against the wall of ventral median fissure (arrows). **B**. In longitudinal spinal cord slices, axonal fibers are labeled against $P2X_2$ (**$B_1$**) and GAD (**$B_2$**). Adapted from Stoeckel *et al.*, 2003.

### 1.3. Distribution and localization of CSF-cNs

CSF-cNs represent a heterogeneous population of neurons because of variances present at the morphological level, but also because of different localization among the CNS. CSF-cNs are found in contact with the ventricular systems of the brain and the CC in the brainstem and spinal cord, in the regions that contain the CSF. The main type of CSF-cNs is located in medullo-spinal area (Vígh *et al.*, 2004), but the presence of CSF-cNs was reported in several brain regions, including hypothalamus, circumventricular organs (paraventricular organ and

vascular sac), photoreceptor areas, or telencephalon (Vigh & Vigh-Teichmann, 1998; Vígh *et al.*, 2004; Jalalvand *et al.*, 2018).

Medullo-spinal CSF-cNs extend from the medulla oblongata just before the CC expands into the cavity of the 4$^{th}$ ventricle to the terminal filum (Vígh *et al.*, 2004). In the mouse spinal cord, they are present along the CC, with a soma often inserted in subependymal (Djenoune *et al.*, 2014; Orts-Del'Immagine *et al.*, 2014, 2017) or intraependymal layer (Orts-Del'Immagine *et al.*, 2017) around the CC. Regarding the distribution of CSF-cNs around the CC, in the rat spinal cord, CSF-cNs were the most numerous in thoracic spinal cord, followed by cervical spinal cord, while no CSF-cNs were found in medulla oblongata nor in coccygeal region of the spinal cord (Shimosegawa *et al.*, 1986). In contrast, in mouse (Orts-Del'Immagine *et al.*, 2014) and zebrafish (Djenoune *et al.*, 2014) spinal cord, CSF-cNs are found along its whole length, but their density seems to decrease from caudal levels towards the rostral levels of the spinal cord and brainstem, where the CC opens into the 4$^{th}$ ventricle (Orts-Del'Immagine *et al.*, 2014, 2017).

The organization of CSF-cNs around the CC is also different between different levels of the medullo-spinal axis (Figure 10. A). They are mostly organized in a dorso-ventral axis in cervical spinal cord, and this organization changes to a nearly exclusive lateral localization towards more rostral levels (Figure 10. B) (Orts-Del'Immagine *et al.*, 2014, 2017). In zebrafish embryonic and adult spinal cord, CSF-cNs are organized in two rows along the CC, lining dorsal and ventral sides of the CC (Figure 10. B) (Djenoune *et al.*, 2014). Based on this organization, CSF-cNs, called Kolmar-Agduhr (KA) cells in the zebrafish, were divided into two subgroups, dorsal KA' cells and ventral KA" cells (Park *et al.*, 2004; Djenoune *et al.*, 2014). Mainly lateral organization of CSF-cNs around the CC is reported in lamprey spinal cord (*type 1* cells), although another type of CSF-cNs located further from the CC was distinguished (*type 2* cells; Figure 10. B) (Jalalvand *et al.*, 2014).

Furthermore, it was shown that the organization of CSF-cNs around the CC of the spinal cord is not only region-dependent, but also age-dependent (Figure 10. C). In the spinal cord of younger rodents (up to 8 days), CSF-cNs show mainly intraependymal localization, with dendritic processes that are shorter compared to those of older animals (Kútna *et al.*, 2013; Orts-Del'Immagine *et al.*, 2017), and soma that is closer to the CC. With the age, the distance of soma from the CC increases and most CSF-cNs are located subependymally, a property that is seen in all the levels of medullo-spinal axis (Kútna *et al.*, 2013; Orts-

Del'Immagine *et al.*, 2017). Only ventral CSF-cNs in all levels investigated in the study by Orts-Del'Immagine and colleagues showed that somatic distance was decreasing from the CC with aging (Orts-Del'Immagine *et al.*, 2017). To explain such organization variances, the authors measured the pericanal ependymal zone and suggested that re-organization of CSF-cNs around the CC is not due to enlargement of measured zone with aging but is a consequence of increasing the dendritic length (Orts-Del'Immagine *et al.*, 2017). Moreover, Kútna and colleagues suggested that this reorganization could be due to the changes in the organization of the ependymal lining of the CC (Kútna *et al.*, 2013).

The changes in number of medullo-spinal CSF-cNs are age-dependent as well. Two independent studies reported that the number of CSF-cNs decreased with the development (Kútna *et al.*, 2013; Orts-Del'Immagine *et al.*, 2017). This event was explained by spinal cord enlargement with aging, which might cause "dilution" of the cells around and along the CC (Kútna *et al.*, 2013). Nevertheless, the authors speculated about possible migration of CSF-cNs away from CC, but there are still no evidences available on migratiory properties of these neurons.

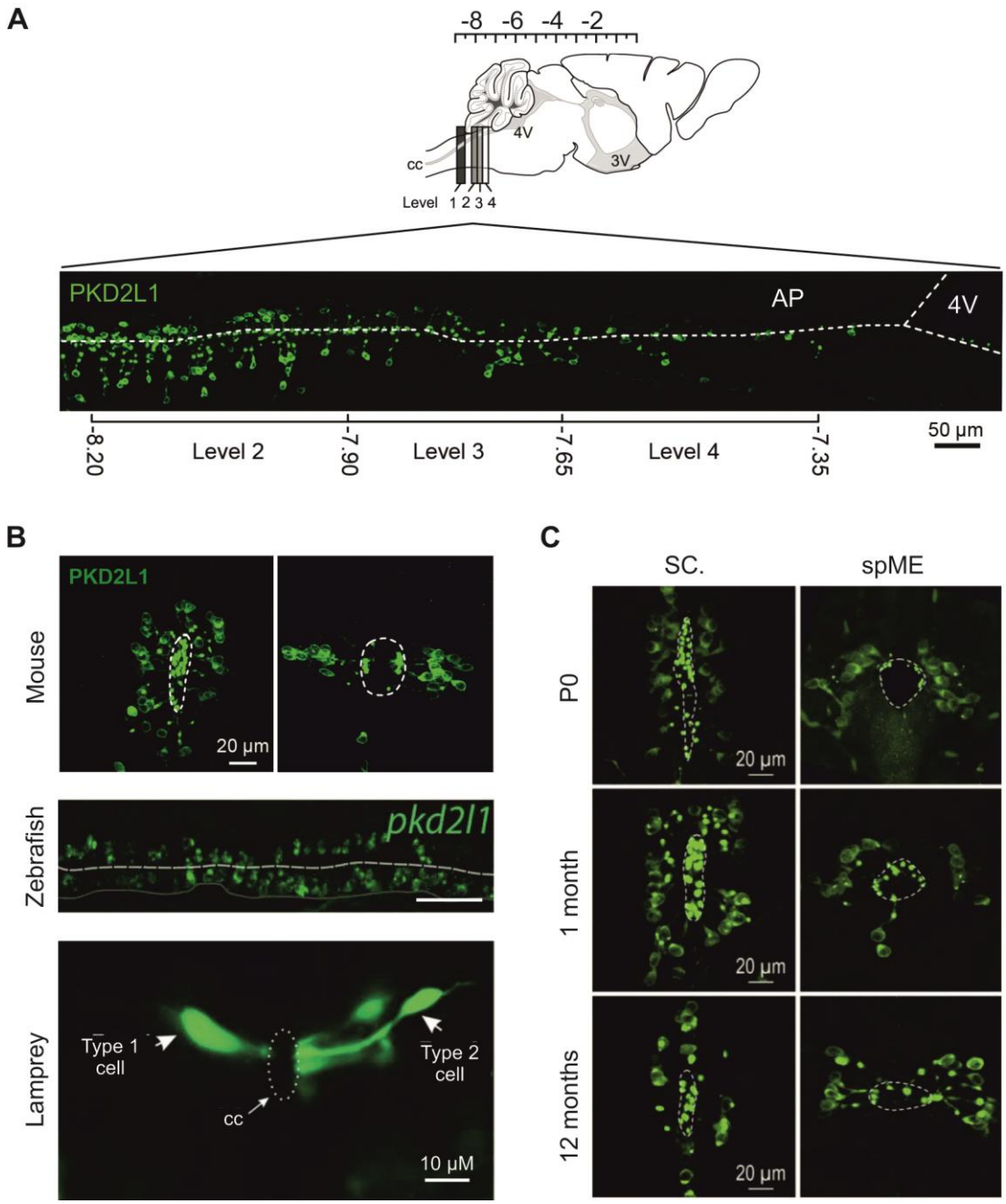


**Figure 10. Organization of CSF-cNs around the central canal is region- and age-dependent**.

**A.** *Top*. Four levels (level 1 – 4) in mouse brain and cervical spinal cord have been selected for describing the distribution of CSF-cNs around the CC. Scale on the top of sagittal scheme represents stereotaxic coordinates in antero-posterior axis. *Bottom.* CSF-cNs positive to PKD2L1 in sagittal section of the medullospinal region are located around the CC from the lower brainstem to the 4$^{th}$ ventricle. Below the image, three levels of the brainstem are indicated based on stereotaxic coordinates (in mm). Dorsal side is on the top, and ventral is on the bottom. Posterior is left, and anterior is right. White dash lines denote central canal (CC) and 4$^{th}$ ventricle (4V). **B.** *Top left.* PKD2L1$^{+}$ CSF-cNs are mostly located in dorsal and ventral positions around the CC in the mouse cervical spinal cord, and they shift to lateral sides of the CC towards more rostral levels (*top left*). *Middle.* Dorso-ventral organization of PKD2L1$^{+}$ CSF-cNs is also seen in sagittal section of adult zebrafish spinal cord. CC is delineated with white dashed line, while dark grey line delineates ventral limit of the spinal cord. Scale

bar = 40 µm. *Bottom*. In adult lamprey spinal cord, two types of CSF-cNs are mainly located laterally around the CC. **C.** In coronal sections from cervical spinal cord (SC.) and sub-postremal medulla (spMe.) of p0-2D, p1M and p12M mice, CSF-cNs (in green, $PKD2L1^+$ cells) shift to lateral sides of the CC towards more rostral regions (spMe.) at all ages tested. They show intraependymal localization at younger age, with soma that is closer to the CC. At older ages (p12M), CSF-cNs are present with lower density. Figures in A and B (mouse) are adapted from Orts-Del'Immagine *et al.*, 2014. Figure in B (zebrafish) is adapted from Djenoune *et al.*, 2014, while figure in B (lamprey) is from Jalalvand *et al.*, 2014. Figure in C is adapted from Orts-Del'Immagine *et al.*, 2017.

## 2. PROPERTIES OF CSF-cNs

Many interesting studies carried out so far have demonstrated that medullo-spinal CSF-cNs represent a specific and quite unique neuronal population. Immunohistochemical and electrophysiological studies showed characteristic developmental phenotype for these neurons, which are characterized by the selective expression of PKD2L1 channel. In this part of the Introduction, a special attention will be given on describing properties of CSF-cNs, including developmental, functional, and electrophysiological properties.

### 2.1. Developmental properties and origin of CSF-cNs

CSF-cNs are a unique type of neurons, not only because of their simple and characteristic morphology, but also because of their unique developmental phenotype. In rat and mouse spinal cord, CSF-cNs have been shown to appear around day 12 to 14.5 of embryonic development (E12 to E14.5) (Kútna *et al.*, 2013; Djenoune *et al.*, 2014) and to remain in an intermediate maturation state even in the adulthood. More recently, Petracca and colleagues indicated that spinal CSF-cNs are late born neurons that appear during gliogenesis, a period when all other neuronal types are already present (Petracca *et al.*, 2016). The peculiar CSF-cNs phenotype is further confirmed by the fact that they express markers of both immature (DCX and HuC/D) (Marichal *et al.*, 2009; Kútna *et al.*, 2013; Djenoune *et al.*, 2014; Orts-Del'Immagine *et al.*, 2014; Böhm *et al.*, 2016; Petracca *et al.*, 2016) and mature neurons (NeuN, GAD) (Kútna *et al.*, 2013; Djenoune *et al.*, 2014; Orts-Del'Immagine *et al.*, 2014, 2017). Regarding the expression of neuronal immature markers, CSF-cNs express the early neuronal marker HuC/D, which is co-expressed with doublecortin (DCX) in neonatal rat spinal cord (Marichal *et al.*, 2009). This marker is continuously expressed from first postnatal day (P1) up to adulthood (Kútna *et al.*, 2013). In contrast, the expression of DCX decreases with age in the mouse spinal cord, and it is almost undetectable in the dendrites and terminal

enlargements (Figure 11. A) (Orts-Del'Immagine *et al.*, 2014, 2017). During the first postnatal days, CSF-cNs also express NeuN, a marker of mature neurons (Kútna *et al.*, 2013; Orts-Del'Immagine *et al.*, 2017), although the absence of NeuN immunoreactivity was also reported (Marichal *et al.*, 2009; Petracca *et al.*, 2016). It was shown that expression of NeuN depends on the age and the localization of CSF-cNs in the medullo-spinal axis (Figure 11. B), and its expression increases with aging and towards rostral end of the CC, although it remains low compared to other neuronal populations in the same region (Orts-Del'Immagine *et al.*, 2014, 2017). Since DCX expression classically ends at the time point when NeuN expression begins, during neuronal maturation, it was questioned whether the presence of DCX in postnatal CSF-cNs is a consequence of their delayed developmental stage, as recently described by Petracca and colleagues (Petracca *et al.*, 2016). It was shown that the co-expression of these two markers is present in dorsal and lateral, but not in the ventral CSF-cNs of the mouse spinal cord where NeuN expression is low (Orts-Del'Immagine *et al.*, 2017). Because CSF-cNs show variability in the expression of different markers of neuronal maturity, it was strongly suggested that they form a heterogeneous population of neurons, indicating the possibility that they may have different properties and/or origin.

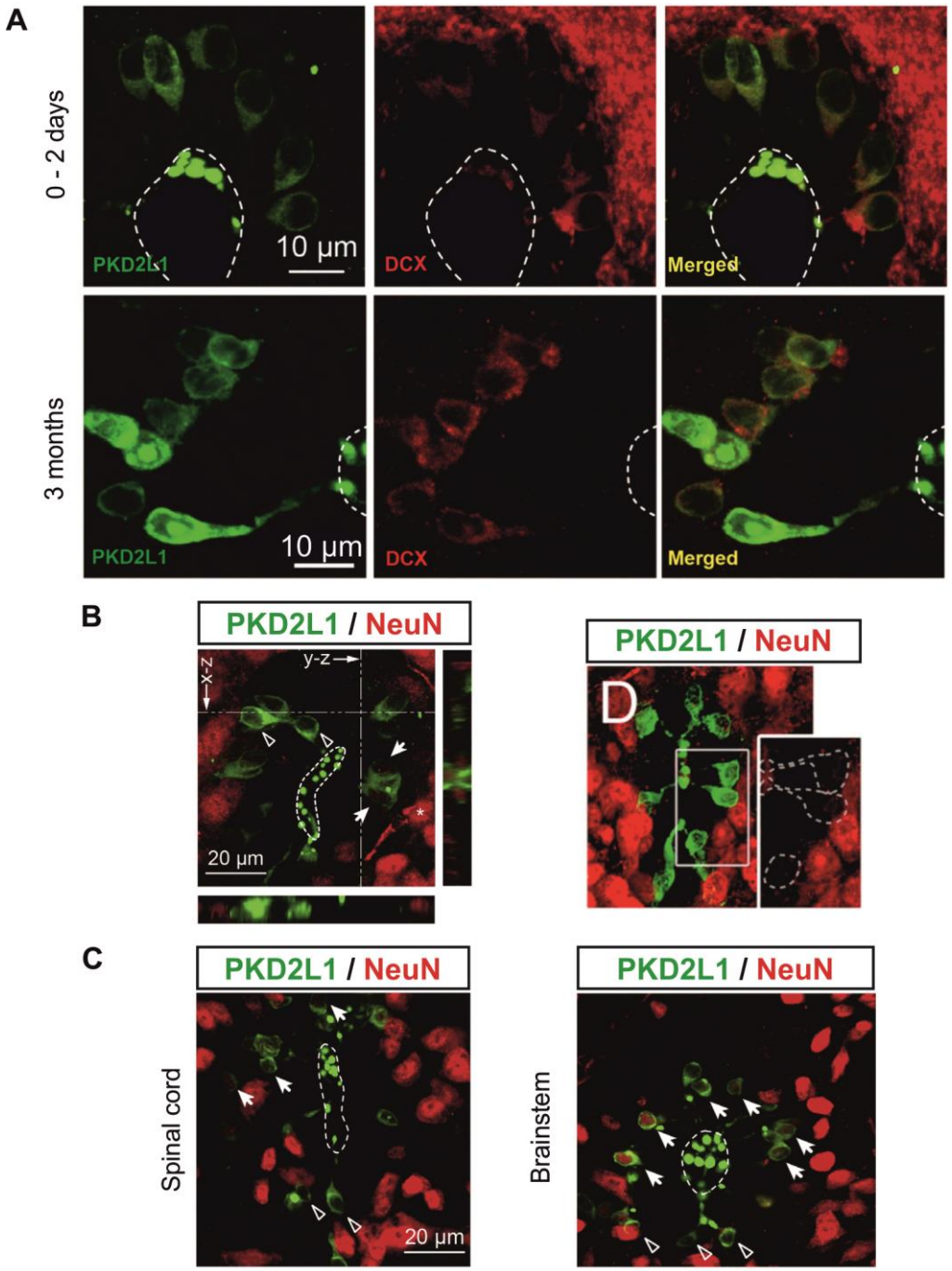


**Figure 11. CSF-cNs express markers of both immature and mature neurons.**

**A.** Murine brainstem coronal sections at 0-2 postnatal days (top panels) and 3 months (bottom panels) show CSF-cNs immunolabeled against PKD2L1 (green), and DCX (red). Note that all PKD2L1$^{+}$ CSF-cNs are also DCX$^{+}$ (Merged). **B.** In neonatal (P0) mouse spinal cord, CSF-cNs immunolabeled against PKD2L1 show weak (left) or absent (right) NeuN immunoreactivity (red). On the left, open arrowhead shows CSF-cN that is NeuN negative, while white arrows indicate NeuN positive CSF-cNs. Orthogonal projections along the *y-z* (right) and *x-z* (bottom) axes are shown. **C.** Higher intensity of NeuN labeling is seen in CSF-cNs located dorsally and laterally from the CC. Note that not all PKD2L1$^{+}$ CSF-cNs are NeuN$^{+}$ (open arrowhead). Figures in A, B (left) and C are adapted from Orts-Del'Immagine *et al.*, 2014 and Orts-Del'Immagine *et al.*, 2017. Figure in B (right) is from Petracca *et al.*, 2016.

Concerning the ***origin*** of CSF-cNs in mammalian spinal cord, 5-bromo-2'-deoxyuridine (BrdU) administration during the rat embryonic period demonstrated that CSF-cNs are derived from the ventricular zone of the spinal cord from 12 days of embryonic development (E12) and their generation continues until birth (Kútna *et al.*, 2013). Consistent with this finding, experiments carried out in the embryonic mouse spinal cord demonstrated that CSF-cNs start to develop in ventral spinal cord at E13.5, and their number increase until E16.5 (Petracca *et al.*, 2016). This interesting study by Petracca and colleagues showed that CSF-cNs located in ventral and lateral regions around the CC in the mouse spinal cord express Gata2/3 and derive from two distinct neuronal progenitor domains around the CC that generate distinct neuronal subtypes (Figure 12. A). A majority of CSF-cNs, so called CSF-cNs', located in lateral walls around the spinal cord CC, were shown to derive from progenitors in the p2 domain and the dorsal half of pOL domain, ventricular domains that express Nkx6-1 and Pax6. Importantly, Pax6 is a crucial factor involved in formation of CSF-cNs' (Petracca *et al.*, 2016). Among this population of cells, about 70 % of CSF-cNs are derived from p2 progenitor domain, while 30 % of CSF-cNs originate from pOL domain. A second, but minor, CSF-cNs" population is derived from p3 precursor cells that border the floor plate, and these neurons are positive for p3 markers, Nkx2-2 and Foxa2 (Figure 12. B) (Petracca *et al.*, 2016). The results of the same study showed that dual origin of CSF-cNs influences the postnatal organization of these neurons around the CC. Therefore, CSF-cNs' originating from p2 and pOL domains are located in lateral walls around the CC, while p3 domain-originating CSF-cNs" are found ventral to the central (Petracca *et al.*, 2016). The question that remains open is whether these two populations of CSF-cNs have different functions in mammalian CNS.

Dual origin of CSF-cNs was also confirmed in zebrafish spinal cord (Djenoune *et al.*, 2014). Using transgenic zebrafish models (Figure 12. C), it was shown that CSF-cNs originate from two neural progenitor domains, p3 and pMN (Park *et al.*, 2004; Djenoune *et al.*, 2014). In a model in which pMN domain was GFP-labeled, only dorsal CSF-cNs (KA' cells) were also $GFP^+$ (Djenoune *et al.*, 2014), and were expressing *olig2* transcription factor (Park *et al.*, 2004). In contrast, ventral CSF-cNs (KA" cells) were $GFP^+$ in GFP-labeled p3 domain, and were expressing nkx2.2a transcription factor (Djenoune *et al.*, 2014). Therefore, originating from pMN domain, KA' cells show similarities with mouse CSF-cNs', while KA" cells originating from p3 domain are highly homologous to mouse CSF-cNs".

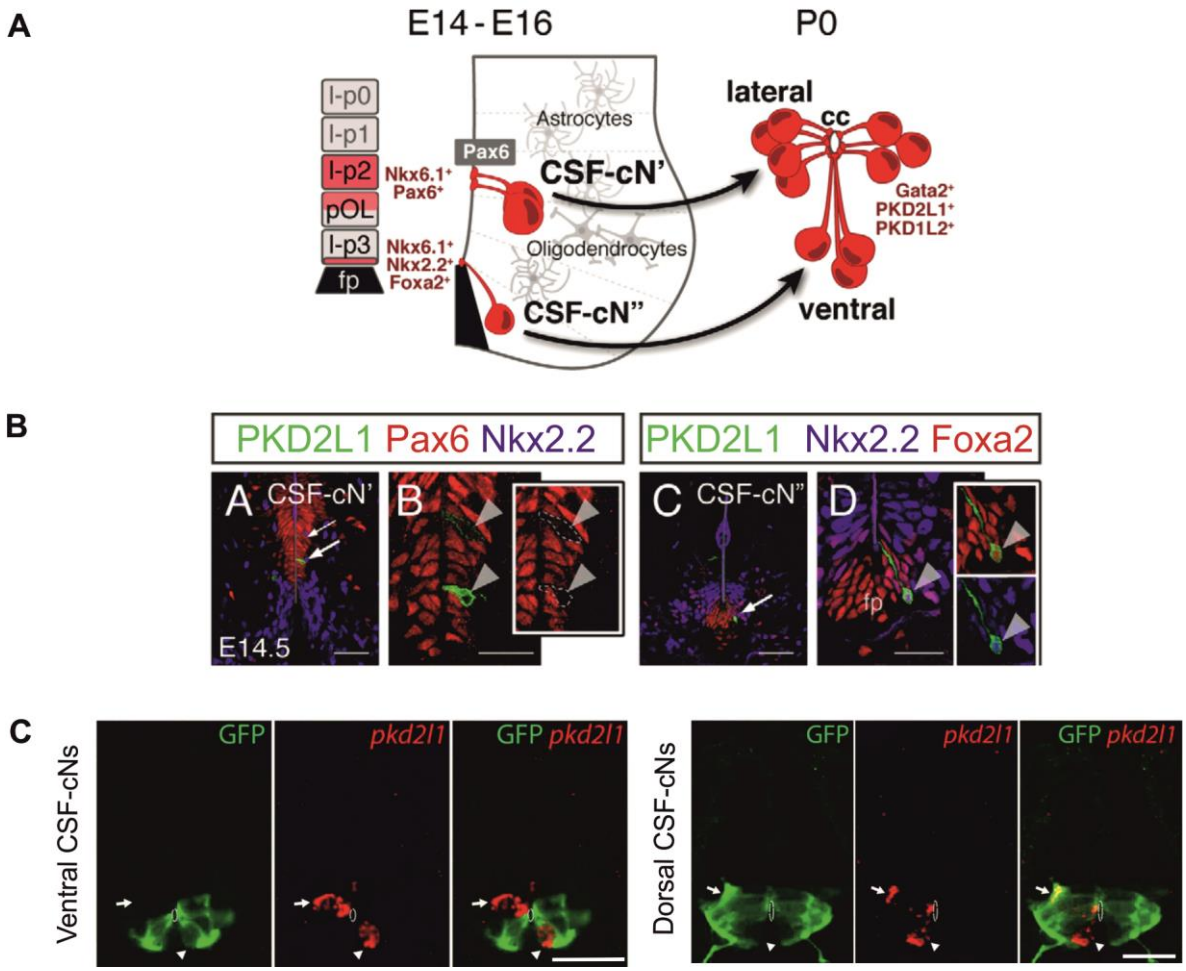


**Figure 12. Dual origin of CSF-cNs.**

**A.** Schematic illustration of murine ventral spinal cord at 14-16 embryonic days (E14-16; left) and organization of CSF-cNs in the postnatal spinal cord (P0; right). During embryonic development, Gata2$^{+}$/3$^{+}$ CSF-cNs differentiate along with astrocytes and oligodendrocytes progenitor cells. CSF-cNs' derive from Nkx6-1$^{+}$ and Pax6$^{+}$ progenitors in p2 domain and dorsal half of pOL domain. CSF-cNs'' derive from Nkx6-1$^{+}$ and Foxa2$^{+}$ progenitors in p3 domain bordering the floor plate (fp). In the postnatal spinal cord, CSF-cNs' are located laterally from the CC, while CFS-cNs'' are organized ventral to the CC. **B.** In E14.5 spinal cord, PKD2L1$^{+}$ CSF-cNs' (green) are found in Pax6-expressing zone (red; panel A). Low expression of Pax6 can be also detected in CSF-cNs' (panel B, upper arrowhead). The expression of Nkx2-2 (blue) is not detectable. Ventral PKD2L1$^{+}$ (green) CSF-cNs'' originating from the region close to the floor plate (panel C) express Nkx2-2 (blue) and Foxa2 (red; panel D). **C.** In transgenic zebrafish, p3 domain (left panels) is labeled with GFP. Ventral CSF-cNs (arrowhead) immunoreactive to PKD2L1 (red) in transverse section of zebrafish embryonic spinal cord express GFP (green) while dorsal CSF-cNs do not express GFP (arrow). In transgenic zebrafish embryo where pMN domain is labeled with GFP (right panels), only dorsal PKD2L1$^{+}$ (red) CSF-cNs (arrow) express GFP (green) while ventral CSF-cNs lack the expression of GFP (arrowhead). Figures A and B are adapted from Petracca *et al.*, 2016, figures in C are from Djenoune *et al.*, 2014. Scale bars = 40 µm in B (panels A and C), 20 µm in B (panels B and D) and C.

### 2.2. Phenotype and functional properties of CSF-cNs

CSF-cNs of many species, including mouse (Djenoune *et al.*, 2014; Orts-Del'Immagine *et al.*, 2014), zebrafish, macaque (Djenoune *et al.*, 2014) or lamprey (Jalalvand *et al.*, 2016) have been shown to selectively express polycystic kidney disease 2-like 1 (PKD2L1) channel, a member of TRP superfamily of non-selective cationic channels (Chen *et al.*, 1999; Huang *et al.*, 2006; Djenoune *et al.*, 2014; Orts-Del'Immagine *et al.*, 2014). PKD2L1 channel was described to be sensor responsible for sour taste when expressed in taste cell buds in the tongue, and it was found to be a specific marker for medullo-spinal CSF-cNs (Huang *et al.*, 2006). Its expression is so far described in several vertebrate species, including mouse, zebrafish and macaque (Orts-Del'Immagine *et al.*, 2012, 2014; Djenoune *et al.*, 2014). In mouse medullar CSF-cNs, expression of PKD2L1 was observed in soma and dendrite, with high level of expression in terminal protrusions contacting the CSF (Djenoune *et al.*, 2014; Orts-Del'Immagine *et al.*, 2014). Similar high expression of PKD2L1 was found in bud of macaque CSF-cNs, while somatic expression was lower (Djenoune *et al.*, 2014). Moreover, PKD2L1 was never found to be expressed in axon-like structure (Orts-Del'Immagine *et al.*, 2014).

CSF-cNs are primarly GABAergic neurons (γ-aminobutyric acid), a phenotype that has been reported in several studies (Marichal *et al.*, 2009; Kútna *et al.*, 2013; Djenoune *et al.*, 2014; Orts-Del'Immagine *et al.*, 2014). Immunohistochemical studies showed that CSF-cNs are positive for GABA and the glutamate decarboxylase enzyme (GAD65/67) (Kútna *et al.*, 2013; Djenoune *et al.*, 2014; Orts-Del'Immagine *et al.*, 2014; Jalalvand *et al.*, 2014). In medullo-spinal CSF-cNs, this immunoreactivity against GABA and GAD67 is observed in the soma but also in the bud (Orts-Del'Immagine *et al.*, 2014). In addition, medullo-spinal CSF-cNs are also immunoreactive for $GABA_{B1}$ subunit of $GABA_B$ receptors mainly in the soma and the dendrite (Jurčić *et al.*, 2019). In the spinal cord of non human primates, CSF-cNs were immunolabeled with antibodies against GAD65/67 and vesicular GABA transporter (vGAT), although at a lower extent in the bud (Djenoune *et al.*, 2014).

Moreover, the expression of various markers, including somatostatin, serotonin, vasoactive intestinal polypeptide (VIP) or Met-Enk-Arg-Gly-Leu, was also identified in CSF-cNs by previous studies (LaMotte & de Lanerolle, 1986; Shimosegawa *et al.*, 1986; Djenoune *et al.*, 2014; Jalalvand *et al.*, 2014). They were found to express somatostatin in lamprey (Jalalvand *et al.*, 2014) and zebrafish (Djenoune *et al.*, 2014), but not in mouse spinal cord

(Petracca *et al.*, 2016). In zebrafish, the expression of only one paralog of somatostatin, *sst1.1* is found to be present solely in dorsal CSF-cNs (Djenoune *et al.*, 2014). In contrast, ventral CSF-cNs, that lack expression of somatostatin, are serotoninergic (immunolabeled against 5-HT). Interestingly, the expression of 5-HT is transient and localized, since it could only be detected 48 hours post fertilization (48 hpf) and not in all ventral CSF-cNs. Further, the expression of 5-HT was not present in rostral spinal cord in later stages of development (Djenoune *et al.*, 2014). In the rat spinal cord, CSF-cNs are strongly immunoreactive to methionine-enkephalin-Arg$^{6}$-Gly$^{7}$-Leu$^{8}$ (Met-Enk-Arg-Gly-Leu), an endogenous octapeptide isolated from bovine adrenal chromaffin granules, and contained in preproenkephalin A (Shimosegawa *et al.*, 1986). Finally, although CSF-cNs do not appear to express tyrosine hydroxylase, a selective marker of catecholaminergic neurons, there are reports for the presence of the L-aromatic amino acid decarboxylase (AAAD) and therefore the expression of trace amines (Nagatsu *et al.*, 1988).

To date, little is known about the functional properties of CSF-cNs although in the recent years there is a growing interest to characterize them. CSF-cNs express functional ionotropic receptors for GABA, glycine (Figure 13. A), acetylcholine and glutamate, as demonstrated by local pressure application of selective agonists (Marichal *et al.*, 2009; Orts-Del'Immagine *et al.*, 2012; Corns *et al.*, 2013; Jalalvand *et al.*, 2014; Orts Del'Immagine *et al.*, 2015). Regarding the function of ionotropic $GABA_A$ receptors, there is an opened question about their inhibitory or excitatory effect upon activation. Most studies were carried out in whole-cell configuration, a non-physiological condition where chloride homeostasis, and therefore GABA activity, is perturbed. However, using perforated patch-clamp recordings with gramicidin to prevent changes in physiological concentration of intracellular $Cl^-$ ($[Cl^-]_i$), it was reported that GABA may exhibit both inhibitory and excitatory effects on CSF-cNs (Marichal *et al.*, 2009). In one type of cells, GABA induced hyperpolarization from the resting membrane potential (RMP; Figure 13. $B_1$), and current induced by GABA reversed at -67 mV. In another type of CSF-cNs, GABA induced depolarization that led to generation of action potentials (APs; Figure 13. $B_2$), and in these cells, GABA-induced current reversed at -46 mV. Considering the differences in reversal potentials of currents induced by GABA application, it was suggested that CSF-cNs may express different levels of $Na^+$-$K^+$-$2Cl^-$ (NKCCl) transporters involved in regulation of $[Cl^-]_i$ (Marichal *et al.*, 2009; Wright, 2009). This would support the idea of CSF-cNs as neurons in different stages of maturation and the important role of GABA in neuronal maturation. Indeed, in immature neurons, GABA

provides depolarizing action because of the activity of NKCCl transporter that increases intracellular levels of $Cl^-$. With neuronal maturation, $K^+$-$Cl^-$ transporter (KCC2) reduces $[Cl^-]_i$ and it reverses the effect of GABA to elicit an inhibitory effect (Wright, 2009).

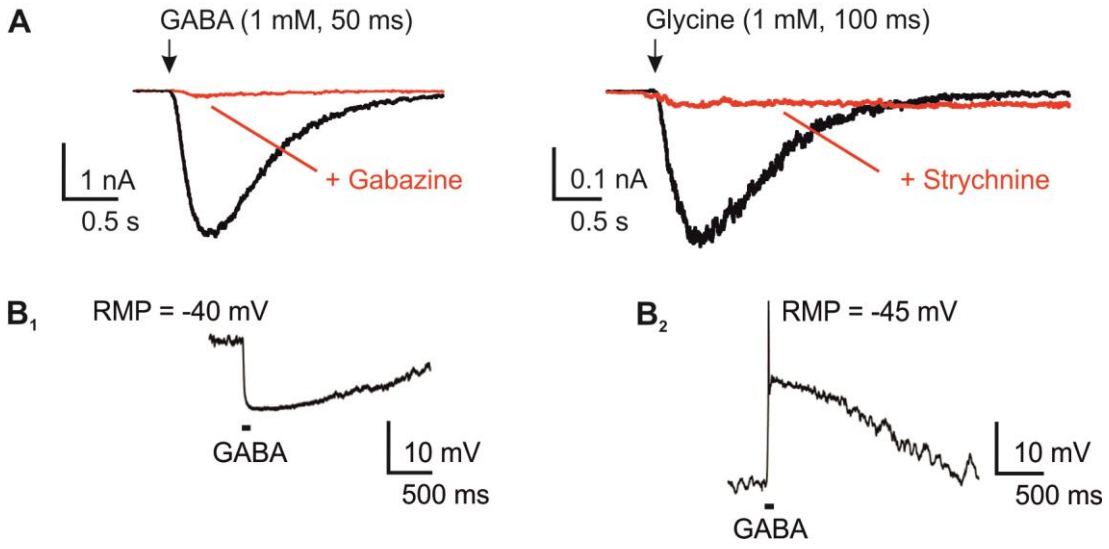


**Figure 13. CSF-cNs express functional ionotropic receptors for GABA and glycine.**

**A.** Current traces are recorded from CSF-cNs at -80 mV. Pressure application of GABA (left) and glycine (right) induced inward currents that were inhibited by pressure application of gabazine (10 µM; red trace on left) and strychnine (10 µM; red trace on right), respectively. **B.** Using grandamicin perforated patch-clamp technique, GABA application induced hyperpolarization from rest (**$B_1$**). In some cells, GABA induced strong depolarization (**$B_2$**) that evoked generation of AP. Figures in A are adapted from Orts-Del'Immagine *et al.*, 2012. Figures in B are adapted from Marichal *et al.*, 2009.

Murine medullo-spinal CSF-cNs express excitatory receptors for AMPA/kainate, and nicotinic acetylcholine (nACh) (Orts Del'Immagine *et al.*, 2015), and functional inhibitory glycine receptors that respond to glycine pressure application by generating inward current sensitive to strychnine application, a selective antagonist for glycine receptors (Orts-Del'Immagine *et al.*, 2012). Moreover, Stoeckel and colleagues reported, in the rat spinal cord CSF-cNs, the expression of $P_2X_2$ receptors, the ionotropic form of purinergic receptors gated by ATP (Stoeckel *et al.*, 2003). It was suggested that $P_2X_2$ receptors activation would enable CSF-cNs to sense changes in extracellular ATP levels (Stoeckel *et al.*, 2003). Marichal and colleagues tested the function of $P_2X_2$ receptors in CSF-cNs using ATP application and showed that their activation induced the generation of fast inward current and an increase in CSF-cNs excitability (Marichal *et al.*, 2009). In contrast to spinal CSF-cNs, medullar CSF-

cNs failed to respond to ATP pressure application, suggesting that purinergic $P_2X_2$ receptors are not expressed in the mouse or at least not in medullar CSF-cNs (Orts-Del'Immagine *et al.*, 2012).

### 2.3. Electrophysiological properties

CSF-cNs are small neurons (diameter ~10 µm) with a high input resistance, between 2.1 and 5.9 GΩ (Marichal *et al.*, 2009; Orts-Del'Immagine *et al.*, 2012; Jalalvand *et al.*, 2014; Petracca *et al.*, 2016; Sternberg *et al.*, 2018), and a small mean membrane capacitance (3 - 6 pF) in agreement with their somatic diameter (Orts-Del'Immagine *et al.*, 2012). Their RMP is between -40 mV and -70 mV, depending on the species considered (Russo *et al.*, 2004; Marichal *et al.*, 2009; Orts-Del'Immagine *et al.*, 2012; Jalalvand *et al.*, 2014).

In all the vertebrates investigated, CSF-cNs showed spontaneous firing of APs at RMP undelying functional voltage-dependent sodium channels (Russo *et al.*, 2004; Marichal *et al.*, 2009; Orts-Del'Immagine *et al.*, 2012; Jalalvand *et al.*, 2014; Orts Del'Immagine *et al.*, 2015). CSF-cNs appear to express specific voltage-dependent potassium channels. The one of the A-type ($I_A$) exhibits fast onset and prominent voltage- and time-dependent inactivation, while a second type corresponds to delayed rectifier potassium channels, $I_{KD}$ (Marichal *et al.*, 2009).

Based on the AP discharge pattern induced by DC current injections in current-clamp mode, CSF-cNs can be divided into two main subpopulations: single spike CSF-cNs (or phasic CSF-cNs) and repetitive spiking (or tonic CSF-cNs) (Figure 14. A) (Marichal *et al.*, 2009; Orts-Del'Immagine *et al.*, 2012; Petracca *et al.*, 2016). Orts-Del'Immagine and colleagues (2012) reported a greater representation of single spiking CSF-cNs, compared to the study by Petracca and colleagues (2016), where tonic CSF-cNs were more prevalent (Orts-Del'Immagine *et al.*, 2012; Petracca *et al.*, 2016). Marichal and colleagues (2009) described three different types of CSF-cNs. These findings support dual origin of CSF-cNs, but the age-dependent differences cannot be excluded. The first type of CSF-cNs, identified by their high input resistance of 6 GΩ, shows slow depolarizing potentials (Figure 14. $B_1$) that are inhibited by manganese ($Mn^+$), indicating the contribution of $Ca^{2+}$ channels in this process, while $Na^+$ channels are negligible (Marichal *et al.*, 2009). The second type of CSF-cNs expresses mean input resistance of 4 GΩ and responds to depolarization by generating a

single spike from hyperpolarized membrane potential (-60 mV), which is inhibited by TTX (Figure 14. $B_2$), indicating the involvement of $Na^+$ conductances in the response (Marichal *et al.*, 2009). When these CSF-cNs were hyperpolarized, a late depolarizing response was evoked that prevented the cell to generate APs, which suggested the presence of $K^+$ current of A-type ($I_A$) (Marichal *et al.*, 2009). Finally, the third type of repetitively spiking cells (Figure 14. $B_3$) have mean input resistance of 4 GΩ, and hyperpolarized membrane potential similar of that for single spiking CSF-cNs. However, APs of these cells had larger spike amplitudes, shorter half-time spike and developed slow after-hyperpolarization (sAHP) (Russo *et al.*, 2004; Marichal *et al.*, 2009; Jalalvand *et al.*, 2014). As seen for single spiking cells, the APs in repetitive spiking cells are mediated by $Na^+$ conductances (Marichal *et al.*, 2009). These different electrophysiological phenotypes of CSF-cNs, *i.e.* single or repetitive spiking activity, were explained by the density and nature of the voltage-dependent channels expressed in CSF-cNs (Marichal *et al.*, 2009; Petracca *et al.*, 2016). Thus, phasic CSF-cNs presented a lower density in $Na^+$ current compared to tonic ones, and along delayed rectifying $I_{KD}$ with similar properties they expressed inactivating currents mediated by $I_A$ (Marichal *et al.*, 2009). Taken together, these results strongly suggest that CSF-cNs represent a heterogenous neuronal population with dual origin, but the age-dependent differences and the localization (brainstem *vs.* spinal cord) cannot be excluded. The difference observed in CSF-cN discharge activity, led some authors to defend the idea that CSF-cNs are neurons in an immature state of development. In study by Marichal and colleagues (2009) it was suggested that CSF-cNs with predominating $Ca^{2+}$ conductances involved in generating slow APs might represent immature neurons (Marichal *et al.*, 2009). With advanced differentiation of neurons, capacity for repetitive spiking appears, and it is controlled by an increase in the density of $Na^+$ channels (Russo *et al.*, 2004; Marichal *et al.*, 2009).

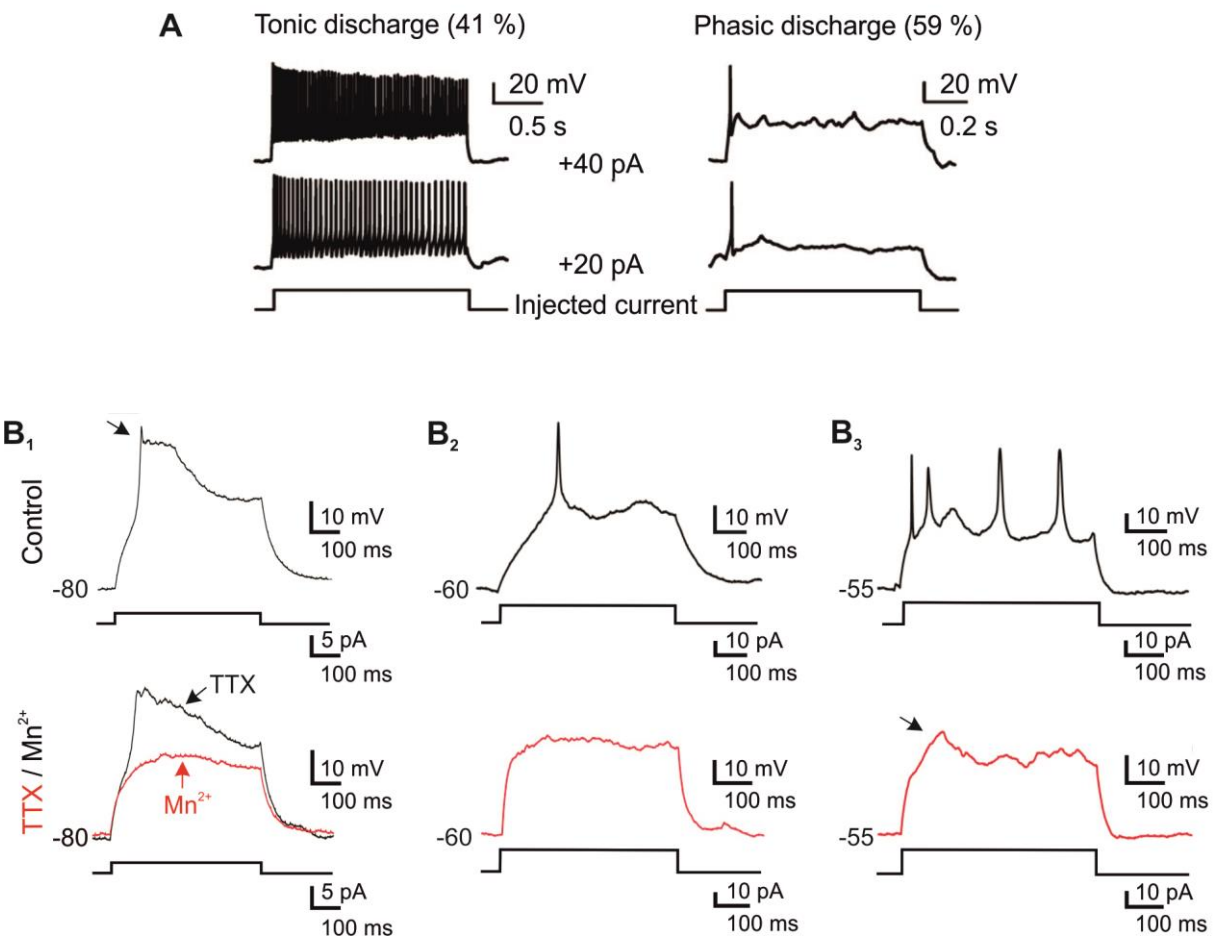


**Figure 14. CSF-cNs exhibit different discharge patterns.**

**A.** CSF-cNs recorded from the mouse acute brainstem slices exhibit tonic (left) or phasic (right) AP discharge upon positive current injection (+40 pA, upper traces; +20 pA, lower traces). **B.** CSF-cNs recorded from the rat spinal cord are divided into three groups based on their discharge activity. CSF-cNs show slow depolarizing potential (**$B_1$**, upper trace) which exhibits brief transient at the beginning of the response (arrow) that is sensitive to TTX (1 µM, black arrow, black lower trace). In the presence of 3 mM $Mn^{2+}$, slow depolarizing potential is completely abolished (red arrow, red lower trace). The AP in both single spiking cells (**$B_2$**, upper trace) and in repetitive spiking cells (**$B_3$**, upper trace) are mediated by $Na^{2+}$ conductances and inhibited by 1 µM TTX (lower traces in **$B_2$** and **$B_3$**). The arrow in **$B_3$** indicates remained slow depolarizing event. Figure A is from Orts-Del'Immagine *et al.*, 2012, figures in B are adapted from Marichal *et al.*, 2009.

In addition to spontaneous firing of sodium-mediated APs, using classical whole-cell patch-clamp recordings from CSF-cNs in spinal cord and brainstem acute slices, it was demonstrated that these neurons typically exhibit spontaneous depolarizing events when recorded at the RMP in current-clamp mode, or according inward current when recorded in voltage-clamp mode (Figure 15. A). These currents strongly resemble to post-synaptic inputs with the characteristic fast onset and exponential recovery (Orts-Del'Immagine *et al.*, 2012;

Jalalvand *et al.*, 2014). These results therefore indicate that medullo-spinal CSF-cNs are inserted in a neuronal network that needs to be characterized (see below).

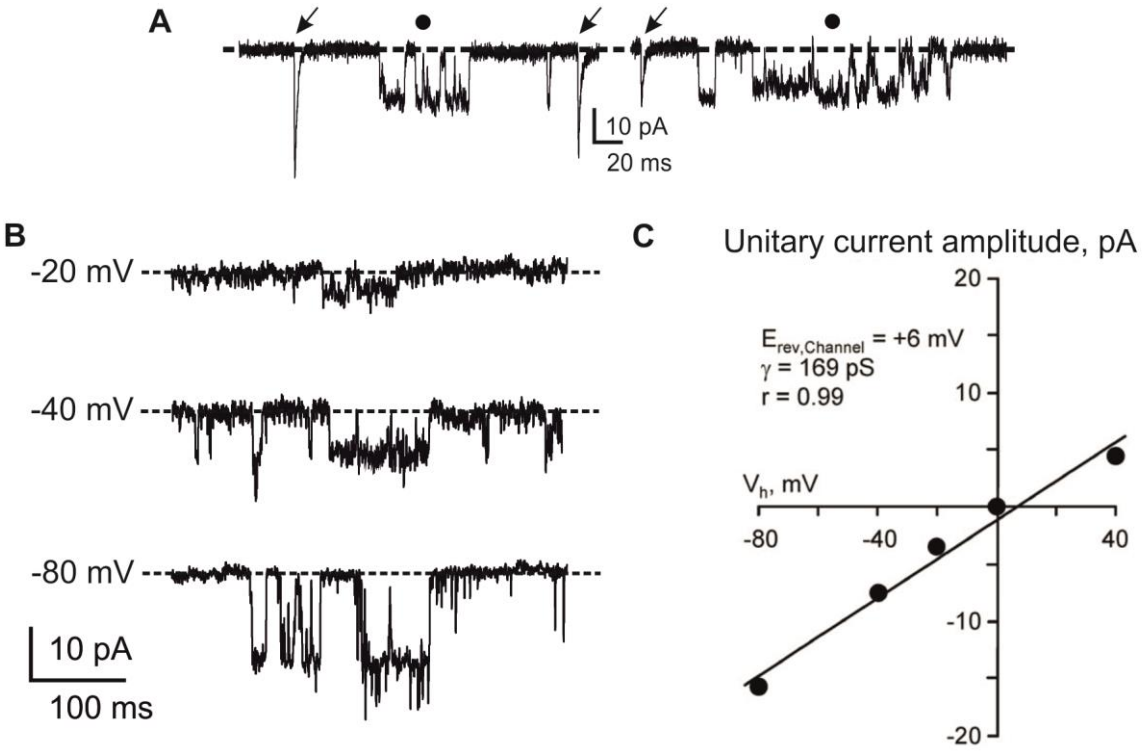


**Figure 15. CSF-cNs exhibit spontaneous synaptic events and unitary single-channel activity.**

**A.** CSF-cNs recorded from mouse acute brainstem slice in voltage-clamp mode at -80 mV exhibit fast inward currents (arrows) typical of synaptic activity and unitary single-channel activity (filled circle). **B.** Spontaneous single-channel current recorded from single CSF-cNs at different holding potentials between -20 mV and -80 mV, with 20 mV increments. Dashed lines indicate closed state of the channel. **C.** Unitary current amplitude measured from the cell in **B** is plotted against each holding potential to determine current-voltage relationship. Reversal potential ($E_{rev,\ Channel}$) and the channel conductance (γ) were calculated from the linear fit of the experimental data points. Figures in A and B are from Orts-Del'Immagine *et al.*, 2012.

One of the major characteristics and peculiarities of medullo-spinal CSF-cNs is the presence, along synaptic currents, of another spontaneous unitary current activity with an overall amplitude similar to that of synaptic events (Orts-Del'Immagine *et al.*, 2012, 2014). Detailed analyses demonstrated that the inward unitary current is due to the opening of cationic non-selective PKD2L1 channel which exhibits large single channel conductance of about 150 pS and low mean open probability around 0,04 (Figure 15. B, C). This result is in agreement with whole-cell recordings from human embryonic kidney (HEK293T) cells and

from the *Xenopus* oocytes, in which overexpressed PKD2L1 showed similar large single channel conductance and permeability to cations. Moreover, in heterologous systems, PKD2L1 was shown to be highly permeable to $Ca^{2+}$ and modulated by $Ca^{2+}$. First, $Ca^{2+}$ appears to activate PKD2L1, and subsequent increase in intracellular $Ca^{2+}$ concentration induces channel inactivation (Chen *et al.*, 1999). Whether similar $Ca^{2+}$ dependent properties for PKD2L1 exist in murine medullo-spinal CSF-cNs remains to be demonstrated. Interestingly, PKD2L1 channel was shown to modulate excitability of CSF-cNs (Orts-Del'Immagine *et al.*, 2012; Orts Del'Immagine *et al.*, 2015). It was demonstrated that PKD2L1 activity can be modulated by changes in extracellular pH with an increase in channel opening probability upon extracellular alkalization. (Shimizu *et al.*, 2009; Orts-Del'Immagine *et al.*, 2012; Jalalvand *et al.*, 2016*a*). As a consequence, CSF-cN exposure to alkaline pH induced an increase in discharge frequency (Figure 16. A). Because the pH-dependent increase in discharge activity was not observed in mice lacking PKD2L1 channels, it was suggested that PKD2L1 was crucial for modulating CSF-cN excitability as a function of the extracellular environment (Orts-Del'Immagine *et al.*, 2012). These data argued that the opening of PKD2L1 channels with a conductance that is large enough to efficiently depolarize CSF-cN membrane potential was capable of generating APs in CSF-cN, a neuron with high input resistance. Further, the authors argued that the cellular localization of PKD2L1 on CSF-cNs may be an important factor in determining PKD2L1 channel ability to trigger the APs in CSF-cNs (Orts Del'Immagine *et al.*, 2015). Therefore, to demonstrate this hypothesis, they developed a model neuron to study the influence of PKD2L1 (soma, dendrite, bud, cilium and axon) on CSF-cN activity. The results indicate that regardless of its localization on the CSF-cNs, a single opening of PKD2L1 is able to sufficiently depolarize CSF-cN membrane potential to generate APs in the soma (Orts Del'Immagine *et al.*, 2015). It is important to note that opening of single PKD2L1 channel for 20 ms represents the minimal threshold duration necessary to trigger the APs, while longer duration might even trigger train of APs in CSF-cNs (Figure 16. B). According to the data obtained from mice CSF-cNs, single channel opening of high conducting PKD2L1 is sufficient to trigger the generation of APs in zebrafish CSF-cNs (Sternberg *et al.*, 2018). In summary, a single opening of PKD2L1 channel of long duration may trigger the APs in CSF-cNs. Therefore, PKD2L1 represents a spike generator in CSF-cNs able to modulate the neuronal excitability at the level of a single channel (Orts Del'Immagine *et al.*, 2015).

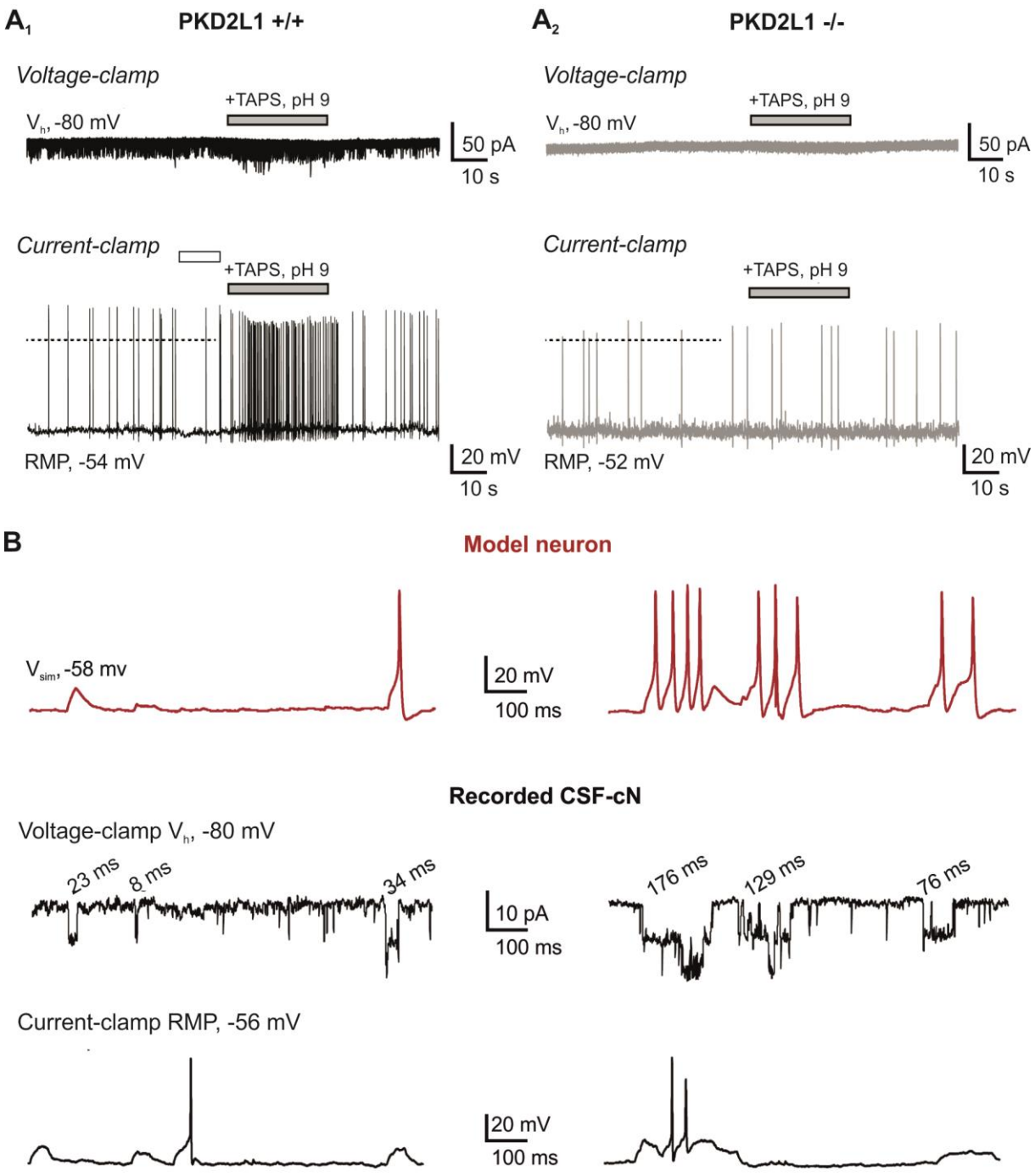


**Figure 16. Opening of PKD2L1 channel triggers action potentials in CSF-cNs.**

**A.** PKD2L1 current traces recorded in CSF-cNs from mouse acute brainstem slices. In wild-type CSF-cN (**$A_1$**), extracellular alkalization induced by TAPS (grey horizontal bar) increases PKD2L1 channel activity in voltage-clamp mode (top trace) and AP frequency in current-clamp mode (bottom trace). In mice lacking PKD2L1 channel (**$A_2$**), extracellular alkalization fails to induce changes in PKD2L1 current response (top trace) or AP frequency (bottom trace). Dashed lines in $A_1$ and $A_2$ indicate 0 mV. **B.** Unitary PKD2L1 current traces recorded in voltage-clamp mode from a "real" CSF-cN (middle traces) are injected in the model neuron (top traces). Long PKD2L1 channel opening can trigger burst of APs in model neuron. Similarly, long depolarization can trigger single AP or burst of APs in "real" CSF-cN (bottom traces). Opening duration of unitary current events are indicated above voltage-clamp traces. Adapted from Orts Del'Immagine *et al.*, 2015.

## 3. POTENTIAL ROLES OF CSF-cNs

Since the discovery of CSF-cNs, many researchers questioned the role of these unique neurons and the answer is still elusive, especially in mammals. Based on CSF-cN properties, it was suggested that CSF-cNs would represent a novel neuronal population with a sensory role. Such a role is supported by the characteristic morphology of CSF-cNs with dendrite extending towards the CC and ending with a ciliated protrusion in the contact with the CSF (Vigh-Teichmann & Vigh, 1989; Orts-Del'Immagine *et al.*, 2014; Djenoune *et al.*, 2017). Further, CSF-cNs are strategically located around the CC, being in a direct contact with the CSF on one side and sending an axon on the other side, towards partners largely unkown to date. This might indicate their involvement in transmitting the information received from the CSF or in releasing the information into the CSF. To further support such a function, CSF-cNs selectively express PKD2L1, a channel capable of detecting changes in temperature, pH, osmolarity or even mechanical stimulations (Huang *et al.*, 2006; Shimizu *et al.*, 2009; Orts-Del'Immagine *et al.*, 2012; Böhm *et al.*, 2016; Jalalvand *et al.*, 2016*b*) and therefore acting both as chemosensor and mechanosensor. Moreover, it was demonstrated that the expression of PKD2L1 in zebrafish CSF-cNs would be necessary to maintain normal curvature of the spinal cord (Sternberg *et al.*, 2018). Recent studies conducted in zebrafish larvae and lamprey indicated that CSF-cNs would play a role as neuromodulator of locomotor activity (Wyart *et al.*, 2009; Jalalvand *et al.*, 2016*b*) In addition, the apparent immature phenotype of CSF-cNs and their presence in the spinal cord stem cell niche around the CC would argue for a role in reparatory and/or neuroregenerative processes. However, there is still no experimental data confirming such a role for CSF-cNs and thus this potential function remains to be established. Finally, spinal CSF-cNs appear to represent a heterogenous neuronal population divided at least into two subpopulations based on their origin, their localization around the CC and different physiological properties (Djenoune *et al.*, 2014, 2017; Orts-Del'Immagine *et al.*, 2014; Petracca *et al.*, 2016). It was suggested that they might also have a different function in the CNS.

### 3.1. Secretory function of CSF-cNs

One of the early roles assigned to CSF-cNs was a secretory one (Vigh *et al.*, 1977). Silver impregnated axons of CFS-cNs were seen to contact endfeet of glial cells at the ventrolateral surface of the spinal cord, where they form terminal enlargements containing

synaptic and granular vesicles. The authors indicated the possibility of vesiclular release from the axonal terminals into the external CSF or possible direct contact with meaningeal vessels (Vigh *et al.*, 1977). Several studies reported the presence of bioactive substances in soma and axon of CFS-cNs, such as monoamines or amino acids, which were suggested to be released from these neurons into the CSF or subarachnoid space of the spinal cord (Vigh *et al.*, 1977; Vigh & Vigh-Teichmann, 1998). In pleurodeles, axon terminals were shown to contact the blood vessels close to the basal lamina of the spinal cord surface and to contain granular vesicles, suggesting that they may participate in the control of vascular circulation of the spinal cord (Vigh *et al.*, 1977, 1983). In lamprey (Jalalvand *et al.*, 2014, 2016*b*) and zebrafish (Djenoune *et al.*, 2017) CSF-cNs express somatostatin, and once it is released, somatostatin can modulate the frequency of locomotor activity (Jalalvand *et al.*, 2016*b*). Nevertheless, limited data are available on secretory function of CSF-cNs. Further studies need to be carried out to fully demonstrate the involvement of the released bioactive substances in the regulation of CNS homeostasis or activity (Vigh & Vigh-Teichmann, 1998).

### 3.2. Sensory function of CSF-cNs is mainly mediated by activation of PKD2L1 channels

An interesting and specific characteristic of CSF-cNs is their dendritic extension that projects into the CC and ends with a ciliated protrusion in contact with the CSF (Orts-Del'Immagine *et al.*, 2012; Djenoune *et al.*, 2014; Orts Del'Immagine *et al.*, 2015; Petracca *et al.*, 2016). For that reason, it was argued that CSF-cNs might have sensory functions (Vigh *et al.*, 1977; Böhm *et al.*, 2016; Jalalvand *et al.*, 2016*b*) by receiving the information from the inner CSF in the spinal cord, or by releasing the information into the CSF originating from distal parts of the CNS. Selective expression of PKD2L1 channel further supports the sensory role for CSF-cNs (Huang *et al.*, 2006; Djenoune *et al.*, 2014; Orts-Del'Immagine *et al.*, 2014; Sternberg *et al.*, 2018).

The presence of ciliated structures on the bud of CSF-cNs supports the ***mechanosensory function*** for these neurons. Kinocilium and many stereocilia have been identified on the bud of CSF-cNs in many species, including turtle (Vigh *et al.*, 1977), zebrafish (Böhm *et al.*, 2016) and mouse (Orts-Del'Immagine *et al.*, 2014). It was previously shown that dendritic terminal enlargements of CSF-cNs share great similarity with known receptor cells, such as mechanoreceptors of the inner ear (Vigh *et al.*, 1977). Kinocilium of

CSF-cNs comes in the contact with Reissner's fiber, which may enable them to monitor the changes in CSF flow or pressure (Vigh *et al.*, 1977; Vígh *et al.*, 2004). Reissner's fiber is a fibrous structure that extends from the subcommissural organ, situated under the posterior commissure, through the cerebral aqueduct, the 4$^{th}$ ventricle and the entire length of the spinal CC. It was suggested that Reissner's fiber, together with CSF-cNs, form sensory organ capable of sensing the movements of the vertebrate column, which may cause dislocation of Reissner's fiber, detected by sensory processes of CSF-cNs in the CC (Vígh *et al.*, 2004).

Mechnosensory role of CSF-cNs has been described in lamprey spinal cord, where CSF-cNs are able to sense changes in the motion of the CSF (Jalalvand *et al.*, 2016*b*). In this model, CSF-cNs were activated by short fluid pulses in close proximity of the bud, which induced both cilia bending and generation of APs (Figure 17. A). ASIC3 channels expressed in CSF-cNs of the lamprey, which were shown to mediate chemosensitive response in CSF-cNs, are also involved in mechanotransduction in these neurons (Jalalvand *et al.*, 2016*b*). The response observed was shown to be direct, specific to CSF-cNs and not mediated through any synaptic activity (Jalalvand *et al.*, 2016*b*).

In contrast to ASIC3 channels in CSF-cNs of lamprey spinal cord, recent study demonstrated that mechanosensory function of CSF-cNs in zebrafish is strongly dependent on the expression of PKD2L1 channel (Sternberg *et al.*, 2018). High expression of PKD2L1 was found in the apical process (bud) of CSF-cNs in mouse (Orts-Del'Immagine *et al.*, 2014; Djenoune *et al.*, 2017), macaque, and zebrafish (Djenoune *et al.*, 2017; Sternberg *et al.*, 2018), indicating that CSF-cNs could sense the changes in CSF flow *via* PKD2L1 activity. Indeed, mechanical stimulation of cultured CSF-cNs from zebrafish embryo induced an increase in PKD2L1 channel open probability, which was not the case in PKD2L1 mutant CSF-cNs (Figure 17. B). Therefore, CSF-cNs *in vivo* may detect and respond to the flow of CSF (Sternberg *et al.*, 2018).

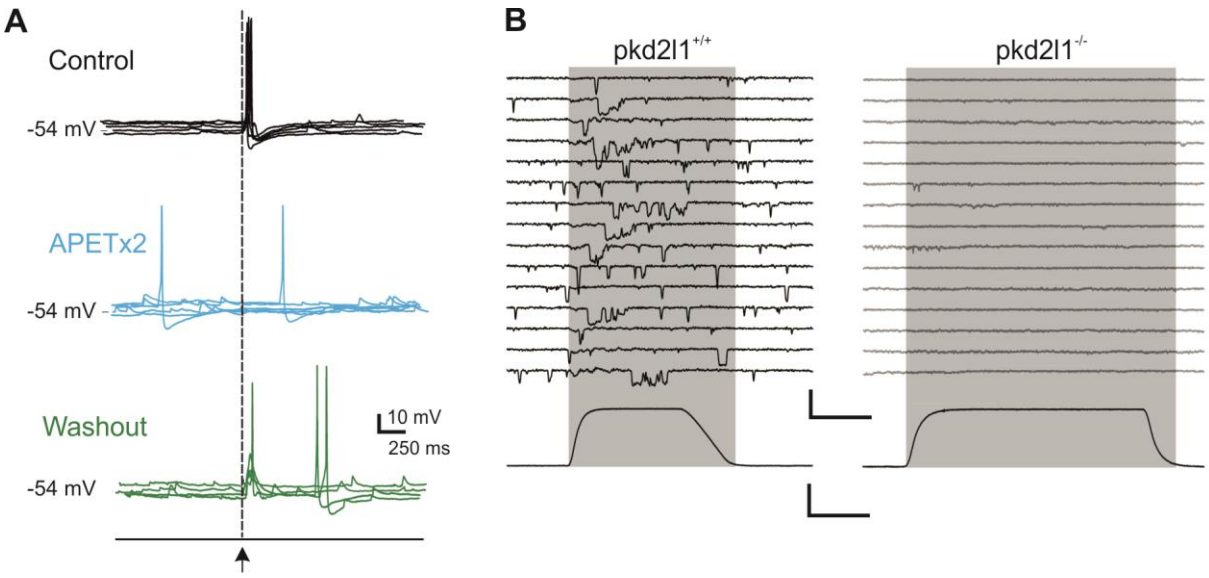


**Figure 17. CSF-cNs respond to mechanical stimulations.**

**A.** The response of CSF-cN in the lamprey spinal cord to mechanical stimulation (fluid pulse, 20 p.s.i., 80 ms) is mediated by ASIC3 channels, and this response is blocked in the presence of APETx2, a selective inhibitor of ASIC3 channels. **B.** Mechanical stimulation (grey square) of wild-type CSF-cN from cultured zebrafish embryo increases PKD2L1 channel opening (left). Such response is absent in CSF-cN that lacks PKD2L1 channel. Scale on top = 20 ms, 25 pA, bottom = 20 ms, 2 µm. Figure in A is from Jalalvand *et al.*, 2016*b*, figure in B is adapted from Sternberg *et al.*, 2018.

### 3.2.1. PKD2L1 channel in CSF-cNs is sensitive to changes in extracellular pH

CSF-cNs are considered to act as ***chemosensors*** able to sense changes in the CSF composition (Vigh-Teichmann & Vigh, 1989). Such a role was further supported by studies which demonstrated the expression of PKD2L1 channel in CSF-cNs that belong to TRP channel superfamily (Huang *et al.*, 2006; Orts-Del'Immagine *et al.*, 2012). Although the members of TRP superfamily exert different roles, sensory function, including chemosensation, is one of the most prominent roles for these channels (Zheng, 2013). Therefore, as many other TRP members, sensory role has been attributed to PKD2L1 channels. They were shown to be involved in sensing changes in extracellular pH in PKD2L1 expression systems (Shimizu *et al.*, 2009, 2011) but also in CSF-cNs (Orts-Del'Immagine *et al.*, 2012; Jalalvand *et al.*, 2016*b*). It was study by Huang and colleagues (2006) which demonstrated that PKD2L1 channels represent sensory receptors for sour taste when expressed in taste bud cells in the tongue. Mice that lacked PKD2L1 channels lost their sensitivity to sour taste, while responses for other tastes (sweet, bitter, and monosodium glutamate or umami) remained unchanged (Huang *et al.*, 2006). Another evidence for PKD2L1 as a channel bearing sensory function was given by the same study. PKD2L1

expressed in spinal CSF-cNs activated upon extracellular acidification when exposed to solution with a pH ranging from 6.5 to 7.4. In such conditions, CSF-cNs generated APs, which were markedly increased with a more acidic pH values, suggesting a chemosensory role of PKD2L1 in these neurons (Huang *et al.*, 2006).

Similar results were observed in laterally projecting CSF-cNs of lamprey spinal cord, which show high sensitivity to changes in extracellular pH (Jalalvand *et al.*, 2016*b*). It was demonstrated that lowering the pH from 7.4 to 6.9 increased spontaneous AP frequency, and this increase was even more evident with further lowering the pH to 6.5. Nevertheless, the response of CSF-cNs to decrease in extracellular pH was not mediated by PKD2L1 channel but by ASIC3 channel (Figure 18. A), a member of mechano-/chemosensitive acid-sensing ion channels (ASICs) expressed in sensory neurons (Li & Xu, 2011 p.3; Jalalvand *et al.*, 2016*b*). ASIC3-mediated response in CSF-cNs was confirmed in the presence of APETx2, an ASIC3 inhibitor, since changes in extracellular pH failed to evoke any response in CSF-cNs. Furthermore, the authors showed that the sensitivity of CSF-cNs to changes in pH is directly mediated by these neurons, and not by cellular or synaptic interactions (Jalalvand *et al.*, 2016*b*). The same group also reported that CSF-cNs are capable of distinguishing extracellular acidification from alkalization by selective activation of ASIC3 and PKD2L1, respectively. Encouraged by such results, they suggested that CSF-cNs represent a novel homeostatic system responsible for the control of pH variations (Jalalvand *et al.*, 2016*a*).

In agreement with the data obtained from lamprey CSF-cNs, ASIC channels are shown to be involved in sensing the changes of extracellular pH in mouse CSF-cNs (Orts-Del'Immagine *et al.*, 2012; Orts Del'Immagine *et al.*, 2015). When CSF-cNs were recorded in voltage-clamp mode, high acidification evoked fast transitory inward current followed by small amplitude inward current, a response that was sustained and lasted during the time of acidification (Orts-Del'Immagine *et al.*, 2012). To confirm that acidification-evoked inward current in CSF-cNs is mediated by ASIC channels, a selective inhibitor of ASIC1a/2b channels, *Psalmopoeus cambridgei* toxin 1 (PcTx1), was applied and as result, it greatly reduced observed inward current (Figure 18. B) (Orts-Del'Immagine *et al.*, 2012; Orts Del'Immagine *et al.*, 2015). This response was reproducible in PKD2L1$^{-/-}$ mutant mice, which lack the expression of PKD2L1, providing another evidence that CSF-cNs sense the extracellular acidification by activation ASIC but not PKD2L1 channels (Orts Del'Immagine *et al.*, 2015). Along with fast current mediated by ASIC channels activation, acidification

inhibited PKD2L1 channel activity and reduced channel open probability ($NP_o$) (Orts-Del'Immagine *et al.*, 2012). Similar response was recorded in current-clamp mode. There, acidification triggered large depolarization and evoked APs, followed by slowly recovering depolarization of smaller amplitude that lasted during acid application (Orts-Del'Immagine *et al.*, 2012; Orts Del'Immagine *et al.*, 2015). These events were inhibited in the presence of PcTx1, and they were not dependent on the expression of PKD2L1 channels (Orts Del'Immagine *et al.*, 2015). These results obtained from recordings in lamprey (Jalalvand *et al.*, 2016*b*) and mouse (Orts-Del'Immagine *et al.*, 2012; Orts Del'Immagine *et al.*, 2015) suggest that acidification activates ASIC channels and consequently increases CSF-cN excitability.

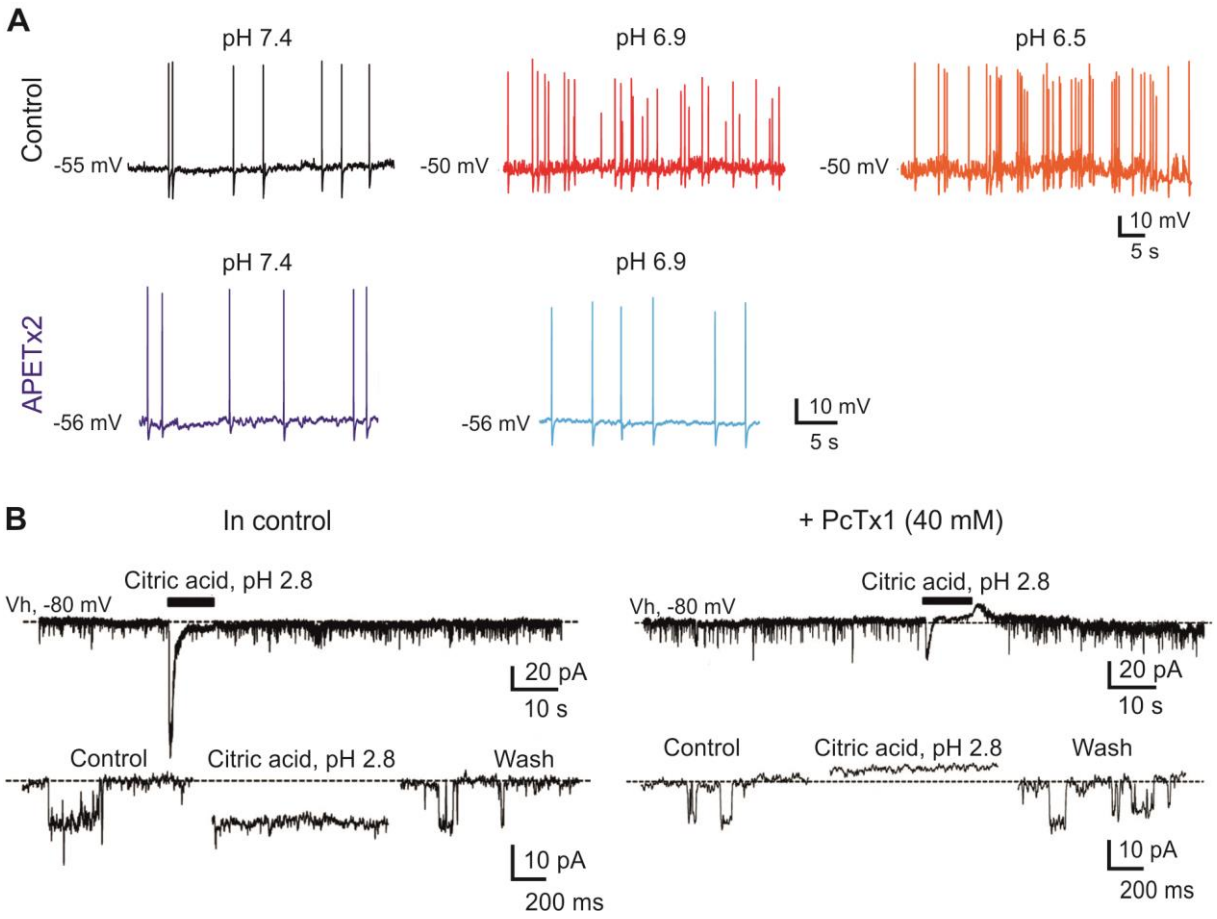


**Figure 18. CSF-cNs sense the changes in extracellular acidification through the activation of ASIC channels.**

**A.** CSF-cNs in the lamprey spinal cord spontaneously fire APs at physiological pH (black trace). Lowering the pH to 6.9 increases the frequency of APs (red trace) which is more pronounced at even lower pH values (6.5, orange trace). APETx2 application eliminates the response to lower pH (violet and blue traces), indicating the involvement of ASIC3 channels in pH sensitivity of lamprey CSF-cNs. **B.** In the mouse brainstem, acidification evokes fast inward current (top trace, left) and inhibits

PKD2L1 channel activity (bottom trace, left). In the presence of PcTx1 (right traces), the amplitude of fast inward current is reduced (top trace), while the PKD2L1 unitary current is unchanged and still inhibited (bottom trace). Figure in A is adapted from Jalalvand *et al.*, 2016*b*, and figure in B is adapted from Orts-Del'Immagine *et al.*, 2012.

In contrast to acid-evoked responses, extracellular alkalization strongly activates PKD2L1 channels. Increase to pH 9 induces an increase in open probability of PKD2L1 channels, without changing the unitary current amplitude (Figure 19. A) (Shimizu *et al.*, 2011; Orts-Del'Immagine *et al.*, 2012) or single channel conductance (Shimizu *et al.*, 2011). When CSF-cNs were recorded in current-clamp mode, increase in spontaneous AP frequency was further observed (Figure 19. B) (Orts-Del'Immagine *et al.*, 2012; Jalalvand *et al.*, 2016*b*). This response was not seen in PKD2L1$^{-/-}$ mutant mice where alkalization did not change current activity, nor the frequency of APs (Orts Del'Immagine *et al.*, 2015). Moreover, a study by Shimizu and colleagues (2011) demonstrated that PKD2L1 channel overexpressed in HEK293T cell respond to alkalization in bell-shaped manner, that is, increase of pH to 9.0 activated PKD2L1 channels, but further increase to pH 10.0 had an opposite, inhibitory effect on channel activity. Dual effect of alkalization on PKD2L1 channel activity may indicate the complexity of channel gating kinetics (Shimizu *et al.*, 2011).

As a member of polycystin subfamily of TRP channels (TRPP), PKD2L1 is a membrane protein which has six transmembrane domains (S1-S6), with both N- and C-terminal domains located intracellularly, a pore loop region between the fifth and sixth domains, and a large extracellular loop between the first and second domains (Venkatachalam & Montell, 2007). A recent study showed that the asparagine residue at position 533 (N533) in the pore loop of the PKD2L1 channel is responsible for channel activity modulation in response to extracellular alkalization (Shimizu *et al.*, 2017). It was clearly demonstrated that PKD2L1 channels carrying a mutation in N533 fail to activate upon alkalization, although the mutation did not affect single-channel conductance (Shimizu *et al.*, 2017). Therefore, the identical role of N533 in modulating the pH sensitivity of PKD2L1 channel in CSF-cNs can be assumed.

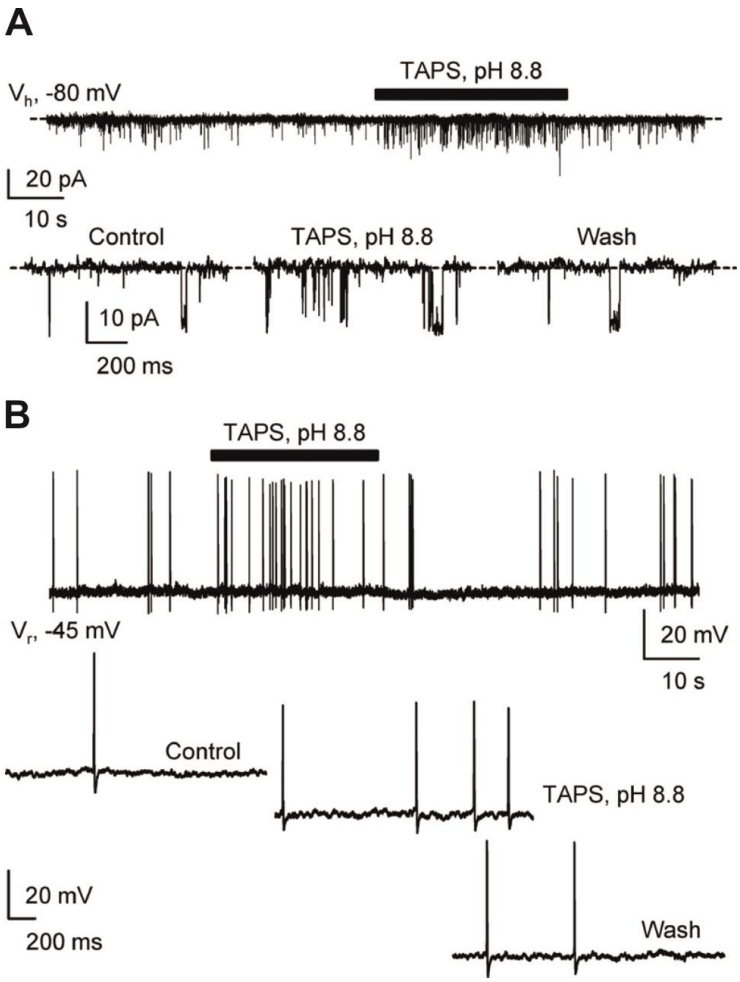


**Figure 19. CSF-cNs sense the changes in extracellular alkalization through the activation of PKD2L1 channels.**

**A.** Recordings from CSF-cNs in the mouse brainstem in voltage-clamp mode show the response to extracellular alkalization induced by 30 s pressure application of TAPS (pH 8.8, black horizontal bar). Current traces (bottom) from recording on the top are expanded at the bottom. Note the increase in PKD2L1 activity during extracellular alkalization. Dashed line represents closed state of the channel. **B.** In current-clamp mode, the same CSF-cNs as in figure A is recorded at RMP ($V_r$ = -45 mV). Traces on the bottom are expanded from the recording at the top. Note the increase in AP frequency during extracellular alkalization. Figure from Orts-Del'Immagine *et al.*, 2012.

### 3.2.2. Modulation of PKD2L1 channel by osmolarity and temperature

CSF-cNs are further argued to sense the changes in osmolarity mediated by PKD2L1 channels (Shimizu *et al.*, 2009; Orts-Del'Immagine *et al.*, 2012). It was demonstrated that hypo-osmotic conditions increase PKD2L1 single channel activity (Shimizu *et al.*, 2009; Orts-Del'Immagine *et al.*, 2012), while hyper-osmotic solutions decrease channel open probability ($NP_o$) without changing single-channel conductance (Figure 20. A). Therefore, PKD2L1 channel activity is modulated by changes in cell volume due to changes in osmolarity both in

heterologous expression systems (Shimizu *et al.*, 2009) and in CSF-cNs (Orts-Del'Immagine *et al.*, 2012).

In addition to osmosensitive, thermosensitive function is attributed to PKD2L1 channels (Higuchi *et al.*, 2014; Shimizu *et al.*, 2017). In *Xenopus* oocyte, elevating the temperature of extracellular solution up to 40°C increases single-channel conductance, but decreases single-channel activity. Interestingly, rapid decrease in the temperature increases channel open probability (Higuchi *et al.*, 2014; Shimizu *et al.*, 2017). Based on temperature-dependent gating mechanism of PKD2L1 channel, it is suggested that PKD2L1 shows three states in the gating kinetics. Thus, temperature may lead to fast transition of PKD2L1 channel from closed (C) to open (O) state, followed by rapid inactivation (I) or closing of the channel. Such gating kinetics differs from those observed in other TRP channels activated by temperature, which show increased open probabilities during heating or cooling. This indicates that PKD2L1 channels are modulated by distinct temperature-dependent mechanism (Higuchi *et al.*, 2014). The important factor in regulating the temperature-sensitive response of PKD2L1 is N533 residue in PKD2L1 channel pore that is also responsible for pH-mediated responses (Figure 20. B) (Shimizu *et al.*, 2017). Therefore, CSF-cNs expressing PKD2L1 may have an important role in sensing the temperature changes of the CSF and modulate the activity of their potential partners.

### 3.2.3. PKD2L1 channels are permeable to $Ca^{2+}$ in heterologous expression systems

Most TRPs are expressed in cellular plasma membrane where they act as non-selective cation channels that regulate the intracellular concentration of different ions, such as $Ca^{2+}$ and $Mg^{2+}$ (Gees *et al.*, 2010; Nilius & Owsianik, 2011; Zheng, 2013). Such properties of PKD2L1 channels were first described by Chen and colleagues (1999), who demonstrated that PKD2L1 is permeable to $Ca^{2+}$ in heterologous expression system. Further, PKD2L1 is modulated by $Ca^{2+}$. As shown by the same study, increase of both extracellular and intracellular $Ca^{2+}$ concentration led to increase in PKD2L1 channel activity without modulating channel conductance. Prolonged exposure to extracellular $Ca^{2+}$ caused desensitization of the channel, resulting in lower channel activity due to increase in intracellular $Ca^{2+}$ concentration (Chen *et al.*, 1999). Recently, in CSF-cNs of zebrafish larvae (so called KA cells), PKD2L1 channels were also shown to be $Ca^{2+}$ permeable (Böhm *et al.*, 2016). However, it is still unknown whether PKD2L1 channels in mammalian CSF-cNs represent $Ca^{2+}$ permeable channels and

whether similar modulation of these channels by extracellular and/or intracellular $Ca^{2+}$ is present. Many members of TRP channels are found in intracellular membranes, such as ER (Zheng, 2013), which represents intracellular $Ca^{2+}$ store (Verkhratsky, 2005). Since PKD2 channels were shown to be present on the ER membrane (Giamarchi *et al.*, 2010), it would be interesting to demonstrate the involvement of PKD2L1 channels in the regulation of $Ca^{2+}$ homeostasis in CSF-cNs.

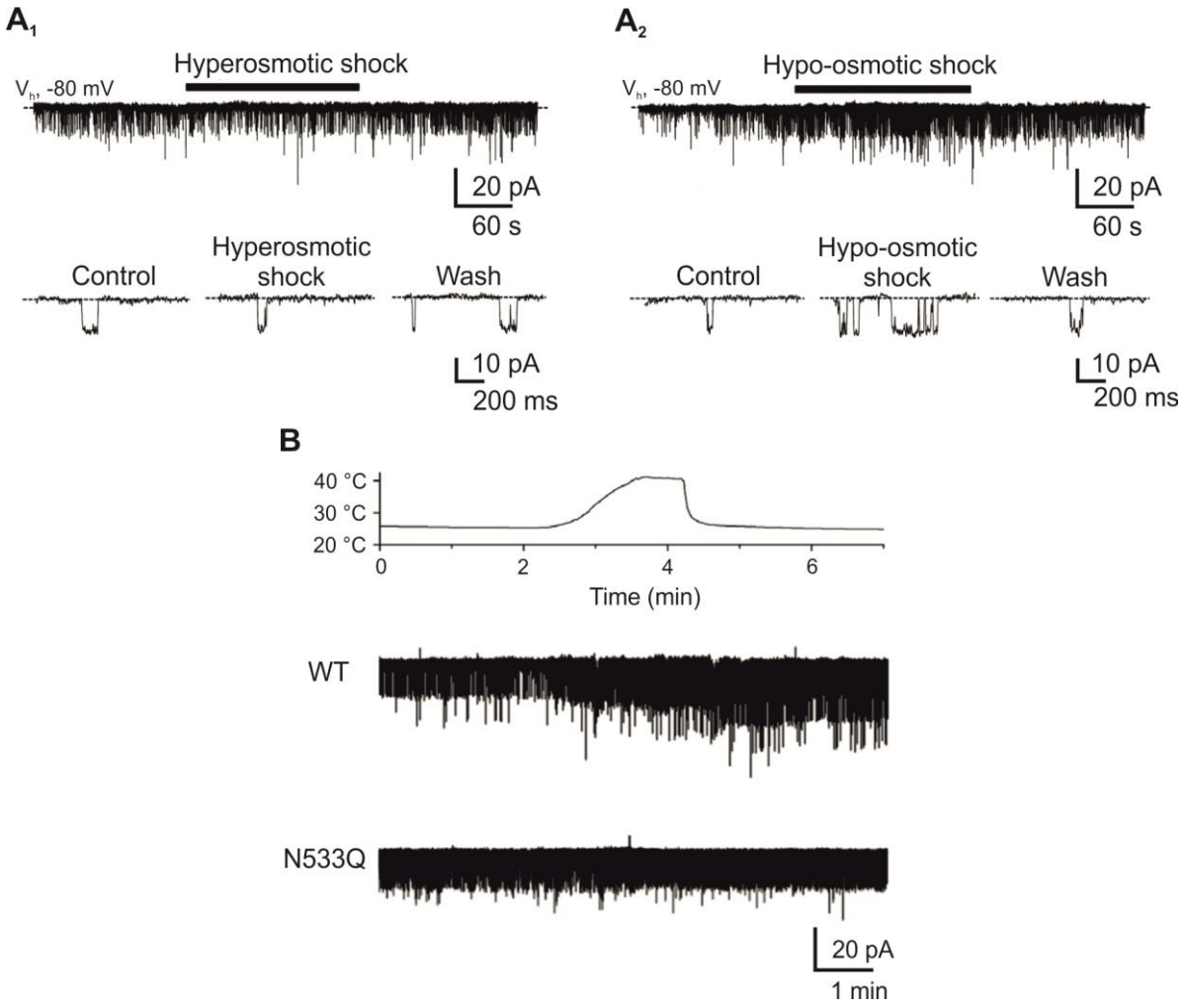


**Figure 20. CSF-cNs are sensitive to changes in extracellular osmolarity and temperature.**

**A.** Voltage-clamp traces recorded in CSF-cN from the mouse brainstem at -80 mV ($V_h$) exposed to pressure application of hyperosmotic solution of ~355 mosmol $kg^{-1}$ (**$A_1$**; 3 min; black horizontal bar) or hypo-osmotic solution of ~265 mosmol $kg^{-1}$ (**$A_2$**; 3 min; black horizontal bar). **$A_1$.** Application of hyperosmotic solution has no effect on PKD2L1 channel current amplitude or open probability. **$A_2$.** Application of hypo-osmotic solution has no effect on PKD2L1 channel current amplitude, but it increases open probability. Bottom traces in $A_1$ and $A_2$ are expanded traces from recordings at the top. **B.** Current traces recorded from HEK293T cells at -60 mV expressing wild-type (WT) PKD2L1 channel and mutant (N533Q). Panel on top shows the changes in temperature of extracellular solution. Figures in $A_1$ and $A_2$ are adapted from Orts-Del'Immagine *et al.*, 2012, figure in B is from Shimizu *et al.*, 2017.

### 3.3. Physiological function of CSF-cNs

The physiological role of mysterious medullo-spinal CSF-cNs in the CNS has intrigued the researchers for a long time. The lack of specific marker for CSF-cNs and their localization deep in the spinal cord around the CC represented obstacles that were difficult to overcome. This issue was recently solved with the demonstration that PKD2L1 is a selective marker for CSF-cNs (Huang *et al.*, 2006; Djenoune *et al.*, 2014; Orts-Del'Immagine *et al.*, 2014) and the development of new methods enabled sophisticated researches to be developed.

CSF-cNs are strategically located between the CSF and the parenchyma where they extend their axons, although their projection partners have not yet been fully described. Using zebrafish larvae model expressing light-gated glutamate receptor, Wyart and colleagues (2009) showed that CSF-cNs are implicated in the modulation of locomotor activity (Wyart *et al.*, 2009). In zebrafish, CSF-cNs, referred as Kolmer-Agduhr cells (KA cells), are GABAergic neurons that have cilia projecting into the CSF, and ascending axon that projects ipsilaterally, forming their terminals in a series of two to six consecutive segments (Wyart *et al.*, 2009; Fidelin *et al.*, 2015). In the study by Wyart and colleagues, optogenetic activation of CSF-cNs induced swim-like behavior in head-restrained zebrafish larvae, as it evoked symmetrical beating of the tail typical for the spontaneous slow swim. This swim-like behavior was reduced when KA cells were genetically silenced. Moreover, in the presence of selective antagonist of $GABA_A$ receptors to inhibit GABA activity, the light-induced response was greatly abolished, suggesting that the modulation of swimming behavior by CSF-cNs is dependent on release of GABA (Wyart *et al.*, 2009). This study suggested that CSF-cNs would project onto the central pattern generators (CPGs) of the spinal cord during the early development, but the targets of these neurons remained unknown.

The same group of researchers took advantage of the zebrafish larvae model and combined optogenetic to electrophysiological recordings to identify CSF-cN synaptic partners and their role in the regulation of CPGs (Fidelin *et al.*, 2015). For the first time, this study showed that KA neurons were directly connected to spinal glutamatergic premotor interneurons ($V0_V$) within the locomotor CPGs that are involved in slow locomotion in zebrafish (Figure 21. A). To test the functional connectivity between CSF-cNs and $V0_V$ interneurons, CSF-cNs that express channelrhodopsin-2 (ChR-2) were optically activated using brief light pulses while performing patch-clamp recordings from $V0_V$ interneurons. GABAergic synaptic events could be elicited in $V0_V$ interneurons following light-stimulation

of CSF-cNs (Figure 21. B), and this response was abolished in the presence of gabazine, a $GABA_A$ receptor antagonist. These results provided the evidence that CSF-cNs form inhibitory GABAergic synapses onto $V0_V$ interneurons (Fidelin *et al.*, 2015). As a consequence, light-activated KA cells were capable of inducing slow forward swim-like behavior from rest (Figure 21. C), a response that involved the recruitment of $V0_V$ interneurons (Fidelin *et al.*, 2015). In contrast, optical activation of KA during naturally ongoing swimming behavior disrupted on-going swimming activity and reduced the duration and frequency of swim bouts (Figure 21. C). The opposite effects of CSF-cNs on swimming behavior in zebrafish larvae were explained by post-inhibitory rebound caused by membrane depolarization following inhibition (Fidelin *et al.*, 2015).

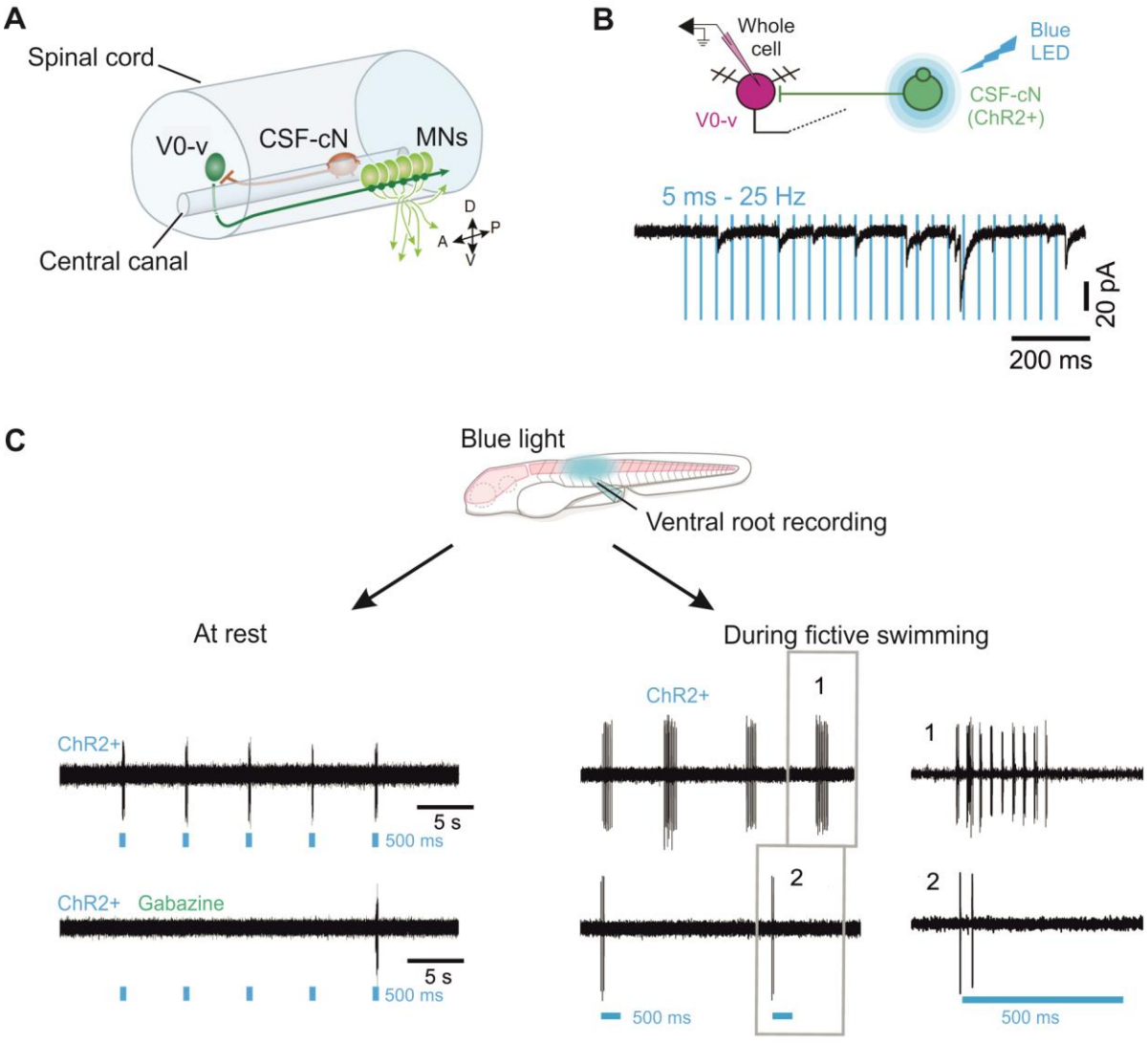


**Figure 21. CSF-cNs synapse onto V0-v glutamatergic interneurons and modulate locomotor activity in the zebrafish larva.**

**A.** Schematic illustration of CSF-cN (orange) that provides GABAergic synaptic input onto $V0_V$ (dark green) which synapses directly with motoneurons (MNs, light green). Motoneurons project towards

the periphery and innervate musculature. **B.** Illustration at the top represents experimental model where the whole-cell voltage-clamp recordings were performed from $V0_V$ interneurons while activating CSF-cNs with blue light. Optical stimulation of channelrhodopsin-2 (ChR2+)-expressing CSF-cN with blue light pulses (blue bars, bottom trace) evokes IPSCs in $V0_V$ interneurons. **C.** Schematic illustration of experimental setup (top). Ventral root recordings were performed to monitor the effects on fictive locomotor outputs while activating CSF-cNs with blue light. Optical stimulation of CSF-cN during the rest induced fictive locomotion in zebrafish larva (top left trace). Swimming response was blocked in the presence of 20 µM gabazine in the extracellular solution (bottom left trace). Application of blue light at the onset of ongoing fictive swimming induced silencing of swimming activity (right traces). Traces 1 and 2 on right are expanded from traces marked with grey square. Schematic illustrations in A and C are from (Jay & McDearmid, 2015). Figures in B and C are from Fidelin *et al.*, 2015.

Further, it was shown that KA cells possess an apical extension (kinocilium and a brush of microvilli) in contact with the CSF that acts as mechanosensing organs (Böhm *et al.*, 2016). The role of these neurons was investigated in the head-restrained zebrafish. The results demonstrated that both active bending of the spinal cord, when muscles contract, and passive bending of the spinal cord due to mechanical stimulation induced $Ca^{2+}$ elevation in KA cells. Notably, only dorsal KA cells ipsilateral to the contracting site responded to active bending of the spinal cord (Figure 22. A). PKD2L1 channels were shown to play a central role in this response, since zebrafish mutant lacking PKD2L1 failed to respond to mechanical activation of CSF-cNs (Böhm *et al.*, 2016). Taken together, these results demonstrate that KA cells would act as mechanosensors in the spinal cord to monitor spine bending through a PKD2L1-mediated $Ca^{2+}$ rise.

A similar role of CSF-cNs in the modulation of the locomotor activity was demonstrated in the lamprey spinal cord (Jalalvand *et al.*, 2016*b*). There, the axons of CSF-cNs were shown to ramify in the grey matter, which raised the possibility that CSF-cNs may directly influence the activity of the neurons that belong to the same locomotor network (Jalalvand *et al.*, 2016*b*). This mechanosensitive role of CSF-cNs is attributed to ASIC3 channels that activate upon extracellular acidification and consequentially increase the excitability of CSF-cNs (Jalalvand *et al.*, 2016*b*). Indeed, a reduction in locomotor burst activity was observed when isolated spinal cord of the lamprey was exposed to acidic pH during on-going fictive locomotion. It was demonstrated that ASIC3 channels were responsible for CSF-cN activation and the subsequent modulation of locomotor rhythm. These results are in agreement with the results obtained from zebrafish (Fidelin *et al.*, 2015).

CSF-cNs of the lamprey spinal cord express somatostatin (Jalalvand *et al.*, 2014). It was suggested that somatostatin might be implicated in the modulation of fictive locomotion as it depressed the locomotion burst rate in isolated spinal cord (Jalalvand *et al.*, 2016*b*). This effect was abolished in the presence of somatostatin antagonist, which also had an inhibitory effect on acidification-mediated decrease of locomotor burst frequency. These findings strongly support the idea that CSF-cNs may have direct modulatory effect on the locomotor activity when pH drops under normal, physiological values (Jalalvand *et al.*, 2016*b*). Furthermore, the isolated spinal cord was a model to test whether CSF-cNs can sense the bending of the spinal cord which occurs during naturally-occurring active swimming behavior. Using $Ca^{2+}$ imaging, it was demonstrated that CSF-cNs activate upon lateral bending of the spinal cord (Figure 22. B), seen as an increase in the fluorescence intensity of a $Ca^{2+}$-indicator (Jalalvand *et al.*, 2016*b*). Similar response of CSF-cNs to spinal cord bending was observed in zebrafish (Böhm *et al.*, 2016).

Taken together, CSF-cNs are strongly suggested to represent a novel population of sensory neurons capable of sensing the changes in their environment and transmitting the information toward their projection partners. In lower vertebrates, CSF-cNs seem to directly modulate the activity of interneurons in CPG involved in the control of the movements in vertebrates (Marder & Bucher, 2001). A similar role for CSF-cNs in mammals remains to be established.

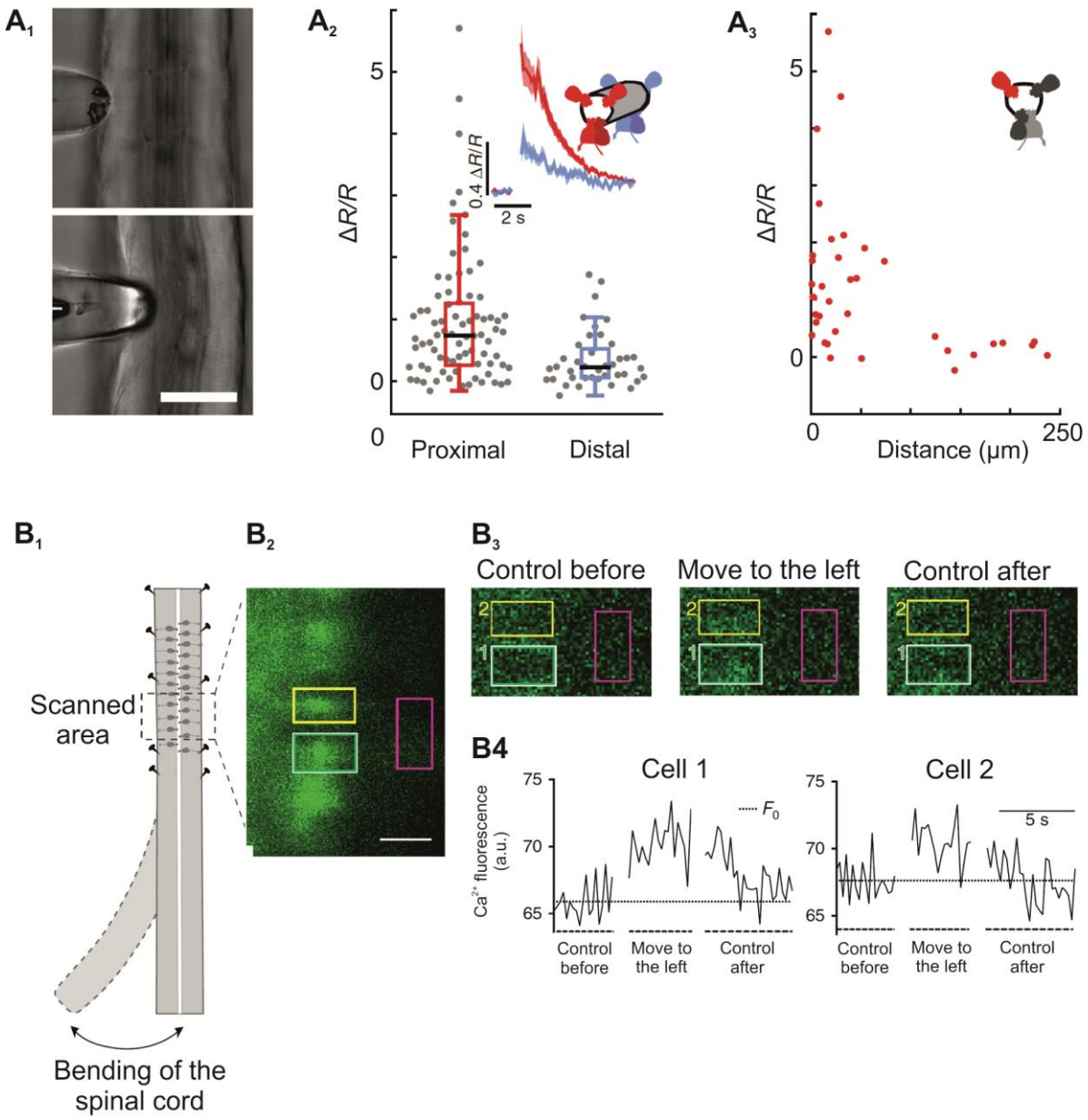


**Figure 22. CSF-cNs respond to spinal cord bending.**

**$A_1$.** Glass probe was used to mechanically stimulate CSF-cNs in paralyzed zebrafish larva. **$A_2$.** Mostly CSF-cNs located close to the site of passive stimulation were activated. **$A_3$.** The amplitude of response decreased with increasing distance from the probe. **$B_1$.** Schematic representation of experimental model in which rostral spinal cord from lamprey is fixed, and caudal end is free to move. **$B_2$.** Image taken in the scanned area indicated in $B_1$ with two CSF-cNs (regions in yellow and green) and reference region to measure background fluorescence (red). **$B_3$.** Changes in fluorescence intensity were measured before spinal cord bending, during the bending to the left and after the return to the control position. **$B_4$.** Traces indicate $Ca^{2+}$ fluorescence intensity from two cells (regions in $B_2$, $B_3$) before, during and after lateral bending of the spinal cord. Dotted line represents mean baseline fluorescence level in control (before bending movement, $F_0$). Scale bars = 50 μm in $A_1$, 20 μm in $B_2$. Figures in A are adapted from Böhm *et al.*, 2016, figures in B are adapted from Jalalvand *et al.*, 2016*b*.

# C) VOLTAGE-GATED CALCIUM CHANNELS

Voltage-gated calcium channels (VGCCs or $Ca_v$s) are present in all excitable cells. Activation of $Ca_v$s upon membrane depolarization mediates $Ca^{2+}$ influx from extracellular space, which makes them an important source for intracellular $Ca^{2+}$. Local increase in intracellular $Ca^{2+}$ concentration initiates many important physiological events, such as neurotransmitter release (Südhof, 2012) or gene expression (Catterall, 2011), indicating the essential role of $Ca_v$s in maintaining normal function of cells.

$Ca_v$s were first discovered by Fatt and Katz in 1953 in crustacean muscle fibers (Fatt & Katz, 1953). The study that aimed at describing the electrical properties and excitability of the crustacean muscle membrane demonstrated that even in the absence of external $Na^+$, the muscle continued to generate APs. This response was maintained in the presence of $Ca^{2+}$, $Mg^+$, $K^+$ and $Cl^-$, suggesting that they may be responsible in transport of the charge underlying the excitation. When these ions were removed one by one from the solution, Fatt and Katz found that only removal of $Ca^{2+}$ suppresses the generation of the AP, highlighting the importance of $Ca^{2+}$ influx for muscle excitability (Fatt & Katz, 1953). Study by Fatt and Ginsborg further supported the finding that the presence of $Na^+$ and $Mg^+$, unlike $Ca^{2+}$, is not necessary for AP generation in crustacean muscle membrane (Fatt & Ginsborg, 1958). By analyzing membrane currents in the starfish eggs to study ionic mechanisms of excitation, Hagiwara and colleagues gave an evidence for the existence of more than one type of $Ca^{2+}$ channels (Hagiwara, 1975). Following these, and many more studies, $Ca_v$s are found in all excitable cells but also in some non-excitable cells (Grafton & Thwaite, 2001).

$Ca_v$s are divided in several subtypes based on their biophysical properties, such as voltage-dependent kinetics, inactivation properties, physiological functions in cell, or sensitivity to various pharmacological agents. $Ca^{2+}$ channels have been designated into three families regarding the expression of α1 subunit which is the main determinant of $Ca^{2+}$ channel type (Catterall, 2011). $Ca_v1$ family consists of L-type $Ca^{2+}$ channels, $Ca_v2$ family is composed of N-, R-, P- and Q-type channels, while $Ca_v3$ family consists of T-type $Ca^{2+}$ channels (Perez-Reyes, 2003; Catterall, 2011). Opening of these channels upon plasma membrane depolarization trigger $Ca^{2+}$ influx into the cell, mediating many principal physiological processes, such as vesicle secretion, fertilization, neurotransmitter release, or muscle contraction, although prolonged elevations of intracellular $Ca^{2+}$ can be lethal for the cell (Berridge *et al.*, 1998; Südhof, 2012). Therefore, $Ca^{2+}$ channels are important factor in

converting the electrical signals generated at the membrane of the cell into the $Ca^{2+}$ transients. An overview on $Ca^{2+}$ channels properties, functions, and subtypes will be presented in this Chapter.

## 1. PROPERTIES AND FUNCTION OF VOLTAGE-GATED CALCIUM CHANNELS

$Ca_v$s open in response to membrane depolarization, and based on their sensitivity to depolarization, they can be divided into two categories (Figure 23.) (Perez-Reyes, 2003; Simms & Zamponi, 2014). High-voltage activated (HVA) channels activate in response to voltage more depolarized than -40 mV and include L-type ($Ca_v1$), N-type, R-type and P/Q-type $Ca^{2+}$ channels ($Ca_v2$). In contrast, low-voltage activated (LVA) channels activate at much more negative potentials (from -70 mV) compared to HVA channels and include only T-type ($Ca_v3$) $Ca^{2+}$ channels (Dolphin, 1995; Catterall, 2011; Simms & Zamponi, 2014). HVA are heteromultimeric proteins that consist of the pore-forming α1 subunit co-expressed with auxiliary cytoplasmic β subunit and extracellular α2δ subunits. $Ca^{2+}$ channels from skeletal muscles express an additional γ subunit, while LVA channels are devoid of any ancillary subunit (Catterall, 2011; Simms & Zamponi, 2014) and consist of α1 subunit only (He *et al.*, 2018). α1 subunit of $Ca_v$s is encoded by ten genes, giving rise to 10 members of $Ca^{2+}$ channels that are divided into 3 subfamilies (Catterall, 2011; Simms & Zamponi, 2014; He *et al.*, 2018). They can be distinguished based on their sensitivity to different pharmacological agents, which represent a reliable tool for separation of distinct $Ca^{2+}$ channel types. Thus, $Ca_v1$ family of $Ca^{2+}$ channels (L-type) has four members, $Ca_v1.1$ - 1.4, and all of them show high sensitivity to inhibitory effect of dihydropyridines (DHPs) (Zamponi, 1997; Lipscombe *et al.*, 2004; Simms & Zamponi, 2014). $Ca_v2.1$ - 2.3, the members of $Ca_v2$ family of $Ca^{2+}$ channels are blocked by distinct agents. P/Q-type of $Ca^{2+}$ channels ($Ca_v2.1$) are selectively inhibited by spider toxin ω-agatoxin IVA, although P-type channels show higher affinity to block mediated by this toxin compared to Q-type channels (Mintz *et al.*, 1992*b*, 1992*a*; Catterall, 2011). N-type $Ca^{2+}$ channels ($Ca_v2.2$) are selectively blocked by ω-conotoxin GVIA isolated from cone snail (McCleskey *et al.*, 1987; Aosaki & Kasai, 1989; Catterall, 2011). R-type or $Ca_v2.3$ channels are sensitive to block by SNX-482, a peptide derived from the tarantula venom (Newcomb *et al.*, 1998). Finally, $Ca_v3$ family of $Ca^{2+}$ channels (T-type) has three members ($Ca_v3.1$ - 3.3) which are potently and irreversibely

inhibited by piperidine-based compound TTA-P2 (Dreyfus *et al.*, 2010; Choe *et al.*, 2011). However, only $Ca_v3.2$ channel can be selectively inhibited by nickel ($Ni^{2+}$), while $Ca_v3.1$ and $Ca_v3.3$ are $Ni^{2+}$-insensitive (Zamponi, 1997; Lee *et al.*, 1999*b*; Catterall, 2011). In addition to α1 subunit, four distinct genes encode for β subunits which bind the α1 subunit with a high affinity. It was demonstrated that one type of α1 subunit can associate with various types of β subunits, which therefore contribute to a great diversity of $Ca_v$s that exhibit specific functions (Catterall, 2011).

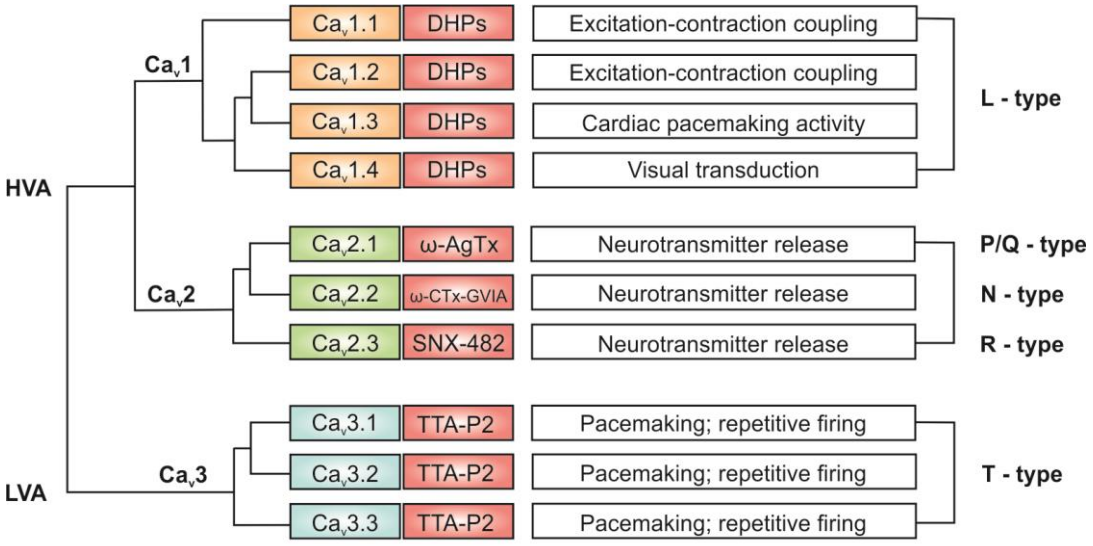


**Figure 23. $Ca^{2+}$ channels subfamilies.**

$Ca^{2+}$ channels are defined as high-voltage activated (HVA) and low-voltage activated (LVA). HVA $Ca^{2+}$ channels include 2 subfamilies of channels – $Ca_v1$ or L-type (orange boxes) and $Ca_v2$ (P/Q-type, N-type, R-type; green boxes). LVA $Ca^{2+}$ channels consist of $Ca_v3$ or T-type channels (blue boxes). Each of these channels type has specific inhibitor that is indicated in red boxes. The main function of each channel subtype is presented. DHPs: dihydropyridines; ω-AgTx: ω-agatoxin; ω-CTx-GVIA: ω-conotoxin GVIA. Adapted from Catterall, 2011; Dolphin, 2012; Dreyfus *et al.*, 2010.

$Ca_v$s are found in all excitable cells and in some non-excitable cells (Grafton & Thwaite, 2001). The function of $Ca_v$s varies depending on $Ca^{2+}$ channel type and its cellular localization. In nerve terminals, N- and P/Q-types $Ca^{2+}$ channels have an important role in synaptic transmission (Ishikawa *et al.*, 2005; Simms & Zamponi, 2014; He *et al.*, 2018), as local increase in intracellular $Ca^{2+}$ concentration upon influx of $Ca^{2+}$ through these channels mediates synaptic vesicle exocytosis and neurotransmitter release (Südhof, 2012). R-type channels are also found to be expressed in neurons where they are involved in

neurotransmitter release, although they do not represent a major neuronal type of $Ca^{2+}$ channels (Catterall, 2011; He *et al.*, 2018). L- and T-type channels are found in various types of tissues and cells, including skeletal muscle, cardiac muscle, or neurons (Perez-Reyes *et al.*, 1998; Lipscombe *et al.*, 2004; Catterall, 2011; Bannister & Beam, 2013). L-type channels, although found to be involved in synaptic transmission, are important in secretion of hormones, and excitation-contraction coupling in skeletal, cardiac and smooth muscles where they are responsible for muscle contractions. In addition, $Ca^{2+}$ entry through L-type $Ca^{2+}$ channels regulates gene transcription in neurons (Catterall, 2011). T-type $Ca^{2+}$ channels are involved in regulation of the neuronal excitability and are important in repetitive-firing tissues (Perez-Reyes, 2003; Catterall, 2011).

Taken together, $Ca^{2+}$ channels are crucial for maintaining normal functions of the cells. The role of each channel depends on its localization, but also the structure. Therefore, more details on each channel are given below.

## 2. CALCIUM CHANNEL SUBUNITS

Five subunits were purified from dihydropyridine-sensitive $Ca^{2+}$ channels from skeletal muscles, namely α1, α2, β, γ and δ (Figure 24.) (Takahashi *et al.*, 1987; Catterall, 2011; He *et al.*, 2018). The main, pore-forming α1 subunit is a transmembrane protein of 190 kDa associated with 170 kDa α2δ dimer linked together with a disulfide bond. The phosphorylated β subunit of 55 kDa is an intracellular subunit without any transmembrane segment, in contrast to γ subunit of 33 kDa that is a transmembrane glycoprotein (Takahashi *et al.*, 1987; Catterall, 2011; He *et al.*, 2018). Each of these subunits exhibit a specific role important for normal channel functioning. The α1 subunit determines the type of $Ca_V$s, it presents a voltage sensor of the channel and the channel pore, but it also provides many binding sites for regulatory proteins and scaffold proteins that enable the regulation of intracellular $Ca^{2+}$ concentration. Auxiliary subunits, α2δ, β, and γ subunit, can modulate the gating properties of the channels and they are involved in regulation of synaptic release at the presynaptic level (Takahashi *et al.*, 1987; Catterall, 2011).

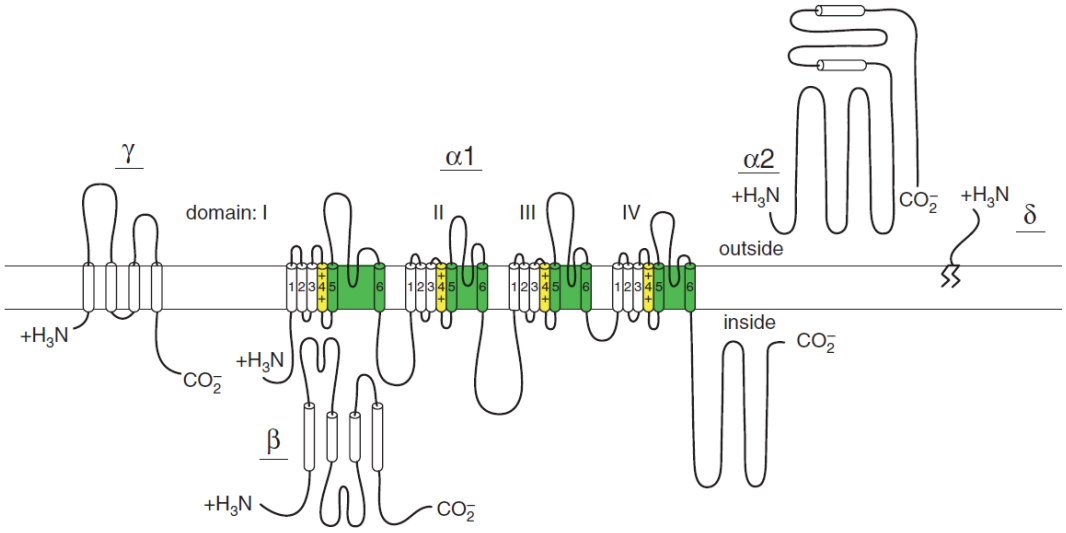


**Figure 24. The structure of $Ca^{2+}$ channels subunits.**

Schematic illustration of $Ca_v$s represented as transmembrane folding models. α-helices are illustrated as cylinders, and the zigzag line on δ subunit shows glycophosphatidylinositol (GPI) anchor. Channel conduction pore (green) includes the segments S5-S6 and a pore loop of each domain. S4 segment with charged amino-acids (+) represent voltage sensing segment and it is indicated in yellow. Figure is adapted from Catterall, 2011.

The pore forming, ***α1 subunit*** of $Ca_v$s is a transmembrane protein with four transmembrane domains (I-IV). Each transmembrane repeat is connected with a cytoplasmic linker and contains six transmembrane segments (S1-S6) and a membrane loop between the segments S5 and S6. Segments S1-S3, S5 and S6 are hydrophobic segments, while the fourth segment (S4) is a positively charged and it consists of five to six arginine or lysine residues in every third position (Takahashi *et al.*, 1987; Catterall, 2011; He *et al.*, 2018). It is suggested that S4 segment represents the voltage sensor of $Ca_v$s involved in regulation of channel activation and gating. In addition to voltage sensing S4 segment, segments S5-S6, together with a pore loop, act as channel conduction pore (Catterall & Few, 2008; Campiglio & Flucher, 2015). The external end of the pore loop between S5 and S6 of each domain contains a pair of glutamate residues which are essential for $Ca^{2+}$-selectivity of the channel (Catterall, 2011). On the contrary, the inner end of the same pore loop is lined by the S6 segments that are strongly implicated to formation of receptor sites that bind the selective pore-blocking drugs of L-type $Ca^{2+}$ channels with high affinity (Hockerman *et al.*, 1997; Catterall, 2011).

There are different isoforms of α1 subunit that determine the main properties of $Ca^{2+}$ currents mediated by distinct $Ca^{2+}$ channel types (Chen *et al.*, 2007; He *et al.*, 2018). It is important to note that the expression of solely α1 subunit in skeletal muscles was shown to be sufficient to form a functional $Ca^{2+}$-permeable channel (Perez-Reyes *et al.*, 1989) although with low level of expression, reduced current density and abnormal kinetic of gating (Perez-Reyes *et al.*, 1989; Catterall, 2011). Moreover, α1 subunit contains binding sites for many regulatory and effector proteins, therefore providing the regulatory role for $Ca_v$s (Bezprozvanny *et al.*, 1995; Campiglio & Flucher, 2015). This subunit further represents a $Ca^{2+}$ sensor (Campiglio & Flucher, 2015), and even short openings of the channels can lead to high increase in intracellular $Ca^{2+}$ concentration. To regulate and prevent excessive $Ca^{2+}$ rise, many regulatory proteins, effector proteins and $Ca^{2+}$ sensors with low affinity are co-localized with $Ca_v$s by binding to large cytoplasmic domains of α1 subunit, such as PKC, CaM etc. (Dai *et al.*, 2009; Catterall, 2011; Campiglio & Flucher, 2015). In addition, α1 subunit of presynaptic $Ca_v$s contains a synaptic protein interaction (synprint) site, a sequence located in the cytoplasmic loop between the domains II and III. This site has an essential role in synaptic vesicle exocytosis through direct interaction with proteins involved in this process, such as SNAP25, synaptotagmin or syntaxin (Watanabe *et al.*, 2010; Catterall, 2011; Campiglio & Flucher, 2015).

The ***β subunit*** of VGCC is an intracellular subunit without any transmembrane segment (Dolphin, 1995; Catterall, 2011; He *et al.*, 2018). Four genes encode for β subunits (Catterall, 2011) and structural analysis have shown that all of them contain non-conserved N- and C-terminal domains, and highly conserved SRC homology 3 (SH3) and guanylate kinase (GK) domains (Catterall, 2011; Dolphin, 2012; Buraei & Yang, 2013) connected by HOOK region. The SH3 and GK domains form core region of β subunits and place these subunits in the family of membrane-associated guanylate kinase (MAGUK) proteins (Dolphin, 2012). SH3 domain of β subunit mediates protein-protein interactions by binding to proline rich sequence (PxxP) in target proteins, while GK domain represents an interaction site with the α interaction domain (AID) of 18 amino acid residues located in the cytoplasmic loop between domains I and II of the α1 subunit (Catterall, 2011; Dolphin, 2012; Buraei & Yang, 2013). The AID domain binds to the GK domain through a hydrophobic groove called AID-binding pocket (ABP), with the high affinity in low nM range. Following interaction between AID and ABP, the AID undergoes structural changes by forming a continuous α helix structure

from a random coil in solution, and this interaction maintains throughout the lifetime of the $Ca_v$s (Catterall, 2011; Buraei & Yang, 2013).

Regarding the functions of β subunits, they are essential for $Ca^{2+}$ channel expression, gating and modulation by G proteins. In general, binding of β subunit to AID of α1 enhances the level of surface expression of $Ca_v1$ and $Ca_v2$ channels. Moreover, it enhances the gating of $Ca^{2+}$ channels by shifting the voltage dependence of both channel activation and inactivation to more hyperpolarized membrane potentials, therefore increasing channel open probability and rate of inactivation (Catterall, 2011; Buraei & Yang, 2013; He *et al.*, 2018). The β subunit of $Ca_v$s is further indicated to be involved in inhibition of $Ca_v1$ and $Ca_v2$ channels by G-protein coupled receptors (GPCRs) mediated by Gβγ subunit. This inhibition is voltage-dependent, since it can be relieved by strong depolarization. However, in the absence of β subunit, Gβγ can still bind to the channels and modulate them, although the inhibition can no longer be reversed by depolarization (Catterall, 2011; Dolphin, 2012; Buraei & Yang, 2013).

***α2 subunit*** of $Ca_v$s is a highly glycosylated extracellular protein linked by disulfide bound to ***δ subunit*** (Catterall, 2011; Dolphin, 2012). This disulfide bound enables the α2 subunit to be attached to the membrane. In mammals, there are four genes that encode for α2δ, namely *CACNA2D1*, *CACNA2D2*, *CACNA2D3*, and *CACNA2D4* which encode for α2δ-1, α2δ-2, α2δ-3, and α2δ-4, respectively (Davies *et al.*, 2007; Dolphin, 2012). α2δ subunits are found to be expressed in central and peripheral nervous system, although with different level of expression. α2δ-1 subunit is expressed in all the tissues tested so far (Klugbauer *et al.*, 2003), including skeletal muscle, and in many neuronal types in cerebellum or hippocampus, where they are located mainly in presynaptic terminals (Davies *et al.*, 2007; Dolphin, 2012). The expression of α2δ-2 is mainly restricted to Purkinje neurons in cerebellum, and low expression of α2δ-2 is found in medulla or hippocampus (Davies *et al.*, 2007). α2δ-3 was found to be expressed throughout the brain (Klugbauer *et al.*, 2003; Dolphin, 2012), while the expression of α2δ-4 is limited to endocrine tissues (Davies *et al.*, 2007; Dolphin, 2012).

It was demonstrated that α2 and δ are the products of the same gene encoding α2δ pre-protein which undergoes post-translational proteolytic cleavage into the α2 and δ proteins (Catterall, 2011; Dolphin, 2012; Campiglio & Flucher, 2015). This complex of α2 and δ subunits is anchored to the membrane with a glycophosphatidylinositol (GPI) region at the C-

terminal domain of the δ subunit (Davies *et al.*, 2010) which appears following post-translational cleavage of the predicted transmembrane segment. Both subunits have extracellular N-terminal domain, and C-terminal hydrophobic domain (Davies *et al.*, 2007; Dolphin, 2012; Campiglio & Flucher, 2015) in addition to von Willebrand factor type A (VWA) region, a protein-protein interaction domain in the extracellular sequence of α2δ subunits. This domain contains so called metal ion-dependent adhesion site (MIDAS) motif that mediates divalent-cation-dependent interactions between the VWA domain and ligands. Mutations in MIDAS motif unable VWA domain from binding divalent cations, indicating that MIDAS motif is important for trafficking function of α2δ subunits (Davies *et al.*, 2007; Dolphin, 2012).

It was reported by several studies that co-expression of α2δ subunits increases the expression and function of $Ca_v$s, although not in the same extent as β subunit. Co-expression of α2δ subunits in heterologous systems was shown to increase the $Ca^{2+}$ current amplitude (Gurnett *et al.*, 1996) mediated by different types of $Ca^{2+}$ channels (Davies *et al.*, 2010), without affecting the single-channel conductance, indicating that this effect is due to an increase in the number of channels expressed at the plasma membrane (Davies *et al.*, 2007). However, it is still unknown whether α2δ subunits can form a specific association with the α1 subunit.

It is interesting to note that α2δ subunits represent an important target for gabapentin (2-(1-(aminomethyl)-cyclohexyl) acetic acid) drugs used as an effective treatment for epilepsy and chronic, but not acute, neuropathic pain (Klugbauer *et al.*, 2003; Davies *et al.*, 2007). These gabapentin drugs were shown to bind α2δ-1 and α2δ-2 subunits at third arginine in the RRR motif, located next to the VMA domain, a motif that is not present in α2δ-3 and α2δ-4 subunits (Klugbauer *et al.*, 2003; Davies *et al.*, 2007; Dolphin, 2012). The mechanism of action for gabapentin drugs is still poorly described. Binding of gabapentin to α2δ subunits has small or no inhibitory effect on $Ca^{2+}$ current amplitude. Nevertheless, an interesting study demonstrated that $Ca^{2+}$ currents in DRG neurons from mice overexpressing α2δ-1 were inhibited by gabapentin, in contrast to $Ca^{2+}$ currents from wild-type mice DRG neurons (Davies *et al.*, 2007; Dolphin, 2012), suggesting that upregulation of α2δ-1 seen in neuropathic pain can increase the effectiveness of the drug. In addition, a chronic use of the drug was shown to diminish the localization of α2δ-1 and α2δ-2 subunits at the surface of the cell, leading to decrease in $Ca^{2+}$ currents upon drug administration (Dolphin, 2012).

Finally, ***γ subunit*** is a glycoprotein with four transmembrane segments (Jay *et al.*, 1990; Catterall, 2011; Campiglio & Flucher, 2015; He *et al.*, 2018) and without any charged amino acid residues, as seen for α1 subunit (Jay *et al.*, 1990). Both N- and C-terminal domains are located intracellularly (Black, 2003). Gene family of γ subunit consists of 8 members, γ1 – γ8 (Black, 2003; Chen *et al.*, 2007), which show great diversity based on the amino acid sequence composition (Black, 2003) and they are grouped into three clusters based on their sequence homology (Chen *et al.*, 2007). Subunits γ1 and γ6 have short C-terminal domain, and are mostly expressed in skeletal muscle, although γ6 is also found in cardiac muscle. Subunits γ5 and γ7 are found in kidneys and brain, while γ2, γ3, γ4, and γ8 subunits are known as transmembrane AMPA receptor regulatory proteins (TARPs) which are predominantly expressed in the brain, where they regulate the gating and trafficking of AMPA receptors (Black, 2003; Chen *et al.*, 2007; Campiglio & Flucher, 2015). However, many studies carried out in heterologous systems to study the effect of γ subunits on $Ca^{2+}$ currents provided the results that were often in conflict with each other. Up to date, it seems that only γ1 and γ6 have a significant effect on $Ca^{2+}$ currents when co-expressed with α1 subunit in $Ca_v1.2$ or $Ca_v3.1$, while little evidence is given on the effect of γ5 and γ7, or TARPs subunits on modulation of $Ca_v$s in neurons (Chen *et al.*, 2007).

## 3. CLASSIFICATION OF VOLTAGE-GATED CALCIUM CHANNELS

As mentioned before, ten different types of $Ca^{2+}$ channels can be identified based on their pharmacological and electrophysiological properties, but also on the expression of different α1 subunits (Catterall, 2011; He *et al.*, 2018). These are L-type, N-type, P/Q-type, R-type and T-type $Ca^{2+}$ channels, also classified as $Ca_v1$, $Ca_v2$ and $Ca_v3$ channels, respectively (Perez-Reyes, 2003; Catterall, 2011; He *et al.*, 2018). In the following section, I will give some insights into the electrophysiological properties, expression, function, and specific pharmacological modulation of each type of $Ca^{2+}$ channel.

### 3.1. L-type calcium channels

L-type $Ca^{2+}$ channels are one of the main types of $Ca_v$s that are determined by expression of $Ca_v1$ type of pore-forming α1 subunit (Catterall, 2011), referred as $Ca_v1.1$, $Ca_v1.2$, $Ca_v1.3$ and $Ca_v1.4$. (Lipscombe *et al.*, 2004; Catterall, 2011). In general, L-type

channels can be distinguished from other types of $Ca^{2+}$ channels primarily by their high sensitivity to DHPs agonists and antagonists (Lipscombe *et al.*, 2004). L-type $Ca^{2+}$ channels are classified as HVA channels that activate at depolarized membrane potentials, with channel activation that becomes evident at the potentials between -20 and -10 mV (Nowycky *et al.*, 1985; Fox *et al.*, 1987). These channels mediate long lasting (L) current that shows small inactivation during depolarization (Nowycky *et al.*, 1985; Aosaki & Kasai, 1989; Koschak *et al.*, 2001, 2003; Lipscombe *et al.*, 2004) and they exhibit large single channel conductance (Nowycky *et al.*, 1985; Aosaki & Kasai, 1989; Lipscombe *et al.*, 2004; Catterall, 2011). Nevertheless, the members of L-type $Ca^{2+}$ channels represent a heterogeneous channel family since not all of the members express the same functional properties. They are localized in various tissues where they mediate distinct functions, such as excitation-contraction coupling in skeletal (Bannister & Beam, 2013; Hernández-Ochoa & Schneider, 2018) or cardiac muscle (Bers, 2002; Kuo & Ehrlich, 2015), pacemaker activity in heart atrial tissue (Platzer *et al.*, 2000; Mangoni *et al.*, 2003), neurotransmitter release in inner hair cell (Platzer *et al.*, 2000; Brandt *et al.*, 2003) or neurotransmitter release from photoreceptors (Lee *et al.*, 2015).

### 3.1.1. $Ca_v1.1$ channels

$Ca_v1.1$ type of $Ca^{2+}$ channels conduct L-type $Ca^{2+}$ current. They are characterized by slow opening kinetics and relatively high sensitivity to inhibition mediated by DHPs (Lipscombe *et al.*, 2004). Among α1 subunit of $Ca_v1.1$ type, $Ca_v1.1$ $Ca^{2+}$ channels express auxiliary α2δ-1 subunits, $\beta_{1a}$, and $\gamma_2$ subunits (Bannister & Beam, 2013). All of these subunits, except α2δ-1, are primarily expressed in skeletal muscle, which is in agreement with the exclusive expression of $Ca_v1.1$ $Ca^{2+}$ channels in skeletal muscles where they have an essential role in excitation-contraction (EC) coupling (Lipscombe *et al.*, 2004; Bannister & Beam, 2013). There, $Ca_v1.1$ channels act as voltage sensing channels that are directly associated with type 1 ryanodine receptors (RyR1) in the sarcoplasmic reticulum (SR) (Lipscombe *et al.*, 2004), the $Ca^{2+}$ store in skeletal muscle (Fill & Copello, 2002). Conformational changes in voltage-sensing domain of $Ca_v1.1$ upon membrane depolarization directly activate RyRs, leading to release of intracellular $Ca^{2+}$ (Catterall, 2011), a mechanism that is not dependent on entry of extracellular $Ca^{2+}$. While α1 intracellular linker between domains II and III is necessary for EC coupling function of $Ca_v1.1$ channels (Bannister & Beam, 2013; Hernández-Ochoa & Schneider, 2018), $\beta_{1a}$ subunit is important in formation of "tetrads", clusters of four $Ca_v1.1$ facing every other RyR1 homotetramer (Bannister & Beam,

2013; Hernández-Ochoa & Schneider, 2018). The organization of coupled RyR1 and those who remain uncoupled, determine the organization of $Ca_v1.1$ on the plasma membrane (Hernández-Ochoa & Schneider, 2018). Therefore, $Ca_v1.1$ channels represent peculiar isoform of VGCCs as they are able to directly couple depolarization of the membrane with RyRs activation.

### 3.1.2. $Ca_v1.2$ channels

$Ca_v1.2$ type of $Ca^{2+}$ channels expressed in cardiac and smooth muscles, in pancreatic cells, and in neurons (Lipscombe *et al.*, 2004) are distinct from $Ca_v1.1$ channels in that they open at membrane potentials around -30 mV with faster kinetics. This difference in gating between $Ca_v1.2$ and $Ca_v1.1$ channels is due to differences in the sequence of extracellular linker between the segments S3 and S4 in first transmembrane domain of α1 subunit (Lipscombe *et al.*, 2004). As $Ca_v1.1$ channels, $Ca_v1.2$ channels also show high sensitivity to DHPs-mediated block, but unlike $Ca_v1.1$, the primarily role of $Ca_v1.2$ channels is to mediate $Ca^{2+}$ influx into the cells where $Ca^{2+}$ initiates various signaling cascades (Lipscombe *et al.*, 2004), such as excitation-contraction coupling in cardiac muscle (Catterall, 2011). In cardiac myocytes, the contraction of muscle is initiated by AP-mediated $Ca^{2+}$ influx through $Ca_v1.2$ channels that leads to elevations in intracellular $Ca^{2+}$ concentrations. Rise in intracellular $Ca^{2+}$ increases the sensitivity to $Ca^{2+}$ of type 2 RyRs (RyR2) located on SR, which triggers RyR2 activation and $Ca^{2+}$ release from SR; a mechanism known as $Ca^{2+}$-induced $Ca^{2+}$ release (CICR) mechanism. Further rise of intracellular $Ca^{2+}$ leads to $Ca^{2+}$ binding to troponin C on actin filaments, which initiates the muscle contraction (Bers, 2002; Kuo & Ehrlich, 2015). The excessive increase in intracellular $Ca^{2+}$ concentration upon $Ca^{2+}$ entry through the $Ca_v1.2$ channels is limited by $Ca^{2+}$-dependent inactivation, and also by $Ca^{2+}$ release from the SR. It was suggested that opening of a single $Ca^{2+}$ channel is sufficient to activate $Ca^{2+}$ release (Bers, 2002). Moreover, in order to relax the contracted muscle, intracellular $Ca^{2+}$ concentration must be reduced, which is accomplished mainly by removal of $Ca^{2+}$ by SR $Ca^{2+}$-ATPase (SERCA) pump, while $Na^+/Ca^{2+}$ exchange (NCX), sarcolemmal $Ca^{2+}$-ATPase (PMCA), and mitochondrial $Ca^{2+}$ uniporter contribute to a lower extent (Bers, 2002; Kuo & Ehrlich, 2015). Except regulating the excitation-contraction coupling in cardiac muscle, $Ca^{2+}$ entry through $Ca_v1.2$ channels regulate the blood pressure and maintain the vascular tone in smooth muscle (Moosmang, 2003).

### 3.1.3. $Ca_v1.3$ channels

It has been reported that $Ca_v1.3$ type of $Ca^{2+}$ channels show different properties compared to $Ca_v1.1$ and $Ca_v1.2$. Although $Ca_v1.3$ channels are classified as HVA channels, they require lower threshold for the activation (Figure 25. A), which is between 15-25 mV more hyperpolarized from that of $Ca_v1.2$ channels (Koschak *et al.*, 2001; Xu & Lipscombe, 2001; Mangoni *et al.*, 2003). This low-voltage activation represents one of the main properties of $Ca_v1.3$ $Ca^{2+}$ channels. In addition, $Ca_v1.3$ channels, like $Ca_v1.2$ channels, show fast kinetic of activation, which is faster than that of $Ca_v1.1$ $Ca^{2+}$ channels (Koschak *et al.*, 2001; Lipscombe *et al.*, 2004; Helton, 2005). Interestingly, $Ca_v1.3$ show lower sensitivity to DHPs-mediated inhibition compared to $Ca_v1.2$ channels (Figure 25. B) (Koschak *et al.*, 2001; Xu & Lipscombe, 2001) and application of DHPs often leads to uncomplete inhibition of $Ca_v1.3$ channels (Koschak *et al.*, 2001; Xu & Lipscombe, 2001; Brandt *et al.*, 2003). For this reason, pharmacological separation of L-type $Ca^{2+}$ current mediated by $Ca_v1.3$ channels from other types of $Ca^{2+}$ currents does not represent an effective method. As specific inhibitors of different $Ca^{2+}$ current subtypes failed to block DHP-insensitive $Ca_v1.3$-mediated $Ca^{2+}$ current, it has been suggested that $Ca_v1.3$ channels contribute to fraction of the R-type $Ca^{2+}$ current (Brandt *et al.*, 2003; Lipscombe *et al.*, 2004). Moreover, inhibition of $Ca_v1.3$ by DHPs is voltage-dependent, since the inhibition is more potent at depolarized membrane potential when channels are opened, compared to less effective inhibition at hyperpolarized potentials when most of the channels are in their closed state (Koschak *et al.*, 2001; Lipscombe *et al.*, 2004).

$Ca_v1.3$ channels are expressed in many cells in which $Ca_v1.2$ channels are also found. They were shown to have an important role in pacemaker activity in heart atrial tissue, but not in ventricular tissue where $Ca_v1.3$ are not expressed (Platzer *et al.*, 2000; Mangoni *et al.*, 2003). Studies showed that mice with inactivated $Ca_v1.3$ channels developed sinus bradycardia and arrhythmia due to sinoatrial node (SAN) cells dysfunction (Platzer *et al.*, 2000; Mangoni *et al.*, 2003). Other studies demonstrated that $Ca_v1.3$ couple membrane depolarization to synaptic transmission in inner hear cells of cochlea (Platzer *et al.*, 2000; Brandt *et al.*, 2003; Lipscombe *et al.*, 2004), and mice with missing $Ca_v1.3$ channels are deaf, since the inner hair cells are unable to respond to sound stimulation (Platzer *et al.*, 2000). As a consequence of $Ca_v1.3$ channels lack, and therefore the $Ca^{2+}$ entry through these channels, inner hair cells fail to develop normally and synaptic transmission is disrupted (Brandt *et al.*, 2003).

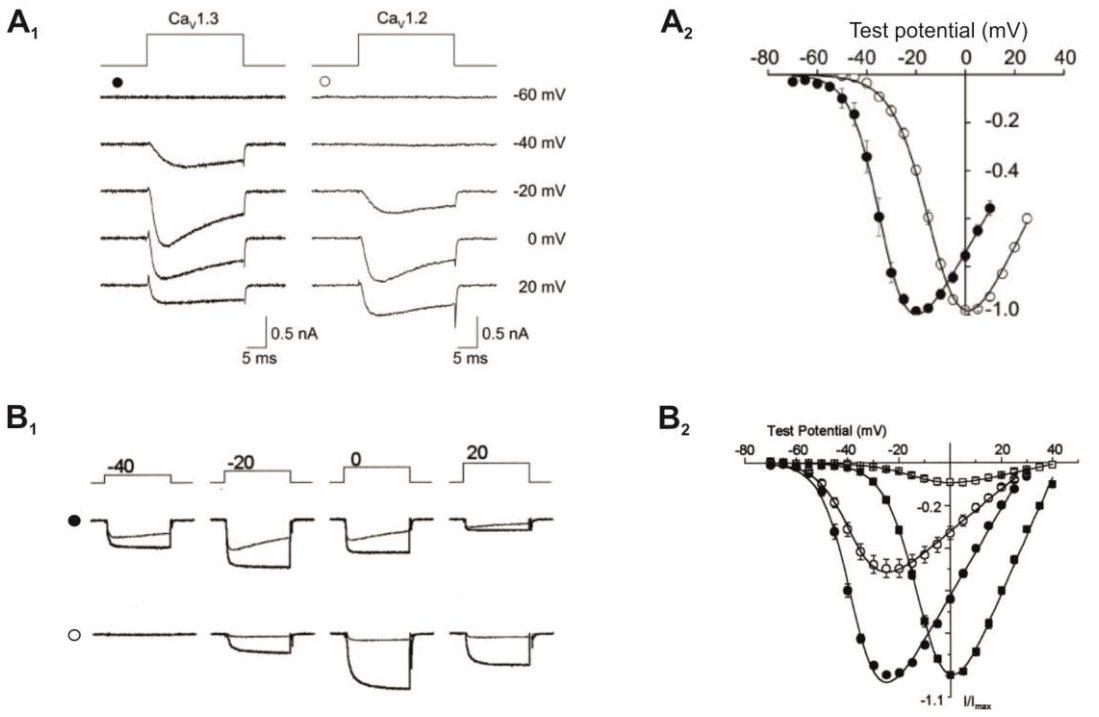


**Figure 25. Properties of $Ca_v1.3$ and $Ca_v1.2$ L-type $Ca^{2+}$ channels.**

**$A_1$.** $Ca_v1.3$ (black circle) and $Ca_v1.2$ (open circle) currents were activated from a holding potential of -100 mV to different test potentials. Note that $Ca_v1.3$ channels start to activate at more hyperpolarized potentials compared to $Ca_v1.2$ channels. **$A_2$.** Current-voltage relationships for $Ca_v1.3$ and $Ca_v1.2$ channels. **B.** $Ca_v1.3$ and $Ca_v1.2$ show different sensitivity to inhibition by DHPs. **$B_1$.** $Ca_v1.3$ (black circle) and $Ca_v1.2$ (open circle) currents were activated from from a holding potential of -80 mV to different test potentials, in the absence (thick traces) and presence (thin traces) of 1µM nimodipine. $Ca_v1.3$ channels show lower sensitivity to inhibition by nimodipine. **$B_2$.** Current-voltage relationships for $Ca_v1.3$ and $Ca_v1.2$ channels in the absence (black circle, black square) and presence (open circle, open square) of nimodipine. Figures in A are from Lipscombe *et al.*, 2004, and figures in B are from Xu & Lipscombe, 2001.

### 3.1.4. $Ca_v1.4$ channels

$Ca_v1.4$ channels share similar properties with $Ca_v1.3$ channels, as they require low activation threshold, therefore activate at more hyperpolarized potentials than $Ca_v1.2$ channel, but slightly more depolarized potentials than $Ca_v1.3$ channels (Koschak *et al.*, 2003; Lipscombe *et al.*, 2004). Like $Ca_v1.3$ channels, $Ca_v1.4$ activate with the fast kinetic (Koschak *et al.*, 2003), which is supported by the fact that these two types of channels share high level of sequence homology (Lipscombe *et al.*, 2004), however they show slower voltage-dependent inactivation compared to $Ca_v1.3$ channels (Koschak *et al.*, 2001, 2003). In addition, $Ca_v1.4$ channels show smaller single channel conductance than other L-type $Ca^{2+}$ channels (Doering *et al.*, 2005). A significant property of $Ca_v1.4$ channels is their low sensitivity to

inhibition by DHPs (Koschak *et al.*, 2003; Lipscombe *et al.*, 2004), which tends to be about 15-folder lower compared to $Ca_v1.2$ currents (Koschak *et al.*, 2003). Inhibition of $Ca_v1.4$ currents is strongly voltage-dependent and it is more effective at more depolarized membrane potentials (Koschak *et al.*, 2003). $Ca_v1.4$ channels are unique among other $Ca_v1$ channels in that they do not show $Ca^{2+}$-dependent inactivation (CDI), which is well described for other L-type channels (Koschak *et al.*, 2003; Lipscombe *et al.*, 2004). An interesting study demonstrated that CDI is inhibited by a still unknown mechanism in the C-terminal domain of $\alpha 1$ subunit (Singh *et al.*, 2006).

$Ca_v1.4$ channels are expressed primarily in synaptic terminals of photoreceptor cells in the retina (Lipscombe *et al.*, 2004; Lee *et al.*, 2015), where they regulate the exocytosis of neurotransmitters. It has been reported that mutations in human $Ca_v1.4$ channels lead to stationary night blindness (Lipscombe *et al.*, 2004) characterized with low visual activity in the dark (Lee *et al.*, 2015). It was found that more hyperpolarized potentials for $Ca_v1.4$ channels activation and slow $Ca^{2+}$ current inactivation during depolarization allow these channels to better control neurotransmitter release from photoreceptors, which is required for transmission of visual stimuli (Koschak *et al.*, 2003; Lee *et al.*, 2015).

***Dihydropyridines are selective inhibitors of L-type $Ca^{2+}$ channels***

Dihydropyridines (DHPs) are organic compounds that include several $Ca^{2+}$ channels antagonists, such as nimodipine, nifedipine, or nitredipine (Nowycky *et al.*, 1985; Fox *et al.*, 1987; Aosaki & Kasai, 1989; Randall & Tsien, 1995; Zamponi, 1997; Xu & Lipscombe, 2001). DHPs show high selectivity to L-type $Ca^{2+}$ channels (Zamponi, 1997; Lipscombe *et al.*, 2004), although T-type $Ca^{2+}$ channels were also reported to be DHPs-sensitive (Randall & Tsien, 1995). Other families of $Ca^{2+}$ channels do not respond to DHPs, and therefore are DHPs-insensitive (Mintz *et al.*, 1992*a*; Randall & Tsien, 1995; Lipscombe *et al.*, 2004; Catterall, 2011).

Numerous studies have demonstrated that DHPs can act as both agonists and antagonists of L-type $Ca^{2+}$ channels, depending on DHP drug structure, membrane potential or conformational state of the channel (Hockerman *et al.*, 1997). Inhibitory effect of DHPs is well described and it is known to be voltage-dependent (Aosaki & Kasai, 1989; Koschak *et al.*, 2001, 2003; Lipscombe *et al.*, 2004), indicating that the inhibition by DHPs is more effective at the depolarized membrane potentials when the channels are opened (or inactive), while the inhibition is less prominent at hyperpolarized potential when channels are in their

closed state (Hockerman *et al.*, 1997; Koschak *et al.*, 2003; Helton, 2005). In addition, $Ca_v1.3$ and $Ca_v1.4$ show lower sensitivity to DHPs inhibition (Koschak *et al.*, 2001, 2003; Xu & Lipscombe, 2001), and the same concentrations of the DHPs do not inhibit all L-type $Ca^{2+}$ channels to the same extent (Helton, 2005). The receptor site for both DHP agonists and antagonists is located at the extracellular surface of the membrane, and it is positioned about 25% into the membrane (Peterson *et al.*, 1996; Hockerman *et al.*, 1997). This is supported by the results which demonstrate that DHPs applied intracellularly do not modulate L-type $Ca^{2+}$ channels (Hockerman *et al.*, 1997). The receptor site for DHPs is described to be located within the loop that connects segments S5 and S6 in transmembrane domains III and IV of α1 subunit (Peterson *et al.*, 1996; Hockerman *et al.*, 1997). Further studies have identified amino acids in IIIS6 and IVS6 which are unique for DHPs-sensitive $Ca^{2+}$ channels (Hockerman *et al.*, 1997), and which are required for high affinity DHP binding (Peterson *et al.*, 1996).

### 3.2. P/Q-type calcium channels

$Ca_v2.1$ type of pore-forming α1 subunit is a determinant of P/Q-type $Ca^{2+}$ channels (Catterall, 2011) that belong to HVA $Ca^{2+}$ channels (Randall & Tsien, 1995; Catterall, 2011). P-type channels were first described by Llinás in Purkinje cells (Llinás *et al.*, 1989), while Q-type channels were first described in granule neurons by Randall and Tsien (Randall & Tsien, 1995). As P- and Q-type $Ca^{2+}$ channels share similar properties and are difficult to distinguish, they are often referred as P/Q-type $Ca^{2+}$ channels (Nimmrich & Gross, 2012). Nevertheless, these two types of the channels differ in their activation and inactivation kinetics. Both P- and Q-type channels are activated at depolarized membrane potentials with fast kinetics (Stea *et al.*, 1994), although P-type channels activate at slightly more positive potentials than Q-type channels (Mermelstein *et al.*, 1999). Upon depolarization, both of these channels inactivate slowly (Randall & Tsien, 1995; Mermelstein *et al.*, 1999), and P-type channels were described to inactivate with much slower kinetics than Q-type channels (Figure 26.), showing almost no inactivation during depolarization (Randall & Tsien, 1995; Mermelstein *et al.*, 1999). It is interesting to note that Q-type channels do not show the same inactivation kinetics in all neurons they are expressed in (Figure 26.), which was suggested to be due to the expression of different β subunits (Mermelstein *et al.*, 1999). Indeed, slowly inactivating Q- and P-type channels express $\beta_{2a}$ subunit, while rapidly inactivating Q-type channels express $\beta_{1b}$ subunit (Mermelstein *et al.*, 1999). Another important property of these

$Ca^{2+}$ channels is their high sensitivity to inhibition by ω-agatoxin IVA (Mintz *et al.*, 1992*b*, 1992*a*; McDonough *et al.*, 1997), which enables to easily distinguish these channels from other types of $Ca^{2+}$ channels, however Q-type channels show lower sensitivity to this blocker (Stea *et al.*, 1994; Randall & Tsien, 1995; Mermelstein *et al.*, 1999). In contrary, P/Q-type channels are insensitive to DHPs and ω-conotoxin GVIA, selective inhibitors of L- and N-type $Ca^{2+}$ channels, respectively (Llinás *et al.*, 1989; Mintz *et al.*, 1992*a*).

Regarding the distribution of P/Q-type $Ca^{2+}$ channels, they are widely expressed throughout the CNS in various neurons, but with different levels of expression (Mintz *et al.*, 1992*a*; Stea *et al.*, 1994; Catterall, 2000). For example, P-type channels are highly expressed in Purkinje neurons, but show mediate expression in spinal interneurons, while in sympathetic neurons, these channels are completely absent (Mintz *et al.*, 1992*a*). In neurons, P/Q-type $Ca^{2+}$ channels are localized at synaptic terminals where they initiate the neurotransmitter release mediated by $Ca^{2+}$ influx through these channels (Takahashi & Momiyama, 1993; Ishikawa *et al.*, 2005; Catterall, 2011). Many studies showed that P/Q channels interact with $Ca^{2+}$-binding proteins and undergo $Ca^{2+}$-dependent inactivation and facilitation which may regulate their activity (Lee *et al.*, 1999*a*, 2002; Catterall, 2011). Calmodulin (CaM) binding domain (CBD) was found to be located on C-terminal of $Ca_v2.1$ α1 subunit and to represent a binding site for $Ca^{2+}$ and CaM (Lee *et al.*, 1999*a*). $Ca^{2+}$ binding to CBD stimulates inactivation of $Ca_v2.1$ channels, it improves the recovery of the channels following inactivation, and it enhances $Ca^{2+}$ influx through these channels by facilitating $Ca^{2+}$ current, therefore preparing the channels to response upon continuous stimuli (Lee *et al.*, 1999*a*). In contrast to CaM, $Ca^{2+}$-binding protein 1 (CaBP1) enhances the rate of channel inactivation when it binds CBD on α1 subunit, it causes a positive shift in the voltage dependence of activation, and it does not support $Ca^{2+}$-dependent facilitation (Lee *et al.*, 2002). Hence, this protein may have an important role in defining the role of neuronal P/Q-type $Ca^{2+}$ channels.

***ω-agatoxin IVA is selective inhibitor of P/Q-type $Ca^{2+}$ channels***

P/Q-type $Ca^{2+}$ channels are inhibited by ω-agatoxin IVA with high affinity (Mintz *et al.*, 1992*b*, 1992*a*; Takahashi & Momiyama, 1993; McDonough *et al.*, 1997). This toxin was first isolated from the venom of funnel web spider *Agelenopsis aperta* as a peptide of 48 amino acids (Mintz *et al.*, 1992*b*). ω-agatoxin IVA was shown to be selective to P/Q-type channels, since it failed to inhibit other types of $Ca^{2+}$ channels, including L-, N- or T-type $Ca^{2+}$ channels (Mintz *et al.*, 1992*b*, 1992*a*). In addition, it was demonstrated that ω-agatoxin preferentially

binds channels in their closed state, it stabilizes this state of the channel, which then requires higher depolarizations for the activation (Mintz *et al.*, 1992*b*; McDonough *et al.*, 1997). The affinity for toxin binding decreases with more positive potentials (McDonough *et al.*, 1997). Moreover, the inhibition is voltage dependent and train of large depolarizations can relieve the inhibitory effect of the toxin, even when it is still present in the extracellular space (Mintz *et al.*, 1992*b*; McDonough *et al.*, 1997) or bound to the channel (Randall & Tsien, 1995; McDonough *et al.*, 1997). Finally, complete unbinding of ω-agatoxin IVA from the channel can be achieved by repeated strong depolarizations (McDonough *et al.*, 1997). Studying the mechanisms by which ω-agatoxin IVA inhibits the channel, it was demonstrated that this toxin rather changes the voltage dependent gating of the channel than blocking its pore. Therefore, moderate depolarization can no longer activate the channel, which would normally occur in the absence of inhibitor (McDonough *et al.*, 1997).

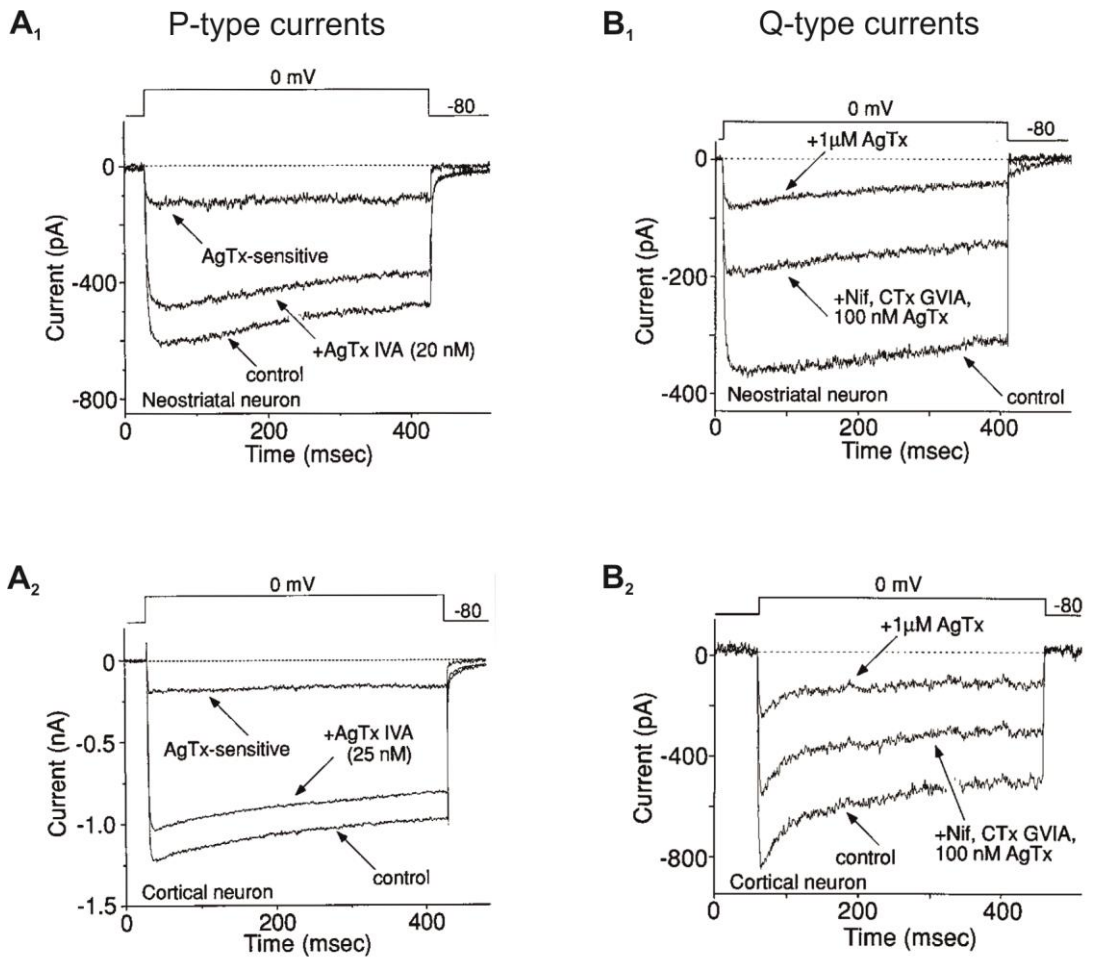


**Figure 26. Properties of P/Q-type $Ca^{2+}$ channels.**

**A.** P-type currents in neostriatal neuron (**$A_1$**) and cortical neuron (**$A_2$**) show slow inactivation during depolarization. Bath application of 20 - 25 μM ω-agatoxin inhibits P-type currents in both types of

neurons. **B.** Q-type currents in neostriatal neuron (**$B_1$**) and cortical neuron (**$B_2$**) show different inactivation during depolarization, being faster in cortical neurons, while it shows almost no inactivation in neostraital neurons. In both types of neurons, Q-type current was isolated by bath application of nifedipine (5 µM, L-type current inhibitor), ω-conotoxin GVIA (2 µM, N-type current inhibitor), and ω-agatoxin (100 nM, P-type current). In all four panels, both P- and Q-type currents were isolated by subtracting the current evoked before the toxin application from the current evoked after 3-5 min of toxin exposure. Figures in A and B are from Mermelstein *et al.*, 1999.

### 3.3. N-type calcium channels

N-type $Ca^{2+}$ channels expressing $Ca_v2.2$ α1 subunit (He *et al.*, 2018) were first identified in dorsal root ganglion (DRG) sensory neurons as ″neither T nor L″ channels since they were shown to express distinct biophysical properties compared to L- and T-type $Ca^{2+}$ channels (Nowycky *et al.*, 1985). N-type channels have small single channel conductance (about 13 pS) (Aosaki & Kasai, 1989). They belong to HVA channels that activate at intermediate membrane potentials, which are more negative than potentials required to activate L-type channels, but more positive than potentials activating T-type channels (Nowycky *et al.*, 1985; Fox *et al.*, 1987; Catterall, 2000). Inactivation rate of N-type $Ca^{2+}$ channels also differs from L- and T-type $Ca^{2+}$ channels, being slower compared to T-type channels, but faster compared to L-type channels (Nowycky *et al.*, 1985; Fox *et al.*, 1987; Catterall, 2000). When comparing N-type channels with P/Q-type channels, they both show similar kinetics of inactivation, although P/Q-type $Ca^{2+}$ channels require more negative potentials for activation (Ishikawa *et al.*, 2005). However, pharmacological approach is the most reliable tool to separate and isolate N-type current from other types of $Ca^{2+}$ currents, as these nickel ($Ni^{+}$)- and DHP-resistant channels are potently inhibited by ω-conotoxin GVIA (Fox *et al.*, 1987; Aosaki & Kasai, 1989; Boland *et al.*, 1994; Catterall, 2000; Ishikawa *et al.*, 2005). In addition to ω-conotoxin GVIA, cadmium ($Cd^{2+}$) strongly inhibits these channels, although $Cd^{2+}$ block is not N-type channel specific (Nowycky *et al.*, 1985; Fox *et al.*, 1987).

N-type $Ca^{2+}$ channels are highly expressed throughout the CNS where they, together with P/Q-type channels, mediate neurotransmitter release by increasing presynaptic $Ca^{2+}$ concentration mediated by generation of APs (He *et al.*, 2018). At the presynaptic sites, SNARE protein complex regulates the fusion of vesicles containing neurotransmitters with the cellular plasma membrane. This synaptic core complex consists of membrane proteins syntaxin-1, 25K synaptosome-associated protein (SNAP-25), and vesicle associated membrane protein (VAMP)/synaptobrevin (Bezprozvanny *et al.*, 1995; Sheng *et al.*, 1996;

Catterall, 2011; Campiglio & Flucher, 2015; He *et al.*, 2018). $Ca_v2.2$ channels directly bind SNARE proteins at synprint site that is located at cytoplasmic loop between domains II and III of α1 subunit (Sheng *et al.*, 1994, 1996; Campiglio & Flucher, 2015). SNARE proteins are regulated by $Ca^{2+}$ sensor protein synaptotagmin, which can bind synprint site on N-type channels (Catterall, 2011; Campiglio & Flucher, 2015), and it enables fast release of neurotransmitters (He *et al.*, 2018). The interaction between SNARE proteins and N-type $Ca^{2+}$ channels depends on the level of intracellular $Ca^{2+}$ concentration. It was suggested that docking vesicles bind N-type channels with low affinity *via* syntaxin/SNARE-25 dimer at resting concentration of intracellular $Ca^{2+}$, and the affinity of binding increases with increase in $Ca^{2+}$ influx. The binding of this protein complex with N-type $Ca^{2+}$ channels becomes maximal at 20 μM $Ca^{2+}$, which represents a threshold for vesicles release. At this point, binding affinity of the synaptic core complex decreases, enabling syntaxin/SNARE-25 dimer to dissociate from the channel and to permit the fusion of synaptic vesicles (Sheng *et al.*, 1996). When the interaction between SNARE proteins and synprint of N-type $Ca^{2+}$ channels is disrupted, synaptic transmission is inhibited, indicating the importance of this coupling for synaptic vesicles release (Catterall, 2011). Moreover, it was shown that syntaxin can have an inhibitory effect on N-type $Ca^{2+}$ channels when it is co-expressed with $Ca_v2.2$ channels. In such conditions, syntaxin shifts the voltage dependence for channel inactivation to more hyperpolarized membrane potentials, therefore inhibiting the activity of $Ca^{2+}$ channels and $Ca^{2+}$ influx when there are not enough docked synaptic vesicles to be released (Bezprozvanny *et al.*, 1995; Catterall, 2011).

### *ω-conotoxin GIVA is selective inhibitor of N-type $Ca^{2+}$ channels*

ω-conotoxin GVIA is a fraction of ω-conotoxin isolated from the venom of cone snail *Conus geographus* (Boland *et al.*, 1994). It is a peptide of 27 amino acids which selectively and irreversibly inhibits N-type $Ca^{2+}$ channels with high affinity (McCleskey *et al.*, 1987; Aosaki & Kasai, 1989), although it has been reported that L-type current can also be reversibly blocked by this toxin (McCleskey *et al.*, 1987; Aosaki & Kasai, 1989). The inhibition of N-type channels is time- and dose-dependent (Figure 27.), but it does not show voltage-dependence, as toxin inhibits the current at any potential tested. Since there is no passing of neither inward nor outward current, it is argued that the block of the channel is complete (Boland *et al.*, 1994). Therefore, the toxin can bind the channel in any of its gating states, whether it is in its open, closed or inactivated state, and physically block the channel

pore (Zamponi, 1997). Such independence of toxin binding on gating state of N-type $Ca^{2+}$ channels has also been demonstrated in DRG neurons. The results of this study showed that ω-conotoxin GVIA applied to external side of the plasma membrane inhibited the channels by direct binding regardless of the channel opening (McCleskey *et al.*, 1987).

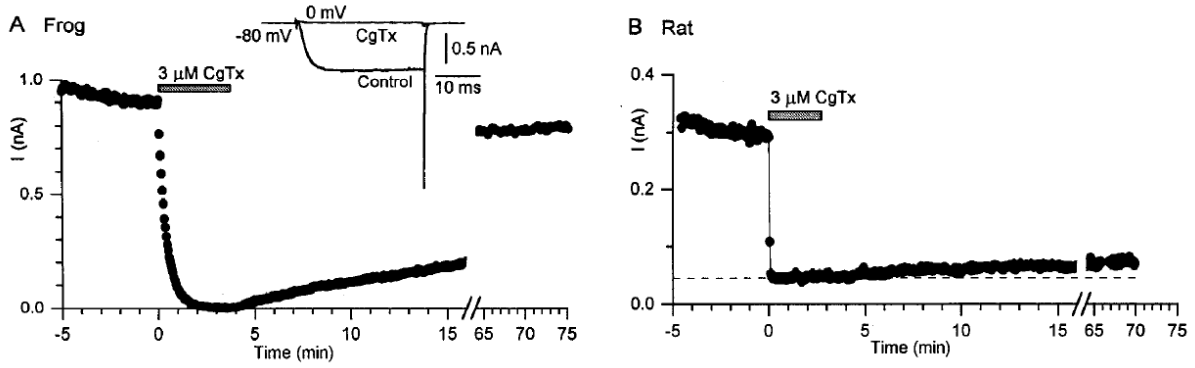


**Figure 27. ω-conotoxin potently inhibits N-type $Ca^{2+}$ channels.**

In frog (**A**) and rat (**B**) sympathetic neurons, N-type current was evoked from a holding potential of -80 mV to 0 mV. Application of 3 µM ω-conotoxin (CgTx) inhibits almost completely N-type currents in both frog and rat sympathetic neurons, although with faster development of block in rat neurons. In contrast, current recovery in rat neurons is much slower compared to current in frog neurons. Inset in **A** shows N-type current in control, and after exposure to CgTx. Figures in A and B are from Boland *et al.*, 1994.

### 3.4. R-type calcium channels

Recordings from cerebellar granule neurons revealed an additional type of $Ca^{2+}$ channel that conducts R-type $Ca^{2+}$ current (Zhang *et al.*, 1993; Randall & Tsien, 1995). $Ca_v2.3$ α1 subunit is determinant of HVA R-type $Ca^{2+}$ channels (Sochivko *et al.*, 2002) that activate at potentials more positive than -40 mV with fast activation kinetic (Zhang *et al.*, 1993; Randall & Tsien, 1995). R-type channels mediate fast inactivating current that recovers progressively over time and slower compared to T-type $Ca^{2+}$ channels (Randall & Tsien, 1995). In contrast, when compared with P/Q, N- or L-type channels, R-type current inactivates with faster kinetics (Zhang *et al.*, 1993). Pharmacological separation of R-type channels is mediated by SNX-482 (Newcomb *et al.*, 1998; Sochivko *et al.*, 2002; Dietrich *et al.*, 2003; Catterall, 2011), although they are also sensitive to $Ni^{2+}$ and ω-agatoxin IIIA. R-type channels are insensitive to inhibitory effect of DHPs and ω-conotoxin MVIID, inhibitors of L- and N-type $Ca^{2+}$ channels, respectively (Zhang *et al.*, 1993; Randall & Tsien, 1995; Sochivko *et al.*,

2002). However, in many neurons they are expressed in, R-type $Ca^{2+}$ channels show different properties.

R-type $Ca^{2+}$ channels are present in various neurons throughout the CNS. They can be found in CA1 pyramidal and neocortical neurons, and in hippocampal dendate granule cells (Sochivko *et al.*, 2002). These channels are expressed in presynaptic terminals where they can induce neurotransmitter release, although in the lower extent than N- and P/Q-type channels (Wu *et al.*, 1998*a*; Dietrich *et al.*, 2003). In the mossy fibers, pharmacological separation of R-type channels demonstrated that this $Ca^{2+}$ channel type triggers long-term potentiation (LTP), and reduction in LTP was seen in $Ca_v2.3$ deficient mice (Dietrich *et al.*, 2003). However, the same role of R-type channels was not found in other neurons (Dietrich *et al.*, 2003).

***SNX-482 inhibits R-type $Ca^{2+}$ channels***

A potent inhibitor of R-type $Ca^{2+}$ channels is SNX-482, a toxin derived from the venom of tarantula *Hysterocrates gigas* (Newcomb *et al.*, 1998; Bourinet & Stotz, 2001). The mechanism of inhibition by SNX-482 resembles a lot to mechanism of inhibition by ω-agatoxin IVA. SNX-482 mediates both dose- and voltage-dependent inhibition of R-type channels. At more depolarized potential, the inhibitory effect of this toxin is more effective, and it can be reviled by train of strong depolarizing potentials. Moreover, the block by SNX-482 is fast and complete, and it cannot be fully reversed upon the washout. SNX-482 slows the kinetic of channel activation at depolarized potentials and it inhibits the channels by preventing their activation (Bourinet & Stotz, 2001). The sensitivity of R-type channels to SNX-482 may differ among different neurons (Sochivko *et al.*, 2002), such as R-type channels in cortical neurons and dentate granule neurons show higher sensitivity to SNX-482 blocking effect compared to those expressed in CA1 neurons (Sochivko *et al.*, 2002). However, this toxin is not fully selective to R-type $Ca^{2+}$ channels, since reversible inhibition of L-type channels by SNX-482 can occur (Bourinet & Stotz, 2001).

### 3.5. T-type $Ca^{2+}$ channels

T-type (transient) $Ca^{2+}$ channels are determined by $Ca_v3$ α1 subunits encoded by 3 different genes. Therefore, $Ca_v3$ family of the channels consists of three T-type $Ca^{2+}$ channel subtypes, $Ca_v3.1$, $Ca_v3.2$, and $Ca_v3.3$ (Catterall, 2011). This type of $Ca^{2+}$ channels shows distinct electrophysiological and pharmacological properties compared to other types of $Ca^{2+}$

channels. Notably, $Ca_v3$ channels consist of α1 subunit only, and they lack the expression of auxiliary subunits (Simms & Zamponi, 2014), which are not necessary for normal functioning of the channel (Perez-Reyes *et al.*, 1998). Furthermore, they require hyperpolarized potentials for the activation, and represent the only member of low voltage activated (LVA) $Ca^{2+}$ channels (McCleskey *et al.*, 1987; Mintz *et al.*, 1992*a*; Perez-Reyes *et al.*, 1998; Catterall, 2011). Indeed, T-type channels activate at potentials around -70 mV (Fox *et al.*, 1987), show rapid decay that increases with depolarization, and fast inactivation (Nowycky *et al.*, 1985; McCleskey *et al.*, 1987; Fox *et al.*, 1987; Mintz *et al.*, 1992*a*; Perez-Reyes *et al.*, 1998) which is similar to N-type channels (Nowycky *et al.*, 1985). Their single channel conductance is small (Nowycky *et al.*, 1985; Fox *et al.*, 1987; Perez-Reyes *et al.*, 1998) and characteristic for LVA channels (Perez-Reyes *et al.*, 1998). When comparing activation and inactivation properties of T-type channels against R-type channels, T-type channels activate with slightly slower kinetic, and they show faster recovery from inactivation (Figure 28.) (Randall & Tsien, 1995). It is important to note that T-type channels exhibit overlap in voltage range between activation and inactivation, which enables them to generate a maintained current during small depolarization from rest, and therefore alter the excitability of neurons (Randall & Tsien, 1995; Nelson *et al.*, 2006).

It has been previously mentioned that pharmacological identification of $Ca^{2+}$ channels is a reliable method to distinguish different types of HVA $Ca^{2+}$ channels. For a long time, T-type channels were lacking the selective inhibitor. However, recent findings demonstrated that TTA-P2 (3,5-Dichloro-N-[1-(2,2-dimethyl-tetrahydro-pyran-4-ylmethyl)-4-fluoro-piperidin-4-ylmethyl]-benzamide), a synthetic compound derived from piperidine, is a selective and potent inhibitor of LVA $Ca^{2+}$ channels that shows no effect on HVA channels (Dreyfus *et al.*, 2010; Choe *et al.*, 2011). This blocker was suggested to preferentially bind the channels in their inactive state and to induce more potent inhibition at more depolarized potentials (Choe *et al.*, 2011). The inhibition produced by TTA-P2 is voltage-dependent, it slows the closure of the channels after repolarization, but it does not affect the activation or inactivation kinetics (Choe *et al.*, 2011).

In addition to TTA-P2, $Ca_v3$ are susceptible to block by $Ni^{2+}$ (Fox *et al.*, 1987), although they show different sensitivity to $Ni^{2+}$ inhibitory effect, as $Ni^{2+}$ inhibits $Ca_v3.2$ channels in low micromolar concentrations, while the same concentration fails to inhibit $Ca_v3.1$ and $Ca_v3.3$ channels (Lee *et al.*, 1999*b*). The sensitivity of T-type channels to DHPs is

controversial. Randall and Tsien reported T-type $Ca^{2+}$ channels that were reversibly inhibited to DHPs (Randall & Tsien, 1995), in contrast to previous data by Fox and colleagues (1987). They are insensitive to P/Q-type channels inhibitors ω-agatoxin IVA (Mintz *et al.*, 1992*a*), and ω-agatoxin IIIA (Randall & Tsien, 1995), and inorganic blocker cadmium ($Cd^{2+}$) which potently inhibits L- and N-type $Ca^{2+}$ channels (Nowycky *et al.*, 1985).

T-type $Ca^{2+}$ channels are mainly expressed in the brain, with the highest level of expression in amygdala, cerebellum, and thalamus. They are also found at a lower extent in the heart, placenta, kidney, and lung (Perez-Reyes *et al.*, 1998). In many neurons they are expressed in, $Ca_v3$ channels mediate low-threshold $Ca^{2+}$ spikes (LTS) that generate burst firing upon depolarization from RMP near -70 mV. In mice that lack $Ca_v3.1$ channels, tonic firing is elicited in neurons by depolarization from RMP near -55 mV, while lowering the RMP down to -70 mV failed to elicit firing (Perez-Reyes, 2003). In mouse thalamic neurons, $Ca_v3$ channels have an important role in modulation of sleep states during non-rapid eye movement (NREM) sleep. They were shown to be crucial for generation of delta waves, and sleep spindles states, but not in the generation of slow waves during NREM sleep (Lee *et al.*, 2004). This is in contrast to the study conducted on rat thalamic neurons, where the same type of channels was shown to be involved in generation of slow waves during sleep, a result argued to be due to different classification of electroencephalon (EEG) waves (David *et al.*, 2013). Moreover, abnormalities in thalamic T-type $Ca^{2+}$ channels are linked to absence epilepsy (Catterall, 2011; Nelson *et al.*, 2006; McCafferty *et al.*, 2018). In such conditions, they show upregulated expression and overactivity, which consequentially leads to switch in firing mode of many neurons, from tonic to bursting mode. $Ca_v3.2$ channel genes are mutated in childhood absence epilepsy (CAE), and these mutations were shown to alter the voltage-dependence of channel gating. Two antiepileptic drugs, ethosuximide and methyl-phenyl-succinimide (MPS), potently block all three T-type $Ca^{2+}$ channels at clinically relevant concentrations (Perez-Reyes, 2003; Nelson *et al.*, 2006). More recent study reported that firing of thalamocortical neurons is decreased during the absence seizure. Inhibition of T-type channels in these neurons does not affect the absence seizure, however the block of such channels in cortical and nucleus reticularis thalami neurons reduces the seizure (McCafferty *et al.*, 2018). Furthermore, $Ca_v3$ channels contribute to pain processing in nociceptive neurons, and they represent a promising drug target for neuropathic pain treatment by anesthetic and analgesics, such as isoflurane, or nitrous oxide (Perez-Reyes, 2003; Nelson *et al.*, 2006).

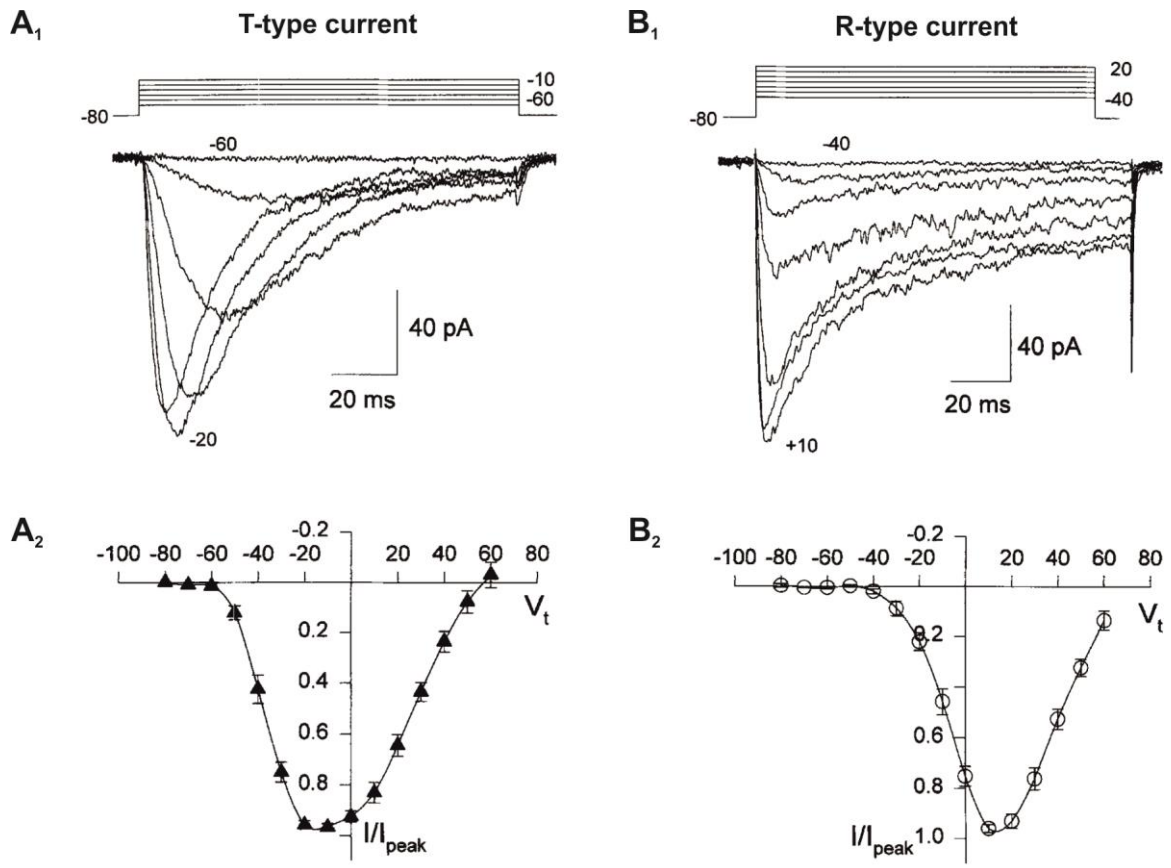


**Figure 28. Activation properties of T- and R-type $Ca^{2+}$ currents.**

**$A_1$.** T-type currents elicited from a holding potential of -80 mV start to activate at potentials more positive than -60 mV. **$A_2$.** Current-voltage relationship for T-type current. **$B_1$.** R-type currents elicited from a holding potential of -80 mV start to activate at potentials more positive than -40 mV. **$B_2$.** Current-voltage relationship for R-type current. Figure is adapted from Randall & Tsien, 1995.

## 4. REGULATION OF VOLTAGE-GATED CALCIUM CHANNELS

It is generally accepted that generation of single (or more) AP activates local $Ca^{2+}$ channels at presynaptic terminals, which results in rapid transient increase in intracellular $Ca^{2+}$ from resting concentrations of around 100 nM up to 100 µM (Grienberger & Konnerth, 2012). This intracellular $Ca^{2+}$ rise triggers the release of neurotransmitters that are contained in synaptic vesicles, which initiates synaptic transmission (Südhof, 2012). The main types of $Ca^{2+}$ channels that are involved in synaptic transmission are N- and P/Q-type $Ca^{2+}$ channels (Ishikawa *et al.*, 2005; He *et al.*, 2018), while R-type $Ca^{2+}$ channels are involved to a lower extent (Wu *et al.*, 1998*b*). Activation of $Ca^{2+}$ channels is therefore mediated by AP generation that depolarize membrane potential, and this voltage-dependent modulation of $Ca^{2+}$ channels represents an important mechanism that control $Ca^{2+}$ entry. Neurotransmitter release upon

$Ca^{2+}$ influx is a rapid and controlled process that takes place within several microseconds. In order to regulate $Ca^{2+}$ influx and $Ca^{2+}$-mediated neurotransmitter release, specific molecular mechanisms are present in the cells that aim at preventing the excess of intracellular $Ca^{2+}$ concentration and modulation of the neurotransmitter release, such as long- or short-term facilitation or depression (Rusakov, 2006).

$Ca^{2+}$ channels are widely distributed in the body in all excitable cells, but also in non-excitable cells (Grafton & Thwaite, 2001), where $Ca^{2+}$ influx through these channels regulates many cellular processes by acting as intracellular messenger (Berridge *et al.*, 1998). In accordance with the interest of my research, only control of $Ca^{2+}$ channels involved in neurotransmitter release by the most important mechanisms, $Ca^{2+}$-dependent $Ca^{2+}$ channel inactivation, and modulation by G protein-coupled receptors, is going to be described in this chapter. Mechanisms of $Ca^{2+}$ removal from the cytoplasm will be discussed later.

### 4.1. $Ca^{2+}$-dependent modulation of voltage-gated calcium channels

Calcium plays an important role in many cellular processes, from cellular proliferation to cellular death (Berridge *et al.*, 1998). Therefore, intracellular $Ca^{2+}$ concentrations should be precisely controlled to avoid the undesirable effects of prolonged $Ca^{2+}$ channels activation. Inactivation of $Ca^{2+}$ channels upon sustained depolarization is now a well described regulatory mechanism to maintain the resting levels of intracellular $Ca^{2+}$ concentration (Berridge *et al.*, 1998; Budde *et al.*, 2002; Rusakov, 2006). This ***$Ca^{2+}$-dependent inactivation (CDI)*** mechanism that depends on intracellular $Ca^{2+}$ elevations can be identified based on several criteria (Budde *et al.*, 2002). First, $Ca^{2+}$ current subjected to CDI shows U-shaped inactivation curve as a result of double-pulse protocol consisting of conditional depolarizing pulses to various potentials, and a test pulse to the voltage that activates the maximal $Ca^{2+}$ current, with a brief gap between these two pulses. Current amplitudes evoked by both conditioning and test pulses consequentially give U-shaped inactivation curves in current-voltage (I-V) plots (Budde *et al.*, 2002; Cens *et al.*, 2006). Further, substitution of $Ca^{2+}$ for $Ba^{2+}$ as a charge carrier reduces the inactivation of $Ca^{2+}$ channels mediated by CDI mechanism (Figure 29.) (Budde *et al.*, 2002; Cens *et al.*, 2006; Rusakov, 2006). The addition of exogenous buffers, such as BAPTA or EGTA, can also attenuate the CDI by increased $Ca^{2+}$ buffering (Budde *et al.*, 2002), although $Ca^{2+}$ buffers are prone to saturate near the channel pore during prolonged $Ca^{2+}$ influx (Rusakov, 2006).

Not all types of $Ca^{2+}$ channels are subjected to CDI modulation. HVA $Ca^{2+}$ channels are the most susceptible to CDI (Cens *et al.*, 2006). Direct inactivation of $Ca^{2+}$ channels pore-forming α1 subunit is the best described for neuronal L-, N-, and P/Q-type $Ca^{2+}$ channels, while R- and T-type channels are excluded from CDI (Budde *et al.*, 2002; Cens *et al.*, 2006). In L-type $Ca^{2+}$ channels, CDI can be initiated by influx of $Ca^{2+}$ through a single channel, and it is seen as decrease in channel open probability during prolonged depolarizing pulses in the presence of $Ca^{2+}$ as a charge carrier (Cens *et al.*, 2006). The CDI becomes maximal at the potentials which activate the most of $Ca^{2+}$ current. In contrast to L-type channels, the opening of a single channel is not sufficient to drive CDI in P/Q-type channels (Cens *et al.*, 2006), and both decay and inactivation of the current is similar even in the presence of $Ba^{2+}$ as a charge carrier. However, it was shown that $Ca^{2+}$ influx through P/Q-type $Ca^{2+}$ channels enhances CDI in the presence of lower concentrations of EGTA as $Ca^{2+}$ chelator through $Ca^{2+}$/CaM binding (Lee *et al.*, 1999*a*). This suggests that CDI of P/Q-type channels is more pronounced when auxiliary $\beta_{2a}$ subunit is co-expressed with $\alpha_1$ subunit, compared to co-expression of $\beta_{1b}$ subunit, and CDI is slowed in the presence of $Ba^{2+}$ as charge carrier (Lee *et al.*, 1999*a*).

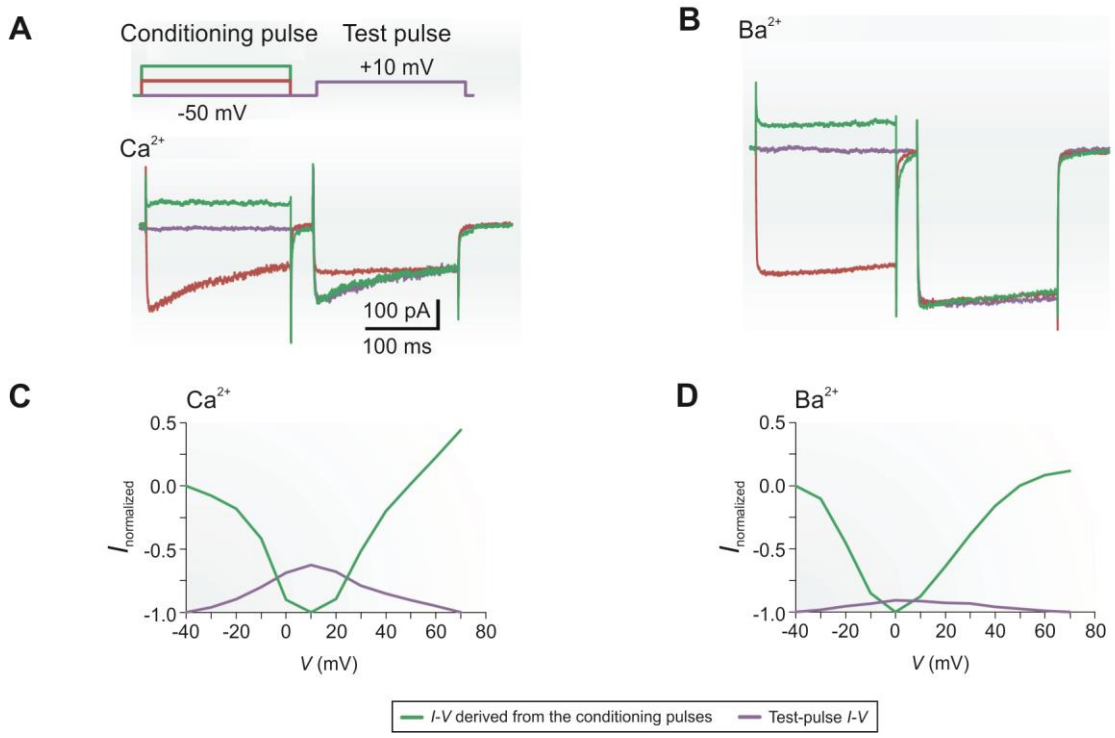


**Figure 29. The main properties and mechanisms for the CDI in neurons.**

**(A-B).** Wholle-cell recordings from thalamocortical neurons in which $Ca^{2+}$ (**A**) and $Ba^{2+}$ (**B**) currents are evoked using double-pulse protocol (top trace in A). The protocol consists of conditioning pulse to varying potentials and it is followed by a test pulse to the voltage at which maximal current amplitude is activated. **A.** Near maximal current amplitude during the test pulse (green trace) is evoked following

a conditioning step to a voltage close to or positive to the $Ca^{2+}$ reversal potential. Similar amplitude during the test pulse is obtained following a conditioning pulse to -50 mV at which most of $Ca^{2+}$ channels are closed (blue trace). In contrast, activation of maximal $Ca^{2+}$ current amplitude during the conditioning pulse (orange trace) will elicit decreased current amplitude in test pulse due to CDI, which is not observed when $Ca^{2+}$ is replaced by $Ba^{2+}$ as a charge carrier (**B**). (**C-D**). Plotting the test current amplitude against the conditioning pulse potential gives a U-shaped dependency of the test current amplitude (**C**) that is reduced in the presence of $Ba^{2+}$ (**D**) as a charge carrier. Adapated from Budde *et al.*, 2002.

### 4.1.1. Main mechanisms that control CDI in neurons

In HVA channels, CDI can be induced by several mechanisms. One of the main mechanisms involves ***calmodulin (CaM) complex*** that interacts with $Ca^{2+}$ entering the cell. CaM is a $Ca^{2+}$ -binding protein that consists of four EF-hands, two at N-terminal lobe, and two at C-terminal lobe, with former showing low, and latter showing high affinity for $Ca^{2+}$ (Cens *et al.*, 2006). It was demonstrated that CaM is constantly attached to the channels in close proximity to the inner pore even at resting $Ca^{2+}$ concentrations. Increase in intracellular $Ca^{2+}$ levels upon its influx leads to the activation of C-terminal lobe of CaM, structural changes in $Ca^{2+}$ channels, and consequently to the CDI (Cens *et al.*, 2006). Another mechanism that determines CDI is ***channel dephosphorylation*** mediated by activation of protein phosphatase calcineurin (PP2B), an enzyme activated by $Ca^{2+}$ and CaM (Budde *et al.*, 2002; Groth *et al.*, 2003). PP2B exerts its effect through protein phosphatase 1 (PP1), whose activity is inhibited by endogenous inhibitor-1 (Groth *et al.*, 2003), or inhibitor-2 (Budde *et al.*, 2002). Calcineurin can dephosphorylate endogenous inhibitors and therefore remove the inhibition of PP1 activity. Consequently, PP1 dephosphorylates $Ca_v$s and induces CDI modulation (Budde *et al.*, 2002; Groth *et al.*, 2003). Furthermore, CDI can be initiated by ***destabilization of cytoskeleton*** components, that are microtubules and microfilaments, upon increase in intracellular $Ca^{2+}$ concentrations (Budde *et al.*, 2002). It is suggested that $Ca^{2+}$-induced destabilization of cytoskeleton is due to the interruption of structural connection between mentioned cytoskeletal components and the channel. It was reported that β-subunit of $Ca_v$s contains interaction sites for the cytoskeleton protein, including SH3 domain of the subunit, PDZ domain and guanylyl kinase (GK) domain. Therefore, these sites could be important in CDI-mediated cytoskeleton destabilization. Further, fast mechanism for CDI has been proposed to be involved. This mechanism considers ***direct binding of $Ca^{2+}$*** to the

channels, which can lead to inactivation of several $Ca^{2+}$ channels (so called “domain” model) or all $Ca^{2+}$ channels of the membrane (“shell” model) (Budde *et al.*, 2002).

Regarding $Ca^{2+}$ channel structural components, the proximal third of C-terminal domain of $Ca_v1.2$ channels is essential for CDI, and it is called the $Ca^{2+}$-inactivation region (Budde *et al.*, 2002; Cens *et al.*, 2006). There are several regions in this domain which are involved in CDI. These are an EF hand motif located downstream of S6 in the IV transmembrane domain on the α1 subunit, IQ-type motif which binds CaM (Budde *et al.*, 2002; Cens *et al.*, 2006), and CaM tethering site which is responsible for docking CaM at the inner channel pore (Cens *et al.*, 2006). Therefore, C-terminal domain of $Ca^{2+}$ channels has a crucial role in CDI.

In summary, $Ca^{2+}$ channels are involved in release of neurotransmitters upon membrane depolarization and the amount of released neurotransmitters strongly depends on presynaptic $Ca^{2+}$ concentrations. Inactivation of the channels that mediate release of synaptic vesicles containing neurotransmitters depends on the frequency of stimulation, and increased frequency leads to increased channel inactivation. It is strongly suggested that CDI has a neuroprotective role and it contributes to $Ca^{2+}$-dependent synaptic plasticity (Lee *et al.*, 1999*a*; Budde *et al.*, 2002).

### 4.2. G proteins-mediated modulation of voltage-gated calcium channels

Heterotrimeric G proteins activated by G protein coupled receptors (GPCRs), together with $Ca^{2+}$-dependent inactivation, have an important role in providing a negative feedback that regulate the activation of main neuronal $Ca^{2+}$ channels of N- and P/Q type (Catterall, 2011). The inhibition of R-type $Ca^{2+}$ channels can also occur but in lower extent (Zamponi & Currie, 2013). The mechanism of inhibition involves direct binding of G protein βγ subunit (Gβγ) to $\alpha_1$ subunit of $Ca_v$s (Herlitze *et al.*, 1996). This G protein mediated inhibition is voltage-dependent as it can be significantly diminished upon large depolarizing pulses. There are several neurotransmitters that can inhibit $Ca^{2+}$ channels by binding to GPCRs, and therefore inhibit synaptic transmission (Wettschureck & Offermanns, 2005). Regarding the importance of GPCR regulatory mechanism for $Ca^{2+}$ channels modulation, the main properties of this mechanism are going to be briefly described.

### 4.2.1. G proteins and G protein coupled receptors – structure and coupling

***G proteins*** are heterotrimeric proteins consisting of three subunits, α, β, and γ, that are located at the inner membrane of the cell (Cabrera-Vera *et al.*, 2003). α subunits of G proteins are encoded by sixteen genes, and they are classified into four main families including $G_{i/o}$, $G_{q/11}$, $G_s$, and $G_{12/13}$ (Cabrera-Vera *et al.*, 2003; Wettschureck & Offermanns, 2005; Zamponi & Currie, 2013). Membrane-bound Gβ subunit is encoded by 5 genes, and it is linked with N-terminal amphipathic helix to Gγ subunit that is encoded by 12 genes (Cabrera-Vera *et al.*, 2003; Tedford & Zamponi, 2006; Zamponi & Currie, 2013). GPCRs are proteins with seven transmembrane domains, linked with three intracellular loops (I-II, III-IV, and V-VI) and three extracellular loops (II-III, IV-V, VI-VII), an extracellular N-terminal domain, and an intracellular C-terminal domain that binds G proteins (Tedford & Zamponi, 2006; Zamponi & Currie, 2013).

The binding of the ligand to GPCRs initiates downstream signaling cascades, including the inhibition of $Ca_v$s. In general, the mechanism of inhibition begins upon agonist binding to the GPCRs which interact with heterotrimeric G proteins containing α, β, and γ subunits. Activated GPCR catalyzes the exchange of Gα subunit-bounded GDP to GTP, leading to conformational changes of G proteins and dissociation of Gα-GTP from Gβγ heterodimer (Figure 30.) (Cabrera-Vera *et al.*, 2003; Tedford & Zamponi, 2006; Zamponi & Currie, 2013). The signaling is terminated by the intrinsic GTPase activity of Gα subunit that hydrolyses GTP back to GDP, and allows reassociation of Gα-GDP subunit with the Gβγ heterodimer. The continuous presence of an agonist can also induce termination of this signaling pathway by desensitization (Tedford & Zamponi, 2006; Zamponi & Currie, 2013). There are several mechanisms of desensitization, including heterologous and homologous desensitization (Tedford & Zamponi, 2006). Heterologous desensitization involves phosphorylation of GPCRs at their third intracellular loop mediated by protein kinase A or protein kinase C, which inhibits the interaction between GPCRs and Gα subunit, therefore terminating GPCR activity. G protein coupled receptor kinases (GRKs) mediate GPCRs desensitization by phosphorylation of C-terminal domain residues of GPCRs in the presence of agonist, which is a characteristic of homologous desensitization (Tedford & Zamponi, 2006).

GPCRs that are involved in G protein mediated inhibition of $Ca^{2+}$ channels include $GABA_B$ receptors, muscarinic receptors, α2-adrenoceptors, μ and δ opioid receptors, and adenosine A1 receptors (Dolphin, 2003; Wettschureck & Offermanns, 2005). The

involvement of $GABA_B$ receptors in $Ca^{2+}$ current modulation has now been well established. ***$GABA_B$ receptors*** ($GABA_B$Rs) are metabotropic receptors for GABA, the main inhibitory neurotransmitter in the brain, which couple specifically to $G_{i/o}$ type of G proteins that are sensitive to pertussis toxin (Bettler *et al.*, 2004; Padgett & Slesinger, 2010; Huang *et al.*, 2015). $GABA_B$ receptor is a heterodimer that consists of $GABA_{B1}$ and $GABA_{B2}$ subunits, and both of them are required to be expressed to form functional $GABA_B$Rs (Bettler *et al.*, 2004; Padgett & Slesinger, 2010). $GABA_{B1}$ and $GABA_{B2}$ share about 35% of sequence homology and they both have extracellular N-terminal domain, seven transmembrane domains, and intracellular C-terminal domain. $GABA_{B1}$ subunit of $GABA_B$Rs contains ER retention signal that prevents incorrectly folded $GABA_B$ receptors to reach the surface of the cell. Dimerization of $GABA_{B1}$ subunit with $GABA_{B2}$ masks the ER retention signal of $GABA_{B1}$ and facilitates its surface expression. It was clearly demonstrated that intracellular C-terminal domains of these two subunits allow the heterodimerization mediated by coiled-coil domains (Bettler *et al.*, 2004; Padgett & Slesinger, 2010). Moreover, extracellular N-terminal domain of $GABA_{B1}$ subunit represents the ligand-binding site. This binding site supports so called ″Venus flytrap″ mechanism in which two lobes of N-terminal binding domain, lobe I and lobe II, close in the presence of ligand (Galvez *et al.*, 1999; Padgett & Slesinger, 2010). Co-expression of $GABA_{B2}$ subunit with $GABA_{B1}$ subunit increases the affinity of $GABA_{B1}$ for ligand binding. Therefore, $GABA_{B1}$ and $GABA_{B2}$ must be co-expressed to form functional receptors (Galvez, 2001). In contrast to $GABA_{B1}$, $GABA_{B2}$ is not involved in ligand binding, but it couples to G proteins (Padgett & Slesinger, 2010). It was shown that all intracellular segments of $GABA_{B2}$ subunit, including intracellular loops and intracellular C-terminal domain, are crucial for specific binding of $GABA_B$Rs to G proteins (Margeta-Mitrovic *et al.*, 2001). Interestingly, co-expression of $GABA_{B1}$ subunit enhances coupling efficacy of $GABA_{B2}$ for G proteins (Galvez, 2001).

$GABA_B$ receptors are located at both presynaptic and postsynaptic levels where they modulate $Ca^{2+}$ channels, $K^+$ channels and adenylyl cyclase (Figure 30.). Activation of $GABA_B$Rs that couple to $G_{i/o}$ type of G proteins leads to inhibition of N- and P/Q-type $Ca^{2+}$ channels which are involved in release of neurotransmitters (Bettler *et al.*, 2004). It was recently reported that activation of $GABA_B$R by baclofen can also modulate LVA $Ca^{2+}$ channels of T-type in DRG neurons, although through a different mechanism than for HVA $Ca^{2+}$channels, since LVA are sensitive to redox modulation which can be reversed in the presence of dithiothreitol (DTT) (Huang *et al.*, 2015). At the postsynaptic level, $G_{i/o}$-coupled

$GABA_BRs$ selectively activate inwardly rectifying $K^+$ channels (GIRK or Kir3) leading to $K^+$ efflux, membrane hyperpolarization and inhibition of neuronal activity (Bettler *et al.*, 2004; Padgett & Slesinger, 2010). $GABA_BRs$ have the ability to inactivate an enzyme adenylyl cyclase through activation of α subunit of $G_{i/o}$ proteins. In contrast, $G_s$ protein-coupled receptors stimulate adenylyl cyclase to produce cAMP, and activation of $GABA_BR$ enhances this production. The mechanism that underlies stimulation of adenylyl cyclase activity involves simultaneous activation of $GABA_BRs$, $G_s$-coupled GPCRs and expression of appropriate adenylyl cyclase isoform (Bettler et al., 2004).

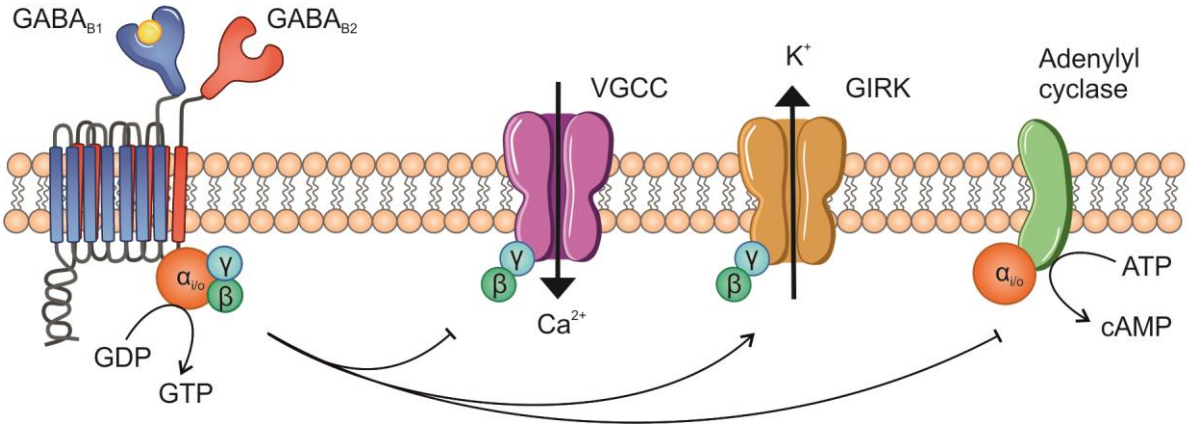


**Figure 30. Role of $GABA_B$ receptors coupled to $G_{i/o}$ type of G proteins.**

Activation of $GABA_{B1}$ subunit by ligand binding initializes the exchange of Gα bound GDP to GTP, which in turn leads to dissociation of GTP-Gα from Gβγ heterodimer. Released Gβγ heterodimer directly binds and inhibits voltage-gated $Ca^{2+}$ channels (VGCC), while it activates inwardly rectifying potassium channels (GIRK). GTP- Gα complex couples to adenylyl cyclase and inhibits the exchange of ATP to cyclic adenosine monophosphate (cAMP).

### 4.2.2. Properties of GPCRs-mediated inhibition of $Ca_v$s

The activation of GPCRs causes conformational changes and dissociation of G proteins into Gα and Gβγ heterodimer. It is now well described that Gβγ subunits of $G_{i/o}$ protein family directly bind α1 subunits of N-, and P/Q-type $Ca^{2+}$ channels, leading to the inhibition of these channels (Herlitze *et al.*, 1996; Ikeda, 1996; Wettschureck & Offermanns, 2005; Tedford & Zamponi, 2006). Therefore, close localization of GPCRs and $Ca^{2+}$ channels is crucial for binding of Gβγ heterodimer to the channels (Tedford & Zamponi, 2006). The inhibition is generally characterized by a shift of voltage-dependence of channel activation to more positive potentials, which was first demonstrated by Bean in 1989. Moreover, slowing of both

$Ca^{2+}$ current activation and inactivation kinetics due to increased delay in channel opening is another characteristic of Gβγ-mediated $Ca^{2+}$ current inhibition (Tedford & Zamponi, 2006; Dolphin, 2009; Catterall, 2011). Increased latency to channel opening is suggested to be caused by stabilization of channel in its closed state when it is bound to Gβγ (Tedford & Zamponi, 2006), which is consistent with the gating models introduced by Bean (Bean, 1989). These models consider that $Ca^{2+}$ channels can exist in two modes that are in equilibrium with each other: "willing" and "reluctant" mode. Channels are considered to be in "willing" mode in the absence of neurotransmitters or agonists which would activate GPCRs and induce G protein modulation of $Ca^{2+}$ channels. Channels in such mode can be opened by small or moderate depolarizations. Once the neurotransmitters bind GPCRs leading to consequential binding of Gβγ to $Ca^{2+}$ channels, there is a shift in the voltage-dependence of $Ca^{2+}$ channels that are opened by larger depolarizations (reluctant state) (Bean, 1989). Dissociation of Gβγ induces fast transition from reluctant back to willing state (Dolphin, 2003). Finally, the mechanism by which G proteins inhibit $Ca^{2+}$ channels opening involves slowing down of voltage sensor movement and subsequent channel opening (Jones *et al.*, 1997).

Ikeda (1996) was the first to demonstrate, in sympathetic neurons, the requirement of Gβγ expression for $Ca^{2+}$ channel inhibition, which strongly mimicked the inhibitory effect of noradrenaline in the same neurons (Figure 31.) (Ikeda, 1996). In contrast, Gα subunit fails to modulate $Ca^{2+}$ channels (Herlitze *et al.*, 1996; Ikeda, 1996). By using triple-pulse protocol consisting of conditional depolarizing pulse to high potentials (up to +80 mV), inserted between two depolarizing test pulses, the inhibition of $Ca^{2+}$ current mediated by Gβγ can be greatly relieved, indicating that the inhibition is voltage-dependent (Ikeda, 1991, 1996; Catterall, 2011). Re-inhibition of the channels after the high depolarizing pulse appears due to rebinding of Gβγ, and the amount of the repeated inhibition depends on the concentration of activated G proteins. It is still unknown whether re-inhibition involves dissociation and association of G proteins from the channels (Dolphin, 2003). High frequency train of APs (Zamponi & Currie, 2013) can also be used to reduce the inhibition. Moreover, it was demonstrated that the activation of protein kinase C (PKC) signaling pathway can diminish Gβγ inhibition of $Ca^{2+}$ channels, which represents another regulating mechanism for GPCR mediated inhibition (Tedford & Zamponi, 2006).

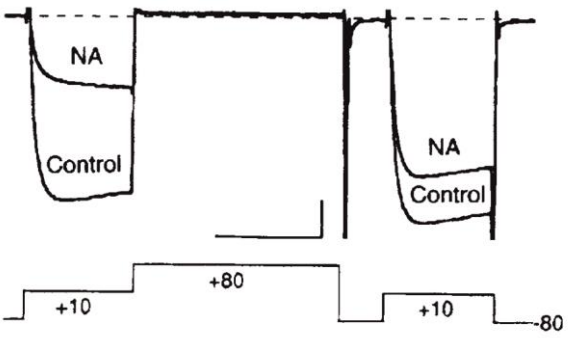


**Figure 31. Strong depolarization can diminish $GABA_B$ inhibition.**
Whole-cell $Ca^{2+}$ current was recorded from rat sympathetic neurons following triple-pulse protocol (lower trace). G proteins were activated by application of 10 μM noradrenaline to activate $\alpha_2$-adrenergic receptors. The inhibition of $Ca^{2+}$ current is markedly relieved following depolarizing pulse to + 80 mV. Adapted from Ikeda, 1996.

Interestingly, it was noted that inhibition of $Ca_v2.1$ and $Ca_v2.2$ channels by Gβγ shows different properties in that Gβγ inhibits $Ca_v2.2$ $Ca^{2+}$ current amplitude to a higher extent than $Ca_v2.1$ $Ca^{2+}$ current (Currie & Fox, 1997; Zamponi & Currie, 2013). In contrast, high frequency train of APs can relieve more successfully the inhibition of $Ca_v2.1$ channels than the inhibition of $Ca_v2.2$. These differences are suggested to be due to different affinity of Gβγ to $\alpha_1$ subunit of $Ca_v2.1$ and $Ca_v2.2$ (Zamponi & Currie, 2013). However, the inhibition of $Ca_v2$ by Gβγ also depends on the Gβγ complex. It was shown that $G\beta_1\gamma_2$, $G\beta_1\gamma_3$, $G\beta_1\gamma_7$ (Ikeda, 1996), and $G\beta_2\gamma_3$ (Herlitze *et al.*, 1996) mediate the most effective inhibition of $Ca_v2$, although some other combinations have been reported to have a similar or larger effect, and this inconsistency was suggested to be due to different experimental conditions for each study (Tedford & Zamponi, 2006). Data obtained from these studies indicate the complexity of interactions between $Ca_v2$ and Gβγ heterodimer.

### 4.2.3. Role of $Ca_v$ components in modulation of $Ca_v$s by G proteins

The evidence for direct effect of Gβγ subunit came from electrophysiological recordings in cell-attached configuration, when it was shown that only agonist present in the patch pipette can inhibit the channel, which was not the case when agonist was present in the bath solution (Dolphin, 2003; Zamponi & Currie, 2013). Several studies reported that intracellular linker between domain I and II of α1 subunit represents a binding site for Gβγ, although there are evidences for both C- and N-terminal domains as essential regions for Gβγ binding

(Dolphin, 2003; Tedford & Zamponi, 2006; Catterall, 2011; Zamponi & Currie, 2013). The Gβγ binding site on I-II linker of $Ca_v$α1 subunit overlaps with the AID binding site for $Ca_v$β subunit, and both Gβγ and $Ca_v$β subunits can bind $Ca^{2+}$ channels simultaneously. The presence of $Ca_v$β subunit is necessary for voltage-dependent reversal of Gβγ-mediated $Ca^{2+}$ channels inhibition, since in its absence, Gβγ can still inhibit the channels, but this inhibitory effect cannot be releaved by strong depolarizations (Herlitze *et al.*, 1996; Zamponi & Currie, 2013). Moreover, depletion of $Ca_v$β subunit was shown to cause an increase in $GABA_B$- and μ-opioid receptor-induced inhibition of $Ca_v2$ channels (Dolphin, 2003; Tedford & Zamponi, 2006), indicating that $Ca_v$β subunit and Gβγ compete for the same binding site on $Ca_v$α1 subunit (Dolphin, 2003). The expression of different $Ca_v$β subunit isoforms plays an important role in determining the dissociation kinetics of Gβγ from $Ca_v2$, and they can have different effects on activation kinetics of $Ca_v2$ too (Tedford & Zamponi, 2006).

Regarding the importance of C-terminal domain, it was suggested that it improves the affinity of $Ca^{2+}$ channels for Gβγ binding, while N-terminal domain contributes to Gβγ-mediated inhibition by physically interacting with I-II linker of $Ca_v$α1 subunit (Tedford & Zamponi, 2006). There is an 11 amino acid motif YKQSIAQRART in N-terminal domain which was found to be crucial for $Ca^{2+}$ channels modulation by G proteins, and mutations induced by replacement of YKQ or RAR amino acids with AAA enables G proteins modulations of $Ca^{2+}$ channels (Dolphin, 2003).

## 5. REGULATION OF INTRACELLULAR $Ca^{2+}$ CONCENTRATIONS

Calcium entry through $Ca_v$s and subsequent increase in its intracellular concentrations trigger numerous processes in the cell, such as synaptic transmission (He *et al.*, 2018), muscle contraction (Bannister & Beam, 2013) or gene transcription (Berridge *et al.*, 1998). In addition to $Ca_v$s, sarcoplasmic reticulum (SR) in striated muscle and ER in other cells are actively involved in the regulation of intracellular $Ca^{2+}$ concentrations ($[Ca^{2+}]_i$). These organelles represent a source of intracellular $Ca^{2+}$, and they also act as $Ca^{2+}$ storage organelles that accumulate $Ca^{2+}$ upon its uptake from the cytoplasm. Two families of $Ca^{2+}$-releasing channels regulate $Ca^{2+}$ efflux from the ER/SR stores, including ryanodine receptors (RyRs), and inositol 1,4,5-trisphosphate receptors ($IP_3Rs$). $Ca^{2+}$ accumulation back into the stores is mediated by the activity of sarco(endo)plasmic reticulum (SERCA) pumps. Both $[Ca^{2+}]_i$ and luminal $Ca^{2+}$ concentrations ($[Ca^{2+}]_L$) represent an important regulator of $Ca^{2+}$ release from

ER/SR stores, and they can determine the availability of $Ca^{2+}$ releasing channels. In the presence of low $[Ca^{2+}]_L$, stores tend to accumulate $Ca^{2+}$, and $Ca^{2+}$ entering the cell upon membrane depolarization is taken up into ER/SR stores. Consequentially, increase in $[Ca^{2+}]_L$ will increase permeability of RyRs and $IP_3$Rs for $Ca^{2+}$ release (Verkhratsky, 2005). $Ca^{2+}$ efflux from ER/SR stores contributes to regulation of neuronal excitability, synaptic plasticity and neurotransmitter release (Verkhratsky, 2005). Here, a special attention will be given to RyRs and $IP_3$Rs, and SERCA pumps, their function and modulation.

### 5.1. Ryanodine receptors

$Ca^{2+}$ release from ER/SR stores is mediated by RyRs, ligand-gated cation channels that show high $Ca^{2+}$ permeability (Verkhratsky & Shmigol, 1996). RyRs family of channels shows large conductance (50-500 pS) (Bezprozvanny, 1991; Santulli *et al.*, 2017; Meissner, 2017) and the ability to conduct both monovalent and divalent cations (Meissner, 2017). RyRs consist of three isoforms. These are RyR1, also known as ″skeletal muscle″ type, RyR2 or "heart" type, and RyR3 or "brain" type (Verkhratsky, 2005). RyRs are heterotetramers consisting of four 550 kDa monomers (Santulli *et al.*, 2017). Recently, 3D reconstruction using cryogenic electron microscopy revealed the mushroom-like structure of RyR1 purified from rabbit skeletal muscle. It was shown that RyR1 consists of four protomers that surrounds the central transmembrane pore, and each protomer is found to surround α-solenoid repeats, or repeats of α helix subunits (Zalk *et al.*, 2015). Similar structural organization was found for RyR2 (Peng *et al.*, 2016), which is in agreement with their 65-70% sequence homology (Verkhratsky & Shmigol, 1996; Lanner *et al.*, 2010).

The expression of all RyR isoforms has been found in neurons (Verkhratsky, 2005). RyR1 isoform is also expressed in skeletal, cardiac and smooth muscles, kidney, or cerebellum. RyR2 isoform is abundant in heart and Purkinje neurons, while RyR3 isoform is mainly found in the brain (Lanner *et al.*, 2010). RyRs expressed in skeletal and cardiac muscles are involved in excitation-contraction coupling, but also in synaptic transmission and synaptic plasticity when expressed in neurons (Lanner *et al.*, 2010; Thomas & Williams, 2012; Zalk *et al.*, 2015).

#### 5.1.1. Activation and modulation of RyR channels

RyRs are considered as $Ca^{2+}$-dependent $Ca^{2+}$ channels since $Ca^{2+}$ is the main ligand that triggers their activation. Among the main RyRs isoforms, only RyR1 is activated upon

membrane depolarization as it directly couples to L-type ($Ca_v1.1$) $Ca^{2+}$ channels (Thomas & Williams, 2012), although the interaction sites are still not well described. In contrast, RyR2 and RyR3 are activated by intracellular $Ca^{2+}$ through a mechanism known as $Ca^{2+}$-induced $Ca^{2+}$ release (CICR) (Verkhratsky, 2005). CICR mechanism, and therefore RyRs activation, strongly depends on $[Ca^{2+}]_i$. RyRs show biphasic or bell-shaped response to varying concentrations of free $Ca^{2+}$ (Bezprozvanny, 1991). At low cytosolic $Ca^{2+}$ concentrations, that range between 100 and 200 nM, RyR are closed and start to open following an increase in $[Ca^{2+}]_i$, reaching the maximum of activation at around 10 µM of $[Ca^{2+}]_i$. In presence of higher $Ca^{2+}$ concentrations (> 10 µM), channel open probability decreases (Santulli *et al.*, 2017; Meissner, 2017). However, RyR isoforms undergo different regulation processes mediated by cytosolic $Ca^{2+}$. RyR2 and RyR3 isoforms activate at lower cytosolic $Ca^{2+}$ concentrations and require higher concentration of cytosolic $Ca^{2+}$ to inactivate compared to RyR1 isoform (Meissner, 2017).

In order to determine $Ca^{2+}$ content in intracellular $Ca^{2+}$ stores, caffeine and ryanodine are often used as pharmacological tools for RyR modulation (Bezprozvanny, 1991; Usachev *et al.*, 1993). ***Caffeine*** is a natural methylxanthine, which is widely used as a potent, although not selective, activator of RyRs (Thomas & Williams, 2012). It rapidly diffuses through the plasma membrane and it lowers the sensitivity of RyRs for intracellular $Ca^{2+}$. Therefore, resting $[Ca^{2+}]_i$ can successfully induce $Ca^{2+}$ release from ER stores (Usachev *et al.*, 1993). Caffeine-induced $Ca^{2+}$ release from intracellular stores can be evoked regardless of the extracellular $Ca^{2+}$ concentrations ($[Ca^{2+}]_e$), indicating that increase in $[Ca^{2+}]_i$ upon RyRs activation is indeed the result of $Ca^{2+}$ release from intracellular stores (Usachev *et al.*, 1993; Verkhratsky & Shmigol, 1996; Verkhratsky, 2005). Repeated activations of RyRs by caffeine deplete the stores (Usachev *et al.*, 1993), which can be rapidly refilled following $Ca^{2+}$ influx (Verkhratsky, 2005). In rat DRG neurons, uptake of intracellular $Ca^{2+}$ was sufficient to refill the stores, and no additional source of $Ca^{2+}$ was necessary. However, in the presence of low $[Ca^{2+}]_e$, stores refilling becomes slower, strongly indicating that $Ca^{2+}$ influx may contribute to the refilling process (Usachev *et al.*, 1993).

***Ryanodine***, a plant derivate from *Ryania speciosa*, is another exogenous RyR activator. It preferentially binds the channels in their opened state (Verkhratsky, 2005). Ryanodine specifically binds to RyRs from the cytosolic side and its effect is strongly concentration-dependent. Ryanodine at low concentrations (5-40 nM) activates RyRs and increases the

frequency of channel open probability (Verkhratsky, 2005). Similar effect can be induced by lower micromolar (1-5 μM) concentrations of ryanodine, which promotes channel open probability, but it inhibits $Ca^{2+}$- and caffeine-mediated $Ca^{2+}$ release from stores. High concentrations (50-100 μM) of ryanodine completely and irreversibly block RyRs (Usachev *et al.*, 1993; Verkhratsky, 2005). Different effects of ryanodine are suggested to be due to the presence of ryanodine-binding sites with low- and high-affinity on RyRs (Verkhratsky, 2005).

### 5.2. Inositol 1,4,5-trisphosphate receptors

$IP_3Rs$, together with RyRs, mediate $Ca^{2+}$-release from intracellular $Ca^{2+}$ stores. As RyR channels, $IP_3Rs$ are large conducting cation channels (Taylor & Tovey, 2010) that consists of three isoforms, $IP_3R1$, $IP_3R2$, and $IP_3R3$ (Verkhratsky, 2005). $IP_3R$ isoforms share about 65% of sequence homology which indicates that they may have similar structure. Cryogenic electron microscopy studies confirmed homo- or heterotetrameric structure of $IP_3R$ channels (Taylor & Konieczny, 2016; Santulli *et al.*, 2017) that consist of four 300 kDa monomers (Santulli *et al.*, 2017). Mushroom-like structure described for RyRs has also been attributed to $IP_3Rs$, which are anchored in the ER membrane by the "mushroom stalk". This stalk represents $Ca^{2+}$-permeable channel pore that is surrounded by six transmembrane helices from $IP_3R$ channel subunits, linked to C-terminal region (Taylor & Tovey, 2010; Taylor & Konieczny, 2016; Santulli *et al.*, 2017). C-terminal region of one monomer interacts with N-terminal domain of adjacent monomer, and each N-terminal region contains $IP_3$-binding core (IBC) (Santulli *et al.*, 2017) which represents binding site for $IP_3$ (Taylor & Konieczny, 2016).

$IP_3R$ are expressed abundantly in the ER of many cells with different levels of expression (Taylor, 1998; Verkhratsky, 2005). $IP_3R1$ is the main isoform found in the brain, $IP_3R2$ is largely epressed in the spinal cord, while $IP_3R3$ is also expressed in several brain regions although to a lower extent compared to $IP_3R1$ (Verkhratsky, 2005). In addition, $IP_3R$ in ER are co-expressed together with RyRs.

#### 5.2.1. Activation and modulation of $IP_3R$ channels

Inositol 1,4,5-trisphosphate ($IP_3$), a second messenger that is formed as result of phospholipase C activation by GPCR, is the main activator of $IP_3Rs$ (Verkhratsky, 2005; Taylor & Konieczny, 2016). In general, activation of GPCRs by extracellular ligand such as neurotransmitters leads to dissociation of G proteins (as described in the previous Chapter). $G_\alpha$ subunit activates the membrane enzyme phospholipase C (PLC) which drives the

hydrolysis of phosphatidylinositol 4,5-bisphosphate ($PIP_2$) into $IP_3$ and 1,1-Diacylglycerol (DAG). $IP_3$ binds to $IP_3$Rs and initialize $Ca^{2+}$ release from intracellular $Ca^{2+}$ stores into the cytoplasm (Berridge, 2016; Santulli *et al.*, 2017). It has been demonstrated that each $IP_3$R channel monomer must bind $IP_3$ to induce $Ca^{2+}$ release (Alzayady *et al.*, 2016). $IP_3$R channel gating is also affected by cytosolic $Ca^{2+}$ (Bezprozvanny, 1991; Taylor & Tovey, 2010) which acts as co-agonist together with $IP_3$ (Finch & Turner, 1991). $IP_3$R channels show bell-dependence on cytosolic $Ca^{2+}$ (Bezprozvanny, 1991). At low free $Ca^{2+}$ concentrations between 10 nM and 1 µM, increased $IP_3$R open probability leads to enhanced $Ca^{2+}$ release from the stores independently on $IP_3$ levels, while free $Ca^{2+}$ concentrations higher than 100 µM inhibit $IP_3$R channels gating (Bezprozvanny, 1991; Finch & Turner, 1991). Modulation of $IP_3$R channel activity by cytosolic $Ca^{2+}$ represents an important mechanism for $IP_3$R channel regulation.

Screening of a chemical library led to identification of 2,4,6-trimethyl-*N*-(*meta*-3-trifluormethyl-phenyl)-benzosulfonamide (***m*-3M3FBS**) which was found to directly activate all PLC isoforms and to induce $Ca^{2+}$ release from the intracellular stores in a concentration-dependent manner (Bae, 2003). $Ca^{2+}$ increase induced by *m*-3M3FBS is described in many cells, and it is independent on extracellular $Ca^{2+}$ concentrations, supporting intracellular origin of $Ca^{2+}$ (Bae, 2003; Krjukova *et al.*, 2004; Szebenyi *et al.*, 2014).

### 5.3. Sarco(endo)plasmic reticulum pumps

Together with plasma membrane $Ca^{2+}$ pumps and mitochondrial $Ca^{2+}$ regulatory mechanisms, sarco(endo)plasmic reticulum (SERCA) pumps play an important role in the regulation of intracellular $Ca^{2+}$ levels and its removal from cytoplasm. They have a high affinity for $Ca^{2+}$ and are responsible for its uptake into ER stores and their refilling (MacLennan *et al.*, 1997; Verkhratsky, 2005). SERCA pumps belong to P-type ATPases that transport two $Ca^{2+}$ ions in the exchange of hydrolysis of one ATP molecule (Guerrero-Hernandez *et al.*, 2010). SERCA family of proteins is encoded by three gene products, including SERCA1, SERCA2, and SERCA3. Additionally, alternative splicing of SERCA2 produces two more isoforms, SERCA2a, and SERCA2b (Verkhratsky, 2005; Vandecaetsbeek *et al.*, 2011). Structural analysis demonstrated that SERCA proteins have highly conserved ten transmembrane helices (M1-M10) and cytosolic domains including phosphorylation (P), nucleotide-binding (N), and actuator (A) domains (Toyoshima *et al.*, 2000; Vandecaetsbeek *et*

*al.*, 2011). In contrast, SERCA2b is the only SERCA isoform that has 11 transmembrane helices (Camacho *et al.*, 2013). SERCA1 is mainly expressed in skeletal muscle, and SERCA2a is the main cardiac muscle isoform. SERCA2b is expressed in both smooth muscle and non-muscle tissues, while SERCA3 is the main non-muscle tissue isoform (MacLennan *et al.*, 1997).

The activity of SERCA pumps is carefully controlled by free $Ca^{2+}$ concentration in the ER lumen, $[Ca^{2+}]_L$. It is now well described that increase in $[Ca^{2+}]_L$ decreases the activity of SERCA pumps, while store depletion (e.g. upon repeated caffeine applications) (Usachev *et al.*, 1993) and $Ca^{2+}$ leak activate these pumps to restore $Ca^{2+}$ levels in ER lumen (Verkhratsky, 2005). Interestingly, calreticulin, a $Ca^{2+}$-binding protein, plays an important role in SERCA activity (Camacho *et al.*, 2013). Specific interactions between SERCA2b and calreticulin have been described in *Xenopus* oocyte expression system (Camacho *et al.*, 2013). Calreticulin directly activates SERCA2b pumps when $[Ca^{2+}]_L$ decreases and inhibits its activity when ER stores are full (Verkhratsky, 2005; Camacho *et al.*, 2013).

SERCA pumps are effectively and irreversibly inhibited by ***thapsigargin***, a widely used natural inhibitor isolated from plant *Thapsia garganica* (Treiman *et al.*, 1998). Thapsigargin exerts its inhibitory effect in nanomolar concentrations (Verkhratsky, 2005) and its application is usually followed by slow $Ca^{2+}$ leak from stores into the cytosol by still unknown mechanism (Camello *et al.*, 2002). Low concentrations of thapsigargin (20 nM) are sufficient to inhibit caffeine-induced $Ca^{2+}$ release from ER stores and its uptake into the stores in a time-dependent manner, while higher concentrations (200 – 2000 nM) can inhibit $Ca^{2+}$ influx through HVA $Ca^{2+}$ channels (Shmigol *et al.*, 1995).

In summary, ER, and sarcoplasmic reticulum in striated muscle, possesses highly effective machinery that contributes to the regulation of intracellular $Ca^{2+}$ concentration levels. This involves $Ca^{2+}$-releasing channels (RyRs and $IP_3$Rs) and SERCA pumps whose activity is essential in maintaining physiological $Ca^{2+}$ concentrations important for intracellular signaling (Figure 32.).

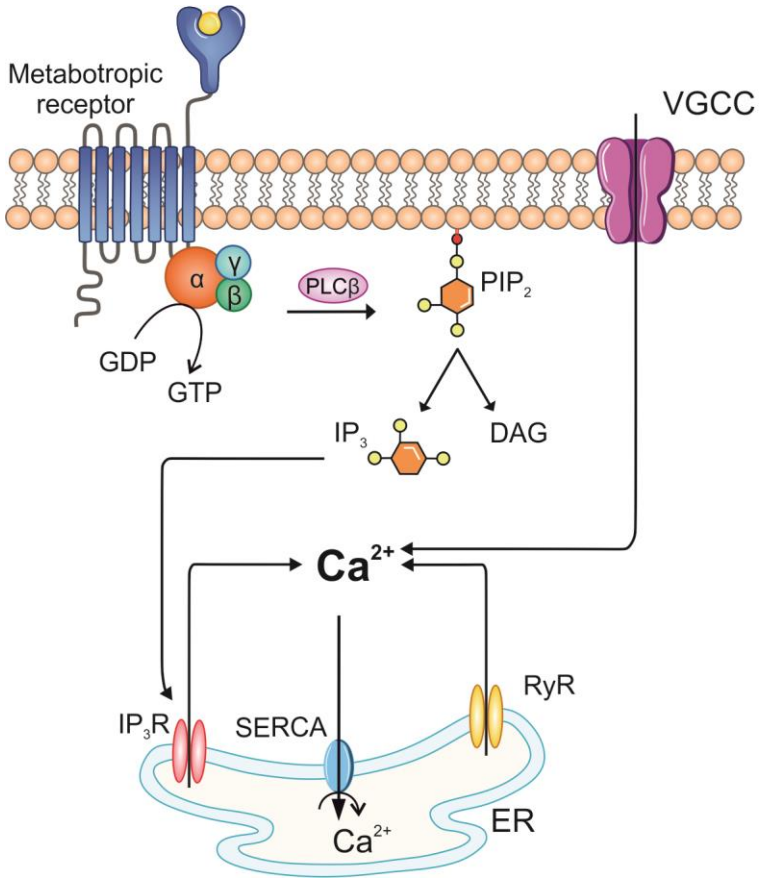


**Figure 32. Schematic illustration of intracellular $Ca^{2+}$ regulation.**

$Ca^{2+}$ entering the cell through the voltage-gated $Ca^{2+}$ channels (VGCC) can directly bind ryanodine receptor (RyR) on endoplasmic reticulum (ER), increasing the sensitivity of these channels to $Ca^{2+}$ and initializing $Ca^{2+}$ release from ER stores. Another pathway for $Ca^{2+}$ release involves activation of metabotropic receptors on the cellular membrane which in turn activates phospholipase C (PLCβ). PLCβ drives the hydrolysis of phosphatidylinositol 4,5 bisphosphate ($PIP_2$) into inositol 1,4,5-triphosphate ($IP_3$) and 1,1-diacylglycerol (DAG). $IP_3$ binds $IP_3$ receptor ($IP_3R$), inducing $Ca^{2+}$ release from the ER. $Ca^{2+}$ is uptaken back into ER stores through the activity of sarco/endoplasmic reticulum (SERCA) pumps.

# II. MATERIALS AND METHODS

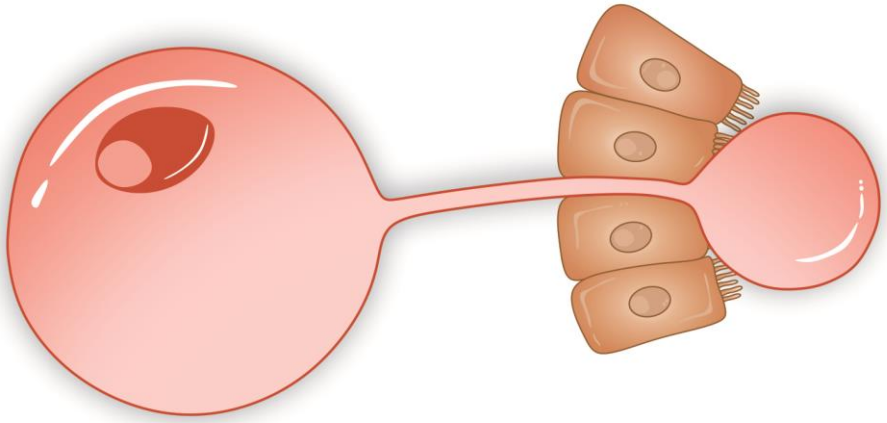

# II. MATERIALS AND METHODS

## A) ETHICAL STATEMENT

All experiments were performed in strict accordance with the guidelines and rules set by the EC Council Directive (2010/63/UE) and the French "Direction Départementale de la Protection des Populations des Bouches-du-Rhône" (Licence No. 13.435 held by J.T. and No. 13.430 held by N.W). The experimental procedures were approved by the local Animal Care Ethical Committee (Comité Ethique de Provence APAFIS 17596; license No. 13.435 held by J.T. and No. 13.430 held by N.W.). All animals used in this study were kept at constant temperature (21°C) under 12 h light – 12 h dark cycle, with food (pellet AO4, UAR, Villemoisson-sur-Orge, France) and water provided *ad libitum.* All efforts were aimed to minimize animal suffering and to reduce the number of animals used in this study.

## B) ANIMALS

This study has been conducted using wild-type C57BL/6 mice, and transgenic mice models of both sexes (females and males), aging from 6 to 9 weeks (25 – 30 g). Following transgenic mice lines were used:

**A) PKD2L1-IRES-Cre mice**, the transgene mouse line in which IRES-Cre recombinant gene is inserted downstream of gene coding for PKD2L1 channel, allowing selective expression of Cre recombinase in $PKD2L1^{+}$ cells (Figure 33. A, B). PKD2L1-IRES-Cre mice were a generous gift from Dr. Emily Liman (University of Southern California).

**B) DREADDs (Designer Receptors Exclusively Activated by Designer Drugs) mice** which represent a chemogenetic model based on engineered G protein-coupled receptors that can be activated solely by clozapine-*N*-oxide, a pharmacological inert molecule (Urban & Roth, 2015). In our model, mutated human muscarinic M4 receptors are coupled to inhibitory $G_i$ proteins (hM4Di). Such receptors are generated by two amino acid substitution ($Y113C^{3.33}$/$A203G^{5.46}$), and can no longer be activated by native agonist, acetylcholine (ACh). $G_i$-DREADD mice (R26-LSL-Gi-DREADD obtained from The Jackson Laboratory) express HA-tagged DREADD protein, which allows

immunohistochemical confirmation of receptor localization in the cell, and contain mCitrine reporter that follows DREADD sequence, enabling cell visualization by fluorescence microscopy. Mice with $G_i$-DREADD-expressing CSF-cNs were developed by crossing $G_i$-DREADD mouse line with PKD2L1-IRES-Cre genetic line that removes the flox cassette and enables the selective expression of CAG promotor-driven DREADDs in CSF-cNs (Figure 33. A).

**C)** Mice expressing **Channelrhodopsin-2 (ChR2)**, a blue (~490 nm) light-activated cation channel known to inhibit the activity of neurons in which it is expressed in (Madisen *et al.*, 2012). In our mouse model (Ai32(RCL-ChR2(H134R)/EYFP) obtained from The Jackson Laboratory), ChR2 with a single point mutation at H134R is fused with enhanced yellow fluorescent protein (EYFP). Mice with CSF-cNs that selectively express ChR2 were generated by crossing mice with CAG-driven construct in which ChR2(H134R) is fused with EYFP with PKD2L1-IRES-Cre mice, which allowed deletion of STOP cassette and selective expression of ChR2 in CSF-cNs (Figure 33. B).

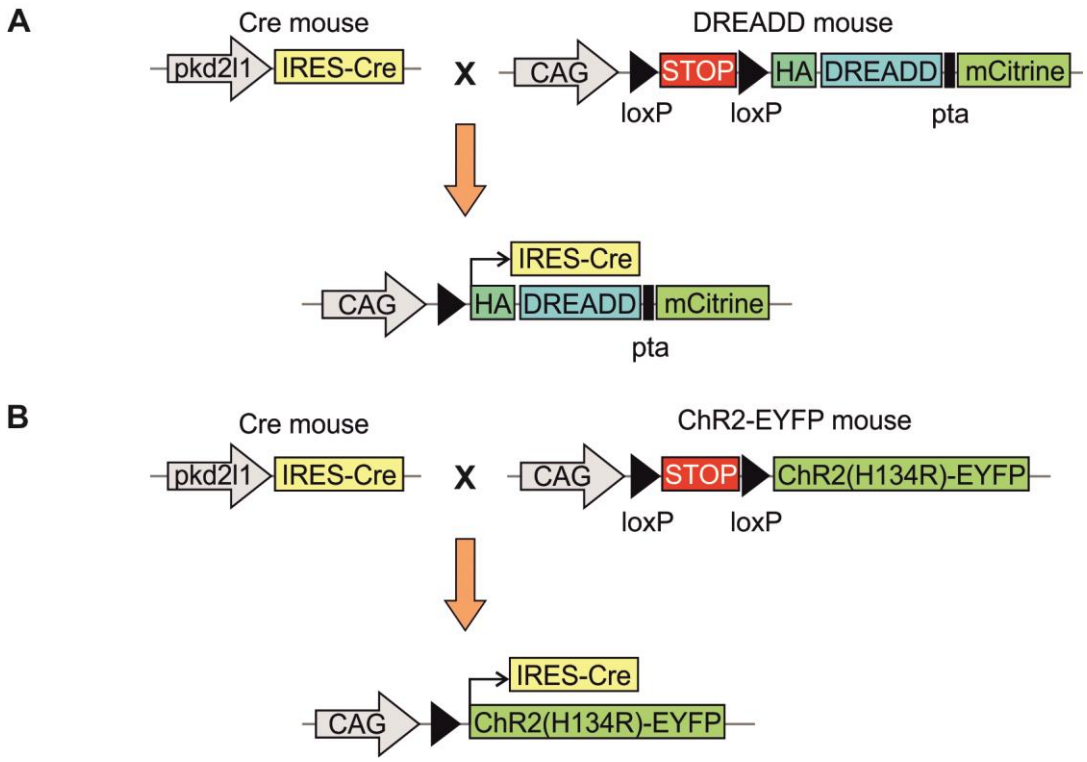


**Figure 33. Transgenic mice models used in the study.**

**A.** Mouse model with CSF-cNs expressing inhibitory $G_i$-DREADDs is generated using Cre-Lox technology by crossing PKD2L1-IRES-Cre mice with mice expressing CAG-driven construct

consisting of HA-tagged DREADD followed by mCitrine reporter. **B.** ChR2-expressing CSF-cNs are generated by crossing PKD2L1-IRES-Cre mice with mice expressing CAG-driven construct consisting of ChR2 fused with EYFP.

# C) SLICE PREPARATION

## 1. BRAINSTEM SLICE PREPARATION

Coronal brainstem slices were prepared as previously described by Orts-Del'Immagine and colleagues (2012). Briefly, one adult mouse per experiment was anesthetized with an intraperitoneal injection of ketamine (Carros, France) and xylazine (Puteau, France) mixture (100 and 15 mg/kg, respectively). When mouse lost its reflexes, it was decapitated, brain was removed and immersed in ice-cold (0-4 °C), oxygenated (95% $O_2$, 5% $CO_2$), low calcium/high magnesium slicing artificial cerebrospinal fluid solution (S-aCSF), containing (in mM): NaCl 75, $NaH_2PO_4$ 1.25, $NaHCO_3$ 33, KCl 3, $MgCl_2$ 7, sucrose 58, glucose 15, ascorbic acid 2, myo-inositol 3, sodium pyruvate 2, $CaCl_2$ 0.5 (pH 7.35-7.40, osmolality of 300-310 mosmol.$kg^{-1}$). Meninges was removed using fine forceps, and brainstem was glued with cyanoacrylate glue onto the cutting plate, where a small block of agar was used to support the brain during the slicing. Coronal brainstem slices (250 µm thick) were cut using a vibratome (Leica VT1000S) and incubated for 15-20 min in a submerged recovery chamber filled with an oxygenated (95% $O_2$, 5% $CO_2$) recording artificial cerebrospinal fluid (R-aCSF) at 35 °C, containing (in mM): NaCl 115, $NaH_2PO_4$ 1.25, $NaHCO_3$ 26, KCl 3, $MgCl_2$ 2, glucose 15, ascorbic acid 2, myo-inositol 3, sodium pyruvate 2, $CaCl_2$ 2 (pH 7.35-7.40, osmolality of 300-310 mosmol.$kg^{-1}$). Slices were left to recover from 35 °C to room temperature for 1h under continuous oxygenation until their transfer one by one to the recording chamber.

## 2. LUMBAR SPINAL CORD SLICE PREPARATION

Spinal cord slices were prepared from adult mice that were injected intraperitoneally with a ketamine (Carros, France) and xylazine (Puteau, France) mixture (100 and 15 mg/kg, respectively). When anaesthetized mice lost their toe pinch reflex, they were placed on cold plate. Transcardial perfusion was carried out with ice-cold, oxygenated (95% $O_2$, 5% $CO_2$), low calcium/high magnesium S-aCSF, containing (in mM): NaCl 75, $NaH_2PO_4$ 1.25,

$NaHCO_3$ 33, KCl 3, $MgSO_4$ 7, glucose 15, ascorbic acid 2, myo-inositol 3, sodium pyruvate 2, $CaCl_2$ 0.5 (pH 7.35-7.40, osmolality of 300-320 $mosmol.kg^{-1}$). Following decapitation, ventral laminectomy was performed to isolate the spinal cord. Precisely, ventral skin and viscera were removed in order to expose vertebral column. The latter was further isolated together with ribs by detaching the column from dorsal skin and cutting the femurs. Spinal column was immersed in ice-cold (0-4 °C) S-aCSF, and under continuous oxygenation, spinal cord was exposed by cutting the vertebrae from the ventral side (laminectomy) using iridectomy micro scissors. To completely separate spinal cord from the column, roots were cut and pulled together with overlying meninges. Lumbar enlargement of the spinal cord was isolated and placed in a groove made in an agarose block. The block was subsequently glued vertically onto the cutting plate using cyanoacrylate glue. Coronal spinal cord slices (250 µm thick) were cut using a vibratome (Leica VT1000S) and incubated for 15-20 min in a submerged recovery chamber filled with an oxygenated (95% $O_2$, 5% $CO_2$) R-aCSF at 35 °C, containing (in mM): NaCl 115, $NaH_2PO_4$ 1.25, $NaHCO_3$ 26, KCl 3, $MgSO_4$ 2, glucose 15, ascorbic acid 2, myo-inositol 3, sodium pyruvate 2, $CaCl_2$ 2 (pH 7.35-7.40, osmolality of 300-310 $mosmol.kg^{-1}$). Slices were left to recover from 35 °C to room temperature for 1h under continuous oxygenation until their transfer to the recording chamber.

## D) ELECTROPHYSIOLOGY

Electrophysiological recordings were performed on acute brainstem and lumbar spinal cord slices using patch-clamp recordings from neurons located around the CC, exhibiting typical morphology of CSF-cNs.

At the beginning of each experiment, one slice was transferred to the recording chamber mounted on an upright Zeiss Axioscop 1FS, and fixed using U-shaped platinum slice holder (harp). The slice was continuously perfused with oxygenated R-aCSF at room temperature, with an exchange rate of 2.5 $mL.min^{-1}$. CSF-cNs around the CC were visualized under infra-red differential interference contrast imaging (IR-DIC) illumination using 63x water immersion objective mounted on a microscope equipped with a p1 precisExcite LED epifluorescence system (excitation light at 490 nm or 590 nm; CoolLED, Roper) and a CoolSNAP HQ2 cooled CCD camera (Photometrics) connected to a computer through a frame grabber (CoolSNAP LVDS interface card, Photometrics) and controlled by MetaView software (Molecular Devices Inc., Sunnyvale, CA, USA) (Figure 34.).

Whole-cell patch clamp recordings were performed at room temperature in voltage- and current-clamp mode using Multiclamp 700B patch-clamp amplifier connected to Digidata 1322A interface (Molecular Devices Inc., San Jose, CA, USA). Patch pipettes were pulled from borosilicate glass capillaries (Harvard Apparatus, Holliston, MA, USA) using a horizontal P-97 Flaming/Brown type micropipette puller (Sutter Instrument Co., Novato, CA USA) and filled with an intracellular solution chosen based on experimental purpose (Table 4.). AlexaFluor 594 (10 µM, excitation 590 nm/emission 610 nm, Invitrogen) was added to the intracellular solution in all the experiments to confirm typical morphology of CSF-cNs during the whole-cell recording (Orts-Del'Immagine *et al.*, 2012; Orts Del'Immagine *et al.*, 2015). Patch pipette resistance was between 4-6 MΩ when filled with the intracellular solution. Series resistance ($r_s$) in the whole-cell configuration ranged between 10-20 MΩ and it was monitored throughout each experiment by applying a -20 mV calibration pulse to control for the quality of the recording, the electrical access and to measure the intrinsic properties (input resistance, cell capacity) of recorded neuron. Recordings were discontinued when $r_s$ exceeded more than 25% the original value. For voltage-gated calcium currents recordings, series resistance was compensated by 70-80%. Cells were recorded at a membrane potential of -70 mV. Signals were filtered at 2-2.4 kHz, digitized between 10 and 20 kHz and acquired on a computer using the Clampex 9.2 software (Molecular Devices Inc.).

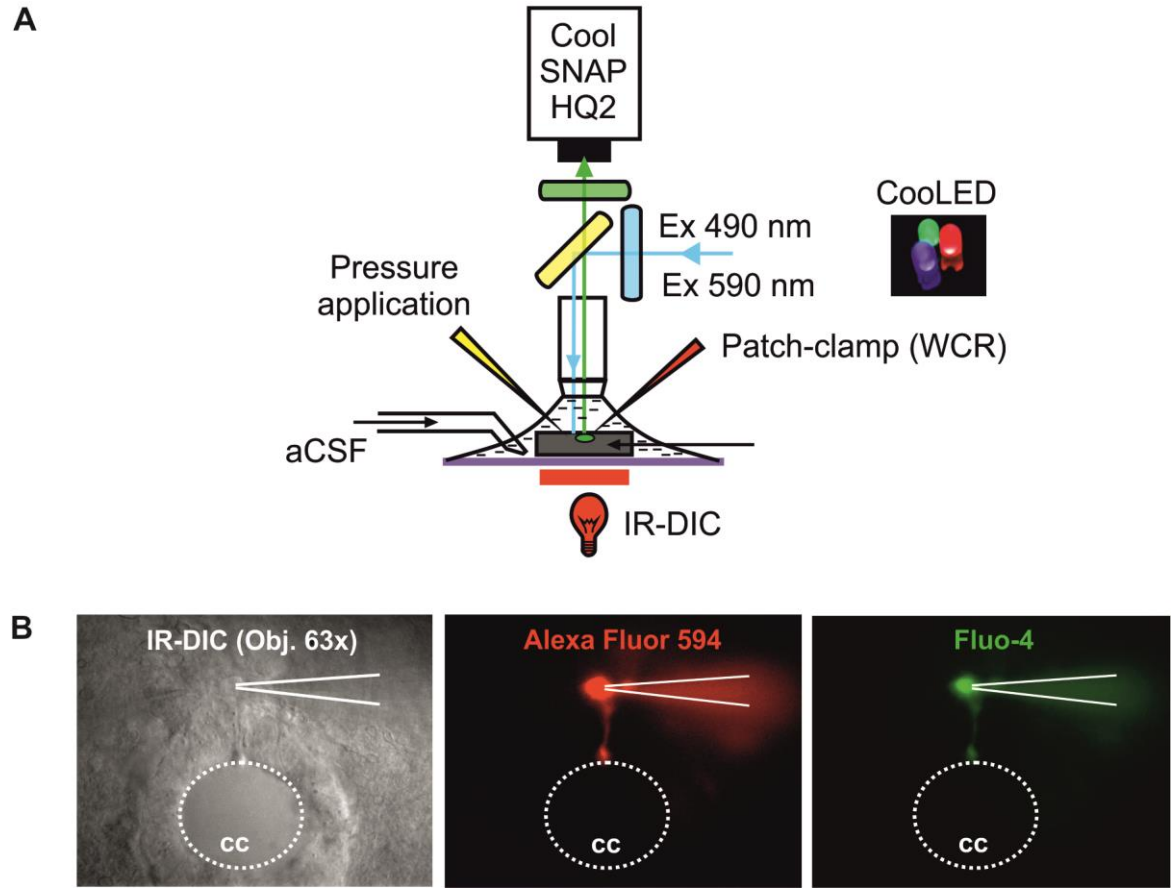


**Figure 34. Experimental setup used for electrophysiological recordings and $Ca^{2+}$ imaging.**

**A.** Schematic illustration of the setup used for electrophysiological recordings in whole-cell configuration (WCR), equipped with infra-red differential interference contrast imaging (IR-DIC) and LED illumination, and CCD camera. **B.** Acute spinal cord slices observed under IR-DIC illumination (left). The 590 nm illumination (middle) and 490 nm illumination (right) enable the visualization of CSF-cN dialyzed with AlexaFluor 594 to confirm the morphology and with Fluo-4 fluorescent $Ca^{2+}$ probe, respectively. White lines illustrate the position of the patch pipette. White dashed line delineates the central canal (cc).

## 1. RECORDING OF VOLTAGE-GATED CALCIUM CURRENT

To characterize voltage-gated calcium channels ($Ca_v$), patch pipettes were filled with a solution based on caesium acetate (CsAc) with or without tetraethylammonium chloride (TEA-Cl) (Table 4.), supplemented with EGTA as $Ca^{2+}$ chelator. TEA-Cl containing solution with high level of EGTA was used to study the nature of $Ca_v$s and their modulation by $GABA_B$ receptors and muscarinic receptors. EGTA was replaced with BAPTA when the stability of $Ca^{2+}$ current amplitude over time was tested. Selective antagonists were added to the oxygenated R-aCSF and bath applied to the recorded neurons with the aim to block

different receptors and ionic channels. $GABA_A$ receptors were inhibited with 10 µM gabazine (SR 95531), and glycine receptors were inhibited with 1 µM strychnine. To isolate $Ca^{2+}$ current, voltage-gated sodium channels were inhibited with 0.5 µM tetrodotoxine (TTX), while voltage-gated potassium channels were blocked with 20 mM TEA-Cl. Calcium currents were elicited using 100 ms steps from a holding potential of -70 mV to +30 mV, with 10 mV increments ($V_{step}$). The same protocol was used in the presence of cadmium (200 µM, 30 s) to block whole-cell $Ca^{2+}$ current. The current-voltage relationship was obtained by plotting the $Ca^{2+}$ peak current amplitude recorded against the test potential ($V_{step}$). The properties and voltage-dependence of $Ca^{2+}$ current were analyzed with a Boltzmann fit using the following equation: $I(V) = g_{max}(V - V_{rev})/[1 + exp(V_{50} – V)/k]$, where $I$ represents the current amplitude as a function of voltage ($V$), $g_{max}$ is the maximum whole-cell channel conductance, $V_{rev}$ is the current reversal potential, $V_{50}$ is the voltage for half-maximal channel activation, and $k$ is a slope factor that is equal to RT/zgF, where zg is the valency of the voltage sensor of the $Ca_v$.

To determine the nature of $Ca_v$s and current inhibition by $GABA_B$ receptors and muscarinic receptors, the effect of different toxins and receptors activation was assessed on $Ca^{2+}$ current peak amplitude elicited with a single 100 ms step from a holding potential of -70 mV to +10 mV every 20-30 s over a 10 min period. N-type $Ca_v$s are sensitive to ω-conotoxin GVIA (500 nM, 5 min), P/Q-type $Ca_v$s to ω-agatoxin IVA (500 nM, 5 min), and L-type $Ca_v$s to nifedipine (1 µM, 5 min). $GABA_B$ receptors were activated by selective agonist baclofen (100 µM, 1 min), while muscarinic receptors were activated by selective agonist oxotremorine-M (100 µM, 1 min). All $Ca^{2+}$ channel inhibitors, including cadmium, and agonists of $GABA_B$ and muscarinic receptors were added to R-aCSF and applied by pressure, using a pressure application pipette (~1 µm tip diameter) located ~50 µm away from the recorded cells and connected to a pressure application system (Toohey Company, Hollis, NH, USA). CGP 54626A (2 µM), a selective antagonist of $GABA_B$ receptors, and atropine (10 µM), a selective antagonist of muscarinic receptors, were added to the R-aCSF and bath applied to the neurons.

The molecular mechanism by which $GABA_B$ receptors and muscarinic receptors activation modulates $Ca^{2+}$ currents was studied with a triple-pulse voltage protocol consisting of two 50 ms long test pulses from a holding potential of -70 mV to +10 mV, separated by a 50 ms conditioning pulse to +100 mV. Pulses were recorded every 30 s over a 10 min period. The inhibition of $Ca^{2+}$ currents induced by application of baclofen or oxotremorine-M was

compared before (prepulse) and after (postpulse) the large depolarizing conditioning pulse (Herlitze *et al.*, 1996; Ikeda, 1996).

| | CsAc | TEA-10E | TEA-2E | TEA-B | KGlu |
|---|---|---|---|---|---|
| CsCl | 3 | 3 | 3 | 3 | / |
| CsAc | 120 | 100 | 120 | 100 | / |
| KCl | / | / | / | / | 3 |
| K-gluconate | / | / | / | / | 120 |
| NaCl | 5 | 5 | 5 | 5 | 5 |
| $MgCl_2$ | 1 | 1 | 1 | 1 | 1 |
| TEA-Cl | / | 20 | 20 | 20 | / |
| $CaCl_2$ | 1 | 1 | 0.25 | 0.5 | 0.25 |
| EGTA | 10 | 10 | 2 | / | 2 |
| BAPTA | / | / | / | 10 | / |
| Free $[Ca^{2+}]_i$ (nM) | 13.5 | 11.8 | 15.1 | 20.2 | 15.1 |
| HEPES | 10 | 10 | 10 | 10 | 10 |
| $Na_2$-Phosphocreatine | 10 | 10 | 10 | 10 | 10 |
| Mg-ATP | 4 | 4 | 4 | 4 | 4 |
| $Na_3GTP$ | 0.2 | 0.2 | 0.2 | 0.2 | 0.2 |
| pH | 7.34 | 7.36 | 7.35 | 7.35 | 7.33 |
| Adjustment of pH | CsOH 1 M | CsOH 1 M | CsOH 1 M | CsOH 1 M | KOH 1 M |
| Osmolality ($mosmol.kg^{-1}$) | 294 | 289 | 303 | 297 | 295 |
| Reversal potential of ions at 20 °C (mV) | | | | | |
| $E_{Cl}$ | -61.4 | -61.4 | -64.8 | -63.6 | -64.6 |
| $E_{Na}$ | 45.7 | 45.7 | 45.7 | 45.7 | 43.8 |
| $E_{Ca}$ | 65.2 | 65.2 | 65.2 | 65.2 | 61.5 |
| $E_K$ | / | / | / | / | -93.7 |

**Table 4. Intracellular solutions used for electrophysiological recordings.**

All internal solutions were used with particular purpose (see text for more details). When prepared, solutions were filtered by using 0.22 µM pore filter and stored at -20 °C until use.

## 2. RECORDING OF CHOLINERGIC CURRENTS

To record acetylcholine (ACh)-mediated currents (ionotropic nicotinic currents), patch pipettes were filled with CsAc solution enriched with TEA-Cl and 10 mM EGTA (Table 4.). Acetylcholine-mediated currents were elicited by ACh pressure application (1 mM, 1 s) in the presence of 10 µM gabazine, 1 µM strychnine, 10 µM atropine, and 20 µM DNQX, a selective AMPA/kainate receptor antagonist.

## 3. DUAL PATCH-CLAMP RECORDING AND RECORDING OF CURRENT ACTIVITY FROM THE TERMINAL ENLARGEMENT

Two patch electrodes filled with K-gluconate based intracellular solution (Table 4.) were used for dual patch-clamp recordings. AlexaFluor 594 (10 µM) and AlexaFluor 488 (10 µM, excitation 490 nm/emission 525 nm, Invitrogen) were added to the intracellular solution to confirm the morphology of CSF-cNs and distinguish cellular compartment when patch-clamped from soma and terminal enlargement ("bud"). Spontaneous activity in CSF-cNs was recorded in voltage-clamp mode from a holding potential of -70 mV maintained in both patch electrodes, while perfusing the neurons with normal R-aCSF. Current-clamp recordings were performed from the RMP. APs were triggered with 5 consecutive trains of 500 ms direct current (DC) pulses (+20 pA) after a period of baseline.

To record from the "bud", patch pipette was filled with K-gluconate-based intracellular solution (Table 4.). Ionic currents were elicited by 100 ms steps, from a holding potential of -70 mV to +30 mV, with 10 mV increments ($V_{step}$) in the presence of normal R-aCSF.

## 4. RECORDING OF CSF-cNs EXPRESSING $G_i$-DREADD

The cells expressing hM4Di-mCitrine were recorded using patch electrodes filled with K-gluconate based intracellular solution (Table 4.) and visualized with 480 nm excitation light using p1 precisExcite LED epifluorescence system and a CoolSNAP HQ2 cooled CCD camera. Clozapine-*N*-oxide (CNO, 5 µM and 10 µM), a selective DREADD activator, was added to the R-aCSF containing 10 µM gabazine and 1 µM strychnine, and bath perfused to the recorded neurons. To assess the effect of CNO on the membrane potential, neurons were recorded in current-clamp mode from the RMP. APs were induced by 500 ms current steps

from the RMP, with 10 pA increments after a period of baseline. The current-voltage relationship was constructed for every cell by plotting the injected current and recorded membrane potential.

## E) CALCIUM IMAGING

For calcium imaging experiments, patch pipettes were filled with an intracellular solution based on K-gluconate or TEA-2E (Table 4.). Cells were loaded with the fluorescent $Ca^{2+}$ probe Fluo-4 (50 µM, Invitrogen, Carlsbad, CA, USA) through the patch pipette and illuminated with 490 nm excitation light using CoolLED epifluorescence system (p1 PrecisExcite). Emitted fluorescent light (peak emission at 520 nm) was captured at 10 MHz with CoolSNAP HQ2 cooled CCD camera. The selectivity of the excitation and emission was optimized using a fluorescence filter cube with bandpass filters for excitation and emission set at 490 ± 30 nm, and 535 ± 30 nm, respectively, and a dichroic mirror set at 515 nm (Chroma). To optimize imaging conditions and to reduce fluorescence quenching, a square region of interest (ROI) was drawn around the recorded neurons, and illumination intensity was set to 25% of the maximum power. Images were acquired in time lapse mode with a 2x2 binning for 100 ms every 0.2 s for 60 s period (151 images, activation of $Ca^{2+}$ currents in current-clamp mode), every 0.1 s over 10 s period (61 images, activation of $Ca^{2+}$ currents in voltage-clamp mode), or every 0.5 s over 120 s (201 images, caffeine application).

To activate $Ca^{2+}$ currents, CSF-cNs were recorded in current-clamp mode from the RMP. 5 consecutive trains of APs at a frequency of 0.5 Hz were triggered with 500 ms direct current (DC) pulse (+20 pA) after a period of baseline recording to induce $Ca^{2+}$ influx following membrane depolarization and monitor increase in intracellular $Ca^{2+}$. To confirm that $Ca^{2+}$ elevations were due to $Ca_v$ activation, recordings were also performed in voltage-clamp mode with TEA-2E intracellular solution, that is CsAc-based intracellular solution enriched with TEA-Cl and containing low levels of EGTA (2 mM). Fluo-4 was added to the intracellular solution for each experiment. CSF-cNs were depolarized to +10 mV for 100 ms from a holding potential of -70 mV and increase in Fluo-4 fluorescence was simultaneously recorded. To assess $Ca^{2+}$ release from the ER, caffeine (50 µM, 30 s) was pressure applied to selectively activate RyRs in recorded CSF-cNs (Verkhratsky, 2005). The intracellular nature of caffeine-induced $Ca^{2+}$ elevations was confirmed by using R-aCSF in which 2 mM $CaCl_2$ was replaced with 2 mM $MgCl_2$ ($Ca^{2+}$ free R-aCSF). Thapsigargin (50µM), an antagonist of

sarco/endoplasmic reticulum ATPase (SERCA) pump was added to the R-aCSF containing 10 µM gabazine and 1 µM strychnine to assess the role of SERCA pumps in intracellular $Ca^{2+}$ uptake.

## F) OPTOGENETIC ACTIVATION OF CHANNELRHODOPSIN-2

To record CSF-cNs expressing channelrhodopsin-2 fused with EYFP (ChR2-EYFP), patch electrodes were filled with an intracellular solution based on K-gluconate (Table 4.). Cells were activated with 490 nm excitation light using CoolLED epifluorescence system (p1 PrecisExcite). Emitted fluorescent light (peak emission at 520 nm) was captured at 10 MHz with CoolSNAP HQ2 cooled CCD camera. Ilumination intensity was set to 25% of the maximum power. In the presence of 10 µM gabazine and 1 µM strychnine, a series of 150 ms long blue excitation light was delivered every 1 s over 10 s. To compare APs elicited by blue light with those elicited by current injections, 480 nm light was delivered for 100 ms, with 100 ms increments over a 700 ms period. To elicit APs by current injections, CSF-cNs were recorded from the RMP and 100 ms long current pulses (+20 pA) were delivered with 100 ms increments over a 700 ms period.

## G) REAGENTS

All reagents were purchased from Sigma-Aldrich, except: gabazine (SR 95531), (R)-baclofen, oxotremorine-M, atropine, clozapine-*N*-oxide, and thapsigargin from Tocris Bioscience (Bristol, UK). ω-conotoxin GVIA, ω-agatoxin IVA, and nifedipine from Alomone labs (Jerusalem, Israel). Tetrodotoxine (TTX) from Latoxan (Portes-lés-Valence, France). 6,7-dinitroquinoxaline-2,3-dione disodium salt (DNQX) from Abcam Biochemicals. CGP 54626A was a gift from Bernhard Bettler (University of Basel, Switzerland) and it was initially produced by Novartis Pharma AG (Basel, Switzerland).

# H) STATISTICAL ANALYSIS

## 1. DATA ANALYSIS

$Ca^{2+}$ current was analyzed using Clampfit 10.0 suite (Molecular Devices Inc.) and Excel 2016 (Microsoft). Peak current amplitude and mean current amplitude were taken into account for current-voltage responses (see below).

RMP was determined in current-clamp mode just after the whole-cell configuration was achieved as well as by averaging in the current-clamp recordings a ~1 s period in the absence of APs and of current injection ($I_{injection}$ = 0 pA). Properties of APs were analyzed from recordings of spontaneous discharge activity (10–30 s) or from trains of APs elicited by +20 pA current injections for 500 ms using the "Threshold Search" routine from Clampfit 10.0 with a threshold set at 0 mV. For each condition, principal parameters of APs (amplitude, width, frequency, 10 – 90% rise time) were determined. Threshold potential (TP) was determined in current-clamp mode following current injection ($I_{injection}$ = +20 pA) by averaging the current traces at potentials that elicited the APs.

When $Ca^{2+}$ current was recorded over a period of 10 min, decrease in $Ca^{2+}$ amplitude, known as rundown, was constantly observed (see Discussion). To account for this phenomenon when $Ca^{2+}$ current amplitude was compared over time for each cell recorded, baseline data points before drug application (control) were fitted using a linear regression function ($y = ax + b$; where $y$ is recorded peak current amplitude, $x$ is time, while $a$ and $b$ are constants). The current amplitude in the presence of drug was measured from the raw data and compared to the value in control calculated at the same time points from the linear regression. This procedure avoided an overestimation for the degree of inhibition.

Changes in intracellular calcium concentrations ($[Ca^{2+}]_i$) over time, seen as changes in fluorescence intensity, were measured in ROIs drawn around the soma and bud of the recorded CSF-cN and the background on the recorded image. Background fluorescence intensity was subtracted from the somatic data and data from bud to calculate the net fluorescence rise (F). The average intensity before the application of the stimulus ($Ca_v$ activation or train of APs), so called basal intensity ($F_0$), was calculated. $\Delta F/F_0$ ratio or $(F - F_0)/F_0$ was used to calculate the net rise of fluorescence intensity (F), and it is expressed as percentage. The average fluorescence intensity was plotted over the time to illustrate $Ca^{2+}$ transients and the peak amplitude of the fluorescence rise measured and compared between

the control and the test conditions. When using imaging with epifluorescence and diffusion of Fluo-4 into the cell through the patch pipette, fluorescence signal exhibits a progressive decrease in intensity over time, known as bleaching or quenching. To compute the amount of quenching over time, baseline data were fitted using a linear regression function ($y = ax + b$; where $y$ is $\Delta F/F_0$ value, $x$ is time, while $a$ and $b$ are constants) and subtracted from the raw data points in a point to point manner. To compare the amplitude of the fluorescence rise (control vs. baclofen), the maximum amplitude recorded after the 5$^{th}$ train of APs was normalized against that of the 1$^{st}$ train for each CSF-cN recorded.

## 2. STATISTIC

Data were expressed as mean ± SD and represented as box-whisker plot using Tukey's method with RStudio 1.1.456 (R Studio Team 2018). For each dataset, median and the 25$^{th}$ to the 75$^{th}$ percentiles (lower and upper limits of each bar, respectively) are calculated. The interquartile distance (IQR) is determined as the difference between the 25$^{th}$ and 75$^{th}$ percentiles and the whisker limits calculated as the 75$^{th}$ percentile plus 1.5 times IQR and the 25$^{th}$ percentile minus 1.5 times IQR. All data with values either higher or lower than whisker limits are represented as individual data points and considered as outliers. In all the figures where data are presented with box- and whiskers plots, the thick horizontal line represents the median. For all data, *n* represents the number of recorded cells. All data were tested for normal distribution using Shapiro-Wilk test using R statistics. Data with normal distributions were analyzed with a one-way ANOVA followed by Dunn's multiple comparison *post hoc* test for the statistical comparison of multiple groups. Student's two-tailed paired *t* test was used for comparison of two groups. Data without normal distributions were analyzed using Friedman or Kruskal-Wallis test followed by Dunn's multiple comparison *post hoc* test for comparison of multiple groups. Mann-Whitney or Wilcoxon matched-pairs signed rank test was used when comparing multiple groups.

For statistical analysis of $Ca^{2+}$ current inhibition by blockers or toxins, modulation by baclofen or oxotremorine-M, and the reduction of intracellular $Ca^{2+}$ elevation following activation of $GABA_B$ receptors or muscarinic receptors, dependent variables (data within a group) and independents variables (data between groups) were considered. For given cell, measured parameter or variable (current amplitude or $Ca^{2+}$ elevation) and its inhibition/modulation by a drug is considered as a variable dependent on the condition

(baseline or drug) within a given group while the same variable represents an independent factor when considered between different groups (control and drug of different types). The statistical analyses require the use of a mixed effect model considering in a hierarchical way both dependent and independent variables. The drug effects within a group and between different groups on the analyzed variable represent fixed factors (Condition and Group). The choice of the cell recorded in this study was random, therefore, it was necessary to implement a statistical model with a factor corresponding to this random effect. The statistical analyses were carried out using the linear mixed effect (lme version 3.1-128) routine (Pinheiro *et al.* 2016). The lme model was subsequently tested using an ANOVA (ANOVA.lme) followed by *post hoc* Dunn's multiple comparison test. When an interaction between the variables and the conditions was statistically significant, *P* value was reported. The differences were considered significant when $P < 0.05$. Figures were prepared and finalized using CorelDraw 2018 (Corel Corporation, Ottawa, ON, Canada).

# III. RESULTS

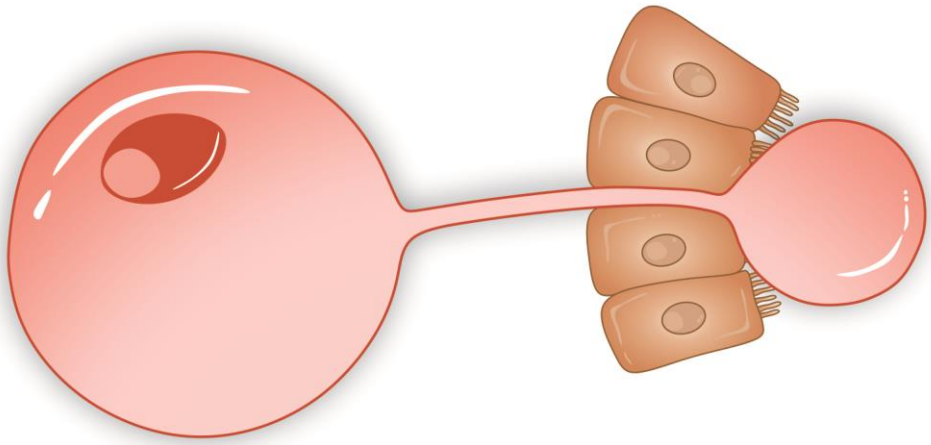

# III. RESULTS

In the first part of this chapter, I will present the data from experiments aimed at describing the expression and modulation of $Ca^{2+}$ channels in medullo-spinal CSF-cNs, and $Ca^{2+}$ homeostasis in these neurons. The second part is dedicated to the description of the functional relationship and communication between CSF-cN soma and bud, an enigmatic compartment for which little is known. In the last part, I will present the development and validation of novel transgenic mouse models (chemogenetic and optogenetic models, respectively) that selectively target CSF-cNs. These models are crucial to address *ex-vivo* and potentially *in vivo* the function of CSF-cNs in mammalian CNS.

## A) CALCIUM CHANNELS AND CALCIUM HOMEOSTASIS IN MEDULLO-SPINAL CSF-cNs

### 1. CHARACTERIZATION OF VOLTAGE-GATED CALCIUM CHANNELS IN MEDULLO-SPINAL CSF-cNs

As mentioned in the introduction, voltage-gated $Ca^{2+}$ channels ($Ca_V$s) play a crucial role in $Ca^{2+}$ signaling in neurons as they participate in the modulation of their activity and physiology, as well as in neurotransmission (Simms & Zamponi, 2014). Nevertheless, to date there is little known about $Ca_V$s expression and modulation in CSF-cNs. However, one necessary step to understand CSF-cN role the CNS is to describe their physiology, a study that includes the characterization of $Ca_V$s. Here, I will present the results of electrophysiological studies combined to $Ca^{2+}$ imaging that were carried out on acute brainstem and spinal cord slices from wild-type mice. I will describe the presence of $Ca_V$s, their modulation by metabotropic receptors and the consequences of their activation on intracellular $Ca^{2+}$ signaling.

#### 1.1. Medullo-spinal CSF-cNs express functional voltage-gated $Ca^{2+}$ channels

There is a little information available about the nature of $Ca_V$s expressed in medullo-spinal CSF-cNs. It was previously reported in immature CSF-cNs from spinal cord of neonatal rats that $Ca_V$s mediate the generation of slow depolarizing potentials in these neurons (Marichal *et al.*, 2009). However, there are no data available about the type of $Ca_V$s that CSF-

cNs express neither about their modulation. To determine whether CSF-cNs from the mouse brainstem express $Ca_v$s, voltage-clamp recordings were performed from CSF-cNs (Figure 35. A) showing the characteristic PKD2L1 channel activity (Figure 35. B). The recordings were conducted with an extracellular solution containing tetrodotoxine (TTX, 1 µM), a selective antagonist of sodium channels, and inhibitors of $GABA_A$ and glycine receptors, gabazine and strychnine, respectively. Caesium acetate (CsAc)-based intracellular solution was used to block potassium channels (see Material and methods). $Ca^{2+}$ currents were evoked using classical activation protocol in which 100 ms long depolarizing voltage steps were applied from a holding potential of -70 mV to +30 mV, with +10 mV increasing steps (ΔV = +10 mV; Figure 35. C). Evoked inward $Ca^{2+}$ current of increasing amplitude showed fast activation and reached the peak amplitude of -167.42 ± 68.16 pA at a membrane potential of +12.61 ± 0.70 mV ($n$ = 16). However, large outward current corresponding to $K^+$ current could still be observed in all recordings and "contaminated" the recorded $Ca^{2+}$ current. To confirm that the elicited currents were carried by $Ca^{2+}$ channels and to eliminate the outward potassium current, recordings were repeated in the presence of cadmium ($Cd^{2+}$; 200 µM, pressure application), a selective blocker of all $Ca_v$s (Swandulla & Armstrong, 1989). In control, elicited $Ca^{2+}$ current reached the average peak amplitude of -161.81 ± 86.67 pA ($n$ = 11) and it was completely inhibited in the presence of $Cd^{2+}$ (peak current amplitude: +25.57 ± 47.74 pA; Figure 35. C; $n$ = 11; $P < 0.001$, Wilcoxon matched-pairs signed ranked test). Subtraction of current recorded in the presence of $Cd^{2+}$ from the current recorded in control gives $Cd^{2+}$-sensitive current that corresponds to "pure" $Ca^{2+}$ current (Figure 35. C). The current-voltage relationship (*I-V* curve) was then generated from the $Cd^{2+}$-sensitive current, where peak $Ca^{2+}$ current amplitudes were plotted as a function of the command voltage steps and fitted using Boltzmann function (see Materials and methods). Figure 35. D illustrates the average *I-V* curve for subtracted $Ca^{2+}$ current and show that it activates at membrane potentials more positive than -50 mV, indicating that $Ca_v$s expressed in CSF-cNs belong to high-voltage activated (HVA) $Ca^{2+}$ channels (Catterall, 2011)

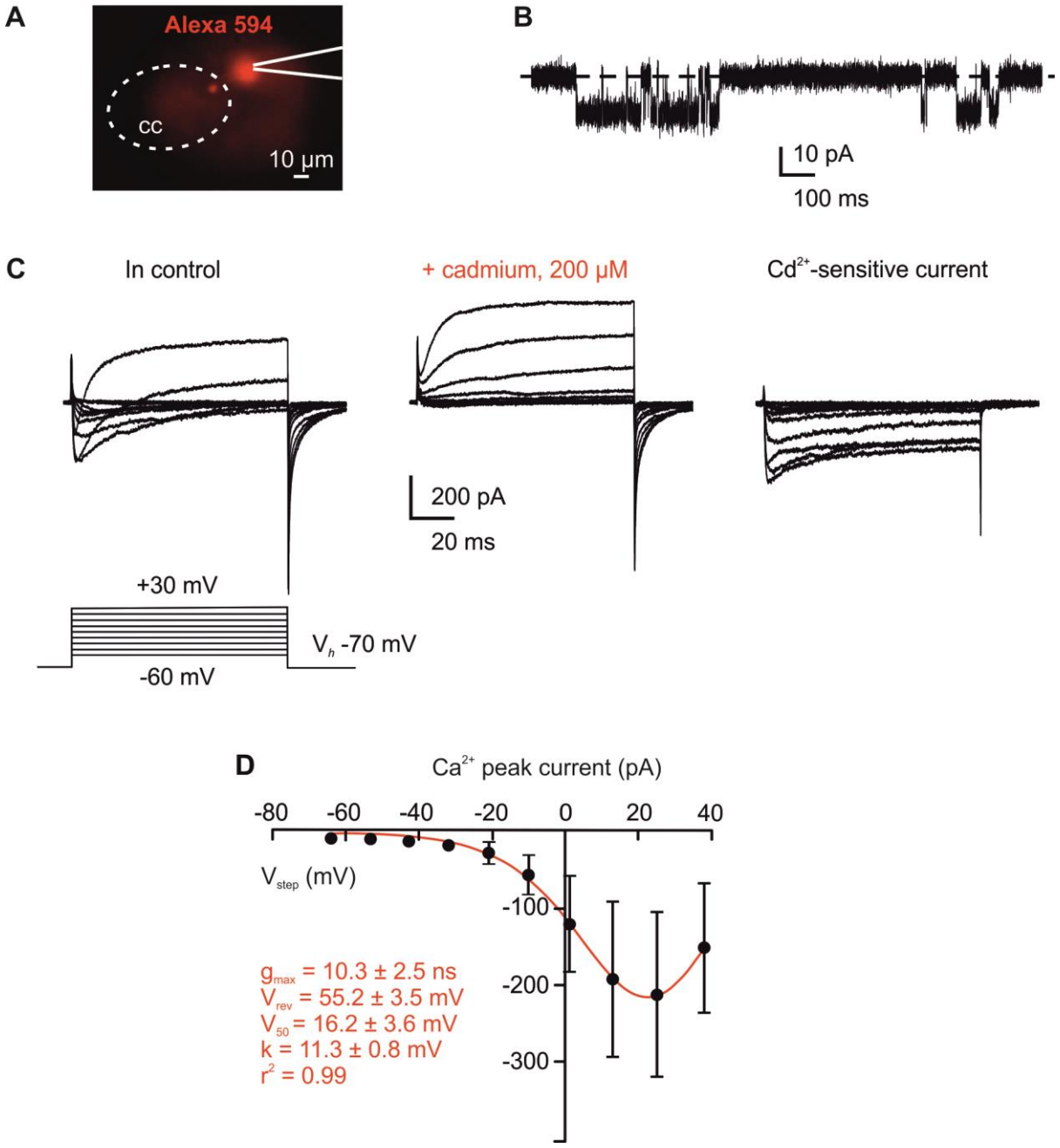


**Figure 35. Voltage-gated $Ca^{2+}$ channels are expressed in CSF-cNs from mouse brainstem.**

**A.** Micrograph shows cell loaded with 10 µM Alexa 594 to confirm the morphology of CSF-cN. White lines indicate the position of the patch pipette. Dashed line delineates the central canal (cc). **B.** Representative voltage-clamp recording from one CSF-cN at a holding potential of -70 mV, showing unitary current carried by PKD2L1 channel. Dashed line represents channel closed state. **C.** Representative whole-cell $Ca^{2+}$ current traces evoked from a holding potential ($V_h$) of -70 mV to +30 mV with +10 mV increments. Activation protocol is illustrated under the current traces. $Cd^{2+}$ sensitive $Ca^{2+}$ current (right trace) is obtained by subtracting current recorded in the presence of 200 µM $Cd^{2+}$ (middle trace) from current recorded in its absence (control; left trace). Note the presence of outward $K^+$ current in the control trace. **D.** Average current-voltage relationship (*I-V* curve) of subtracted $Ca^{2+}$ peak current amplitudes evoked during depolarizing steps to various potentials ($n$ = 16). Data are fitted using a Boltzmann function (red trace, see Materials and methods). The inset in red gives the values

that define the properties of $Ca^{2+}$ current in CSF-cNs obtained from the Boltzmann fit of the average data.

To eliminate large outward $K^+$ current that remained throughout all recordings when using the CsAc-based intracellular solution, tetraethylammonium-Cl (TEA-Cl), another selective inhibitor of $K^+$ channels, was added to both intracellular and extracellular solutions to isolate $Ca^{2+}$ currents (see Materials and methods). In such conditions, currents were evoked using the same activation protocol as illustrated in Figure 35. C, and in all CSF-cNs recorded, outward $K^+$ current was completely inhibited upon membrane depolarization. Elicited inward $Ca^{2+}$ current exhibited fast activation and little inactivation during increasing depolarizing voltage steps (Figure 36. A), it reached maximal amplitude of -129.72 ± 54.91 pA at a membrane potential of +11.60 ± 0.43 mV, and it reversed at +37.84 ± 0.69 mV (Figure 36. B; $n$ = 13). In agreement with recordings of $Ca^{2+}$ currents obtained when using CsAc-based intracellular solution only, pressure application of 200 µM $Cd^{2+}$ completely blocked the elicited current. Peak amplitude of $Ca^{2+}$ current in control was measured at -177.00 ± 38.36 pA and +7.25 ± 21.32 pA in the presence of $Cd^{2+}$ (Figure 36. C; $n$ = 12; $P < 0.01$, Wilcoxon matched-pairs signed ranked test). This confirmed that the observed inward current was carried by $Ca^{2+}$ (Figure 36. C.).

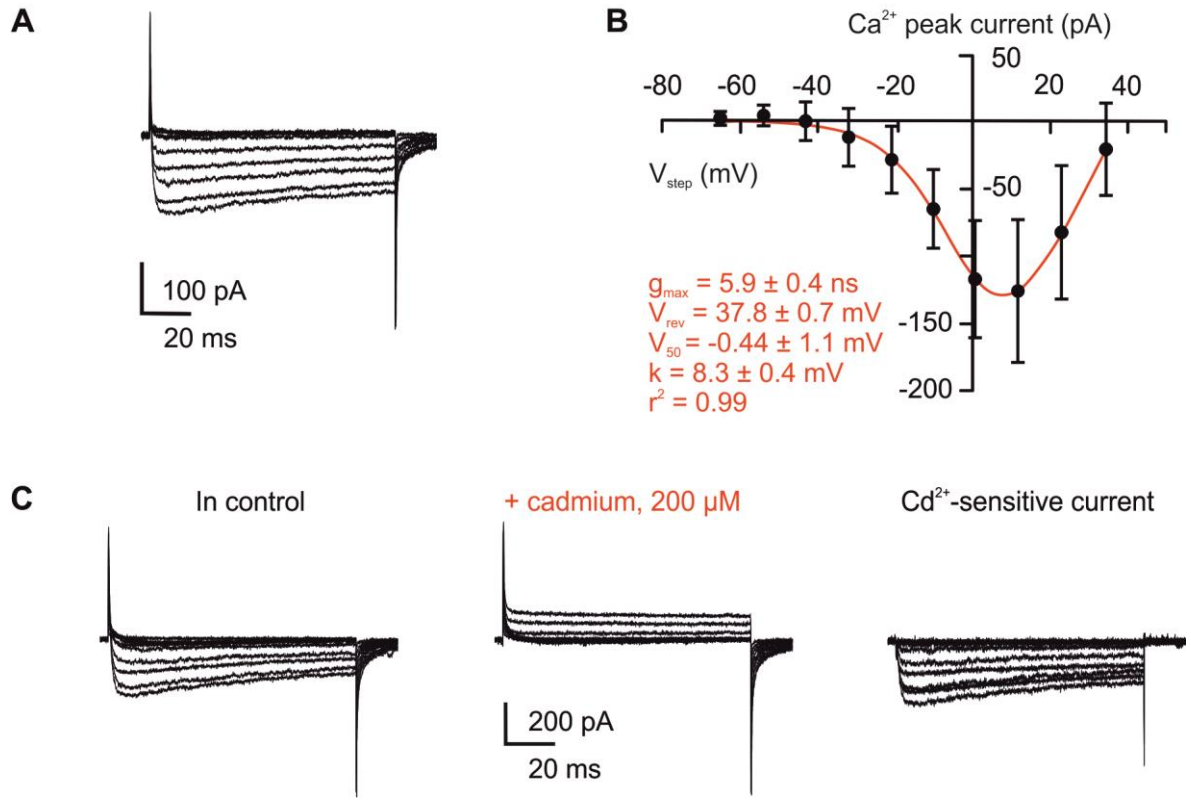


**Figure 36. Isolation of $Ca^{2+}$ current following inhibition of $K^+$ current with TEA-Cl-based solutions.**

**Figure 36. Isolation of $Ca^{2+}$ current following inhibition of $K^+$ current with TEA-Cl-based intracellular solution. A.** Representative $Ca^{2+}$ current trace recorded in voltage-clamp mode from a holding potential of -70 mV to +30 mV with 10 mV increments (voltage protocol is indicated in Figure 35. C), in the presence of 20 mM TEA-Cl in both intracellular and extracellular solutions. Note that outward $K^+$ current is completely inhibited. **B.** Average current-voltage relationship (*I-V* curve) of $Ca^{2+}$ peak current amplitudes elicited during depolarizing steps to various potentials ($n$ = 13). Data are fitted using Boltzmann function (red trace). The inset in red gives the value that define the properties of $Ca^{2+}$ current in CSF-cNs obtained from the Boltzmann fit of the average data. **C.** $Cd^{2+}$ sensitive $Ca^{2+}$ current (right trace) is obtained by subtracting current recorded in the presence of 200 µM $Cd^{2+}$ (middle trace) from current recorded in control (left trace).

The expression of $Ca_v$s was further investigated in spinal CSF-cNs using intracellular and extracellular solutions supplemented with TEA-Cl. Spinal CSF-cNs (Figure 37. A) were depolarized using the same protocol as described before to elicit $Ca^{2+}$ currents. The recorded current exhibited properties characteristic to $Ca^{2+}$ current with fast activation and intermediate inactivation (Figure 37. B). As shown on the average *I-V* curve generated from experimental data (Figure 37. C; $n$ = 9), the current started to activate at potentials more depolarized than -40 mV, it reached a maximum peak amplitude of -283.36 ± 100.66 pA at a membrane potential of +10.10 ± 2.97 mV and it reversed at +46.82 ± 1.29 mV (Figure 37. C, $n$ = 9). It should be noted that $Ca^{2+}$ currents recorded from spinal CSF-cNs presented larger peak amplitude compared to the currents recorded from medullar CSF-cNs (see above; $P < 0.001$, Mann-Whitney test).

Taken together, these results demonstrate that medullo-spinal CSF-cNs express functional voltage-gated $Ca^{2+}$ channels activated by membrane depolarization. These channels show properties of HVA $Ca_v$s and are strongly and selectively inhibited by cadmium, indicating that evoked inward current is indeed carried by $Ca^{2+}$.

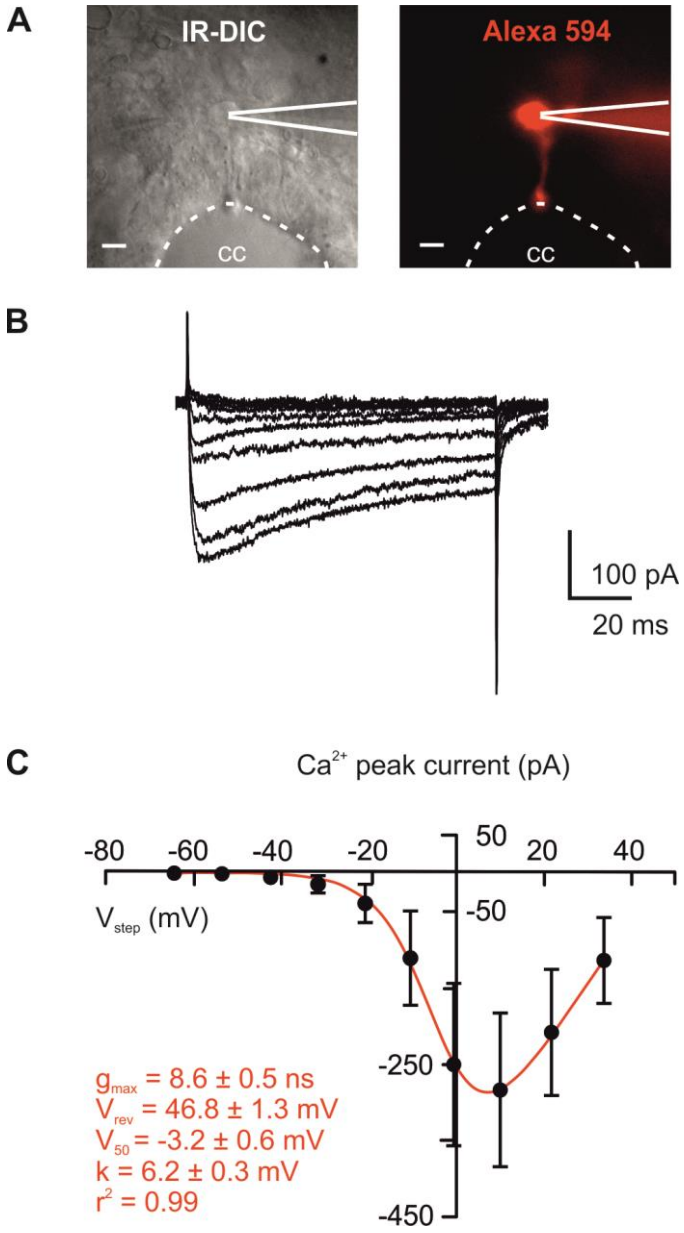


**Figure 37. Voltage-gated $Ca^{2+}$ channels are present in spinal CSF-cNs.**

**A.** Micrographs show one spinal CSF-cN illuminated with IR-DIC (left) and dialyzed with 10 µM Alexa 594 (right) to confirm its morphology. Dashed lines indicate central canal (cc). Scale bare = 10 µm. **B.** Representative $Ca^{2+}$ current trace recorded in voltage-clamp mode following the activation protocol presented in Figure 36. C. **C.** Average current-voltage relationship (*I-V* curve) of $Ca^{2+}$ peak current amplitudes evoked during depolarizing steps to various potentials ($n$ = 9). Data are fitted using Boltzmann function (red trace, see Materials and methods). The inset in red gives the values that define the properties of $Ca^{2+}$ current in CSF-cNs obtained from the Boltzmann fit of the average data.

### 1.2. N-type $Ca^{2+}$ channels represent the main $Ca^{2+}$ channel subtype expressed in CSF-cNs

$Ca_v$s have been divided into three main families that consist of ten members. Pharmacological approach was shown to be the most reliable tool to separate different types of $Ca_v$s (Catterall, 2011). To determine the nature of $Ca_v$s in medullar CSF-cNs, voltage-clamp recordings were carried out in the presence of selective pharmacological inhibitors of the main $Ca_v$s subtypes. However, to describe the inhibitory effect of a given toxin and to avoid over-estimation of current inhibition, it was necessary to determine the stability of $Ca^{2+}$ current amplitude during repeated activations of $Ca_v$s over time. Therefore, intracellular solution supplemented with 10 mM EGTA was used to strongly buffer intracellular $Ca^{2+}$ concentration. Inward $Ca^{2+}$ current was elicited every 20 s with 100 ms long depolarizing pulses from a holding potential of -70 mV to +10 mV, where the maximum of $Ca_v$s are activated and the largest peak current amplitude is seen. Over 10 min of recording, $Ca^{2+}$ peak current amplitude decreased by 26.34 ± 5.48 % (peak current amplitudes: -201.12 ± 1.69 pA during the first minute and –147.59 ± 3.26 pA during the last minute of recording; data not shown; $n$ = 3). To test whether such current rundown over time may be the result of insufficient buffering of intracellular $Ca^{2+}$ in the presence of EGTA, recordings were repeated with an intracellular solution containing 10 mM BAPTA. While voltage activation step remained the same as previously described, duration between depolarizations was increased to 30 s. Since BAPTA is faster $Ca^{2+}$ chelator than EGTA, current was expected to show less rundown and to remain relatively constant due to rapid buffering of intracellular $Ca^{2+}$ with BAPTA. However, even in the presence of BAPTA, $Ca^{2+}$ current still showed rundown by 9.59 ± 5.30 % as peak current amplitude measured during the first minute of recording decreased from -216.72 ± 39.39 pA to -195.73 ± 32.34 pA at the end of recoding (data not shown; $n$ = 4). Considering that current rundown in the presence of BAPTA is not statistically different from the current rundown in the presence of EGTA ($P$ = 0.06; Mann-Whitney test), recordings were continued with the intracellular solution containing EGTA.

After establishing the stability of $Ca^{2+}$ current amplitude (or its rundown), the effect of selective $Ca^{2+}$ channel blockers was tested on $Ca^{2+}$ currents from medullar CSF-cNs. In this study, the effects of 500 nM ω-conotoxin GVIA (N-type $Ca^{2+}$ channels inhibitor), 500 nM ω-agatoxin IVA (P/Q-type $Ca^{2+}$ channels inhibitor) and 1 µM nifedipine (L-type $Ca^{2+}$ channels inhibitor) were investigated. To prevent $Ca^{2+}$ current rundown as much as possible, $Ca^{2+}$ current was elicited with depolarizing steps every 30 s from a holding potential of -70 mV to

+10 mV over 10 min. Pressure application of ω-conotoxin GVIA for 5 min resulted in strong and irreversible reduction of $Ca^{2+}$ current amplitude (peak currents amplitude: -141.71 ± 19.59 pA in control and -52.57 ± 28.14 pA in the presence of ω-conotoxin GVIA; Figure 38. A; $n$ = 7; $P$ < 0.05, Wilcoxon matched-pairs signed ranked test). In contrast, pressure application of ω-agatoxin IVA for 5 min induced small inhibition of evoked $Ca^{2+}$ current. The average peak current amplitude of -162.64 ± 75.60 pA in control was reduced to -144.00 ± 60.84 pA in the presence of ω-agatoxin IVA (Figure 38. B; $n$ = 11; $P$ < 0.01, Wilcoxon matched-pairs signed ranked test). Similar extent of current inhibition was observed in the presence of nifedipine, as it induced a small decrease in $Ca^{2+}$ current amplitude (peak currents amplitude: -123.17 ± 49.39 pA in control and -97.33 ± 29.37 pA in the presence of nifedipine; Figure 38. C; $n$ = 6; $P$ < 0.05, Wilcoxon matched-pairs signed ranked test). The rundown of $Ca^{2+}$ current in control was taken into account when measuring the inhibitory effect for each toxin (red line in Figure 38. A-E). Taking into the consideration that ω-conotoxin GVIA induced the largest inhibition of whole-cell $Ca^{2+}$ currents in medullar CSF-cNs, its inhibitory effect on $Ca^{2+}$ currents recorded from spinal CSF-cNs was tested using the same protocol with an intracellular solution containing 10 mM BAPTA. $Ca^{2+}$ current evoked during 10 min exhibited an average peak amplitude of -264.78 ± 65.03 pA that was reduced by 24.21 ± 11.57% in the presence of ω-conotoxin GVIA (peak current amplitude: -203.43 ± 67.62 pA, data not shown, $n$ = 7). The smaller extent of current inhibition by ω-conotoxin GVIA in spinal CSF-cN may indicate that N-type $Ca^{2+}$ channels do not represent the majority of $Ca_V$s, although the presence of BAPTA instead of EGTA in the intracellular solution should be considered.

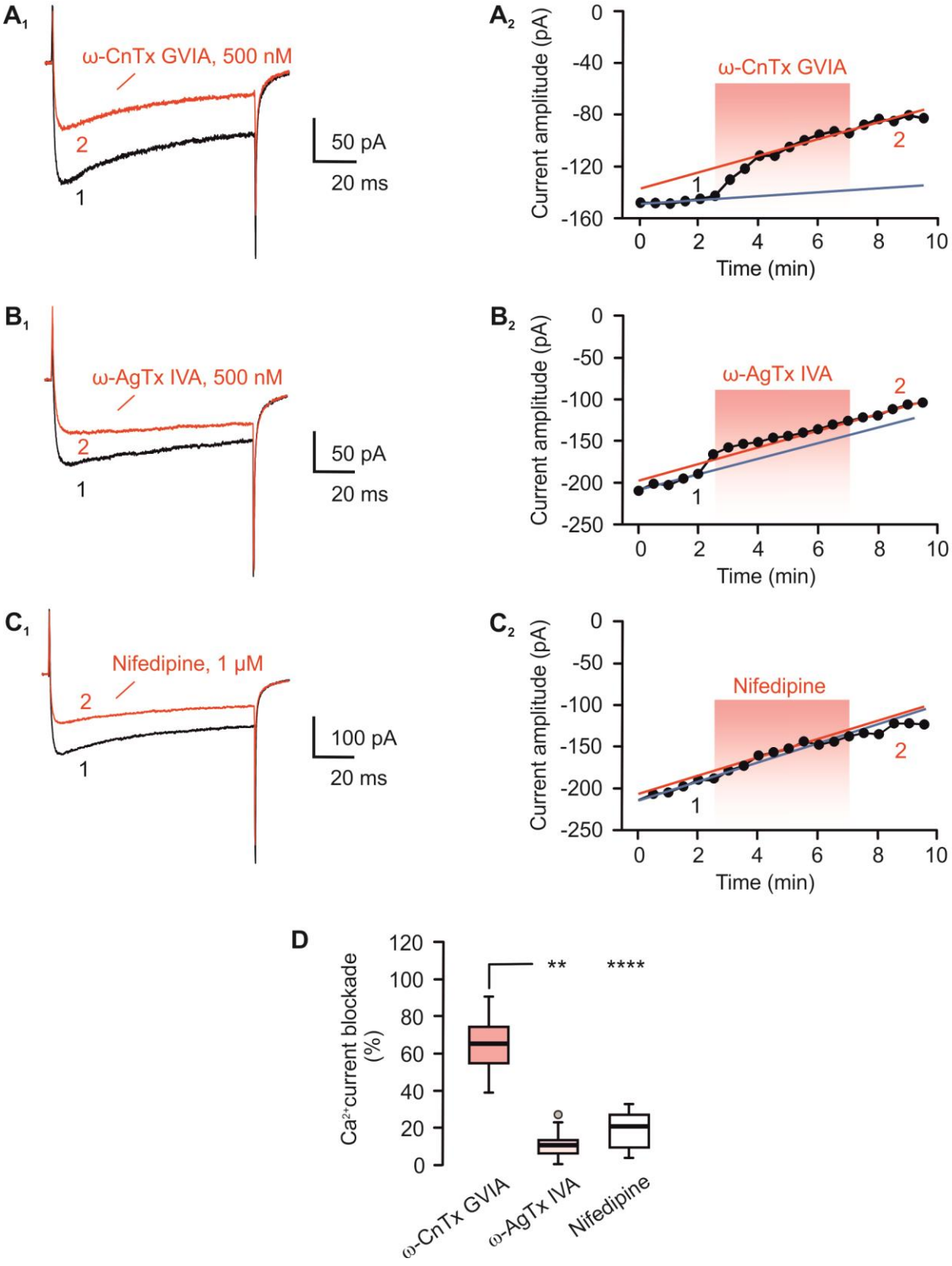


**Figure 38. Medullar CSF-cNs express mainly N-type $Ca^{2+}$ channels.**

**A–C.** The effect of different toxins on $Ca^{2+}$ current was monitored over time. Representative $Ca^{2+}$ current traces from CSF-cNs recorded in control (**$A_1$**, **$B_1$**, **$C_1$**, black traces, 1) and in the presence of ω-conotoxin GVIA (**$A_1$**, ω-CnTx GVIA, red trace, 2), ω-agatoxin IVA (**$B_1$**, ω-AgTx GVIA, red trace, 2), or nifedipine (**$C_1$**, red trace, 2) during time period of 10 min. Time courses of $Ca^{2+}$ peak current amplitude for recordings presented in **$A_1$**, **$B_1$** and **$C_1$** (black circles) are presented in **$A_2$** for ω-conotoxin

GVIA, **$B_2$** for ω-agatoxin IVA and **$C_2$** for nifedipine. Toxins were applied by pressure for 5 min as indicated by red bar. Blue regression line is fitted from data points taken in control (1), while red regression line is fitted from data points at the end of recording, where maximum of current inhibition is seen (2). **D.** Summary box-and-whiskers plots of the averaged percentage of $Ca^{2+}$ current blockade in the presence of ω-conotoxin GVIA (red box; 64.2 ± 6.5%; *n* = 7), ω-agatoxin IVA (light red box; 10.7 ± 2.4%; *n* = 11), and nifedipine (white box; 16.7 ± 4.2%; *n* = 6). $Ca^{2+}$ current sensitivity to ω-conotoxin GVIA is significantly higher compared to its sensitivity to ω-agatoxin IVA and nifedipine (**$P$ < 0.01, ****$P$ < 0.0001; Kruskal-Wallis/Dunn's *post hoc* multiple comparison test).

In summary, our results demonstrate that medullar CSF-cNs express mainly N-type $Ca^{2+}$ channels ($Ca_v2.2$), since pressure application of ω-conotoxin GVIA induced the largest inhibition of whole-cell $Ca^{2+}$ currents. Spinal CSF-cNs are less sensitive to inhibitory effect of ω-conotoxin GVIA, although those recordings were performed in different experimental conditions. Moreover, the inhibition of medullar $Ca^{2+}$ currents in CSF-cNs by ω-agatoxin IVA and nifedipine suggest that these neurons also express P/Q-type ($Ca_v2.1$) and L-type ($Ca_v1$) $Ca^{2+}$ channels.

## 2. MODULATION OF VOLTAGE-GATED $Ca^{2+}$ CHANNELS IN MEDULLO-SPINAL CSF-cNs

The activity of $Ca_v$s is precisely regulated in order to prevent excessive $Ca^{2+}$ entry upon their activation and intracellular $Ca^{2+}$ rise, and to maintain physiological concentrations of intracellular $Ca^{2+}$. One important actor in such regulation are G proteins activated by G protein-coupled receptors (GPCRs). Here, I looked for G protein-mediated regulation of $Ca_v$s in medullo-spinal CSF-cNs. I determined the presence of metabotropic GPCRs, $GABA_B$ and muscarinic receptors, and tested the mechanism of action of these receptors on $Ca^{2+}$ currents expressed in CSF-cNs by using electrophysiological approach together with pharmacological tools in acute brainstem and spinal cord slices obtained from adult wild-type mice.

### 2.1. CSF-cNs express functional metabotropic $GABA_B$ receptors that mainly inhibit N-type $Ca^{2+}$ channels mediated by a Gβγ mechanism

Metabotropic $GABA_B$ receptors that couple to G proteins are well described as modulators of $Ca^{2+}$ channels at pre- and postsynaptic levels (Bettler *et al.*, 2004). In our recent publication, we have presented the results of immunohistochemical study showing that

medullar CSF-cNs in the adult mouse express the $GABA_{B1}$ subunit of $GABA_B$ receptors (Jurčić *et al.*, 2019). This observation is in agreement with the study carried out on the rat spinal cord, where cells with typical morphology of CSF-cNs show strong labeling for the same receptor subunit (Margeta-Mitrovic *et al.*, 1999). To test whether the activation of $GABA_B$ receptors expressed in medullo-spinal CSF-cNs modulate the activity of $Ca_V$s, $Ca^{2+}$ current was evoked following single depolarizing step from a holding potential of -70 mV to +10 mV in control and in the presence of baclofen, a selective agonist of $GABA_B$ receptors, and peak current amplitude was monitored over 10 min of recording. As shown in Figures 39. A and B, baclofen application (100 µM) induced rapid and strong inhibition of $Ca^{2+}$ current in medullar CSF-cNs that persisted during the depolarizing voltage step (peak current amplitudes: -159.48 ± 87.06 pA in control and -88.78 ± 69.16 pA in baclofen; Figure 39. C and D; $n$ = 13; $P < 0.001$, Wilcoxon matched-pairs signed ranked test). Current inhibition induced by baclofen application reversed slowly upon wash out of baclofen, while it was strongly reduced in the presence of 2 µM CGP, a selective $GABA_B$ antagonist (peak current amplitudes: -172.56 ± 66.74 pA in CGP and -154.65 ± 72.62 pA in CGP with baclofen; Figures 39. A-D; $n$ = 14; $P$ = 0.0557, Wilcoxon matched-pairs signed ranked test). Similar results were observed in spinal CSF-cNs, where baclofen application induced a reduction of the $Ca^{2+}$ current amplitude (peak current amplitudes: -272.66 ± 67.38 pA in control and -183.31 ± 70.63 pA in the presence of baclofen; Figure 40. A-D; $n$ = 7; $P$ = 0.0156, Wilcoxon matched-pairs signed ranked test). However, current recorded from spinal CSF-cNs in control showed faster rate of recovery upon wash out of baclofen compared to $Ca^{2+}$ current recorded from medullar CSF-cNs (Figure 40. A, B). Baclofen-induced current inhibition was almost completely reversed in the presence of CGP (peak current amplitudes: -251.95 ± 100.56 pA in CGP alone and -243.09 ± 106.30 pA in CGP with baclofen; Figure 40. A-D; $n$ = 5; $P$ = 0.0625, Wilcoxon matched-pairs signed ranked test), the effect that was also seen in recordings obtained from medullar CSF-cNs.

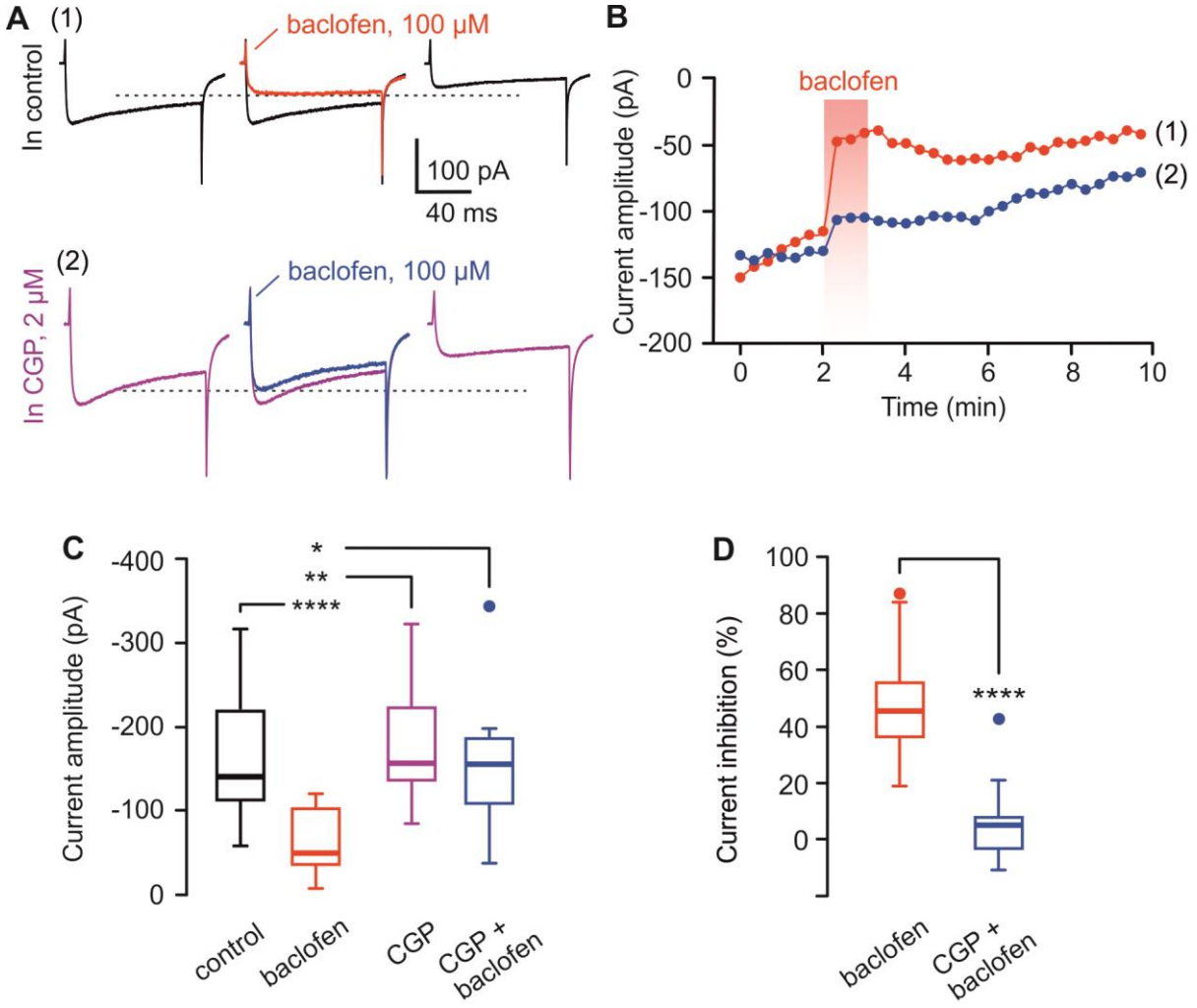


**Figure 39. $Ca^{2+}$ channels in medullar CSF-cNs are modulated by $GABA_B$ receptors.**

**A.** Representative $Ca^{2+}$ current traces elicited from a holding potential of -70 mV to +10 mV in two different medullar CSF-cNs recorded in control (top, 1, black traces) or in the presence of 2 µM CGP (bottom, 1, purple traces), and in the presence of 100 µM baclofen alone (top, 1, red trace) or with CGP (bottom, 2, blue trace). **B.** Time course of $Ca^{2+}$ peak current amplitude for the recordings in **A**, in the absence (red circles) and presence (blue circles) of CGP. Red bar indicates baclofen pressure application (1 min). **C.** Summary box-and-whiskers plots for averaged $Ca^{2+}$ current amplitude in the absence of CGP before (black box) and during (red box) baclofen application, and in the presence of CGP before (purple box) and during (blue box) baclofen application (see text for details; $^{****}P < 0.0001$, $^{**}P < 0.01$, $^{*}P < 0.05$, ANOVA.lme/Dunn's *post hoc* multiple comparison test). **D.** Summary box-and-whiskers plots for the $Ca^{2+}$ current inhibition mediated by baclofen in the absence (red box) and presence of CGP (blue box). Baclofen alone significantly inhibited $Ca^{2+}$ current amplitude, while this inhibitory effect was abolished in the presence of CGP (baclofen: 49 ± 6%, $n = 13$; baclofen in CGP: 7 ± 4%, $n = 14$; $^{****}P < 0.0001$, Mann-Whitney test).

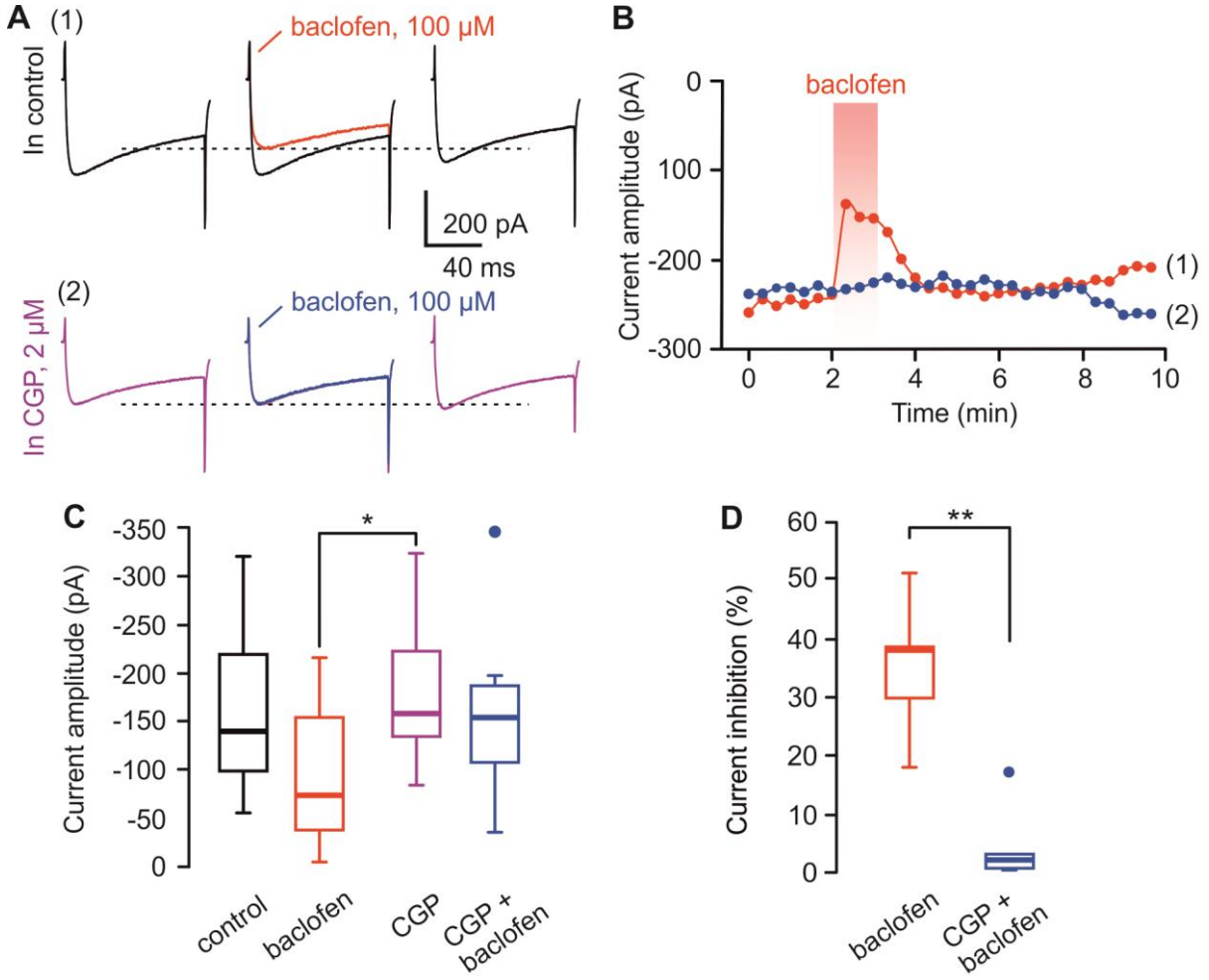


**Figure 40. $Ca^{2+}$ channels in spinal CSF-cNs undergo inhibition mediated by $GABA_B$ receptors activation.**

**A.** Representative $Ca^{2+}$ current traces elicited from a holding potential of -70 mV to +10 mV in two different spinal CSF-cNs recorded in control (top, 1, black traces) or in the presence of 2 µM CGP (bottom, 1, violet traces), and in the presence of 100 µM baclofen alone (top, 1, red trace) or with CGP (bottom, 2, blue trace). **B.** Time course of $Ca^{2+}$ peak current amplitude for the recordings in A, in the absence (red circles) and presence (blue circles) of CGP. Red bar indicates baclofen pressure application (1 min). **C.** Summary box-and-whiskers plots for averaged $Ca^{2+}$ current amplitude in the absence of CGP before (black box) and during (red box) baclofen application, and in the presence of CGP before (purple box) and during (blue box) baclofen application (see text for details; $*P < 0.05$, ANOVA.lme/Dunn's *post hoc* multiple comparison test). **D.** Summary box-and-whiskers plots for the $Ca^{2+}$ current inhibition mediated by baclofen in the absence (red box) and presence of CGP (blue box). Baclofen significantly inhibited $Ca^{2+}$ current amplitude and its inhibitory effect was abolished in the presence of CGP (baclofen: 35 ± 10%, $n = 7$; baclofen in CGP: 5 ± 6%, $n = 5$; $**P < 0.01$, Mann-Whitney test).

It has been previously reported that N- and P/Q-type $Ca^{2+}$ channels involved in neurotransmitter release are mainly susceptible to $GABA_B$ receptor modulation (Bettler *et al.*,

2004). As I have shown, CSF-cNs express mainly N-type $Ca^{2+}$ channels ($Ca_v2.2$). Therefore, I tested whether this type of $Ca^{2+}$ channels undergoes modulation by $GABA_B$ receptors in medullo-spinal CSF-cNs. ω-conotoxin GVIA (500 nM) was pressure applied for 5 min to inhibit N-type $Ca^{2+}$ channels, followed by baclofen application (100 µM) together with ω-conotoxin GVIA (500 nM) for 1 min to activate $GABA_B$ receptors. In medullar CSF-cNs, application of ω-conotoxin GVIA alone reduced peak $Ca^{2+}$ current amplitude by 30.67 ± 10.65% (peak current amplitude: -123.52 ± 60.64 pA in control; -81.84 ± 33.25 pA in ω-conotoxin GVIA; Figure 41. A, B; $n$ = 4, $P$ = 0.0650, Paired t-test). When baclofen was added to ω-conotoxin GVIA, $Ca^{2+}$ current amplitude was further reduced by 19.19 ± 16.74 % (peak current amplitude: -33.44 ± 20.87 pA in ω-conotoxin GVIA with baclofen; Figure 41. A, B; $n$ = 4, $P$ = 0.3367 for ω-conotoxin GVIA alone compared to ω-conotoxin GVIA with baclofen, Mann-Whitney test). Similar pattern of inhibition was seen when $Ca^{2+}$ currents were recorded from spinal CSF-cNs. There, ω-conotoxin GVIA alone reduced peak $Ca^{2+}$ current amplitude by 39.65 ± 17.91% (peak current amplitude: -264.78 ± 65.03 pA in control; -162.99 ± 73.11 pA in ω-conotoxin GVIA; data not shown; $n$ = 7; $P > 0.05$, Friedman test/Dunn's post hoc multiple comparison test). Addition of baclofen to ω-conotoxin GVIA finally reduced peak current amplitude by 36.44 ± 23.95% (peak current amplitude: -113.10 ± 81.25 pA in ω-conotoxin GVIA with baclofen; data not shown; $n$ = 7; $P > 0.05$ for ω-conotoxin GVIA alone compared to ω-conotoxin GVIA with baclofen, Friedman test/Dunn's post hoc multiple comparison test). However, in both brainstem and spinal cord CSF-cNs, baclofen together with ω-conotoxin GVIA did not completely inhibit whole-cell $Ca^{2+}$ currents, indicating the presence of ω-conotoxin GVIA-resistant $Ca^{2+}$ channels that are inhibited by the activation of $GABA_B$ receptors in CSF-cNs.

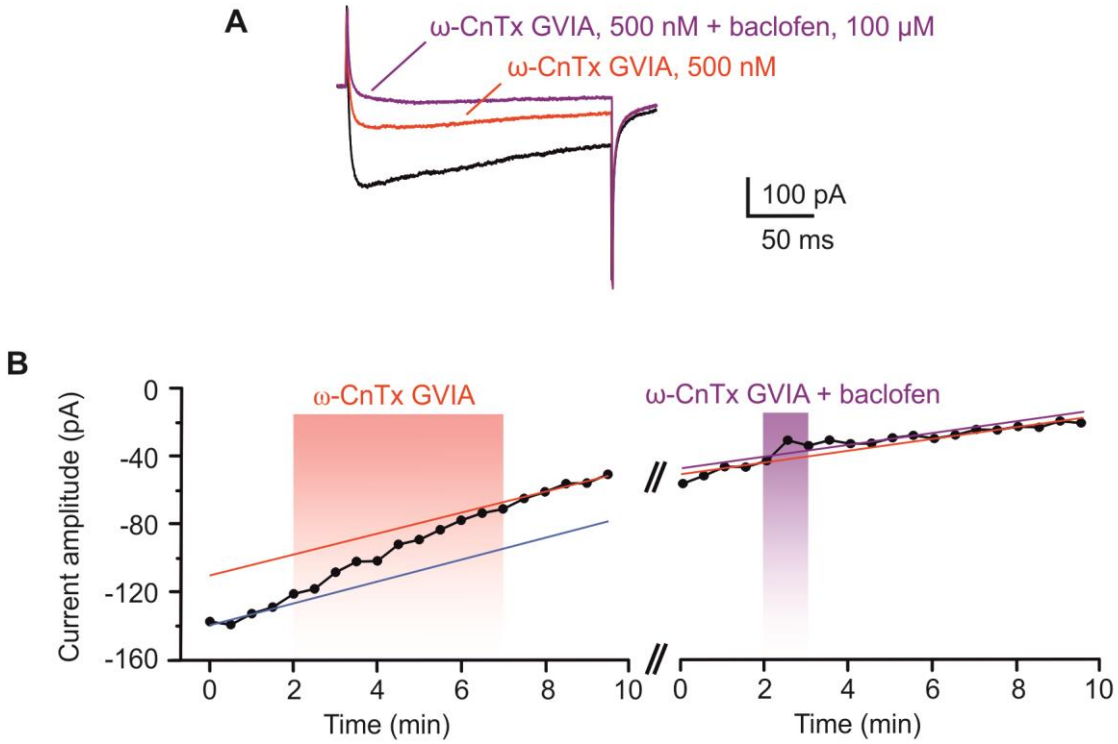


**Figure 41. Activation of $GABA_B$ receptors inhibits mainly N-type voltage-gated $Ca^{2+}$ channels.**

**A.** Representative peak $Ca^{2+}$ currents traces elicited with a voltage step to +10 mV from a holding potential of -70 mV recorded from one CSF-cN in control (black trace), in the presence of 500 nM ω-conotoxin GVIA alone (ω-CnTx, red trace) and with 100 µM baclofen (purple trace). **B.** Time course of $Ca^{2+}$ peak current amplitude for the recording in A. ω-conotoxin GVIA alone was applied by pressure for 5 min (red bar) for current that was recorded during 10 min. Another recording of 10 min was initialized 2 min after the end of the first one (//), when ω-conotoxin GVIA was applied by pressure together with baclofen for 1 min (purple box). Inhibition of $Ca^{2+}$ current by toxins was measured from regression lines which were fitted from data points before toxin application (blue line), from data points at the end of recording for ω-conotoxin GVIA (red line) and from data points at the time of simultaneous pressure application of ω-conotoxin GVIA with baclofen (violet line) where the maximum of current inhibition is seen.

Activation of $GABA_B$ receptors that couple to $G_{i/o}$ type of G proteins leads to direct binding of Gβγ subunits to $Ca_v$s (Bettler *et al.*, 2004), mediating their strong inhibition. This inhibition shows voltage dependence as it can be greatly relieved by strong depolarization (Ikeda, 1991, 1996). To determine if such mechanism of $Ca_v$s inhibition by $GABA_B$ receptors activation is seen in medullo-spinal CSF-cNs, triple pulse protocol was used to activate $Ca_v$s and potentially reduce the inhibition mediated by $GABA_B$ receptors (see Materials and methods). $Ca^{2+}$ current was elicited with a depolarizing step to +10 mV from a holding potential of -70 mV before (prepulse) and after (postpulse) introducing high depolarizing step to +100 mV. In medullar CSF-cNs, $Ca^{2+}$ current evoked by prepulse in control had average

peak current amplitude of -176.83 ± 99.62 pA, and similar current amplitude of -149.43 ± 65.48 pA was elicited by postpulse (Figure 42. A, C, D; $n$ = 9; $P$ = 0.3719 for prepulse amplitude compared to postpulse amplitude in control, ANOVA.lme/Dunn's *post hoc* multiple comparison test). The pre/postpulse ratio was around 95% (Figure 42. F; $n$ = 9). Application of baclofen induced strong reduction of $Ca^{2+}$ currents elicited by the prepulse when compared to control (-61.76 ± 44.41 pA, Figure 42. A, C, E; $n$ = 9; $P$ < 0.0001 when compared to control; ANOVA.lme/Dunn's *post hoc* multiple comparison test) with according reduction in the pre/postulse ratio by around 40% compared to the control situation (Figure 42. F; $n$ = 9). This baclofen-mediated inhibition of $Ca^{2+}$ current was potently reduced by postpulse following the depolarization to +100 mV (-114.66 ± 63.99 pA; Figure 42. A, D, E; $n$ = 9; $P$ < 0.01 when compared to prepulse; ANOVA.lme/Dunn's *post hoc* multiple comparison test). Note that peak $Ca^{2+}$ current recorded in the presence of baclofen for the postpulse reached similar amplitude as seen for postpulse recordings in control ($n$ = 9; $P$ = 0.078 when compared to control; ANOVA.lme/Dunn's *post hoc* multiple comparison test in postpulse). In the presence of CGP, $Ca^{2+}$ current elicited by prepulse had an average peak current amplitude of -179.59 ± 72.86 pA, while current elicited by postpulse exhibited the average peak current amplitude of -154.22 ± 60.94 pA (Figure 42. B-D, $n$ = 9; $P$ = 0.8596 for the prepulse compared to postpulse, ANOVA.lme/Dunn's *post hoc* multiple comparison test). Therefore, the extent of $Ca^{2+}$ current inhibition mediated by baclofen is strongly diminished for both prepulse and postpulse in the presence of CGP (-166.84 ± 79.71 pA for the prepulse and -144.32 ± 59.82 pA for the postpulse, Figure 42. B-E, $n$ = 9; $P$ = 0.8848 for the prepulse compared to postpulse, ANOVA.lme/Dunn's *post hoc* multiple comparison test). When CGP was present alone or with baclofen, the pre/postpulse ratio was similar to that observed in control and it was close to 100% (Figure 42. F; $n$ = 9). Note that the amplitude of $Ca^{2+}$ current in the presence of baclofen in CGP is similar to that observed in CGP in the absence of baclofen for prepulse ($P$ = 0.9835) and postpulse ($P$ = 0.9900; $n$ = 10; ANOVA.lme/Dunn's *post hoc* multiple comparison test).

Similar mechanism of baclofen-mediated inhibition is seen in spinal CSF-cNs. There, the average $Ca^{2+}$ peak current amplitude of -272.88 ± 67.69 pA evoked by prepulse was reduced to -181.66 ± 71.51 pA when evoked by prepulse in the presence of baclofen (data not shown; $n$ = 7; $P$ < 0.05 for prepulse amplitude in control compared to prepulse amplitude in baclofen, ANOVA.lme/Dunn's *post hoc* multiple comparison test). Strong depolarization to +100 mV reduced the inhibitory effect of baclofen on $Ca^{2+}$ current evoked by postpulse (peak

current amplitude: -143.42 ± 39.39 for a postpulse in control; -118.29 ± 37.90 pA for a postpulse in baclofen; $n$ = 7; $P$ = 0.8577, ANOVA.lme/Dunn's *post hoc* multiple comparison test). In control, the pre/post ratio was 194.08 ± 29.10% (data not shown; $n$ = 7), while in the baclofen it was around 155.62 ± 38.23% (data not shown; $n$ = 7; $P < 0.001$, Paired t-test). In the presence of CGP, inhibition of $Ca^{2+}$ current by baclofen was strongly diminished. The average $Ca^{2+}$ peak current amplitude of -251.95 ± 100.56 pA evoked by prepulse in CGP was similar to the average current amplitude evoked by prepulse in the presence of baclofen (-243.09 ± 106.30 pA in the presence of baclofen; data not shown; $n$ = 5; $P$ = 0.9983 for prepulse amplitude in the absence of baclofen in CGP compared to prepulse amplitude in the presence of baclofen in CGP, ANOVA.lme/Dunn's *post hoc* multiple comparison test). $Ca^{2+}$ currents evoked by postpulse in the absence and presence of baclofen in CGP did not show significant difference (peak current amplitude: -141.26 ± 41.64 for postpulse amplitude in CGP; -133.50 ± 41.03 pA for postpulse amplitude in CGP in the presence of baclofen; data not shown; $n$ = 5; $P$ = 0.9988 for the pospulse amplitude in the absence compared to postpulse amplitude in the presence of baclofen in CGP, ANOVA.lme/Dunn's *post hoc* multiple comparison test). In the presence of CGP alone, the pre/postpulse ratio was 178.06 ± 46.47% (data not shown; $n$ = 7), and it was similar to that measured in the presence of baclofen (181.18 ± 56.79%; data not shown; $n$ = 7; $P$ = 0.599, Paired t-test).

Taken together, these results indicate that medullo-spinal CSF-cNs express functional metabotropic $GABA_B$ receptors activated by baclofen. I show that inhibitory effect of baclofen can be strongly reduced in the presence of selective $GABA_B$ antagonist CGP. Further analysis demonstrated that mainly $Ca^{2+}$ channels of N-type are subjected to inhibition mediated by $GABA_B$ receptors. Moreover, I show that the activation of $GABA_B$ receptors by baclofen inhibits $Ca^{2+}$ currents in medullo-spinal CSF-cNs through direct binding of Gβγ subunits of $G_{i/o}$ proteins to $Ca^{2+}$ channels. $Ca^{2+}$ current inhibition by baclofen is reduced in the presence of CGP. More important, the inhibition mediated by Gβγ subunits is voltage-dependent and it can be relieved by strong depolarization, following classical triple-pulse protocol.

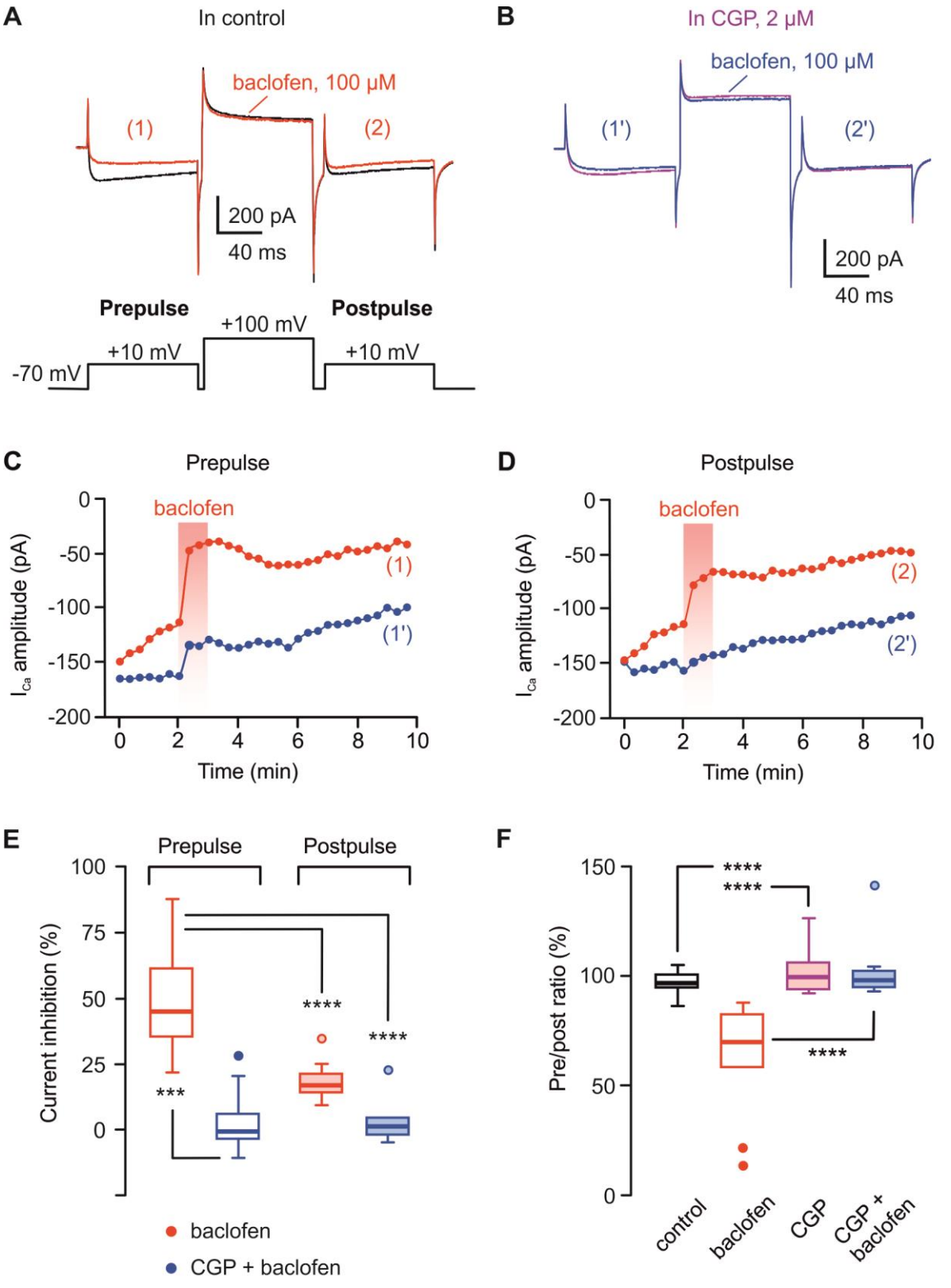


**Figure 42. Activation of $GABA_B$ receptors inhibits $Ca^{2+}$ currents through Gβγ-mediated mechanism.**

**A.** Representative $Ca^{2+}$ current traces recorded from CSF-cNs in control, in response to triple pulse protocol where a depolarizing step to +100 mV (50 ms) is inserted between two voltage steps from a

holding potential of -70 mV to +10 mV (50 ms). The protocol is illustrated under the current trace, where prepulse indicates the voltage step before the depolarization to +100 mV, and postpulse indicates the voltage step after the strong depolarization. $Ca^{2+}$ current traces elicited by prepulse (1) and postpulse (2) are recorded in control (black trace) and in the presence of 100 µM baclofen (red trace). **B.** Representative $Ca^{2+}$ current traces recorded from CSF-cNs in presence of 2 µM CGP, in response to triple pulse protocol as indicated in A**.** $Ca^{2+}$ current traces elicited in prepulse (1') and postpulse (2') are recorded in CGP in the absence (violet trace), and in the presence of baclofen (blue trace). **C.** Time course of $Ca^{2+}$ peak current amplitude for the current traces illustrated in A and B. Baclofen is applied by pressure for 1 min (red box) when $Ca^{2+}$ current is recorded for prepulse in the absence (1, red circles) and presence (1', blue circles) of CGP. **D.** Time course of $Ca^{2+}$ peak current amplitude for the current traces illustrated in A and B. Baclofen is applied by pressure for 1 min (red box) when $Ca^{2+}$ current is elicited by postpulse in the absence (2, red circles) and presence (2', blue circles) of CGP. **C.** Summary box-and-whiskers plots for the averaged percentage of $Ca^{2+}$ current inhibition mediated by baclofen in the absence (red boxes) and presence of CGP (blue boxes) for currents evoked by prepulse (open boxes) and postpulse (closed boxes). In the absence of CGP, baclofen significantly inhibited $Ca^{2+}$ current evoked by prepulse compared to postpulse (52 ± 24% for the prepulse and 19 ± 8% for the postpulse; $n$ = 9). The inhibitory effect of baclofen was strongly reduced in the presence of CGP and the inhibition of current did not differ between prepulse and postpulse (4 ± 12% for the prepulse and 3 ± 7% for the postpulse; $n$ = 10; ****$P$ < 0.0001, ***$P$ < 0.001; ANOVA.lme/Dunn's *post hoc* multiple comparison test). **F.** Summary box-and-whiskers plots for the prepulse/postpulse ratio recorded in control (black box), in baclofen (red box), in CGP alone (violet box) and with baclofen (blue box). The prepulse/postpulse ratio was strongly reduced in the presence of baclofen alone (control: 98 ± 6%, baclofen: 62 ± 27%; $n$ = 9). In the presence of CGP, baclofen failed to reduce the prepulse/postpulse ratio (CGP: 102 ± 11%, baclofen in CGP: 103 ± 14%; n =10; $P$ = 0.999). The prepulse/postpulse ratio measured in the presence of CGP alone, as well as in the presence of CGP with baclofen were both significantly higher then that calculated for baclofen alone (see above; ****$P$ < 0.0001 for the ratio with baclofen alone compared to CGP alone and CGP with baclofen, respectively). Statistical test: ANOVA.lme/Dunn's *post hoc* multiple comparison test.

## 2.2. Activation of muscarinic receptors inhibits voltage-gated $Ca^{2+}$ channels in CSF-cNs mediated by a Gβγ mechanism

Previous study carried out on mice brainstem slices showed that CSF-cNs express functional ionotropic cholinergic receptors of nicotinic type which mediate inward current when activated by acetylcholine (ACh) (Orts Del'Immagine *et al.*, 2015). To test if the same type of ionotropic receptors is expressed on spinal CSF-cNs, recordings were made from CSF-cNs in voltage-clamp mode in response to pressure application of ACh (1 mM). As expected, ACh applied for 1 sec induced inward current with an average amplitude of -4.77 ± 1.98 pA (Figure 43. A, B; $n$ = 15). In the presence of D-tubocurarine (200 µM), a selective antagonist of nicotinic receptors, this inward current was reduced by 77.58 ± 16.05%, and it had an average amplitude of -0.61 ± 0.24 pA (Figure 43. A, B; $n$ = 6; $P$ = 0.0127, Paired t-test).

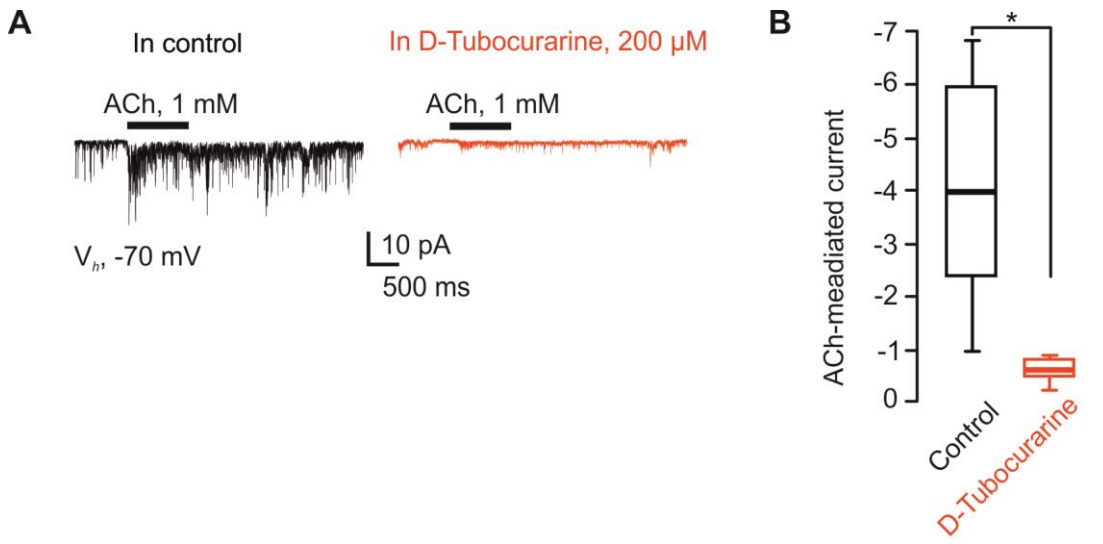


**Figure 43. CSF-cNs express functional cholinergic receptors of nicotinic type.**

**A.** Representative current traces recorded in one CSF-cNs from a holding potential of -70 mV in response to pressure application of 1 mM acetylcholine (ACh, black bar) in control (black trace) and in the presence of 200 µM D-tubocurarine (red trace). Note that inward current elicited by ACh in control is inhibited in the presence of D-tubocurarine. **B.** Summary box-and-whiskers plots of the average inward current amplitude evoked by application of ACh in control (black box) and in the presence of D-tubocurarine (red box). D-tubocurarine significantly reduced ACh-mediated current amplitude (see text for more details; $*P < 0.05$, Paired t-test).

Another type of receptors activated by ACh are muscarinic acetylcholine receptors, metabotropic receptors coupled to G proteins. There are five muscarinic receptors (M1 – M5), and among them, only M2 and M4 couple to inhibitory $G_{i/o}$ proteins (Caulfield, 1993). The same type of inhibitory G proteins couples to $GABA_B$ receptors that were shown to inhibit $Ca^{2+}$ currents in CSF-cNs when activated by baclofen (see previous section). Therefore, I looked for the presence of metabotropic muscarinic receptors and the effect of their activation on $Ca^{2+}$ currents in spinal CSF-cNs. Single depolarizing step from a holding potential of -70 mV to +10 mV was used to elicit $Ca^{2+}$ currents in the presence of oxotremorine-M, a selective agonist of muscarinic receptors, and the peak current amplitude was monitored over time. Pressure application of 100 µM oxotremorine-M (1 min) induced long-lasting inhibition of evoked $Ca^{2+}$ currents, and it reduced the average peak current amplitude from -287.54 ± 118.57 pA measured in control to -114.37 ± 70.01 pA (Figure 44. A-D; $n = 12$; $P < 0.01$, ANOVA.lme/Dunn's *post hoc* multiple comparison test). The inhibitory effect of oxotremorine-M on $Ca^{2+}$ current was reduced in the presence of atropine (10 µM), a selective inhibitor of muscarinic receptors (peak current amplitude: -317.60 ± 144.36 pA in atropine; -

245.88 ± 106.98 pA in atropine in the presence of oxotremorine-M, Figure 44. A-D; $n$ = 6, $P$ = 0.6213, ANOVA.lme/Dunn's *post hoc* multiple comparison test).

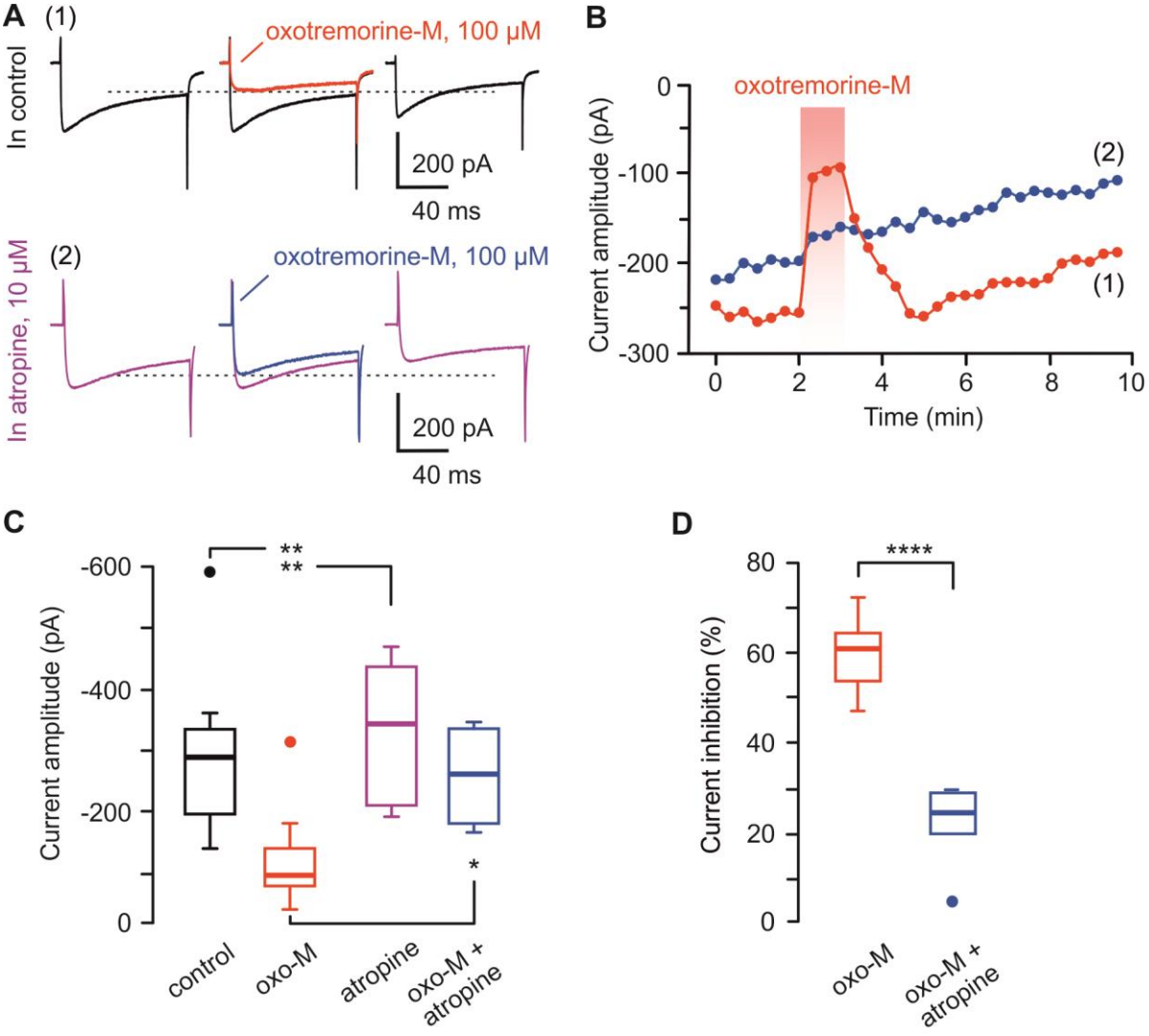


**Figure 44. $Ca^{2+}$ currents in spinal CSF-cNs are inhibited by muscarinic receptors.**

**A.** Representative $Ca^{2+}$ current traces recorded from two spinal CSF-cNs in response to depolarization from a holding potential of -70 mV to +10 mV in control (top, 1, black trace) or in the presence of 10 µM atropine (bottom, 2, violet trace), and in the presence of oxotremorine-M alone (top, 1, red trace) or with atropine (bottom, 2, blue trace). **B.** Time course of $Ca^{2+}$ peak current amplitude for the recordings in A, in the absence (1, red circles) and presence (2, blue circles) of atropine. Oxotremorine-M is applied by pressure for 1 min as illustrated by red bar. **C.** Summary box-and-whiskers plots of the averaged $Ca^{2+}$ peak current amplitude in the absence of atropine before (black box) and during (red box) oxotremorine-M (oxo-M) application, and in the presence of atropine before (purple box) and during (blue box) oxotremorine-M application (see text for details; $^{**}P < 0.01$; ANOVA.lme/Tukey's *post hoc* multiple comparison test). **D.** Summary box-and-whiskers plots of the averaged percentage of $Ca^{2+}$ current inhibition mediated by oxotremorine-M in the absence (red box) and presence of atropine (blue box). Strong $Ca^{2+}$ current inhibition by oxotremorine-M is significantly

reduced in the presence of atropine (oxotremorine-M: 60 ± 2, *n* = 12; oxotremorine-M in atropine: 22 ± 4%, *n* = 6; ****$P$ < 0.0001; Mann-Whitney test).

As G protein coupled receptors, muscarinic receptors act via direct binding of Gβγ subunits to $Ca^{2+}$ channels, a mechanism similar to that observed for $GABA_B$ receptors (see previous section). To determine whether the inhibition of $Ca^{2+}$ current by muscarinic receptors is voltage-dependent in spinal CSF-cNs, triple pulse protocol was used to activate $Ca^{2+}$ channels and to reverse the inhibitory effect of muscarinic receptors activation on $Ca^{2+}$ currents (see Materials and methods). In control, $Ca^{2+}$ current evoked by prepulse reached an average peak amplitude of -300.03 ± 150.81 pA, while current evoked by postpulse had on average a peak amplitude of -159.68 ± 61.96 (Figure 45. A, *n* = 7; *P* = 0.0936 for prepulse amplitude compared to postpulse amplitude in control, ANOVA.lme/Dunn's *post hoc* multiple comparison test). $Ca^{2+}$ current amplitude elicited by prepulse was strongly diminished in the presence of oxotremorine-M when compared to control (-137.73 ± 91.91 pA; Figure 45. A, C, E; *n* = 7; *P* < 0.05 when compared to control, ANOVA.lme/ Dunn's *post hoc* multiple comparison test). When $Ca^{2+}$ current was elicited by postpulse in the presence of oxotremorine-M, current amplitude was similar to that recorded for the postpulse in control (-112.91 ± 49.70 pA; *n* = 7; *P* = 0.9766 when compared to control; ANOVA.lme/ Dunn's *post hoc* multiple comparison). Pre/postpulse ratio was accordingly reduced in the presence of oxotremorine-M when compared to control (Figure 45. F; *n* = 7). In the presence of atropine, $Ca^{2+}$ current evoked by prepulse had average peak amplitude of -339.52 ± 120.88 pA, while current elicited by postpulse exhibited an average amplitude of -260.06 ± 85.45 pA (Figure 45. B; *n* = 6, *P* < 0.05 ANOVA.lme/Dunn's *post hoc* multiple comparison test). The extent of $Ca^{2+}$ current inhibition mediated by oxotremorine-M was strongly reduced in the presence of atropine for the prepulse as current exhibited the averaged amplitude of -167.57 ± 55.29 pA (Figure 45. B, C, E; *n* = 9; *P* = 0.7925, ANOVA.lme/Dunn's *post hoc* multiple comparison test). Inhibition of $Ca^{2+}$ current by oxotremorine-M was further reduced when current was elicited by postpulse, and there was no significant difference when current amplitude was compared to that recorded in atropine alone (-117.07 ± 30.68 pA, Figure 45. B, D, E, *n* = 9; *P* = 0.9766, ANOVA.lme/Dunn's *post hoc* multiple comparison test). In the presence of atropine alone, the pre/postpulse ratio was smaller to that observed in control (Figure 45. F; *n* = 6), and in the presence of atropine with oxotremorine-M, the pre/postpulse ratio was similar to that observed in control (Figure 45. F; *n* = 6).

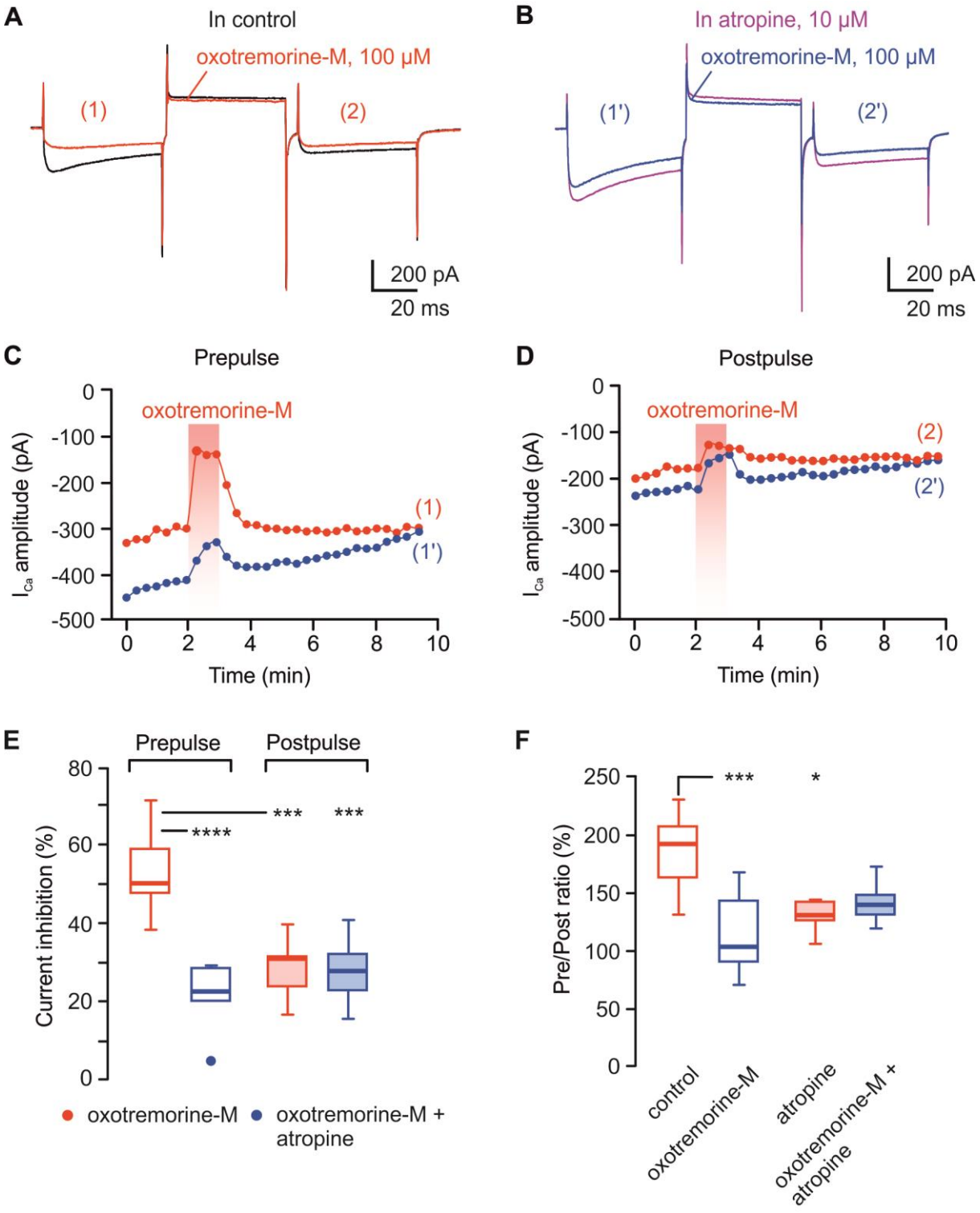


**Figure 45. Muscarinic receptors inhibit voltage-gated $Ca^{2+}$ channels potentially through direct binding of Gβγ.**

**A.** Representative $Ca^{2+}$ current traces recorded from CSF-cNs in response to triple pulse protocol as illustrated in Figure 42. $Ca^{2+}$ current traces elicited by prepulse (1) and postpulse (2) are recorded in control (black trace) and in the presence of 100 µM oxotremorine-M (red trace). **B.** Representative $Ca^{2+}$ current traces recorded from CSF-cNs in presence of 10 µM atropine. $Ca^{2+}$ current traces elicited by prepulse (1') and postpulse (2') are recorded in atropine in the absence (purple trace) and in the presence of oxotremorine-M (blue trace). **C.** Time course of $Ca^{2+}$ peak current amplitude for the

current traces illustrated in A and B. Oxotremorine-M is applied by pressure for 1 min (red box) when $Ca^{2+}$ current is recorded for prepulse in the absence (1, red circles) and presence (1', blue circles) of atropine. **D.** Time course of $Ca^{2+}$ peak current amplitude for the current traces illustrated in A and B. Oxotremorine-M is applied by pressure for 1 min (red box) when $Ca^{2+}$ current is elicited by postpulse in the absence (2, red circles) and presence (2', blue circles) of atropine. **E.** Summary box-and-whiskers plots of the averaged percentage of $Ca^{2+}$ current inhibition mediated by oxotremorine-M in the absence (red boxes) and presence of atropine (blue boxes) for currents evoked by prepulse (open boxes) and postpulse (close boxes). In the absence of atropine, oxotremorine-M significantly inhibited $Ca^{2+}$ current evoked by prepulse compared to postpulse (53 ± 4 % for the prepulse and 28 ± 3% for the postpulse; $n$ = 7; ***$P$ < 0.001, ANOVA.lme/Dunn's *post hoc* multiple comparison test). The inhibitory effect of oxotremorine-M was reduced in the presence of atropine and the inhibition did not differ between prepulse and postpulse (21 ± 4% for the prepulse and 28 ± 3% for the postpulse; $n$ = 6; $P$ = 0.6242, ANOVA.lme/Dunn's *post hoc* multiple comparison test). **F.** Summary box-and-whiskers plots for the pre/postpulse ratio recorded in control (red box), in oxotremorine-M (blue box), in atropine in the absence (red closed box) and the presence of oxotremorine-M (blue closed box). In the presence of oxotrmorine-M, the pre/postpulse ratio was reduced (control: 185.01 ± 35.01%; oxotremorine-M: 115.37 ± 36.79%; $n$ = 7; ***$P$ < 0.001, ANOVA.lme/Dunn's *post hoc* multiple comparison test). In the presence of atropine, oxotremorine-M failed to reduce the pre/postpulse ratio (atropine: 129.85 ± 13.75%; oxotremorine-M in atropine: 141.54 ± 17.75%; $n$ = 6). The pre/postpulse ratio calculated in control was significantly higher than that calculated for atropine alone (see above; *$P$ < 0.05, ANOVA.lme/Dunn's *post hoc* multiple comparison test).

Altogether, these results indicate that spinal CSF-cNs possess functional ionotropic receptors of nicotinic type activated by ACh, which is in agreement with the data obtained in previous study from medullar CSF-cNs (Orts Del'Immagine *et al.*, 2015). Moreover, muscarinic acetylcholine receptors expressed on spinal CSF-cN inhibit $Ca^{2+}$ currents when activated by selective agonist oxotremorine-M, and its inhibitory effect is strongly reduced in the presence of atropine, muscarinic receptor antagonist. The inhibition of $Ca^{2+}$ current is mediated through direct binding of Gβγ subunits of $G_{i/o}$ proteins to $Ca^{2+}$ channels and it is voltage-dependent as inhibition is relieved upon strong depolarization.

## 3. REGULATION OF INTRACELLULAR $Ca^{2+}$ CONCENTRATIONS

Cells possess several mechanisms which regulate intracellular $Ca^{2+}$ concentrations, and therefore prevent large accumulation of intracellular $Ca^{2+}$ that could lead to development of pathological events. $Ca_v$s located on the plasma membrane represent a source of extracellular $Ca^{2+}$, while ER represents an important source of intracellular $Ca^{2+}$ acting as intracellular $Ca^{2+}$ store. Here, I combined whole-cell patch clamp recordings in voltage-clamp or current-clamp

mode with $Ca^{2+}$ imaging to describe the role of $Ca_V$s in $Ca^{2+}$ signaling, and to identify the presence of functional $Ca^{2+}$ stores located in the ER.

### 3.1. Calcium signaling and regulation in medullo-spinal CSF-cNs

To describe $Ca^{2+}$ homeostasis in CSF-cNs, it is important to determine the sources of intracellular $Ca^{2+}$ and the consequences on intracellular $Ca^{2+}$ concentration ($[Ca^{2+}]_i$). Voltage-gated $Ca^{2+}$ channels on plasma membrane are one of the important sources of $Ca^{2+}$ influx into the cells. Therefore, whole-cell patch clamp recordings in voltage-clamp mode were combined with $Ca^{2+}$ imaging to determine the effect of $Ca^{2+}$ channels activation on intracellular $Ca^{2+}$ elevations. CSF-cNs were depolarized from a holding potential of -70 mV to +10 mV to activate $Ca^{2+}$ currents of maximum amplitude. To determine the increase in $[Ca^{2+}]_i$, all CSF-cNs were dialyzed with Fluo-4 (50 µM), a fluorescent $Ca^{2+}$ probe, and changes in fluorescence intensity of Fluo-4 were measured. In medullar CSF-cNs, $Ca^{2+}$ current elicited by membrane depolarization had an average peak amplitude of -234.96 ± 86.38 pA ($n$ = 5), and it was followed by an increase in somatic $[Ca^{2+}]_i$ by 660.02 ± 313.20% ($n$ = 5), seen as an increase in the net fluorescence intensity ($\Delta F/F_0$) of Fluo-4 from the baseline. Consequentially, $Ca^{2+}$ elevations were seen to diffuse from the soma to the bud (see below).

Next, to study $Ca^{2+}$ signaling in a more physiological condition, activation of $Ca^{2+}$ channels was elicited during train of APs. Electrophysiological recordings were performed in current-clamp mode combined with $Ca^{2+}$ imaging on medullar CSF-cNs. $Ca^{2+}$ elevations were induced using 5 successive trains of APs by injecting +20 pA DC current from the RMP (Figure 46. A, B). As shown in Figure 46. C, $[Ca^{2+}]_i$ increased as a function of AP train number. Thus, the first AP train induced an increase in somatic $[Ca^{2+}]_i$ by 13.57 ± 14.38% ($\Delta F/F_0$; $n$ = 12) from the baseline, while the 5$^{th}$ train of AP induced larger increase in $[Ca^{2+}]_i$ (37.70 ± 42.71%, Figure 46. A, C, $n$ = 12). Following the last train of APs, $[Ca^{2+}]_i$ were measured to increase by 292.25 ± 69.76% when normalized to the elevations of $[Ca^{2+}]_i$ recorded upon the 1$^{st}$ train of APs (Figure 46. D, $n$ =12). At the end of 5$^{th}$ train of APs, $[Ca^{2+}]_i$ decreased slowly back to resting levels to a value similar to that observed at baseline (Figure 46. C). Similar intracellular $Ca^{2+}$ elevations were measured from spinal CSF-cNs following the same protocol. There, the first trains of APs induced an increase in fluorescence intensity

by 10.69 ± 6.30% from the baseline ($n$ = 13; $P$ = 0.5865 when compared to the medullar CSF-cNs, Mann-Whitney test), the fluorescence increased further following the 5$^{th}$ train of APs (38.90 ± 19.41%; $n$ = 13; $P$ = 0.2109 when compared to the medullar CSF-cNs, Mann-Whitney test), which corresponded to 393.25 ± 109.52% when elevations of $[Ca^{2+}]_i$ were normalized to elevations recorded for the 1$^{st}$ train of APs (data not shown; $n$ =13; $P < 0.05$ when compared to the medullar CSF-cNs, Mann-Whitney test).

Taken together, these results indicate that depolarization of CSF-cNs elicits increases in the $[Ca^{2+}]_i$ to a similar extent in spinal and medullar CSF-cNs. As expected, the amplitude of the rise in $[Ca^{2+}]_i$ was proportional to the stimulus intensity and decreased over several seconds in an exponential manner indicative for the involvement of $Ca^{2+}$ clearance mechanisms to bring $[Ca^{2+}]_i$ back to resting levels.

CSF-cNs express $GABA_B$ receptors capable of modulating $Ca_v$s. Here, I studied the consequences of $GABA_B$ activation on $Ca^{2+}$ signaling. Therefore, $Ca^{2+}$ influx into the cells was induced using trains of APs in control and while exposing to 100 µM baclofen (Figure 46. A, B). In the presence of baclofen, intracellular $Ca^{2+}$ rise was reduced on the 1$^{st}$ train of APs to 8.09 ± 7.41% ($n$ = 6) and decreased further with subsequent AP trains (reduction by 25.48 ± 24.18% at the end of 5$^{th}$ train; Figure 46. C; $n$ = 6). When normalized to the 1$^{st}$ train of APs, $[Ca^{2+}]_i$ increased only by 165.74 ± 35.32% compared to the control situation (Figure 46. D; $n$ = 6). In agreement with our previous results, the effect of baclofen was strongly diminished in the presence of CGP. In 7 out of 9 recorded cells, baclofen failed to reduce $Ca^{2+}$ elevations following generation of AP trains. Following the 1$^{st}$ train of APs in the presence of baclofen and CGP, somatic $[Ca^{2+}]_i$ increased by 20.71 ± 14.24% ($n$ = 7; $P$ = 0.0774 compared to baclofen alone, Unpaired t-test) and by 64.41 ± 36.67% following the 5$^{th}$ train of APs ($n$ = 7; $P < 0.05$ compared to baclofen alone, Unpaired t-test), which corresponded to 352.46 ± 127.51% when normalized to the increase recorded for the 1$^{st}$ AP train ($n$ = 7; $P < 0.001$ compared to baclofen alone, Unpaired t-test). APs recorded in the presence of baclofen and CGP were of similar amplitudes compared to those recorded in CGP alone (data not shown). Moreover, the application of baclofen did not change the properties of evoked APs or intrinsic properties of CSF-cNs (Table 5.).

These results, therefore, indicate that depolarization of CSF-cNs activates $Ca^{2+}$ channels on the plasma membrane and leads to the large increases in $[Ca^{2+}]_i$ upon $Ca^{2+}$ influx into the cell. These observations are confirmed in more physiological conditions, where $Ca^{2+}$ channels

activation mediated by generation of APs increased $[Ca^{2+}]_i$, an effect that was reduced following the activation of $GABA_B$ receptors by baclofen. Thus, activation of $GABA_B$ receptors and GABA signaling would play a role as modulator of CSF-cN physiology.

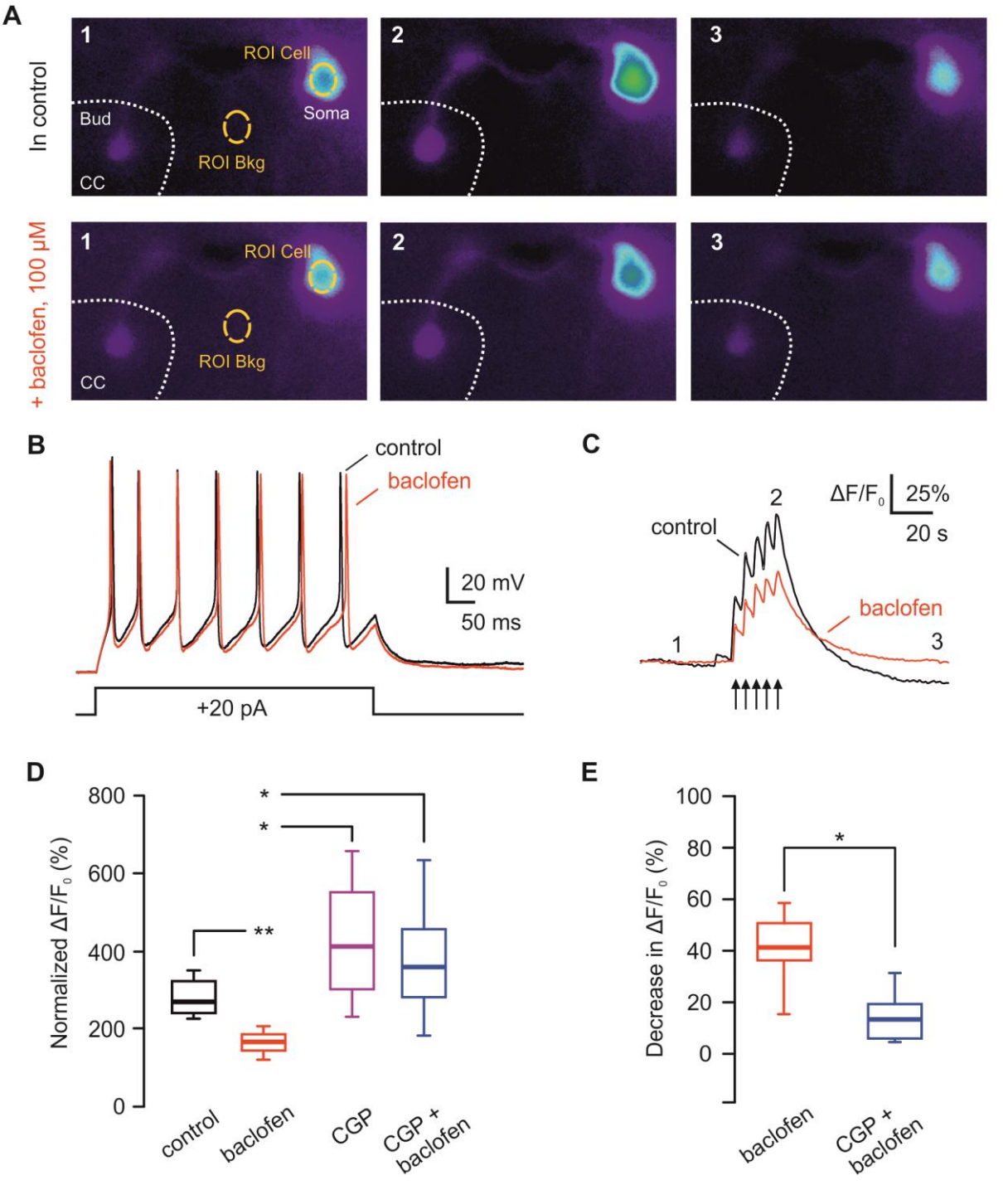


**Figure 46. Activation of $Ca^{2+}$ channels induces intracellular $Ca^{2+}$ rise which is inhibited by $GABA_B$ receptors activation.**

**Figure 46. Activation of $Ca^{2+}$ channels induces intracellular $Ca^{2+}$ rise which is inhibited by $GABA_B$ receptors activation. A.** One CSF-cN is recorded in control (top panels) and in the presence of 100 µM baclofen (lower panels). Cell is recorded in whole-cell configuration in current-clamp mode at the RMP of -56 mV and dialyzed with 50 µM Fluo-4. Average representative images are obtained from 5 successive images acquired for baseline fluorescence (1), for maximum fluorescence increase after 5 trains APs (2) and for the fluorescence at the end of recovery period (3; see also C). Dashed white line indicates the central canal (CC), and yellow dashed lines indicate the regions of interest (ROI) drown in the background (ROI Bkg) and on the soma of the cell (ROI Cell). These two ROIs were used to calculate the net average fluorescence intensity ($\Delta F/F_0$) and generate the fluorescence time course. Five successive trains of APs were generated with +20 pA DC current injection pulse for 500 ms delivered at 0.5 Hz. **B.** Representative trains of APs evoked in control (black trace) and in the presence of baclofen (red trace). Note that traces show the same properties. **C.** Time course of the net fluorescence changes for the cell illustrated in A, acquired in control (black trace) and in the presence of baclofen (red trace) applied during the train of APs. The black arrows indicate the time point when each train of APs was generated. Trace is corrected for fluorescence quenching. **D.** Summary box-and-whiskers plots for the normalized fluorescence increase recorded after the 5$^{th}$ train of APs in control (black box), in baclofen (red box), in CGP alone (purple box) and in the presence of baclofen in CGP (blue box). The application of baclofen reduced the increase in fluorescence intensity, which was significantly reduced in the presence of CGP (control: 292.25 ± 69.76%, $n$ = 12; baclofen: 165.74 ± 35.32%, $n$ = 6; CGP: 429.35 ± 149.07%, $n$ = 9; CGP with baclofen: 392.04 ± 145.63%, $n$ = 9; $^{**}P < 0.01$, $^{*}P < 0.05$, ANOVA.lme/Dunn's *post hoc* multiple comparison test). **E.** Summary box-and-whiskers plots for the decrease in normalized fluorescence increase recorded after the 5$^{th}$ train of APs in the presence of baclofen alone (red box, $n$ = 6) and in the presence of CGP (blue box, $n$ = 7). CGP significantly reduced the decrease in recorded fluorescence increase (baclofen alone: 40 ± 15%; baclofen in CGP: 9 ± 18%; $n$ = 7; $^{*}P < 0.05$, Mann-Whitney test).

| | Control | Baclofen | *P* value |
|---|---|---|---|
| Resting potential (mV) | -57.1 ± 7.4 (*n* = 12) | -53.1 ± 6.7 (*n* = 11) | 0.1079 |
| Threshold potential (mV) | -37.4 ± 4.4 (*n* = 8) | -35.5 ± 4.9 (*n* = 7) | 0.4290 |
| AP amplitude (mV) | 102.3 ± 7.7 (*n* = 8) | 98.7 ± 8.6 (*n* = 7) | 0.2183 |
| AP frequency (Hz) | 17.7 ± 5.9 (*n* = 8) | 19.7 ± 5.8 (*n* = 7) | 0.7345 |
| AP half-width (ms) | 3.8 ± 0.7 (*n* = 8) | 3.8 ± 0.7 (*n* = 7) | 0.8245 |

**Table 5. Electrophysiological properties of CSF-cNs in control and in the presence of baclofen.**

Baclofen (100 µM) application did not change the RMP and TP of CSF-cNs, neither the properties of APs that were elicited by +20 pA DC current step injections of 500 ms (two-tailed paired Student's t-test for all comparisons).

### 3.2. CSF-cNs posses functional intracellular $Ca^{2+}$ stores involved in $Ca^{2+}$ signaling

Together with voltage-gated $Ca^{2+}$ channels expressed on the plasma membrane of the cells, ER is known to play an important role in the regulation of intracellular $Ca^{2+}$ concentrations. This organelle corresponds to an intracellular $Ca^{2+}$ store which can release and/or accumulate $Ca^{2+}$ depending on its luminal and cytoplasmic concentrations. RyRs and $IP_3Rs$ can mediate $Ca^{2+}$ efflux from ER stores (Verkhratsky, 2005). To test whether spinal CSF-cNs possess functional ER stores, $Ca^{2+}$ imaging was performed on CSF-cNs from wild-type mice dialyzed with Fluo-4, and caffeine (50 µM, 10 s), a potent activator of RyRs, was pressure applied onto the recorded CSF-cNs. In 14 out of 23 cells recorded, caffeine application in normal extracellular solution containing 2 mM $Ca^{2+}$ (aCSF, see Materials and methods) induced an increase in the Fluo-4 fluorescence intensity by 34.79 ± 24.79% ($\Delta F/F_0$; Figure 47. A, $n$ = 14) from the baseline. To confirm that the observed rise in intracellular $Ca^{2+}$ is due to $Ca^{2+}$ release from intracellular ER stores, and not due to $Ca^{2+}$ influx through the plasma membrane, recordings were repeated in the absence of extracellular $Ca^{2+}$ ($Ca^{2+}$-free aCSF, see Materials and methods). In 14 out of 29 cells, application of caffeine induced rise in fluorescence intensity by 50.95 ± 38.17%, an increase that was similar to that observed in the presence of extracellular $Ca^{2+}$ (Figure 47. B, $n$ = 14, $P$ = 0.1485, Mann Whitney test).

$Ca^{2+}$ accumulation into ER stores is mediated by SERCA pumps which help to restore the resting concentrations of intracellular $Ca^{2+}$ upon its elevation in the cytoplasm (MacLennan *et al.*, 1997). To determine whether SERCA pumps are involved in $Ca^{2+}$ clearance from CSF-cN cytoplasm, thapsigargin (1 µM), a selective inhibitor of SERCA pumps, was bath applied and caffeine-mediated $Ca^{2+}$ transients were monitored. In normal aCSF, before thapsigargin was added to the bath, caffeine induced rises in fluorescence by 50.58 ±27.13% from the baseline (Figure 47. A; $n$ = 6). In the presence of thapsigargin, caffeine-mediated rise in fluorescence intensity was reduced, as fluorescence increased only by 7.25 ± 6.69% from baseline, although value was not significantly different when compared to the rise induced with caffeine alone (Figure 47. A, $n$ = 6; $P$ = 0.0929, ANOVA.lme/Dunn's *post hoc* multiple comparison test). Similar results were observed in the absence of extracellular $Ca^{2+}$. In such conditions, caffeine-mediated increase in fluorescence was reduced from 76.43 ± 50.65% in the absence of thaspigargin to 16.78 ± 26.67% in the presence of thapsigargin (Figure 47. B, $n$ = 4; $P$ = 0.0509, ANOVA.lme/Dunn's *post hoc* multiple comparison test).

In summary, data reported here indicate that CSF-cNs possess functional intracellular $Ca^{2+}$ stores located in the ER. Our results suggest that $Ca^{2+}$ release from the stores is mediated through RyRs activated by caffeine, a process that does not depend on extracellular $Ca^{2+}$. Moreover, the uptake of $Ca^{2+}$ back into the stores involves the activity of SERCA pumps, which are successfully inhibited by thapsigargin.

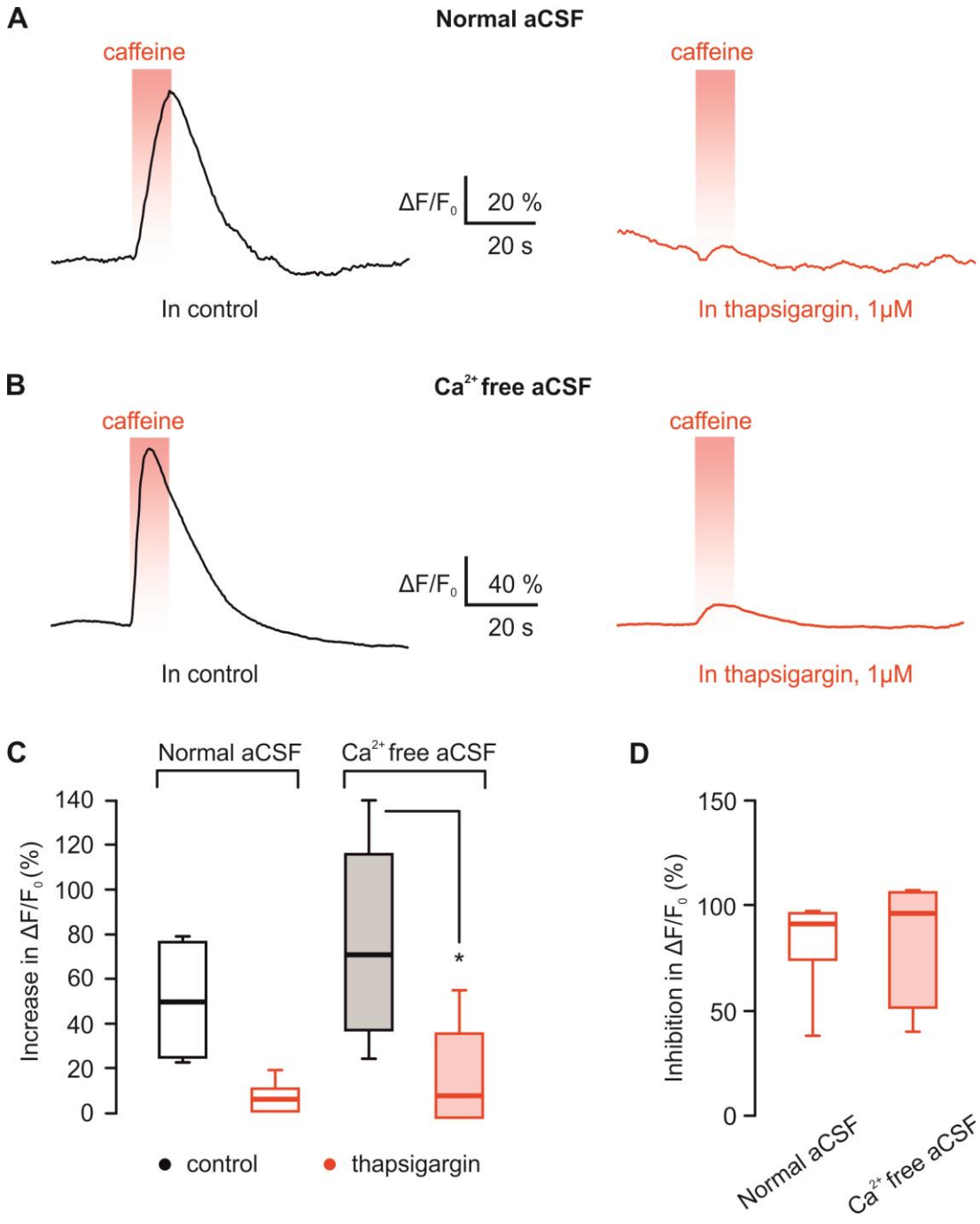


**Figure 47. Functional intracellular $Ca^{2+}$ stores are present in spinal CSF-cNs.**

**A.** Representative traces of fluorescence changes acquired from one CSF-cN recorded in normal aCSF in response to 50 μM caffeine in the absence (black trace) and presence (red trace) of 1 μM

thapsigargin. Pressure application of caffeine is indicated by red bar. Note that caffeine-evoked response is reduced in the presence of thapsigargin. **B.** Similar responses to caffeine pressure application (red bar) in the absence (black trace) and presence (red trace) of thapsigargin are observed in the absence of extracellular $Ca^{2+}$ ($Ca^{2+}$ free aCSF). **C.** Summary box-and-whisker plots for the fluorescence increase in response to caffeine application in the absence of thapsigargin in normal aCSF (black box) and without extracellular $Ca^{2+}$ (light grey box), and in the presence of thapsigargin in normal aCSF (red box) and without extracellular $Ca^{2+}$ (light red box). In the presence of thapsigargin, caffeine induced smaller increase in fluorescence in $Ca^{2+}$ free aCSF when compared to caffeine-induced fluorescence rise in the absence of thapsigargin (see text for details). *$P$ < 0.05, ANOVA.lme/Dunn's *post hoc* multiple comparison test. **D.** Summary box-and-whisker-plots for inhibition in fluorescence induced by caffeine in the presence of thapsigargin in normal aCSF (red box) and in solution without extracellular $Ca^{2+}$ (light red box). There is no difference in fluorescence inhibition induced by caffeine in the presence of thapsigargin between two tested extracellular solutions (normal aCSF: 83.40 ± 22.57%, $n$ = 6; $Ca^{2+}$ free aCSF: 84.84 ± 30.94%, $n$ = 4; $P$ = 0.6095, Mann Whitney test).

### 3.3. Inhibition of SERCA pumps modulates $Ca^{2+}$ signaling

As I have demonstrated above, SERCA pumps in medullo-spinal CSF-cNs represent an important mechanism involved in the intracellular $Ca^{2+}$ uptake back into ER stores. To test whether $Ca^{2+}$ influx through $Ca_v$s is affected by inhibition of SERCA pumps, electrophysiological recordings in voltage-clamp mode from CSF-cNs dialyzed with Fluo-4 $Ca^{2+}$ probe were combined with $Ca^{2+}$ imaging to monitor intracellular $Ca^{2+}$ elevations following membrane depolarization in the absence and the presence of thapsigargin. In control, two depolarizing voltage steps from a holding potential of -70 mV to +10 mV (100 ms) were applied to spinal CSF-cNs with an interval of 8 min between them, which was the time necessary to reach full SERCA pumps inhibition with thapsigargin. As expected, depolarization induced activation of $Ca_v$s and evoked a $Ca^{2+}$ current with an average peak current amplitude of -373.36 ± 110.49 pA ($n$ = 9), followed by an increase in intracellular $Ca^{2+}$ concentration seen by the net fluorescence intensity ($\Delta F/F_0$) increase by 385.17 ± 326.67% from baseline ($n$ = 9). The increase in fluorescence showed fast rise and it returned to baseline with a decay time constant ($\tau$) of 6.17 ± 2.15 s (data not shown; $n$ = 7). Similar results were observed for the second depolarizing step (after 8 min recording). Depolarization elicited a $Ca^{2+}$ current with the average peak current amplitude of -333.22 ± 86.57 pA ($n$ = 9; $P$ = 0.0506, Wilcoxon signed rank test) that induced intracellular $Ca^{2+}$ elevations by 541.60 ± 407.21% from baseline ($n$ = 9; $P$ = 0.0858, Wilcoxon signed rank test). Observed $Ca^{2+}$ transient returned to the baseline with a decay time constant of 6.71 ± 3.98 s (data not shown; $n$ = 7; $P$ = 0.7754, Paired t-test). Therefore, activation of $Ca^{2+}$ channels elicits large elevations

of intracellular $Ca^{2+}$ concentration that slowly returns to its resting levels over several seconds. In the presence of thapsigargin, however, $Ca^{2+}$ current peak amplitude decreased from -327.98 ± 101.44 pA in control to -272.10 ± 91.68 pA (Figure 48. A, B; $n$ = 15, $P$ < 0.001, Wilcoxon signed rank test), while the net fluorescence intensity increased (control: 181.92 ± 201.22%; thapsigargin: 307.05 ± 265.37%; Figure 48. A, C; $n$ = 15; $P$ < 0.01, Wilcoxon signed rank test). The recovery of evoked $Ca^{2+}$ transients to the baseline was similar in the absence and the presence of thapsigargin (control: 8.57 ± 4.61 ms; thapsigargin: 9.62 ± 8.20 s; Figure 48. C; $n$ = 8; $P$ = 0.6744, Wilcoxon signed rank test).

These data indicate that $Ca^{2+}$ influx through voltage-gated $Ca^{2+}$ channels is reduced in the presence of thapsigargin. However, following application of thapsigargin, the depolarization-induced $Ca^{2+}$ transients present larger amplitude, presumably because $Ca^{2+}$ cannot be stored into the ER because SERCA pumps are inhibited. Thus, ER $Ca^{2+}$ stores and SERCA pumps appear to play an important role in regulation of intracellular $Ca^{2+}$.

**Conclusion:**

Altogether, electrophysiological studies conducted on CSF-cNs in adult mouse brainstem and spinal cord slices allowed us to characterize the physiology of these neurons. Here, I demonstrate the presence of voltage-gated $Ca^{2+}$ channels in CSF-cNs. Using pharmacological tools, I show that these channels are mainly of N-type ($Ca_v2.2$) as application of ω-conotoxin GVIA mediated large inhibition of whole-cell $Ca^{2+}$ channels, although the presence of P/Q-type and L-type $Ca^{2+}$ channels was also identified. The activity of $Ca^{2+}$ channels in CSF-cNs is regulated by metabotropic $GABA_B$ receptors as their selective activation by baclofen potently reduces $Ca^{2+}$ currents. $GABA_B$ inhibitory effect is mediated *via* direct binding of Gβγ subunits of inhibitory $G_{i/o}$ proteins to $Ca^{2+}$ channels, an inhibition that is voltage-dependent. In addition to $GABA_B$ receptors, muscarinic acetylcholine receptors are involved in $Ca^{2+}$ channels modulation through a similar mechanim as for $GABA_B$ receptors. Moreover, electrophysiological recordings combined with $Ca^{2+}$ imaging demonstrate that activation of $Ca^{2+}$ channels induces $Ca^{2+}$ influx into CSF-cNs and large increase in intracellular $Ca^{2+}$ concentrations. Functional intracellular $Ca^{2+}$ stores present in ER of CSF-cNs participate in the regulation of intracellular $Ca^{2+}$ concentration by releasing $Ca^{2+}$ in the cytoplasm presumably through RyRs and by its uptake back into the stores mediated by

SERCA pumps. I further show that thapsigargin-mediated inhibition of $Ca^{2+}$ uptake by stores also inhibits $Ca^{2+}$ influx through voltage gated $Ca^{2+}$ channels.

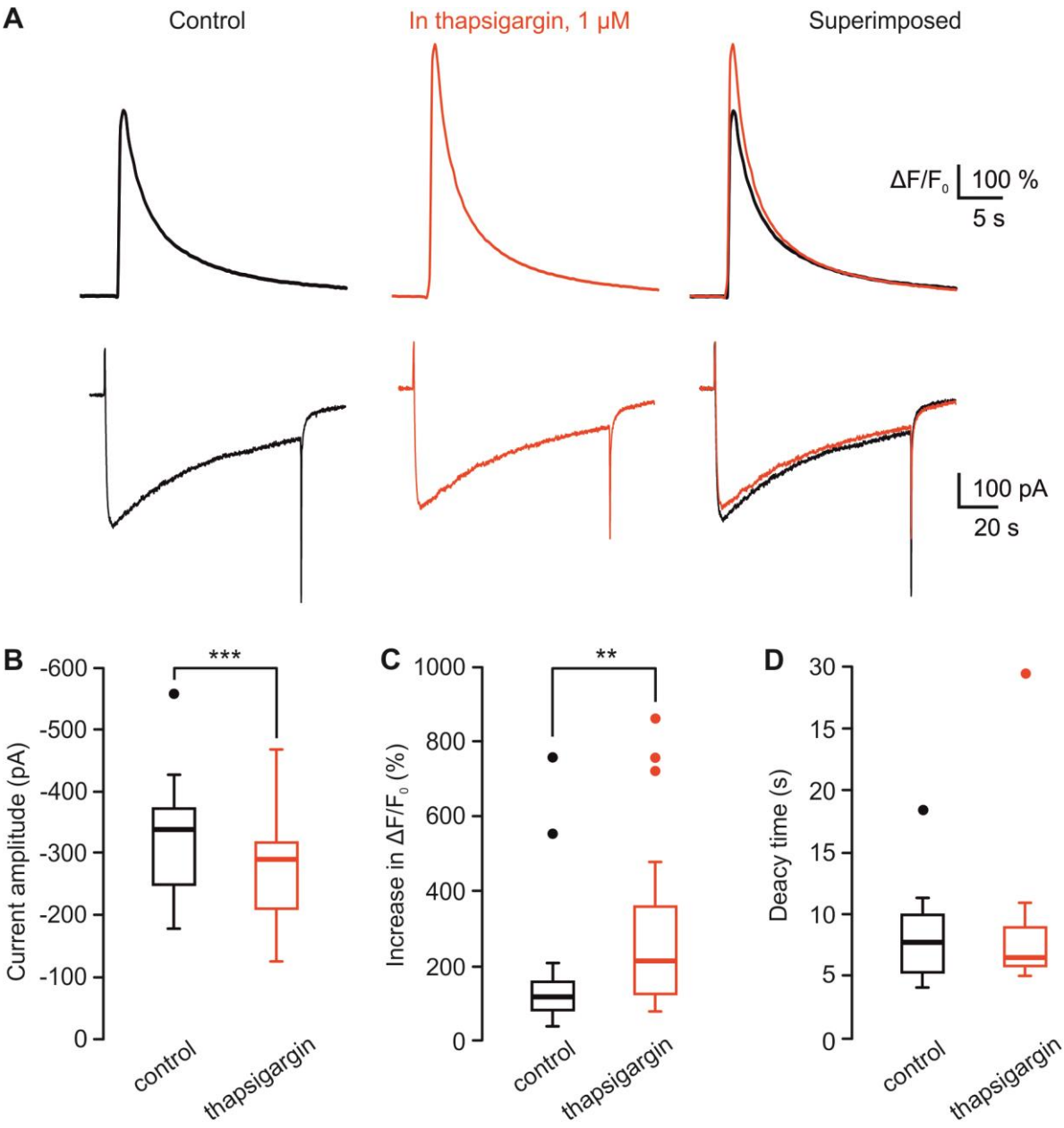


**Figure 48. $Ca^{2+}$ influx and intracellular $Ca^{2+}$ concentration are regulated by intracellular $Ca^{2+}$ stores.**

**A.** Representative traces illustrating the changes in intracellular $Ca^{2+}$ concentrations (top) elicited by corresponding $Ca^{2+}$ current traces (bottom) from one spinal CSF-cN in control (black traces) and in the presence of 1 µM thapsigargin (red traces). Superimposed traces show the difference in intracellular $Ca^{2+}$ rise and $Ca^{2+}$ current peak amplitude in control and thapsigargin. **B-D.** Summary box-and-whisker plots for the average $Ca^{2+}$ current peak amplitude (**B**), increase in net fluorescence (**C**) and average decay time constant (**C**) in control (black box) and in thapsigargin (red box). See text for more details. ***$P < 0.001$, **$P < 0.01$, Wilcoxon signed rank test.

# B) INVESTIGATION OF FUNCTIONAL COMMUNICATION BETWEEN SOMA AND BUD OF CSF-cNs

In this second part of the result section, I will present a set of the experiments that were carried out to describe the properties of the CSF-cN terminal protrusion (bud) in mouse spinal cord slices. I will also present the results from electrophysiological recordings conducted from the soma and/or the bud of CSF-cNs which aimed at understanding the functional relationship between these two cellular compartments.

## 1. $Ca^{2+}$ SIGNALING BETWEEN SOMA AND BUD

CSF-cNs have a well described morphology in many species. The single dendrite of these neurons ends with a terminal enlargement or bud that is inserted in the CC. Nevertheless, the functional properties of this structure and relation between the bud and the soma are still unknown. To answer these questions, whole-cell patch clamp recordings in voltage-clamp mode together with $Ca^{2+}$ imaging were performed from soma of spinal CSF-cNs or technically more challenging, from their bud. The amplitude of $Ca^{2+}$ current and rise in intracellular $Ca^{2+}$ concentrations following membrane depolarization were compared between soma and bud, while either of these structures was patch-clamped and dialyzed with Fluo-4 $Ca^{2+}$ probe. Peak $Ca^{2+}$ current amplitude was elicited from a holding potential of -70 mV to +10 mV (100 ms) and changes in intracellular $Ca^{2+}$ were monitored based on changes in the Fluo-4 fluorescence. When CSF-cNs were recorded from the soma (Figure 49. $A_1$), depolarization evoked $Ca^{2+}$ currents with an average peak amplitude of -337.93 ± 88.82 pA (Figure 49. $B_1$, C; $n$ = 7), followed by an increase in somatic $[Ca^{2+}]_i$ by 442.84 ± 352.54% (Figure 49. $B_1$, D; $n$ = 7). Moreover, depolarization of the soma evoked diffusion of intracellular $Ca^{2+}$ to the bud, where fluorescence increased by 586.15 ± 223.98% from baseline (Figure 49. $B_1$, D; $n$ = 3; $P$ = 0.873, ANOVA.lme/Dunn's *post hoc* multiple comparison test). Next, recordings were reproduced by patching the bud (Figure 49. $A_2$), where $Ca^{2+}$ current elicited by depolarization reached an average peak amplitude of -215.68 ± 89.03 pA (Figure 49. $B_2$, C, $n$ = 6; $P$ = 0.063, Mann-Whitney test). Accordingly, activation of $Ca^{2+}$ channels from the bud evoked an increase in fluorescence intensity by 335.10 ± 232.40% in the bud and 167.92 ± 75.18% in the soma, suggesting the diffusion of intracellular $Ca^{2+}$ from the site of channels activation (Figure 49. $B_2$, D; $n$ = 5; $P$ = 0.770, ANOVA.lme/Dunn's *post hoc* multiple comparison test). $Ca^{2+}$ transients elicited by depolarization of CSF-cNs show faster recovery to baseline in the structure where depolarization was induced. Thus,

$Ca^{2+}$ transients recover faster in the soma than in the bud following somatic depolarization, while depolarization of the bud induces $Ca^{2+}$ transients that recover faster in the bud than in the soma.

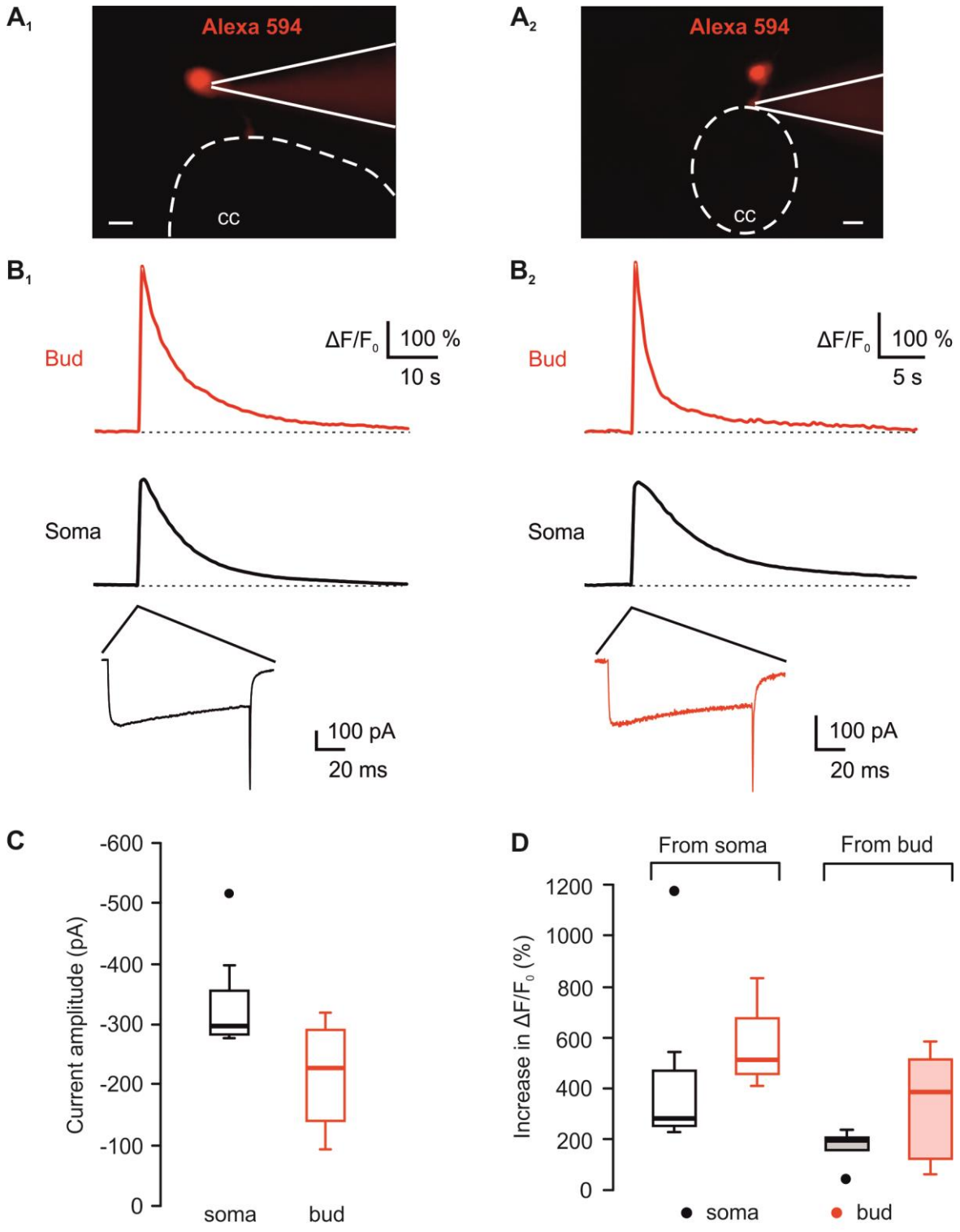


**Figure 49. Intracellular $Ca^{2+}$ elevations diffuse between soma and bud in spinal CSF-cNs.**

**Figure 49. Intracellular $Ca^{2+}$ elevations diffuse between soma and bud in spinal CSF-cNs. A.** Micrographs show two CSF-cNs patched at the soma (**$A_1$**) and bud (**$A_2$**) and dialyzed with Alexa 594 to confirm the morphology. White lines illustrate position of the patch pipette. Dashed line illustrates the central canal (cc). Scale bar = 10 µm. **B.** Representative traces illustrate $Ca^{2+}$ transients (top and middle) elicited in the bud (red trace, top) and the soma (black trace, middle) by corresponding $Ca^{2+}$ current traces (bottom) for a CSF-cNs patched at the soma (**$B_1$**) and at bud (**$B_2$**). **C.** Summary box-and-whisker plots for the average $Ca^{2+}$ peak current amplitude elicited by depolarization of the soma (black box) and bud (red box). There is no difference in current amplitude between two cellular compartments (see text for more details; $P$ = 0.0633, Mann-Whitney test). **D.** Summary box-and-whisker plots for the fluorescence increase induced by depolarization of soma (open box) and bud (closed box), observed in soma (black box) and bud (red box). There is no difference in fluorescence increase between two cellular compartments following depolarization of soma and bud (see text for more details; $P > 0.05$, ANOVA.lme/Dunn's *post hoc* multiple comparison test).

These results demonstrate that membrane depolarization from either of CSF-cN compartment activates $Ca^{2+}$ channels that can be recorded both in the soma and the bud. Large intracellular $Ca^{2+}$ elevation can be recorded in the soma and the bud following $Ca_V$s activation and they present similar amplitude when recorded either from the soma or the bud. $Ca^{2+}$ elevation appear to diffuse from one compartment to the other, suggesting a functional relationship between soma and bud.

## 2. DUAL PATCH-CLAMP RECORDINGS FROM THE SOMA AND THE BUD

Dual patch-clamp recordings from the soma and the bud of spinal CSF-cNs were performed with the aim to elucidate the communication and signal transduction between these two cellular compartments. Two patch electrodes were used to establish 'whole-cell' configuration simultaneously from the cell body and the bud of a single CSF-cN (Figure 50. A, B). In voltage-clamp mode, the two compartments were maintained at a membrane potential of -70 mV and spontaneous current activity was recorded from the two compartments simultaneously. Under these conditions, single channel activity could be recorded in both structures. PKD2L1 channel appears to open at the same time points with the similar unitary current amplitude (soma: -7.49 ± 1.13 pA; bud: -5.77 ± 1.93 pA; Figure 50. C; $n$ = 3; $P$ = 0.1088, Wilcoxon signed rank test). Although PKD2L1 channel activity ($NP_o$) seems to be decreased when recorded from the bud, there is no significant difference compared to channel activity recorded from the soma (soma: 0.007 ± 0.003; bud: 0.009 ±

0.000; Figure 50. C; $n$ = 3; $P$ = 0.2375, Paired t-test). Next, I conducted recordings in current-clamp mode from the RMP and induced the train of APs (DC current injection of +20 pA) in either of the compartments (soma or bud). The responses were recorded simultaneously from both soma and bud. In 3 out of 3 cells recorded, positive somatic current injections induced generation of APs in the soma that were indistinguishable from those recorded in the bud (Figure 50. D). Accordingly, current injections in the bud generated APs that could be recorded in both compartments (Figure 50. E). No differences were observed in the RMP (soma: -53.59 ± 9.62 mV; bud: -52.51 ± 8.64 mV; data not shown; $n$ = 6, $P$ = 0.116, Wilcoxon signed rank test), in the TP (generation from the soma: -25.26 ± 1.97 mV in soma, -24.79 ± 2.07 mV in bud; generation from the bud: -24.86 ± 2.45 mV in soma, -23.79 ± 3.11 mV in bud; Figure 50. F; $n$ = 3; $P$ > 0.05, ANOVA.lme/Dunn's *post hoc* multiple comparison test) or in the amplitude of the generated APs (generation from the soma: 50.38 ± 8.37 mV in soma, 51.41 ± 8.52 mV in bud; generation from the bud: 50.56 ± 8.91 mV in soma, 51.07 ± 9.74 mV in bud; Figure 50. G; $n$ = 3; $P$ > 0.05, ANOVA.lme/Dunn's *post hoc* multiple comparison test) between soma and bud when stimulated from either site.

These results suggest that signals diffuse from soma to the bud, and vice versa as similar current activity can be recorded from soma and from bud in voltage-clamp and current-clamp mode. However, possibility that all recorded signals actually originate from soma should not be excluded.

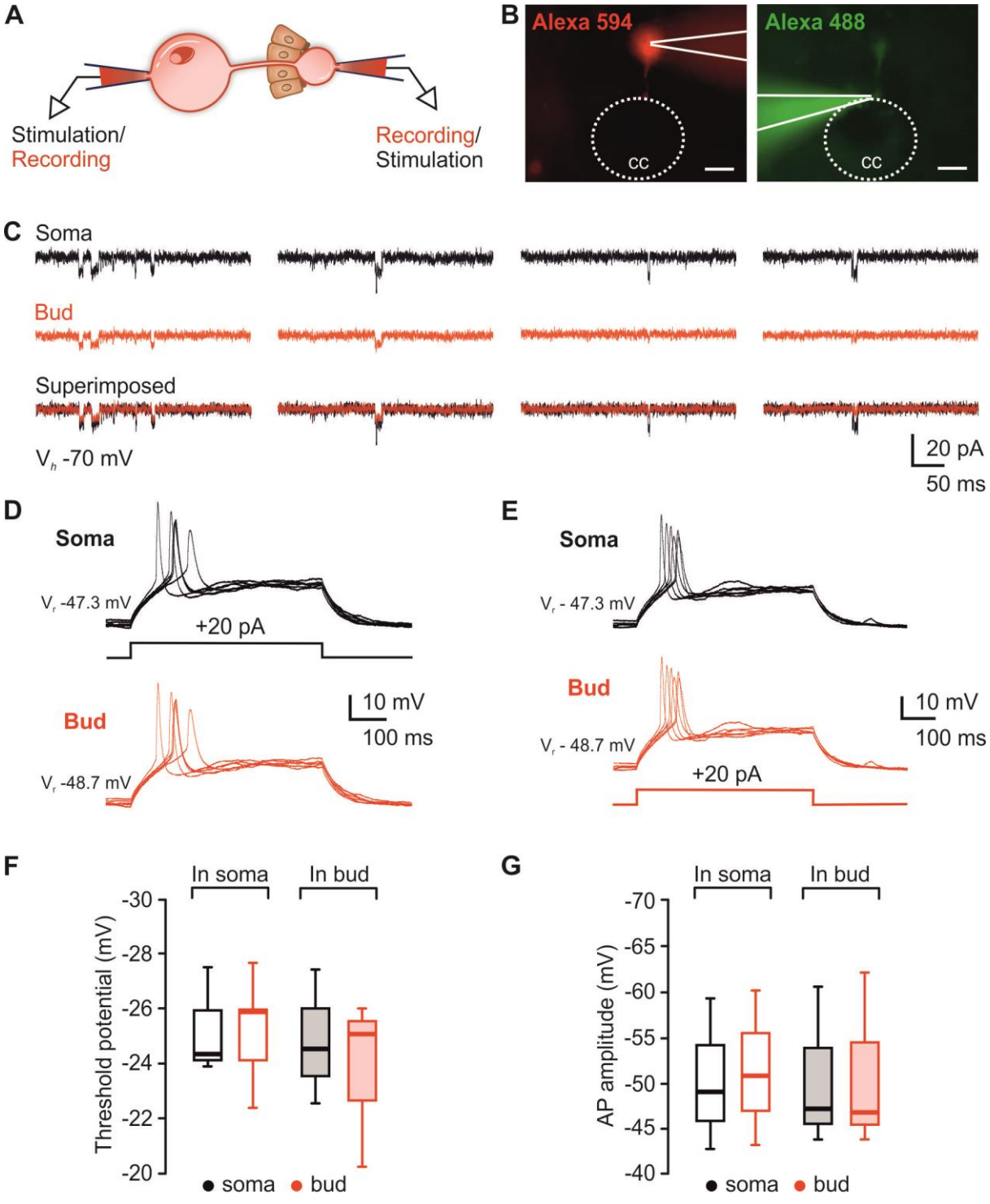


**Figure 50. Dual patch clamp recordings carried out from soma and bud.**

**A.** Schematic illustration of experimental approach. Whole-cell patch clamp recordings are performed using two electrodes to seal to the soma and bud of a single CSF-cN. Both electrodes were used to record the cell in voltage-clamp mode, while one electrode was used to stimulate the neuron in current-clamp mode at soma or bud, while simultaneously recording with another electrode. **B.** Micrographs illustrate spinal CSF-cNs in which dual patch clamp recordings were performed, that are dialyzed with 10 µM Alexa 594 (right) or 10 µM Alexa 488 (left) to confirm its morphology and successful patch from the soma or the bud, respectively. White lines indicate patch pipette. White

dashed line indicates central canal (cc). Scale bare = 10 µm. **C.** Spontaneous single channel activity recorded simultaneously from one CSF-cN in the soma (top, black traces) and the bud (middle, red traces). Traces were superimposed (bottom) to compare the channel open probability and unitary current amplitude between soma and bud. **D.** The five trains of APs (500 ms) were induced with a +20 pA positive DC current injections in the soma of CSF-cN (black trace) while simultaneously recording the response in the bud (red trace). **E.** The five trains of APs were induced in the bud (red trace) while recording the response in the soma (black trace) at the same time. **F-G.** Summary box- and whisker-plot for the TP (**F**) and the amplitude of generated APs (**G**) in soma (black box) and bud (red box) while stimulating at the soma (open box) or bud (closed box).

## 3. RECORDINGS FROM ISOLATED BUD

CSF-cNs were shown to be highly resistive neurons with a long space constant and currents generated from any region of the somato-dendritic compartment would be recorded at the somatic level with little attenuation (Orts Del'Immagine *et al.*, 2015). Therefore, in an attempt to demonstrate the presence of active conductance in the bud, I performed electrophysiological recordings from isolated bud. To realize such experiments, I developed recording approach that would allow to isolate the bud from soma and physically separate these two compartments. First, I established two whole-cell recordings from soma and bud to subsequently pull away the soma using the somatic patch pipette. However, this method resulted in poor survival of the bud probably due to mechanical disruption of the seal on the bud and dialysis of the bud content with extracellular medium through the broken dendrite. I therefore tried another approach that consisted in pressing a fine glass electrode onto the dendrite of the cell while recording from the bud. The recording of a CSF-cN was confirmed by the dialysis through the patched bud of Alexa 594 in the whole-cell configuration (Figure 51. A, $B_1$). Under these conditions, bud patch clamp recordings in voltage-clamp mode reveald the characteristic PKD2L1 current activity (Figure 51. $C_1$) and membrane depolarization from -70 mV to +10 mV ($\Delta V$ = +10 mV) evoked voltage-dependent currents that could be recorded from the bud (Figure 51. $D_1$). Next, the bud was physically separated from the soma by pressing a glass electrode on the dendrite close to the bud (Figure 51. $B_2$) and the same recording was conducted. Under these conditions, spontaneous PKD2L1 current activity could still be recorded, although at a lower frequency (Figure 51. $C_2$). However, when applying the same voltage protocol as before, it was not possible to record any current activity from the isolated bud (Figure 51. $D_2$).

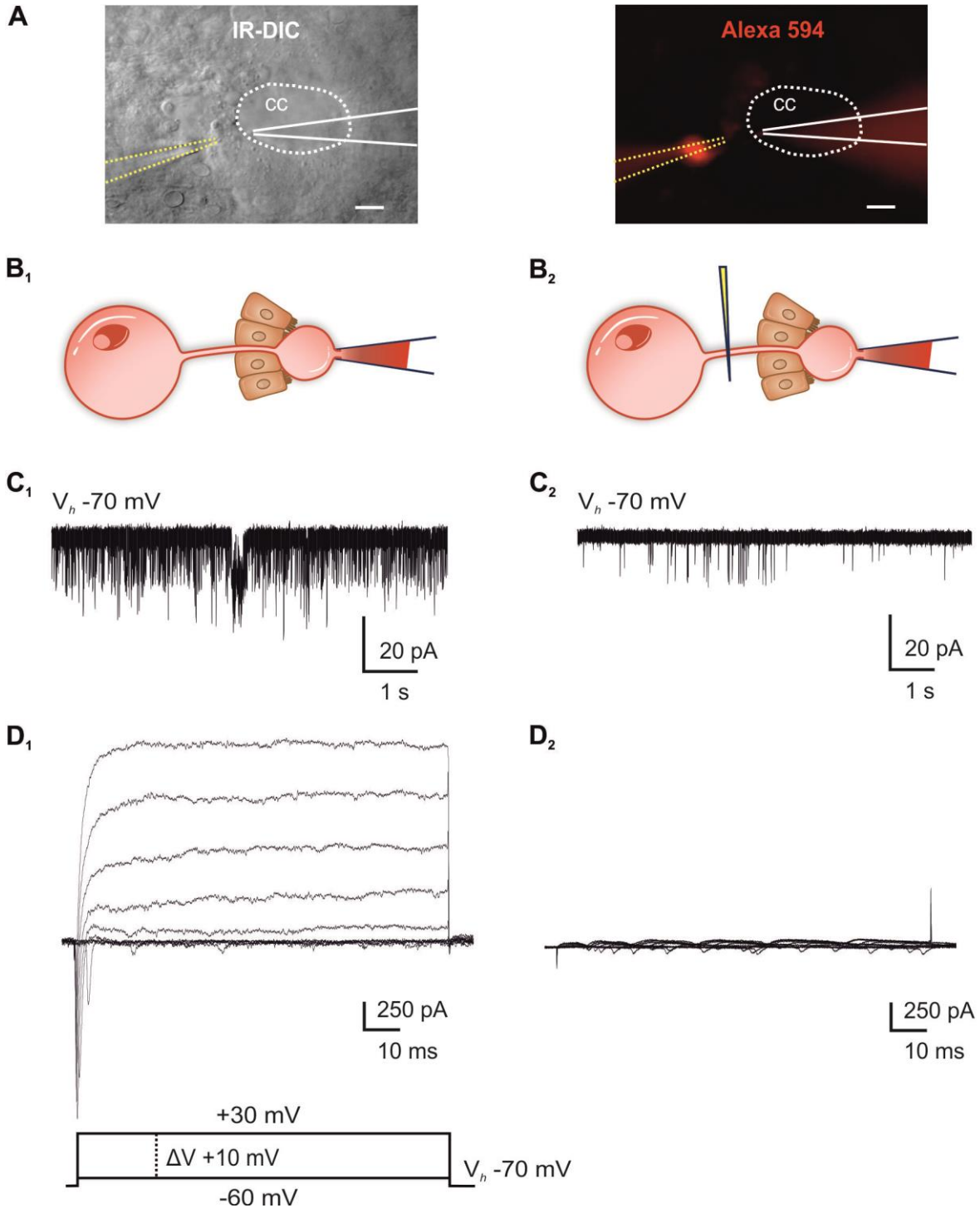


**Figure 51. Isolated bud from spinal CSF-cNs is devoid of current activity.**

**A.** Micrographs illustrate spinal CSF-cN patch-clamped at the bud when illuminated with IR-DIC (left) or dialyzed with 10 µM Alexa 594 (right) to confirm its morphology. White lines indicate the position of the patch pipette, yellow dashed lines indicate the electrode used to press the dendrite, while white dashed line indicates the central canal (cc). Scale bare = 10 µm. **B.** Illustrations show CSF-cN patched at the bud in control (**$B_1$**) and with the electrode used to press the dendrite (**$B_2$**) and to isolate the bud from the soma. **C.** Representative traces showing spontaneous single channel activity recorded in voltage-clamp mode at -70 mV in control (**$C_1$**) and while pressing the dendrite (**$C_2$**). **D.** Representative whole-cell ionic current traces evoked from a holding potential ($V_h$) of -70 mV to +30

mV with +10 mV increments in control (**$D_1$**) and in isolated bud (**$D_2$**). Activation protocol is illustrated under the current trace in **$D_1$**.

These preliminary results strongly suggest that soma and bud are functionally linked, and currents or depolarizing events elicited in either compartment would affect the other. One crucial question concerns the electrophysiological properties of the bud. The results presented here indicate that PKD2L1 channel appear to be expressed in the bud since the characteristic unitary currents can still be recorded from the isolated bud. They further indicate that the bud is devoid of active conductance since no voltage-dependent currents could be elicited from isolated bud.

**Conclusion:**

In summary, electrophysiological recordings were performed on CSF-cNs from adult mouse spinal cord slices to study the communication between soma and bud in these neurons. I was able to record $Ca^{2+}$ currents from both soma and bud and, using $Ca^{2+}$ imaging, I show that depolarization-activated $Ca^{2+}$ channels elicits large elevations in intracellular $Ca^{2+}$ concentrations in both soma and bud, regardless of the site of depolarization. Dual patch-clamp recordings in voltage-clamp mode demonstrate that PKD2L1 channel can be recorded in both soma and bud. Current-clamp recordings indicate that, in CSF-cNs, the RMP is similar between the somatic and the bud compartment and that APs generated by current injections in soma or in bud show similar TP and amplitude, although they are most probably propagating from the soma. Furthermore, I developed a novel technique to separate the bud from the soma so that its properties can be determined independently of the soma. Our preliminary results suggest that signals are mainly generated in the soma and propagate to the bud.

# C) INVESTIGATING THE ROLE OF CSF-cNs

## 1. DEVELOPMENT OF TRANSGENIC MICE MODELS TO STUDY THE ROLE OF CSF-cNs

Concerning medullo-spinal CSF-cNs, one of the major challenges in their study is the determination of their role and function in the CNS *in vivo*. In recent years, studies carried out in lower vertebrates have provided insights to answer this question and suggested they would modulate locomotor activity in the lumbar region. Therefore, CSF-cNs were suggested to represent a novel sensory system intrinsic to the CNS. To date, such a role for CSF-cNs in mammals has not been demonstrated due to anatomical and technological obstacles. First, CSF-cNs are present deep in the spinal cord tissue and their accessibility appears limited. Second, it is a technological challenge to develop imaging and/or recording approaches to manipulate them *in vivo* without disrupting the spinal neuronal network. Nevertheless, with the recent developments in neuroscience and molecular biology, new tools are available, and in this last section, I will present chemo- and optogenetical models I developed and tested to set ground for future *in vivo* studies in the mouse.

### 1.1. Development of chemogenetic mouse model based on DREADD technology

In recent years, inovative chemogenetic strategies have been developed based on modified G-protein coupled receptor systems, namely '*designer receptors exclusively activated by designer drugs*' (DREADDs) (Urban & Roth, 2015). DREADD technology relies on mutated human muscarinic M2 and M4 receptors that couple to inhibitory $G_{i/o}$ proteins (hM2Di and hM4Di, respectively). When expressed in cells, these receptors can only be activated by clozapine-*N*-oxide (CNO), an otherwise pharmacologically inert compoud. The exposure of $G_i$-coupled DREADDs ($G_i$-DREADDs) to CNO triggers the activation of inwardly rectifying potassium channels and the inhibition of $Ca_v$s, leading to a reduced neuronal excitability (Urban & Roth, 2015). Therefore, this model allows to selectively silence one neuronal population of interest using intraperitoneal CNO injection and one animal would serve as its own control. There are transgenic mouse models available where expression of $G_i$-DREADDs can be selectively targeted to a neuronal population using the Cre-Lox technology (R26-LSL-hM4Di-DREADD/mCitrine, see Materials and methods). This model allows verification of DREADD expression in a tissue since a HA-tag is attached to the protein.

I took an advantage of our PKD2L1-IRES-Cre mouse to generate by cross-breading a transgenic mouse where DREADD protein would be selectively expressed in CSF-cNs (see Materials and methods). Considering the localization of CSF-cNs in the spinal cord, this transgenic mouse model appeared to be the best way to manipulate CSF-cNs and test their function *in vivo*. However, prior to launch behavioral studies, it was necessary to validate the model *in vitro*.

In adult mice, the presence of DREADD transcript was confirmed by genotyping the offsprings (Figure 52. A) and the selective expression of DREADD proteins in CSF-cNs was visualized using immunohistochemical staining against PKD2L1 and HA (Figure 52. B). Only mice with confirmed genotype (at least heterozygous for DREADD and Cre) were used to prepare acute spinal cord coronal slices from the lumbar region. Once the whole-cell configuration was established, CSF-cNs were recorded in current-clamp mode from the RMP, and first DC current injection steps were applied (-20 to +30 pA for 500 ms) to analyze the input/output curve, AP properties and frequency (Table 6. and 7.). Then spontaneous activity was recorded over 5 min. This recording sequence was repeated 6 times in total over a 30 min recording period and CNO was bath applied after 8 min recording (Table 6. and 7., Figure 52. C-E). In the presence of 5 µM CNO, a dose classicaly used to activate DREADDs, neither the membrane potential, the intrinsic properties of CSF-cNs nor AP properties were affected (Table 6.). To test whether the absence of CNO effect was due to its insufficient concentration, recordings were reproduced in the presence of 10 µM CNO. In control, some CSF-cNs showed spontaneous AP discharge activity from the RMP (Table 7.) which was not affected in the presence of 10 µM CNO (Figure 52. C). Moreover, the presence of 10 µM CNO in extracellular solution failed to induce hyperpolarization from the RMP (Figure 52. C; Table 7.). When cells were depolarized by current injections, responses similar to those induced by 5 µM CNO were observed, and neurons preserved the ability to generate the APs (Figure 52. D). Accordingly, 10 µM CNO did not increase the TP for generation of APs nor did it alter the properties of the generated APs upon depolarizing current injection steps (Table 7.). When tested on $Ca^{2+}$ currents in voltage-clamp recordings (holding potential -70 mV and test potential to +10 mV), DREADDs activation with CNO also failed to inhibit them (data not shown).

In summary, I was able to selectively express $G_i$-DREADDs in CSF-cNs as confirmed by the positive immunoreactivity of CSF-cNs against the HA-tag. However, despite of its expression in these neurons, application of 5 µM and 10 µM CNO failed to induce membrane

potential hyperpolarization in the recorded cells, neither did it reduced the frequency or stopped the spontaneous firing of the APs or of triggered discharge. Although unlikely, it can be suggested that under our condition, CNO was not able to sufficiently activate $G_i$-DREADDs to alter CSF-cNs activity. Another explanation would be that DREADDs failed to couple to their effector and thus trigger the expected effect. In any case, my results, unfortunately, indicate that the DREADD model is non-functional *in vitro* in CSF-cNs and I could not validate the functionality of chemogenetic DREADD model. I therefore abandoned this DREADD model for further in *vivo* studies because it appeared as an unsuitable model to study the function of CSF-cNs in mammalian CNS.

| | Control | CNO, 5 µM | *P* value |
|---|---|---|---|
| Resting potential (mV) | -48.9 ± 2.9 (*n* = 7) | -47.3 ± 1.3 (*n* = 4) | 0.9213 |
| Threshold potential (mV) | -20.9 ± 1.2 (*n* = 7) | -19.5 ± 0.9 (*n* = 4) | 0.6327 |
| AP amplitude (mV) | 72.7 ± 14.8 (*n* = 7) | 63.3 ± 11.4 (*n* = 4) | 0.559 |
| AP frequency (Hz) | 18.9 ± 4.1 (*n* = 7) | 19.8 ± 3.5 (*n* = 3) | 0.9575 |
| AP half-width (ms) | 3.9 ± 0.8 (*n* = 7) | 3.7 ± 1.3 (*n* = 4) | 0.7647 |

**Table 6. Electrophysiological properties of CSF-cNs-expressing $G_i$-DREADDs in control and in the presence of 5 µM CNO.**

The presence of 5µM CNO did not change the RMP and TP of CSF-cNs, neither the properties of APs that were elicited by current step injections of 500 ms, with 10 pA increments (two-tailed paired Student's t-test for all comparisons).

| | Control | CNO, 10 µM | *P* value |
|---|---|---|---|
| Resting potential (mV) | -48.7 ± 2.2 (*n* = 4) | -39.7 ± 1.4 (*n* = 3) | 0.0934 |
| Threshold potential (mV) | -22.0 ± 1.2 (*n* = 4) | -19.4 ± 0.9 (*n* = 3) | 1.0000 |
| AP amplitude (mV) | 70.5 ± 15.9 (*n* = 4) | 55.2 ± 7.5 (*n* = 3) | 0.2971 |
| AP frequency (Hz) | 33.0 ± 16.6 (*n* = 4) | 13.1 ± 8.0 (*n* = 2) | 0.1907 |
| AP half-width (ms) | 4.9 ± 0.4 (*n* = 4) | 4.9 ± 0.5 (*n* = 3) | 0.8699 |

**Table 7. Electrophysiological properties of CSF-cNs-expressing $G_i$-DREADDs in control and in the presence of 10 µM CNO.**

The presence of 10 µM CNO did not change the RMP and TP of CSF-cNs, neither the properties of APs that were elicited by current step injections of 500 ms, with 10 pA increments (two-tailed paired Student's t-test for all comparisons, except for TP comparison, where Wilcoxon rank sum test was performed).

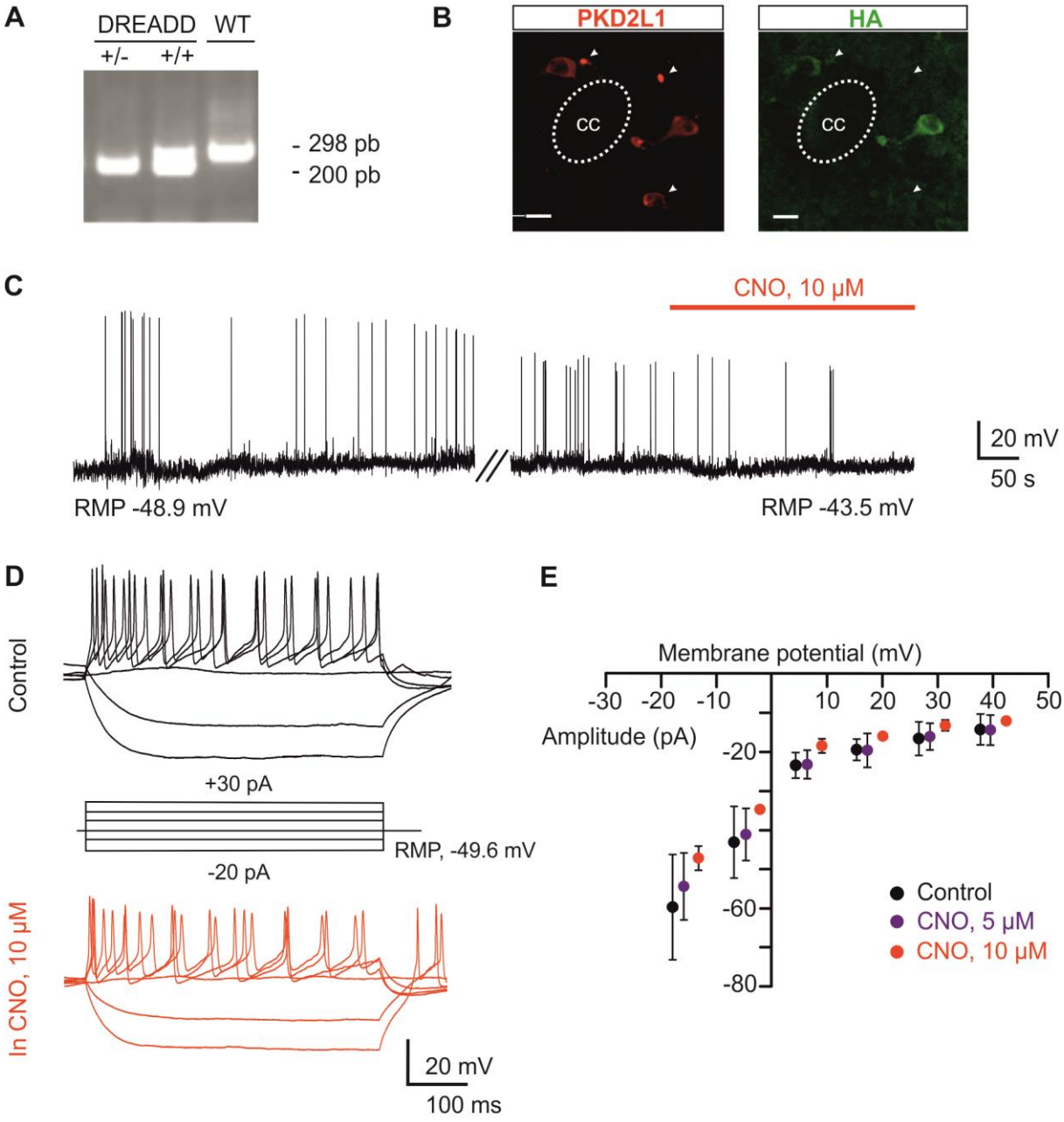


**Figure 52. DREADD do not hyperpolarize CSF-cNs upon CNO application.**

**A.** Illustration of gel electrophoresis showing the results of genotyping for wild-type mouse (WT), heterozygous (+/-) and homozygous (+/+) for DREADD::Cre. **B.** PKD2L1 (red) immunoreactive CSF-cNs from mouse spinal cord coronal sections are also immunolabeled against HA (green). Note that not all PKD2L1$^{+}$ CSF-cNs are HA$^{+}$ (arrowheads). **C.** Representative current-clamp trace recorded from one CSF-cN from the RMP before (left) and after bath perfusion of 10 µM CNO. CNO application did not induce hyperpolarization of recorded cell. **D.** Representative responses of single CSF-cN to current step injections (500 ms, 10 pA increments) from the RMP in the absence (black trace) and presence (red trace) of 10 µM CNO. The activation protocol is illustrated between the traces. **E.** Average input/output curve for the level of depolarization upon current injection steps (500 ms from -20 to +30 pA, as illustrated in panel D) from neurons recorded in control (black dots; $n$ = 11), in the presence of 5 µM CNO (purple dots; $n$ = 4) and in the presence of 10 µM CNO (red dots; $n$ = 3).

### 1.2. Development of optogenetic mouse model with Channelrhodopsin-2-expressing CSF-cNs

Optogenetic represents an innovative tool that is largely used to control the neuronal behaviour by activating photosensitive ionic channels. The most commonly used optogenetic excitatory probe is channelrhodopsin-2 (ChR2), a light-sensitive cation channel that can be easily activated by blue light of ~480 nm (Britt *et al.*, 2012). Optogenetic stimulation of ChR2 activates mostly sodium permeable channels leading to the depolarization of the cell membrane potential and AP firing when expressed in excitable cells. Although difficult to implement for in vivo studies, the optogenetic approach offers a reasonable alternative model to DREADDs allowing CSF-cN modulation in ex-vivo preparation (isolated whole spinal cord and fictive locomotion preparation). Therefore, to test whether optogenetic might represent a suitable approach to asses CFS-cNs role in a more integrated systems, I developed an optogenetic mouse model based on the Cre-Lox technology to generate mice that selectively express light sensitive ChR2-YFP in CSF-cNs (see Materials and methods). Acute spinal cord slices from adult mice were used to record from CSF-cNs expressing YFP-tagged ChR2 (Figure 53. A) in current-clamp mode at RMP. CSF-cNs were recorded and illuminated for 150 ms with a 480 nm excitation light delivered through the objective from our LED illumination system (see Materials and methods). Such a protocol induced AP generation in all CSF-cNs tested. When recording in voltage-clamp mode from a holding potential of -70 mV, CSF-cN illumination elicited an inward biphasic current characteristic of the ChR2 photosensitive current with an initial fast inactivation phase followed by a sustained one (Figure 53. B). As illustrated in Figure 53. C, in neurons recorded in current-clamp mode from the RMP, repetitive light activation induced AP firing. To analyze the effects of optogenetic neuronal activation with classical current injection-mediated activation, the intrinsic properties of CSF-cNs and properties of APs generated by light-activated ChR2 were compared to those induced by current injections in current-clamp mode from the RMP. When optogenetic approach was used to generate APs, CSF-cNs were stimulated with a ‘blue light’ with increasing light duration (100 ms with 100 ms increments; Figure 53. D), and the same neurons were injected with +20 pA current steps with the same parameters (for 100 ms with 10 ms increments) when recorded in current-clamp mode (Figure 53. E). There was no significant difference in RMP of recorded neurons between different activation approaches, neither in the amplitude or frequency of evoked APs. However, the TP was lower for neurons

recorded upon current injection, and half width of APs was smaller for neurons recorded upon optogenetic activation (Table 8.).

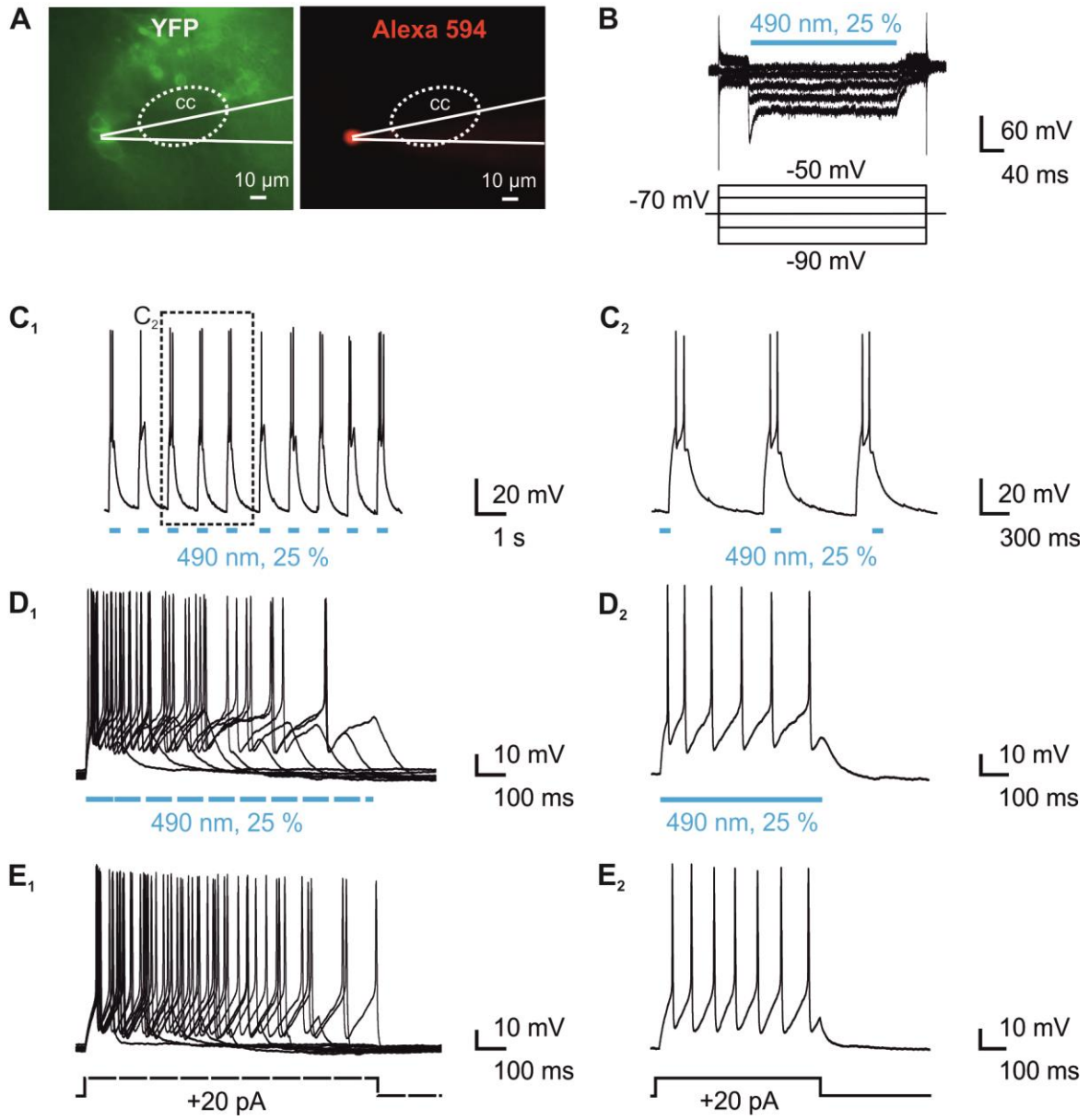


**Figure 53. CSF-cNs generate action potentials upon optogenetic activation.**

**A.** Micrographs show CSF-cNs expressing YFP-tagged ChR2 (left) and dialyzed with Alexa 594 to confirm the morphology (right). White lines illustrate position of the patch pipette. Dashed line illustrates the central canal (cc). **B.** Representative current trace recorded in voltage-clamp mode from a holding potential of -70 mV (voltage steps from -90 mV to -50 mV with 10 mV increments, 700 ms) and elicited by 480 nm light (500 ms) **C.** LED pulses of blue light (blue dashed line) delivered every 1 s elicited APs (**$C_1$**). Traces delineated by dashed square are shown in $C_2$. **D.** Representative APs elicited in one CSF-cN from the RMP (-66.4 mV) by blue light (blue dashed line) of increasing duration (**$D_1$**). Train of APs elicited by 700 ms long LED activation is shown in **$D_2$**. **E.** In the same neuron as shown in panel **D**, APs are elicited by +20 pA current injection of increasing duration from

the RMP (-62.8 mV) (**$E_1$**). Activation protocol is illustrated under the trace. Train of APs elicited by 700 ms long current injection is shown in **$E_2$**.

| | LED activation | Current injection | *P* value |
|---|---|---|---|
| Resting potential (mV) | -64.4 ± 1.1 (*n* = 7) | -63.7 ± 1.3 (*n* = 7) | 0.3038 |
| Threshold potential (mV) | -33.0 ± 3.1 (*n* = 7) | -26.6 ± 1.9 (*n* = 7) | 0.0186 |
| AP amplitude (mV) | 86.9 ± 18.1 (*n* = 7) | 85.5 ± 18.3 (*n* = 7) | 0.9491 |
| AP frequency (Hz) | 12.2 ± 8.4 (*n* = 7) | 13.1 ± 4.9 (*n* = 7) | 0.3173 |
| AP half-width (ms) | 4.7 ± 0.9 (*n* = 7) | 5.4 ± 1.5 (*n* = 7) | 0.2953 |

**Table 8. Electrophysiological properties of CSF-cNs activated by LED illumintion or current injections.**

Activation of spinal CSF-cNs change by blue light (480 nm) or current injection (+20 pA) does not change the RMP of CSF-cNs, neither the properties of APs that, however TP is lower when CSF-cNs are activated by current injections (two-tailed paired Student's t-test for the RMP, TP and AP half-width comparisons; Wilcoxon rank sum test for AP amplitude and frequency comparisons).

My results suggest that ChR2 light-sensitive channels are selectively expressed in spinal CSF-cNs. Optogenetic activation of ChR2-expressing CSF-cNs elicits membrane depolarization and generation of APs when exposed to 480 nm blue light of stable or increasing duration. Therefore, this model represents a promising tool to study the role of CSF-cNs in mammals at least in ex-vivo preparation, a model I am currently testing to asses whether light activation of CSF-cNs is capable to modulate the locomotor activity recorded from lumbar ventral roots (output from motor neurons).

**Conclusion:**

In summary, I generated chemogenetic mouse model in which $G_i$-DREADDs proteins were expressed in CSF-cNs, and optogenetic model in which CSF-cNs express light-sensitive ChR2. My results demonstrate that activation of DREADDs by CNO in spinal CSF-cNs fails to hyperpolarize the membrane of recorded neurons and to inhibit the activity of CSF-cNs. In contrast, light stimulation of ChR2 in spinal CSF-cNs activates CSF-cNs, as it depolarizes membrane of these neurons, leading to generation of APs. These results indicate that chemogenetic DREADD mouse model does not represent a model of interest to study the role

of CSF-cNs *in vivo*, however, optogenetic ChR2 model is validated on spinal cord slices *in vitro* and it can be considered as a model to pursue the functional studies on CSF-cNs role.

# IV. DISCUSSION

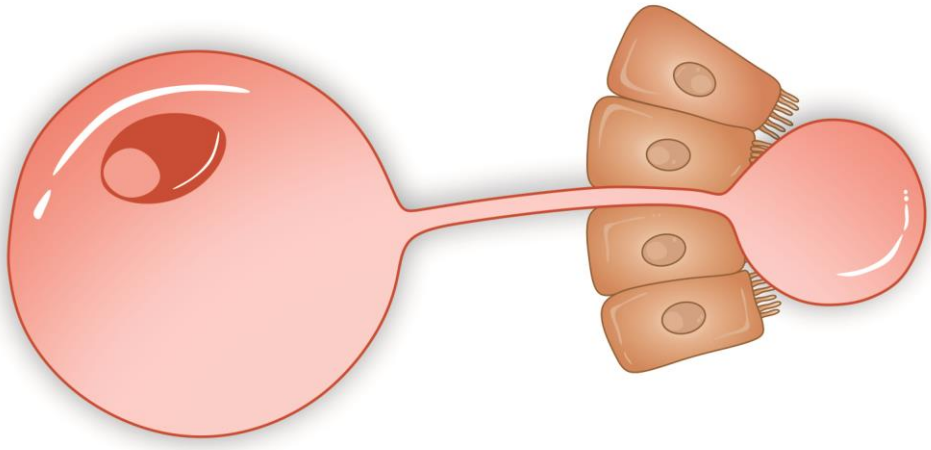

# IV. DISCUSSION

CSF-cNs have been observed for the first time in the late 19$^{th}$ century and since then, they have been extensively characterized at a histological level. However, their properties at a functional level were, until recently, less studied. The main reason was the lack of specific tools to visualize, manipulate and record from them in tissue. With the development of novel molecular tools and transgenic animal models, this technological obstacle starts to be overcome. Several studies have thus been conducted and data on CSF-cN physiology at the cellular level are becoming available.

The work I present in this thesis participates in the better understanding of medullo-spinal CSF-cNs in the mouse. In the first part of my study, I indicate that medullo-spinal CSF-cNs express voltage-gated $Ca^{2+}$ channels ($Ca_v$s), mainly of N-type ($Ca_v2.2$), and that the $Ca^{2+}$ influx eliciteted following their activation generates large rise in the $[Ca^{2+}]_i$ both at the somatic and bud levels. Further, I show that medullo-spinal CSF-cNs express functional metabotropic receptor subtypes for GABA and ACh whose activation leads to the inhibition of $Ca_v2.2$ and consequently to the reduction in intracellular $Ca^{2+}$ elevation. Next, I show that CSF-cNs posses functional $Ca^{2+}$ stores that modulate $Ca^{2+}$ signaling by either releasing or storing intracellular $Ca^{2+}$. Althogether, these results represent the first characterization of $Ca^{2+}$ signaling/homeostasis and modulation in CSF-cNs from mouse brainstem and spinal cord. CSF-cNs have a specific morphology with a bud, their unique and characteristic terminal enlargement in contact with the CSF. This structure is poorly understood and its role as either a receptor or a secretory pole is unknown. In the second part of my study, I addressed this point and I give insights about the bud properties and its functional relationship with the soma. Finally, to answer the ultimate question about the function of CSF-cNs in mammalian CNS *in vivo*, there is a need to develop animal models allowing the selective manipulation of CSF-cNs in more integrated system or for behavioral test *in vivo*. The last part of my thesis deals with the development and validation of chemo- and optogenetic animal models that will allow in a near future to demonstrate the function of medullo-spinal CSF-cN in the mammalian CNS.

# A) PHYSIOLOGY AND CALCIUM HOMEOSTASIS OF MEDULLO-SPINAL CSF-cNs

## 1. MEDULLO-SPINAL CSF-cNs ARE MODULATED BY GABAergic AND CHOLINERGIC IONOTROPIC AND METABOTROPIC RECEPTORS

CSF-cNs were shown to express functional $GABA_A$ as well as glutamatergic AMPA/Kainate ionotropic receptors (Marichal *et al.*, 2009; Orts-Del'Immagine *et al.*, 2012; Jalalvand *et al.*, 2014; Orts Del'Immagine *et al.*, 2015), both receptors being involved in a functional neurotransmission in rat, mouse and lamprey (Marichal *et al.*, 2009; Orts-Del'Immagine *et al.*, 2012; Orts Del'Immagine *et al.*, 2015; Jalalvand *et al.*, 2016*b*) Immunohistochemical studies carried out on rat spinal CSF-cNs (Corns *et al.*, 2015) and mouse medullar CSF-cNs (Orts-Del'Immagine *et al.*, 2012) further demonstrated that these neurons are in close vicinity with cholinergic terminals immunolabeled against ChAT (choline acetyltransferase), suggesting that medullo-spinal CSF-cNs would be modulated by ACh. Indeed, electrophysiological recordings from rat spinal CSF-cNs showed that exogenous application of ACh induced membrane depolarization in rat spinal CSF-cNs (Corns *et al.*, 2015) and fast inward current in mouse medullar CSF-cNs (Orts Del'Immagine *et al.*, 2015). Here, I show that similar responses can be recorded from mouse spinal CSF-cNs where pressure application of ACh evoked inward currents of small amplitude that were blocked in the presence of D-tubocurarine, a nicotinic receptor antagonist. Note that, in mouse medullar CSF-cNs, ACh-mediated currents presented larger amplitudes (Orts Del'Immagine *et al.*, 2015) than in the spinal cord. This result could be explained by a lower density of cholinergic nicotinic receptors in the spinal cord, or by the expression of different receptor subtypes. Regarding activation of cholinergic nicotinic receptors, there is no evidence that these receptors would be involved in synaptic transmission and the mode of activation for these receptors remains elusive. One hypothesis would be that ambient ACh would lead to a tonic activation of CSF-cNs. However, Orts Del'Immagine and colleagues (2015) indicated that such a mechanism was not present for medullar CSF-cNs.

Beside the selective ionotropic receptors activated by GABA, glutamate or ACh, these neurotransmitters also possess metabotropic receptor subtypes. Thus, GABA binds to ionotropic $GABA_A$ receptors and metabotropic $GABA_B$ receptors, which differ in their pharmacological and electrophysiological properties. $GABA_B$ receptors are selectively

inhibited by CGP 55845 and classically activate inwardly rectifying potassium channels (GIRK) and inhibit $Ca_v$s (Bettler *et al.*, 2004). These receptors were found to be expressed in spinal CSF-cNs (Margeta-Mitrovic *et al.*, 1999; Romaus-Sanjurjo *et al.*, 2016). Indeed, in a recent study, we showed that $GABA_B$ receptors are present in medullo-spinal CSF-cNs in the mouse and that they are functional (Jurčić *et al.*, 2019). Further, I present here the evidence to support the expression of functional muscarinic cholinergic receptors (mAChRs) in the same neuronal population (see below). This aspect will be discussed further in a subsequent section. Finally, because CSF-cNs express functional ionotropic glutamatergic receptors, I also tested for the presence of their metabotropic form. However, to date, the collected results were not conclusive, and this study would need to be pursued.

Taken together, these results indicate that in vertebrate, medullo-spinal CSF-cNs are inserted in an neuronal network and in synaptic contact with GABAergic and glutamatergic neurons as well as potentially by cholinergic and serotoninergic neurons (Orts-Del'Immagine *et al.*, 2014). The activity of CSF-cNs appears to be modulated by, at least, inhibitory (GABA) and excitatory (glutamate) neurotransmission through activation of fast ionotropic receptors. Their activity is also modulated by metabotropic receptors that would serve for a more prolonged regulation by activating intracellular cascade. However, the nature of CSF-cN presynaptic partners, their localization and their modulatiory action still remain to be demonstrated.

## 2. FUNCTIONAL VOLTAGE-GATED $Ca^{2+}$ CHANNELS EXPRESSION IN CSF-cNs AND MODULATION BY METABOTROPIC RECEPTORS

Classically, based on electrophysiological properties and sensitivity to different pharmacological agents, $Ca_v$s can be divided into three subfamilies, namely $Ca_v1$ (L-type), $Ca_v2$ (P/Q-, N, and R-type), and $Ca_v3$ (T-type). Moreover, these channels can be further subdivided into high ($Ca_v1$ and $Ca_v2$) voltage-activated (HVA) and low ($Ca_v3$) voltage-activated (LVA) $Ca_v$s (Catterall, 2011; Simms & Zamponi, 2014). Here, using classical whole-cell patch-clamp approach in voltage-clamp mode combined with pharmacological tools, I was able to isolate $Ca^{2+}$ currents in the presence of inhibitors for synaptic receptors and blockers for sodium and potassium voltage-dependent channels. Calcium currents were recorded from both medullar and spinal CSF-cNs, which allowed the comparison of current

properties between neurons located around CC in different segments along the medullo-spinal axis of mouse CNS. I observed on average larger amplitude of whole-cell $Ca^{2+}$ currents recorded from spinal CSF-cNs compared to medullar ones, suggesting a higher $Ca^{2+}$ channel density in CSF-cNs from the spinal cord. Although current density was not calculated, this difference in the current amplitude cannot be due to differences in the cell size since it is on average similar in spinal and medullar CSF-cNs. My results indicate that CSF-cNs possess multiple types of $Ca_v$s, however the N-type $Ca^{2+}$ channels ($Ca_v2.2$, strong inhibition of the $Ca^{2+}$ current by ω-conotoxin GVIA) represent the main $Ca^{2+}$ channel type expressed in CSF-cNs as they contribute to more than 80% of the total $Ca^{2+}$ current. P/Q-type ($Ca_v2.1$) and L-type ($Ca_v1.2$, $Ca_v1.3$) $Ca^{2+}$ channels are also expressed but contribute to less than 20% of the whole-cell $Ca^{2+}$ current. All isoforms of $Ca_v$s identified here are primarily observed in neurons and are considered as neuronal forms of $Ca^{2+}$ channels (Catterall, 2011), confirming the neuronal nature of medullo-spinal CSF-cNs. In this study, $Ca^{2+}$ channels activated at membrane potentials more positive than -40 mV, which is a characteristic of HVA channels. It was reported that CSF-cNs of juvenile rats express T-type ($Ca_v3$) $Ca^{2+}$ channels sensitive to nickel ($Ni^{2+}$) (Marichal *et al.*, 2009). This channel subtype was shown to activate and inactivate at potentials around -60 mV and around -40 mV, respectively (Fox *et al.*, 1987; Catterall, 2011). In my recordings carried out on adult mice ( > 6 week-old), I did not observe $Ca^{2+}$ current activation below -40 mV neither the characteristic shoulder between -60 and -40 mV in the current-voltage relationship present when $Ca_v3$ are expressed. One possible reason, that would need to be tested, for the absence of LVA $Ca^{2+}$ channel types might be explained by the age difference and neuronal maturation of CSF-cNs.

Further, my data indicate that $Ca^{2+}$ current amplitude exhibited a rundown by 26.3 ± 5.5% ($n$ = 3) over 10 min recording, while the access resistance and the holding current remained unchanged. Decrease in $Ca^{2+}$ current amplitude over long period of time has already been reported in whole-cell patch-clamp recordings and was attributed to the increase in intracellular $Ca^{2+}$, and therefore described as $Ca^{2+}$-dependent process (Belles *et al.*, 1988). In my recordings, I used 10 mM intracellular EGTA as $Ca^{2+}$ buffer to control for the intracellular concentration of free $Ca^{2+}$. However, EGTA is so-called slow buffer that might not buffer $Ca^{2+}$ close to the plasma membrane fast enough and therefore might not prevent $Ca^{2+}$-dependent current rundown. I therefore repeated the analysis using 10 mM BAPTA, another type of $Ca^{2+}$ chelator that shows faster binding kinetics and higher buffering capacity compared to EGTA. In the presence of BAPTA, I observed the rundown of current amplitude

by 9.6 ± 5.3% ($n$ = 4; $P$ = 0.06 when compared to recordings with EGTA, Mann-Whitney test; data not shown). This result would suggest that the rundown observed in CSF-cNs is not $Ca^{2+}$-dependent and would involve some other regulatory process. It should be noted that CSF-cNs are small neurons (~10 µm diameter) with little cytosolic space and recordings performed under whole-cell configuration would lead to massive dialysis of the intracellular content necessary for $Ca^{2+}$ channel activity. $Ca_v$s activity is known to be modulated through phosphorylation (Meuth *et al.*, 2002; Budde *et al.*, 2002). Therefore, it is possible that this mechanism is lost, although ATP, GTP and Phosphocreatine were added to the intracellular solution. To address this point, it would be necessary to conduct dedicated sets of experiments to characterize molecular basis of the observed rundown. Nevertheless, I overcame this 'technical' issue by adapting my analysis procedure and taking into accound the rundown (see Materials and methods).

Among the mechanisms that regulate the activity of $Ca_v$s, G protein-mediated inhibition of $Ca^{2+}$ channels is a well described mechanism for $Ca^{2+}$ channels regulation (Catterall, 2011). Metabotropic receptors (G protein-coupled receptors; GPCRs) are known to inhibit main neuronal types of $Ca_v$s (N-, and P/Q-type) through the activation of $G_{i/o}$ proteins that directly bind $Ca_v$s via Gβγ subunits dimer (Herlitze *et al.*, 1996; Ikeda, 1996; Wettschureck & Offermanns, 2005; Tedford & Zamponi, 2006).

The inhibitory effect of $GABA_B$ receptors activation on presynaptic and postsynaptic $Ca^{2+}$ currents was described in supraoptic nucleus (SON) neurons or neocortical pyramidal neurons (Harayama *et al.*, 1998; Pérez-Garci *et al.*, 2013; Booker *et al.*, 2018) as well as in rat hippocampal interneurones (Lambert & Wilson, 1996). In agreement with these observations, my results demonstrate that, in medullo-spinal CSF-cNs, activation of $GABA_B$ receptors by baclofen, its selective agonist, inhibits whole-cell $Ca^{2+}$ current. I show that $Ca^{2+}$ current undergoes inhibition mediated by $GABA_B$ receptors and that this inhibitory effect is selective to $GABA_B$ receptors since it is reversed in the presence of CGP 55845, a potent antagonist of $GABA_B$ receptors. Furthermore, I indicate that ACh application has a similar inhibitory effect as $GABA_B$ activation on $Ca^{2+}$ current both in spinal and medullar CSF-cNs. This effect is mediated by activation of mAChRs since it was reproduced by oxotremorine-M application, a muscarinic receptor agonist and blocked by atropine, a muscarinic receptor antagonist.

Activation of GPCRs induces conformational changes of these receptors associated to G proteins and triggers the activation of Gα and dissociation of Gβγ subunits, each subunit

acting as intracellular regulator. Calcium currents were shown to be inhibited by $G_{i/o}$ coupled metabotropic receptors through the direct binding of Gβγ subunits to the channel (Herlitze *et al.*, 1996; Ikeda, 1996; Tedford & Zamponi, 2006). Classically, $Ca^{2+}$ channel inhibition by GPCRs is voltage-independent or dependent, with the latter characterized by the slowing of current activation and inactivation (Tedford & Zamponi, 2006), and relief of inhibition following large depolarization (Ikeda, 1991, 1996). Such large depolarization is introduced by using triple-pulse protocol consisting of two depolarizing test pulses separated by conditional large depolarizing pulse (Ikeda, 1996). Voltage-dependent inhibition of $Ca^{2+}$ current was demonstrated in chick dorsal root ganglion (DRG) cells. There, $Ca^{2+}$ current inhibition mediated by activation of $GABA_B$ receptors was reduced for the postpulse compared to prepulse, suggesting voltage-dependent recovery of $Ca^{2+}$ currents following the inhibition (Grassi & Lux, 1989). Similar responses were recorded from the rat cultured DRG neurons (Tatebayashi & Ogata, 1992). In mouse medullo-spinal CSF-cNs, $GABA_B$ and mAChRs activation mediates $Ca^{2+}$ current inhibition through a similar Gβγ-voltage-dependent mechanism, since $Ca^{2+}$ current inhibition by baclofen and oxotremorine-M is relieved following strong depolarization.

Muscarinic mAChRs represent another subfamily of G protein-coupled receptors comprised of five isoforms: $M_1$ to M5. $M_1$, $M_3$ and $M_5$ receptors bind $G_{q/11}$ proteins, while $M_2$ and $M_4$ receptors bind $G_{i/o}$ proteins (Caulfield, 1993). In expression systems, $Ca^{2+}$ channels were shown to be inhibited by $M_2$ and $M_4$ types of mAChRs (Higashida *et al.*, 1990). In rat superior cervical ganglion (SCG) sympathetic neurons, $Ca^{2+}$ current of N-type is rapidly inhibited following oxotremorine-M-mediated activation of $M_4$ receptors. The inhibition is voltage-dependent and mediated by Gβγ subunits (Delmas *et al.*, 1998). Similar results were found in neostriatal cholinergic interneurons from rat that mostly express muscarinic $M_2$ and $M_4$ receptors. In these neurons, inhibition of N-type and P-type $Ca_v$s upon muscarinic receptors activation by oxotremorine-M was significantly reduced following strong depolarization, indicating the presence of voltage-dependent inhibitory mechanism mediated by $M_2$ and $M_4$ muscarinic receptors (Yan & Surmeier, 1996). Voltage-dependent inhibition of $Ca^{2+}$ channels mediated by activation of $M_4$ receptors by carbachol or oxotremorine-M was observed in SCG neurons (Fernandez-Fernandez *et al.*, 1999; Kammermeier *et al.*, 2000). In contrast, voltage-independent inhibition of $Ca^{2+}$ currents was observed in SCG neurons but it involved activation of $M_1$ receptors sensitive to $M_1$-toxin (Kammermeier *et al.*, 2000). My results are in agreement with these studies and indicate that, in murine CSF-cNs, mAChRs are

functional and target $Ca^{2+}$ channels. Although I did not determine the subtype of muscarinic receptor involved in modulation of $Ca^{2+}$ currents in CSF-cNs, it can be assumed that the inhibition is mediated through $M_2$ or $M_4$ receptors that couple to inhibitory $G_{i/o}$ proteins known to inhibit $Ca^{2+}$ channels (Herlitze *et al.*, 1996; Ikeda, 1996) as the observed inhibition is voltage-dependent and thus mediated by Gβγ subunits. Of course, the final demonstration of the mAChRs subtype involved in CSF-cNs would need the use of subtype specific agonist and/or antagonists. Note that both $GABA_B$ receptors and mAChRs were shown to activate GIRK current (see Introduction), however in mouse medullo-spinal CSF-cNs activation of either of the two receptors failed to generate such a response (Jurčić *et al.*, 2019). These data would suggest that Kir3 channels are not expressed in this neuronal population.

Facilitation of $Ca^{2+}$ current inhibition by strong depolarization was reported to be effective mostly for Gβγ-mediated inhibition of N-type ($Ca_v2.2$) (Luebke & Dunlap, 1994; Bourinet *et al.*, 1996; Herlitze *et al.*, 1996) and P/Q-type ($Ca_v2.1$) $Ca^{2+}$ channels (Mintz & Bean, 1993; Chen & van den Pol, 1998), although it was recently demonstrated that L-type ($Ca_v1$) $Ca^{2+}$ channels also undergo voltage-dependent inhibition by $GABA_B$ receptors (Pérez-Garci *et al.*, 2013). Accordingly, I show that $Ca_v2.2$ in medullo-spinal CSF-cNs are inhibited by $GABA_B$ receptors and mAChRs, and that this inhibition is mediated by voltage-dependent Gβγ mechanism. CSF-cNs express mainly N-type $Ca^{2+}$ channels (Cav2.2) and to a lower extent L- (Cav1.1 and 1.3) and P/Q- (Cav2.1) channel types. Although a modulation of these latter two $Ca^{2+}$ channel subtypes cannot be excluded, my data indicate that $GABA_B$ receptors and mAChRs would target primarily N-type $Ca^{2+}$ channels. Indeed, in the presence of ω-conotoxin GVIA, there was little supplementary inhibition of the remaining current following baclofen application.

In the future, it would be necessary to characterize the expression of other metabotropic receptors, in particular for neuropeptides, that might be co-released synaptically or circulating in the CSF. Therefore, one of the future lines of research to elucidate the role of medullo-spinal CSF-cNs in mammals would require to identify the signals circulating in the CSF and/or present in the extracellular space (neuropeptides, neurotrophins, hormones,…), to determine whether CSF-cNs express the corresponding receptors and assess the functional consequence on CSF-cN physiology.

## 3. $Ca^{2+}$ SIGNALING AND HOMEOSTASIS IN MEDULLO-SPINAL CSF-cNs

In the present study, I have described for the first time $Ca^{2+}$ homeostasis in medullo-spinal CSF-cNs. I combined electrophysiological recordings to $Ca^{2+}$ imaging and determined the consequences of $Ca^{2+}$ channels activation on intracellular $Ca^{2+}$ concentrations in medullo-spinal CSF-cNs and addressed its regulation by different mechanisms. Classically, elevations of intracellular $Ca^{2+}$ are mediated by $Ca^{2+}$ influx through $Ca_v$s on plasma membrane or by $Ca^{2+}$ efflux from intracellular $Ca^{2+}$ stores found in the ER. To maintain physiological concentrations of intracellular $Ca^{2+}$ around 100 nM (or lower) and normal neuronal activity, $Ca^{2+}$ is extruded from the cytosol out of the cell or accumulated back in the ER (Grienberger & Konnerth, 2012). In this study, I show that membrane depolarization of medullo-spinal CSF-cNs activates mainly N-type $Ca^{2+}$ channels, leading to $Ca^{2+}$ influx through these channels and increase in intracellular $Ca^{2+}$ concentrations seen as increase in fluorescence intensity of Fluo-4 $Ca^{2+}$ probe. Fluo-4 is a single-wavelength probe that indicates relative changes in intracellular $Ca^{2+}$ (Bootman *et al.*, 2013), however it does not allow the precise determination of intracellular $Ca^{2+}$ concentration. I measured high elevations of fluorescence intensity upon membrane depolarization of CFS-cNs (up to 660% from the baseline) which would indicate the large increase in intracellular $Ca^{2+}$ especially because of the small size of these neurons. In physiological conditions, $Ca_v$s are activated by generation of APs. I recreated such conditions and monitored elevations in somatic $Ca^{2+}$ concentrations as a consequence of APs discharge. As expected, trains of APs elicited $Ca^{2+}$ influx into the CSF-cNs and increase in Fluo-4 fluorescence intensity indicating intracellular $Ca^{2+}$ elevations that were proportional to the stimulus intensity. This increase was fast and invaded the entire cell from the soma down to the bud. Further, the response was diminished upon $GABA_B$ receptors activation by baclofen (and presumably by mAChRs activation followed by oxotremorine-M application). These observations further confirm the involvement of $GABA_B$ receptors in modulation of $Ca_v$s and consequential regulation of intracellular $Ca^{2+}$ concentrations. The consequence of such $Ca^{2+}$ influx in CSF-cNs and its modulation through GPCR activation is unknown but it would certainly have an effect on CSF-cN physiology and activity. As calcium is an important intracellular signaling molecule, it would be important to analyze in the future the physiological consequence of $Ca^{2+}$ transient in CSF-cNs and identify the triggered molecular cascade.

One of the questions regarding $Ca^{2+}$ signaling in CSF-cNs, and for which no data are available, concerns the presence of functional intracellular $Ca^{2+}$ stores situated in the ER and whether these stores participate in the regulation of intracellular $Ca^{2+}$ concentrations by either releasing $Ca^{2+}$ into the cytosol or accumulating it in order to maintain the low cytosolic $Ca^{2+}$ concentration. Calcium can be released from the stores through RyRs channels or $IP_3$Rs channels (Verkhratsky, 2005). I induced $Ca^{2+}$ release by using caffeine, known to increase the sensitivity of RyR for cytosolic $Ca^{2+}$ and to induce $Ca^{2+}$ efflux from the ER. Indeed, caffeine application at 50 mM induced $Ca^{2+}$ increase in CSF-cNs, which is mediated by RyRs. Similarly, high concentration of caffeine applied at 40 mM was shown to induce maximal $Ca^{2+}$ efflux from ER in cerebellar granule neurons isolated from neonatal and adult mice (Kirischuk *et al.*, 1996). In contrast, lower concentrations of caffeine ranging between 10-20 mM were sufficient to elicit $Ca^{2+}$ release from the ER in rat and mouse dorsal ganglion neurons in culture (Usachev *et al.*, 1993; Shmigol *et al.*, 1996). However, challenging CSF-cNs with low concentration of caffeine set at 10 mM, I did not observe caffeine-mediated $Ca^{2+}$ increase. It is clear that different concentrations of caffeine are needed to activate $Ca^{2+}$-release channels at the membrane of the ER in different neurons, suggesting variances in functional properties of these channels. The difference observed in CSF-cNs might also be explained by the limitation of the slice preparation and the use of pressure application system rather than bath application that might have reduced caffeine accessibility to neurons and induced its dilution in the perfusion medium. Moreover, out of 23 CSF-cNs recorded in my study to investigate intracellular $Ca^{2+}$ stores, only 14 of them responded to caffeine-mediated $Ca^{2+}$ increase. These results indicate that variabilities in caffeine-sensitivity of RyRs in CSF-cNs might be present among same neuronal population, as it was previously reported for rat sensory neurons (Shmigol *et al.*, 1996). On the other hand, it might reflect different filling level of the ER in different CSF-cNs due to variability in their activity. In agreement with the study by Shmigol and colleagues (1996), I further demonstrate that the response of CSF-cNs to caffeine persists in the absence of extracellular $Ca^{2+}$, confirming intracellular origin of $Ca^{2+}$ that is released from ER through caffeine-sensitive RyR channels, and not due to $Ca^{2+}$ influx through $Ca_v$s or other channels on the plasma membrane. To further confirm the presence of RyRs on the ER of CSF-cNs and their involvement in $Ca^{2+}$ release, it would be necessary to test the effect of direct exposure to RyRs. High concentrations of ryanodine (~100 µM) were shown to have an inhibitory effect on RyRs and $Ca^{2+}$ efflux from stores in granule neurons isolated from mice (Kirischuk *et al.*, 1996). In contrast, ryanodine at low concentrations (between 5-10 nM) mediated $Ca^{2+}$ release from sarcoplasmic reticulum in frog skeletal

muscle cell (Bull *et al.*, 1989), although the same effect could not be confirmed in cultured primary hippocampal neurons from rat (Adasme *et al.*, 2015). I tested on medullo-spinal CSF-cNs in slices the effect of ryanodine but the results were not conclusive mainly because of the difficulty to get ryanodine into the recorded cell. One possible experiment that could address this question would be to develop alternative neuronal populations (primary or organotypic slice culture) that would allow a more efficient way to expose CSF-cNs to ryanodine. Nevertheless, these data indicate that medullo-spinal CSF-cNs present functional ER-$Ca^{2+}$ stores capable of releasing $Ca^{2+}$ in the cytosol most certainly through activation of RyRs but the mechanism by which this release might occurs remains to be determined.

$IP_3$Rs are another $Ca^{2+}$-release channels present on the ER that represent the source of intracellular $Ca^{2+}$ (Verkhratsky, 2005; Taylor & Konieczny, 2016). $IP_3$ is produced by activation of metabotropic receptors coupled to $G_q$ proteins, including muscarinic acetylcholine receptors ($M_1$, $M_3$, $M_5$), $\alpha$1 adrenergic receptors, and glutamatergic receptors (mGluR1, mGluR5), which consequentially activate phospholipase C (Wu *et al.*, 1992; Caulfield, 1993; Pin *et al.*, 1994). Whether these receptors are expressed in CSF-cNs and how their activation would participate in regulation of $Ca^{2+}$ homeostasis in CSF-cNs remain to be determined.

To prevent the excessive rise in intracellular $Ca^{2+}$ concentrations, neurons possess mechanisms which help to extrude cytosolic $Ca^{2+}$ and to restore basal levels of cytosolic $Ca^{2+}$. These systems include $Ca^{2+}$-ATPase pump (PMCA) and $Na^+/Ca^{2+}$ exchanger (NCX) on the plasma membrane or $Ca^{2+}$ accumulation in the ER stores mediated by sarco(endo)plasmic reticulum (SERCA) pumps. Such an involvement of SERCA pumps in $Ca^{2+}$ uptake has already been reported in SCG neurons (Wanaverbecq *et al.*, 2003). My results show that the activity of SERCA pumps in CSF-cNs and $Ca^{2+}$ accumulation into the ER is inhibited by 1 µM thapsigargin. In agreement with my data, thapsigargin was a successful tool to inhibit ER $Ca^{2+}$ accumulation in mouse cerebellar granule neurons (Kirischuk *et al.*, 1996) and DRG neurons (Shmigol *et al.*, 1995), however the effective dose of thapsigargin in these neurons ranged between 20-500 nM. In minority of the recorded CSF-cNs, thapsigargin application induced an initial small increase in cytosolic $Ca^{2+}$ concentration, suggesting $Ca^{2+}$ leak from the ER stores. In my recordings, the same concentration of thapsigargin (1 µM) inhibits $Ca^{2+}$ current induced by membrane depolarization, indicating that thapsigargin exhibits inhibitory effect on both SERCA pumps and $Ca_V$s in CSF-cNs. On the other hand, depolarization of

CSF-cNs in the presence of thapsigargin elicited larger increase in intracellular $Ca^{2+}$ concentrations, suggesting that $Ca^{2+}$ could not be accumulated back into the ER due to simultaneous inhibition of SERCA pumps. It should be tested to what extent SERCA pumps actually contribute to $Ca^{2+}$ extrusion as I did not see any difference in $Ca^{2+}$ transient recovery time between transients elicited in the absence and in the presence of thapsigargin. My observation on the effect of thapsigargin on $Ca_v$s is consistent with data obtained from mouse sensory neurons, where similar concentration of thapsigargin significantly reduced $Ca^{2+}$ current elicited by membrane depolarization (Shmigol *et al.*, 1995). It was demonstrated by the same study that mostly HVA $Ca_v$s are subjected to thapsigargin-mediated inhibition. Here, I showed that CSF-cNs express mainly HVA N-type $Ca^{2+}$ channels, followed by less represented P/Q-type channels, which would strongly indicate that these types of $Ca_v$s undergo blockade by thapsigargin also in CSF-cNs. However, this is in contrast to findings from bovine adrenal zona glomerulosa cells, where application of thapsigargin inhibited both HVA and LVA $Ca_v$s (Rossier *et al.*, 1993).

There are several studies that reported the involvement of PKD2L1 channel in $Ca^{2+}$ homeostasis (Chen *et al.*, 1999; Kaja *et al.*, 2011). PKD2L1 is selective marker for CSF-cNs (Djenoune *et al.*, 2014; Orts-Del'Immagine *et al.*, 2014; Jalalvand *et al.*, 2014), and in mouse it is expressed along the medullo-spinal axis (Orts-Del'Immagine *et al.*, 2014). PKD2L1 was shown to act as mechanoreceptors and chemoreceptor in lamprey, mouse and zebrafish CSF-cNs (Orts-Del'Immagine *et al.*, 2012; Jalalvand *et al.*, 2016*b*; Sternberg *et al.*, 2018). It was previously demonstrated that PKD2L1 is permeable to $Ca^{2+}$ and also modulated by extracellular and intracellular $Ca^{2+}$ in heterologous expression systems (Chen *et al.*, 1999; DeCaen *et al.*, 2016). In such expression systems, increasing concentrations of extracellular $Ca^{2+}$ lead to increase in PKD2L1 channel activity, while prolonged exposure to elevated extracellular $Ca^{2+}$ channel desensitizes PKD2L1 channel resulting in lower channel activity compared to its resting state (Chen *et al.*, 1999). PKD2L1 channels are also expressed on the ER membrane where they may act as $Ca^{2+}$ release channel (Kaja *et al.*, 2011). It cannot be excluded that PKD2L1 channel in CSF-cNs could exhibit the same role. However, the permeability of PKD2L1 to $Ca^{2+}$ and its modulation by $Ca^{2+}$ in mammalian CSF-cNs has not been demonstrated. Recently, PKD2L1 channel was suggested to modulate the activity of CSF-cNs (Orts Del'Immagine *et al.*, 2015; Sternberg *et al.*, 2018). It could be expected that changes in intracellular or extracellular $Ca^{2+}$ in CSF-cNs would modulate the activity of PKD2L1 and therefore the excitability of these neurons. Here I show that activation of

$GABA_B$ receptors and mAChRs inhibits $Ca^{2+}$ channels and reduces $Ca^{2+}$ influx in CSF-cNs, affecting intracellular $Ca^{2+}$ concentrations. Moreover, I show that $Ca^{2+}$ can be released from intracellular ER stores through RyRs and it could also be released through $IP_3Rs$ activated by GPCRs (see above). It is likely that intracellular $Ca^{2+}$ elevations could modulate the activity of PKD2L1 and influence the excitability of CSF-cNs. There are also biomarkers circulating in the CSF or released from synaptic partners that might be capable of modulating the activity of CSF-cNs by activating GPCRs expressed in these neurons and targeting $Ca^{2+}$ signaling. To test the possibility of PKD2L1 modulation by $Ca^{2+}$, I recorded spontaneous activity of PKD2L1 unitary current and changes in intracellular $Ca^{2+}$ concentration following extracellular alkalization, which was already shown to increase the activity of PKD2L1 (Orts-Del'Immagine *et al.*, 2012; Orts Del'Immagine *et al.*, 2015). In my experimental approach, alkalization increased the channel activity, but it decreased the fluorescence intensity of Fluo-4 $Ca^{2+}$ probe most probably due to a direct effect of pH changes on Fluo-4 properties. To test the involvement of PKD2L1 channels, it would be necessary to develop an alternative approach. One of the approaches of interest would involve the use of GCaMP6 transgenic mouse model hosted in our laboratory. This model would enable us to monitor spontaneous $Ca^{2+}$ elevations upon longer openings (>20 ms) of PKD2L1 channel or following modulation of PKD2L1 activity by extracellular alkalization in situation that is close to the physiological situations. In the zebrafish larvae, this approach has been successfully used to demonstrate that upon spinal cord bending, intracellular $Ca^{2+}$ would increase in CSF-cNs and that this phenomenon was mediated by PKD2L1 acting as $Ca^{2+}$ permeable mechanosensor (Sternberg *et al.*, 2018).

The study presented here is the first to characterize $Ca^{2+}$ signaling and homeostasis in medullo-spinal CSF-cNs in the mouse and contribute to better understanding of their physiology. They indicate the potentially important role that $Ca^{2+}$ would play in the regulation of this unique neuronal population. They also open new lines of research, in particular concerning the $Ca^{2+}$-dependent regulation of CSF-cNs following integration of signals circulating in the CSF.

## B) FUNCTIONAL RELATION BETWEEN SOMA AND BUD IN SPINAL CSF-cNs

For the first time, I conducted the set of electrophysiological recordings together with $Ca^{2+}$ imaging to record from the terminal enlargement (bud) of spinal CSF-cNs with the aim to determine its properties and communication with the soma. In the first part of these experiments, I recorded $Ca^{2+}$ current amplitude and intracellular $Ca^{2+}$ elevations following membrane depolarizations while recording in voltage-clamp mode from the soma. I show that depolarization elicits $Ca^{2+}$ current of large amplitude and fast rise in intracellular $Ca^{2+}$ concentrations within several milliseconds. This fast rise is in contrast to slow recovery of fluorescent $Ca^{2+}$ signal back to baseline and resting intracellular $Ca^{2+}$ concentration. Similar kinetics of $Ca^{2+}$ transients is observed in larger neurons, SCG neurons (Wanaverbecq *et al.*, 2003). I was able to measure similar fast rise in intracellular $Ca^{2+}$ and slow recovery of $Ca^{2+}$ transients in the bud following depolarization of the soma. There was no delay in the onset of $Ca^{2+}$ influx in the bud compared to the soma, and intracellular $Ca^{2+}$ elevations are of similar amplitude, suggesting either that $Ca_V$s are expressed in these two cellular compartments or $Ca^{2+}$ diffuses from the soma to the bud with fast kinetics. The main mechanism of $Ca^{2+}$ clearance in SCG neurons involves PMCA pumps, however the activity of SERCA pumps in $Ca^{2+}$ uptake is also involved (Wanaverbecq *et al.*, 2003). In contrast, SERCA pumps were shown to contribute less in $Ca^{2+}$ extrusion from the cytosol in cerebellar granule neurons (Ivannikov *et al.*, 2010). Based on my previous results, I show that the rate of $Ca^{2+}$ clearance upon membrane depolarization is not affected in the presence of thapsigargin. This result could indicate that SERCA pumps are less involved in clearance of $Ca^{2+}$ from cytosol in CSF-cNs, in agreement with observations seen for small cerebellar granule neurons (Ivannikov *et al.*, 2010). Further experiments should be carried out to test whether PMCA would be mainly involved in $Ca^{2+}$ clearance in medullo-spinal CSF-cNs and have a full image of $Ca^{2+}$ homeostasis in these neurons. Interestingly, similar response of CSF-cNs to membrane depolarization was observed when neurons were patch-clamped at the bud. Recorded $Ca^{2+}$ current amplitude and observed intracellular $Ca^{2+}$ rise were indistinguishable from those recorded when neurons were depolarized from the soma. Accordingly, $Ca^{2+}$ elevations were also seen in the soma, indicating that the soma and the bud are functionally connected as signals occurring in one of these compartments would probably affect the other one. To better understand this relation and communication between the soma and the bud, I conducted dual patch-clamp recordings from the soma and the bud of CSF-cNs. I show that spontaneous

PKD2L1 unitary current appears in both structures at the same time points with similar amplitudes and open probability. In addition, APs elicited by positive current injections are identical when recorded from both structures and show similar properties. Considering that CSF-cNs are small neurons with high input resistance and large length constant (Orts Del'Immagine *et al.*, 2015) it can be strongly suggested that signals recorded from the bud would originate from the soma. Therefore, in physiological conditions CSF-cNs could be activated at the level of the bud by biomarkers that circulate in the CSF, and the response elicited in the bud could further generate the response in the soma. Orts Del'Immagine and colleagues (2015) conducted a study with a model neuron which suggested that activation of PKD2L1 channels present at any cellular level could be detected in the soma due to high 'electrotonicity' of CSF-cNs, an assumption that is supported by my observation (Orts Del'Immagine *et al.*, 2015).

To specifically address the properties of the bud and the expression of specific ionic conductance, I performed the experiments aiming at separation/isolating the bud from the soma. So far, my attempts to pull away the soma or the bud, while recording from the bud, were unsuccessful. However, when I pressed the electrode against the dendrite to stop electrical communication between soma and bud, I could record PKD2L1 channel activity from the "isolated" bud, while voltage-dependent conductances were reduced or disrupted. These data would suggest that PKD2L1 is expressed in the bud which is devoid of any active ionic conductance.

Concerning the bud, its physiological role remains to be demonstrated and the experiments conducted in this study will be pursued. To date, there are no evidences indicating its role as receptor pole (integrating signals circulating in the CSF through specific receptors) or a releasing unit as suggested in the literature. Our preliminary electronic microscopy data suggest the presence of vesicles in the bud arguing for a secretory role. However, the mechanisms by which such release might occur is still unknown. On the other hand, if PKD2L1 expression in the bud is confirmed and because of the high 'electrotonicty' of CSF-cNs, it can be suggested that modulation of its activity through circulating signals or mechanical stimuli would have a large impact on somatic activity and excitability. These are open questions crucial to demonstrate the sensory function of medullo-spinal CSF-cNs in the mouse.

# C) INVESTIGATING THE ROLE OF CSF-cNs – DEVELOPMENT OF NOVEL TRANSGENIC MICE MODELS

The physiological role of medullo-spinal CSF-cNs in mammalian CNS is largely unknown. PKD2L1 channel that acts as mechano- and chemoreceptor was shown to be expressed in CSF-cNs from lamprey, zebrafish, mouse and macaque (Djenoune *et al.*, 2014; Orts-Del'Immagine *et al.*, 2014; Jalalvand *et al.*, 2014). Therefore, a sensory role was attributed to these neurons, which are suggested to represent a novel population of sensory neurons. Moreover, CSF-cNs come in contact with the CSF, indicating that they may receive the information that circulate in the CSF and transmit them towards the parenchyma and their synaptic partners. Recent studies carried out in zebrafish and lamprey show that CSF-cNs act as mechanosensors able to modulate the motor activity in the spinal cord (Fidelin *et al.*, 2015; Böhm *et al.*, 2016; Jalalvand *et al.*, 2016*b*). This suggests that a similar role can be attributed to mammalian CSF-cNs. However, the localization of CSF-cNs deep in the spinal cord around the CC in higher vertebrates is the main limitation which makes it difficult to study the role of CSF-cNs in mammals *in vivo.* It is thus necessary to develop more integrated models where CSF-cNs could be selectively manipulated *in vivo*. I took the advantage of chemogenetic approach using "Designer Receptors Exclusively Activated by Designer Drugs" (DREADDs) to try to resolve the problem of cellular accessibility and manipulate CSF-cNs in mice. DREADD technology was used, for example, to study the neuronal circuits underlying the feeding behavior in mice, and it was shown that the activation of mutated human M3 receptors coupled to Gq proteins (hM3Dq) depolarizes AgRP neurons, leading to increased food intake (Krashes *et al.*, 2011). Inhibitory $G_i$-DREADDs activated by clozapine *N*-oxide (CNO) were shown to be an effective strategy to hyperpolarize neurons in epileptic mouse model and to suppress the epileptiform activity in these mice (Avaliani *et al.*, 2016). In my study, the activation of $G_{i/o}$-coupled DREADDs by CNO was expected to reduce the excitability of CSF-cNs. Immunohistochemical staining against HA indicated that HA-tagged mutated hM4Di (DREADDs) were effectively expressed in PKD2L1$^+$ CSF-cNs. In spite of the successful expression of DREADDs in mouse medullo-spinal CSF-cNs, I was not able to validate this model *in vitro*, since the CNO application did not have any effect on RMP of recorded neurons, neither on the AP discharge activity or $Ca^{2+}$ currents. Activation of $G_i$-DREADDs was reported to target GIRKs and to induce hyperpolarization in HEK-293 cells co-expressed with GIRK1/2 subunits (Armbruster *et al.*, 2007). In addition, CNO activation

of Gi-DREADDs in hippocampal neurons also induced silencing of AP firing (Armbruster *et al.*, 2007). Similar effects of CNO were observed in cultured DRG neurons (Saloman *et al.*, 2016) and CA3 pyramidal neurons in organotypic hippocampal slice culture (Avaliani *et al.*, 2016). We have recently reported that activation of $GABA_B$ receptors by baclofen fails to activate GIRK channels in CSF-cNs (Jurčić *et al.*, 2019). This result suggests that GIRK channels are not expressed in mouse CSF-cNs and would therefore explain the lack of the response to $G_i$-DREADD activation in this study. The DREADD model appeared to be an interesting solution to modulate CSF-cNs *in vivo* and we expected to conduct behavioral tests in control and after intraperitoneal CNO application to analyze modification of mice phenotype. Unfortunately, the DREADD model appears inoperant for our purpose.

Optogenetic is commonly used technology that is based on optical activation of proteins to modulate the neuronal activity. It relies on use of channelrhodopsin-2 (ChR2), a naturally occurring light-sensitive ion channel that can be easily activated by illumination with 480 nm blue light (Britt *et al.*, 2012). Here, I developed a mouse model in which CSF-cNs selectively express YFP-tagged ChR2 and show that light stimulation of mouse ChR2-expressing CSF-cNs depolarizes the membrane, leading to AP firing in all CFS-cNs recorded. This photostimulation of CSF-cNs is similar to neuronal activation through electrophysiological protocols. Further, this approach is reliable and reproducible since neuronal discharge follows precisely the illumination frequency. Our results therefore indicate that the optogenetic approach can be used to assess the role of medullo-spinal CSF-cNs at least in *ex-vivo* models. So far, optogenetic manipulations of CSF-cNs from zebrafish provided important information on involvement of these neurons in the regulation of locomotor activity. The optical activation of ChR2-expressing CSF-cNs in spinal cord of zebrafish larvae induced low frequency swimming behavior, a response that was reduced when CSF-cNs (or KA cells in zebrafish) were genetically silenced (Wyart *et al.*, 2009). Using optogenetic approach combined to electrophysiological recordings, activation of CSF-cNs was shown to have differential effects on swimming behavior of the zebrafish depending on the animal states. When CSF-cNs were activated by light during the rest, they induced swim-like behavior. In contrast, activation of CSF-cNs during naturally occurring swimming disrupted swimming activity (Fidelin *et al.*, 2015). It was shown that CSF-cNs target spinal glutamatergic premotor interneurons ($V0_V$) of the fish locomotor central pattern generators (CPGs) (Fidelin *et al.*, 2015). The same group indicates that the effect is mediated by GABA release from CSF-cNs onto $V0_V$ interneurons (Wyart *et al.*, 2009; Fidelin *et al.*, 2015). The functional connectivity of mammalian CSF-cNs

has not been described yet, although similar pattern in modulation of motor activity is expected to be present in vertebrates. CPGs, a spinal network consisting of excitatory and inhibitory interneurons, regulate motor behavior by directing its rhythm and patterns (Brownstone & Bui, 2010; Gosgnach *et al.*, 2017). In mice, neuromodulatory system in the spinal cord is under control of cholinergic V0 interneurons ($V0_C$) (Miles *et al.*, 2007), a subtype of V0 interneurons that are derived from $Dbx1^+$ progenitor cells in p0 domain in the ventral spinal cord (Pierani *et al.*, 2001), and selectively express Pitx2 transcription factor (Zagoraiou *et al.*, 2009). $V0_C$ interneurons form longitudinal clusters on the lateral sides of the CC along the spinal cord (Zagoraiou *et al.*, 2009; Witts *et al.*, 2014), and they provide cholinergic input to motoneurons by forming "C boutons", cholinergic varicosities surrounding the soma and proximal dendrites of motoneurons (Miles *et al.*, 2007; Zagoraiou *et al.*, 2009). Interestingly, $V0_C$ represent the only source of "C boutons" to motoneurons (Zagoraiou *et al.*, 2009). The modulatory activity of $V0_C$ is mediated by muscarinic $M_2$ receptor subtype expressed on "C boutons" and activation of these receptors is shown to increase the excitability of motoneurons they surround (Miles *et al.*, 2007). Mice with genetically disrupted "C bouton" signaling show impaired firing of motoneurons and muscle activation (Zagoraiou *et al.*, 2009). Regarding the synaptic inputs onto $V0_C$ interneurons, they were shown to receive excitatory inputs from glutamatergic interneurons, inhibitory GABAergic inputs and serotonergic inputs from the brainstem (Zagoraiou *et al.*, 2009). In zebrafish, CSF-cNs provide direct GABAergic input on a subset of V0 interneurons and modulate swimming (Wyart *et al.*, 2009; Fidelin *et al.*, 2015). In mammalian, CSF-cNs located around the CC could receive the information from the CSF by monitoring its content and the presence of various neuroactive substances. By sensing the changes in the content of the CSF, they could modulate the activity of $V0_C$ interneurons located in their close proximity and participate in regulation of locomotor activity.

Because the ChR2 model is functional in our model, we are developing a project to test the potential neuromodulator role of CSF-cNs in the locomotion of the mouse. Interestingly, transgenic mouse models to label CSF-cN axons and synaptic terminals indicate that CSF-cNs could come in synaptic contact with $V0_C$ and even motoneurons. Further, using the PKD2L1-ChR2 mouse model, we have initiated an analysis of *ex-vivo* fictive locomotion. Locomotor-like activity was recorded extracellularly from left and right lumbar ventral roots and upon photoactivation of lumbar CSF-cNs, we observed a modification of the locomotor rhythm. Finally, using the same ChR2 model but in lumbar coronal acute slices, we are conducting, in

a similar way as the study from Fidelin and colleagues (2015), experiments to demonstrate the synaptic connections between CSF-cNs and $V0_C$ or motoneurons. Here we are recording neurons surrounded by ChR2-YFP positive fibers or varicosities and expect to record GABAergic synaptic events upon illumination with ‘blue light’. Therefore, the use of optogenetic to activate CSF-cNs provides promising tool to demonstrate for the first time ever the function of medullo-spinal CSF-cNs in the mammalian CNS.

# V. CONCLUSION

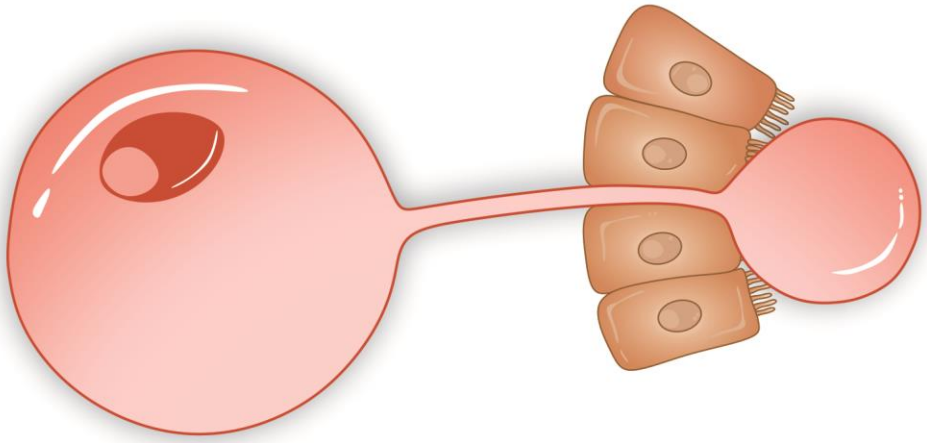

# V. CONCLUSION

In the current study, I performed electrophysiological recordings in combination with $Ca^{2+}$ imaging on CSF-cNs in acute brainstem and spinal cord slices from adult mice. Here, I report the presence of voltage-gated $Ca^{2+}$ channels ($Ca_v$s) on plasma membrane of CSF-cNs that are predominantly of the N-type ($Ca_v2.2$). $Ca^{2+}$ channels represent an important source of extracellular $Ca^{2+}$ and activation of these channels induces large increase in intracellular $Ca^{2+}$ concentrations. I further show that CSF-cNs possess functional intracellular $Ca^{2+}$ stores which are present in ER. These stores are involved in $Ca^{2+}$ signaling in CSF-cNs since they release $Ca^{2+}$ through RyRs and potentially uptake it through SERCA pumps (Figure 54.). I further confirm that CSF-cNs are inserted in neuronal network and modulated by GABAergic and cholinergic signaling. These pathways are capable to regulate $Ca_v$s activity through their metabotropic receptor subtypes *via* the classical $G_{i/o}/G\beta\gamma$ regulatory mechanism. Moreover, I show that CSF-cN soma and bud are functionally coupled and indicate that signals modulating bud activity would leads to somatic activation. Finally, I present data validating an optogenetic approach that is a promising strategy to manipulate CSF-cNs activity with the aim to determine their function *in vivo*.

The study carried out during my *PhD* provides new pieces of evidence on medullo-spinal CSF-cNs in a mammalian model and contribute to better understanding of medullo-spinal CSF-cN physiology and modulation. They also indicate the advances accomplished to resolve the mystery about the role of CSF-cNs in mammalian CNS. However, my study also opens new questions that need to be answered to better understand the function of these neurons.

Because of their morphology, phenotype and localization at the interface between CSF and parenchyma, CSF-cNs possess all characteristics to act as sensory neurons in the mammalian CNS. To confirm this hypothesis, it will be necessary to pursue the identification of the receptors that CSF-cNs express and in parallel determine the signals present in the extracellular space or in the CSF that are susceptible to bind to the identified receptors. Along the same line, the properties, function and role of the bud as a sensory structure would needed to be demonstrated. Moreover, it would be important to determine how CSF-cNs integrate the signals they receive and how they process these signals. It has already been suggested that the

terminal enlargement would participate in receiving the information from the CSF and transmitting them toward the parenchyma and synaptic partners of CSF-cNs. It was further indicated that the "bud" could receive the signals from distal parts of the CNS and release them into the CSF. Therefore, more extensive studies should be carried out to investigate the role of this mysterious neuronal structure and determine how it contributes to the CSF-cNs function.

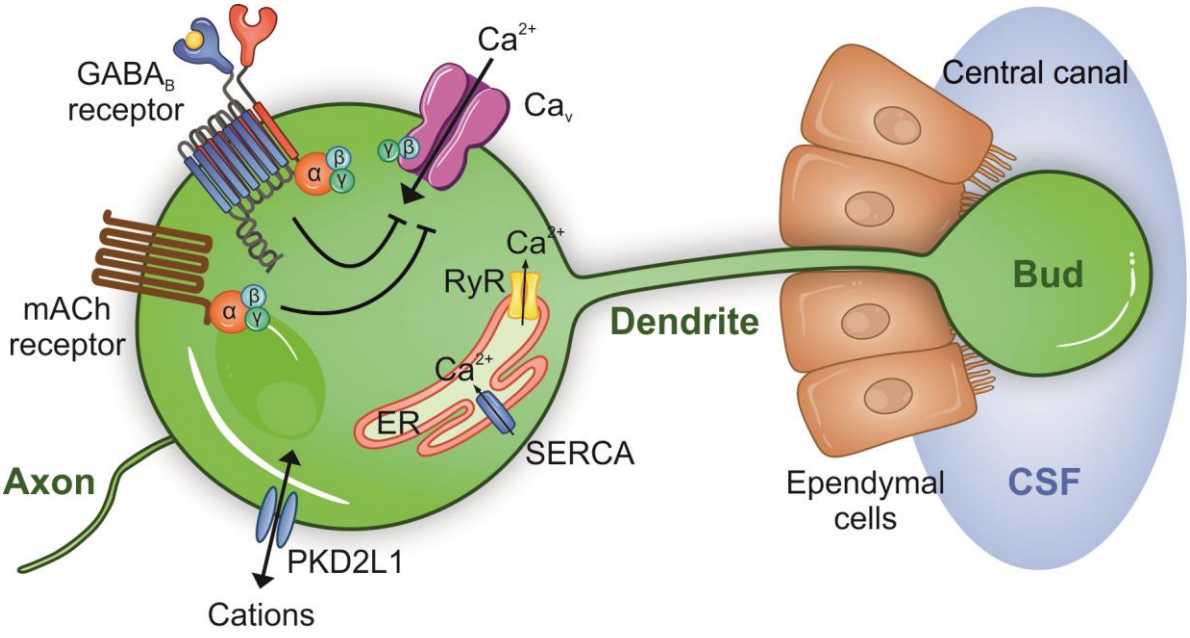


**Figure 44. Regulation of intracellular $Ca^{2+}$ concentrations.**

Medullo-spinal CSF-cNs express voltage-gated $Ca^{2+}$ channels that are inhibited by metabotropic $GABA_B$ receptors and muscarinic acetylcholine receptors (mACh) following recruitment of Gβγ subunits. $Ca^{2+}$ can be also released from intracellular stores located in the endoplasmic reticulum (ER) through ryanodine receptor (RyR) and it can be accumulated back into ER through sarco(endo)plasmic reticulum (SERCA) pump.

The next step will be to demonstrate the identity and localization of CSF-cN presynaptic partners and thus demonstrate the consequence on CSF-cN activity. Up to now, medullo-spinal CSF-cNs in mammals were described to receive GABAergic and glutamatergic synaptic inputs. It could be expected that these inputs modulate CSF-cN activity in different ways depending on their origin and nature. The identification of other neuronal partners that project onto CSF-cNs and their localization would give valuable information on the network CSF-cNs are inserted in. Of course, to have the full picture, the identity and localization of

CSF-cN postsynaptic partners is crucial to demonstrate the consequence of CSF-cN activation on CNS activity. In mouse, CSF-cNs project an axon towards unknown partners. Immunohistochemical and tracing studies would provide a set of data on the territories innervated by CSF-cNs and would indicate potential postsynaptic partners for CSF-cNs. Moreover, connectivity between CSF-cNs and their synaptic partners could be studied by taking advantage of mice that express ChR2 in CSF-cNs. This approach would enable to monitor the responses generated in synaptic partners of CSF-cNs following light stimulation of CSF-cNs. A particular attention will be given to the relationship between CSF-cNs and the spinal motor network.

# VI. REFERENCES

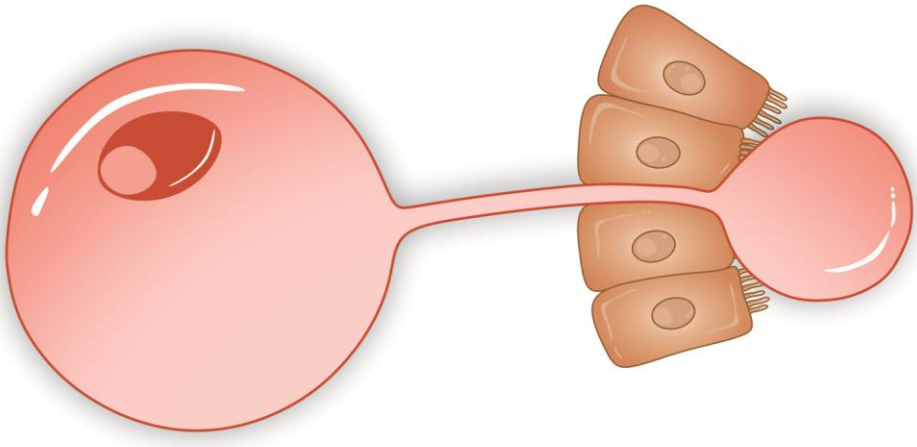

# VI. REFERENCES


Adasme T, Paula-Lima A & Hidalgo C (2015). Inhibitory ryanodine prevents ryanodine receptor-mediated $Ca^{2+}$ release without affecting endoplasmic reticulum $Ca^{2+}$ content in primary hippocampal neurons. *Biochem Biophys Res Commun* **458,** 57–62.

Alzayady KJ, Wang L, Chandrasekhar R, Wagner LE, Van Petegem F & Yule DI (2016). Defining the Stoichiometry of Inositol 1,4,5-Trisphosphate Binding Required to Initiate $Ca^{2+}$ Release. *Sci Signal* **9,** ra35.

Andrews RJ, Bringas JR & Alonzo G (1994). Cerebrospinal Fluid pH and PCO2 Rapidly Follow Arterial Blood pH and $P_{CO2}$ with Changes in Ventilation. *Neurosurgery* **34,** 466–470.

Aosaki T & Kasai H (1989). Characterization of two kinds of high-voltage-activated Ca-channel currents in chick sensory neurons: Differential sensitivity to dihydropyridines and ω-conotoxin GVIA. *Pflüg Arch Eur J Physiol* **414,** 150–156.

Armbruster BN, Li X, Pausch MH, Herlitze S & Roth BL (2007). Evolving the lock to fit the key to create a family of G protein-coupled receptors potently activated by an inert ligand. *Proc Natl Acad Sci U S A* **104,** 5163–5168.

Avaliani N, Andersson M, Runegaard AH, Woldbye D & Kokaia M (2016). DREADDs suppress seizure-like activity in a mouse model of pharmacoresistant epileptic brain tissue. *Gene Ther* **23,** 760–766.

Bae Y-S (2003). Identification of a Compound That Directly Stimulates Phospholipase C Activity. *Mol Pharmacol* **63,** 1043–1050.

Bannister RA & Beam KG (2013). $Ca_V1.1$: The atypical prototypical voltage-gated $Ca^{2+}$ channel. *Biochim Biophys Acta BBA - Biomembr* **1828,** 1587–1597.

Barber RP, Vaughn JE & Roberts E (1982). The cytoarchitecture of GABAergic neurons in rat spinal cord. *Brain Res* **238,** 305–328.

Bean BP (1989). Neurotransmitter inhibition of neuronal calcium currents by changes in channel voltage dependence. *Nature* **340,** 153–156.

Belles B, Malécot CO, Hescheler J & Trautwein W (1988). “Run-down” of the $Ca^{2+}$ current during long whole-cell recordings in guinea pig heart cells: role of phosphorylation and intracellular calcium. *Pflüg Arch* **411,** 353–360.

Berridge MJ (2016). The Inositol Trisphosphate/Calcium Signaling Pathway in Health and Disease. *Physiol Rev* **96,** 1261–1296.

Berridge MJ, Bootman MD & Lipp P (1998). Calcium - a life and death signal. *Nature* **395,** 645–648.

Bers DM (2002). Cardiac excitation–contraction coupling. **415,** 10.

Bettler B, Kaupmann K, Mosbacher J & Gassmann M (2004). Molecular structure and physiological functions of GABA(B) receptors. *Physiol Rev* **84,** 835–867.

Bezprozvanny I (1991). Bell-shaped calcium-response curves of lns(l,4,5)P 3 - and calcium-gated channels from endoplasmic reticulum of cerebellum | Nature. Available at: https://www-nature-com.insb.bib.cnrs.fr/articles/351751a0 [Accessed March 11, 2019].

Bezprozvanny I, Scheller RH & Tsien RW (1995). Functional impact of syntaxin on gating of N-type and Q-type calcium channels. *Nature* **378,** 623–626.

Bishop GA, Berbari NF, Lewis J & Mykytyn K (2007). Type III adenylyl cyclase localizes to primary cilia throughout the adult mouse brain. *J Comp Neurol* **505,** 562–571.

Bjorefeldt A, Illes S, Zetterberg H & Hanse E (2018). Neuromodulation via the Cerebrospinal Fluid: Insights from Recent in Vitro Studies. *Front Neural Circuits*; DOI: 10.3389/fncir.2018.00005.

Black JL (2003). The Voltage-Gated Calcium Channel γ Subunits: A Review of the Literature. *J Bioenerg Biomembr* **35,** 649–660.

Böhm UL, Prendergast A, Djenoune L, Nunes Figueiredo S, Gomez J, Stokes C, Kaiser S, Suster M, Kawakami K, Charpentier M, Concordet J-P, Rio J-P, Del Bene F & Wyart C (2016). CSF-contacting neurons regulate locomotion by relaying mechanical stimuli to spinal circuits. *Nat Commun* **7,** 10866.

Boland M, Morrill A & Bean P (1994). w-Conotoxin Block of N-Type Calcium Channels in Frog and Rat Sympathetic Neurons. *J Neurosci*17.

Booker SA, Loreth D, Gee AL, Watanabe M, Kind PC, Wyllie DJA, Kulik Á & Vida I (2018). Postsynaptic $GABA_BRs$ Inhibit L-Type Calcium Channels and Abolish Long-Term Potentiation in Hippocampal Somatostatin Interneurons. *Cell Rep* **22,** 36–43.

Bootman MD, Rietdorf K, Collins T, Walker S & Sanderson M (2013). $Ca^{2+}$-Sensitive Fluorescent Dyes and Intracellular $Ca^{2+}$ Imaging. *Cold Spring Harb Protoc* **2013,** pdb.top066050.

Bourinet E, Soong TW, Stea A & Snutch TP (1996). Determinants of the G protein-dependent opioid modulation of neuronal calcium channels. *Proc Natl Acad Sci U S A* **93,** 1486–1491.

Bourinet E & Stotz SC (2001). Interaction of SNX482 with Domains III and IV Inhibits Activation Gating of $\alpha_{1E}$ ($Ca_V2.3$) Calcium Channels. *Biophys J*10.

Bouzinova EV, Praetorius J, Virkki LV, Nielsen S, Boron WF & Aalkjaer C (2005). $Na^+$-dependent $HCO_3^-$ uptake into the rat choroid plexus epithelium is partially DIDS sensitive. *Am J Physiol-Cell Physiol* **289,** C1448–C1456.

Brandt A, Striessnig J & Moser T (2003). CaV1.3 Channels Are Essential for Development and Presynaptic Activity of Cochlear Inner Hair Cells. *J Neurosci* **23,** 10832–10840.

Breunig JJ, Arellano JI & Rakic P (2010). Cilia in the brain: going with the flow. *Nat Neurosci* **13,** 654–655.

Britt JP, McDevitt RA & Bonci A (2012). Use of channelrhodopsin for activation of CNS neurons. *Curr Protoc Neurosci Editor Board Jacqueline N Crawley Al* **CHAPTER,** Unit2.16.

Brown PD, Davies SL, Speake T & Millar ID (2004). Molecular mechanisms of cerebrospinal fluid production. *Neuroscience* **129,** 957–970.

Brownstone RM & Bui TV (2010). Spinal interneurons providing input to the final common path during locomotion. *Prog Brain Res* **187,** 81–95.

Budde T, Meuth S & Pape H-C (2002). Calcium-dependent inactivation of neuronal calcium channels. *Nat Rev Neurosci* **3,** 873–883.

Bull R, Marengo JJ, Suárez-Isla BA, Donoso P, Sutko JL & Hidalgo C (1989). Activation of calcium channels in sarcoplasmic reticulum from frog muscle by nanomolar concentrations of ryanodine. *Biophys J* **56,** 749–756.

Buraei Z & Yang J (2013). Structure and function of the β subunit of voltage-gated $Ca^{2+}$ channels. *Biochim Biophys Acta BBA - Biomembr* **1828,** 1530–1540.

Cabrera-Vera TM, Vanhauwe J, Thomas TO, Medkova M, Preininger A, Mazzoni MR & Hamm HE (2003). Insights into G Protein Structure, Function, and Regulation. *Endocr Rev* **24,** 765–781.

Camacho P, John L, Li Y, Paredes RM & Roderick HL (2013). *Calnexin and Calreticulin, ER Associated Modulators of Calcium Transport in the ER*. Landes Bioscience. Available at: https://www.ncbi.nlm.nih.gov/books/NBK6325/ [Accessed March 12, 2019].

Camello C, Lomax R, Petersen OH & Tepikin AV (2002). Calcium leak from intracellular stores—the enigma of calcium signalling. *Cell Calcium* **32,** 355–361.

Campiglio M & Flucher BE (2015). The Role of Auxiliary Subunits for the Functional Diversity of Voltage-Gated Calcium Channels. *J Cell Physiol* **230,** 2019–2031.

Catterall WA (2000). Structure and Regulation of Voltage-Gated $Ca^{2+}$ Channels. *Annu Rev Cell Dev Biol* **16,** 521–555.

Catterall WA (2011). Voltage-gated calcium channels. *Cold Spring Harb Perspect Biol* **3,** a003947.

Catterall WA & Few AP (2008). Calcium Channel Regulation and Presynaptic Plasticity. *Neuron* **59,** 882–901.

Caulfield MP (1993). Muscarinic Receptors—Characterization, coupling and function. *Pharmacol Ther* **58,** 319–379.

Cens T, Rousset M, Leyris J, Fesquet P & Charnet P (2006). Voltage- and calcium-dependent inactivation in high voltage-gated $Ca^{2+}$ channels. *Prog Biophys Mol Biol* **90,** 104–117.

Chen G & van den Pol AN (1998). Presynaptic $GABA_B$ autoreceptor modulation of P/Q-type calcium channels and GABA release in rat suprachiasmatic nucleus neurons. *J Neurosci Off J Soc Neurosci* **18,** 1913–1922.

Chen R-S, Deng T-C, Garcia T, Sellers ZM & Best PM (2007). Calcium channel γ subunits: a functionally diverse protein family. *Cell Biochem Biophys* **47,** 178–186.

Chen XZ, Vassilev PM, Basora N, Peng JB, Nomura H, Segal Y, Brown EM, Reeders ST, Hediger MA & Zhou J (1999). Polycystin-L is a calcium-regulated cation channel permeable to calcium ions. *Nature* **401,** 383–386.

Choe W, Messinger RB, Leach E, Eckle V-S, Obradovic A, Salajegheh R, Jevtovic-Todorovic V & Todorovic SM (2011). TTA-P2 Is a Potent and Selective Blocker of T-Type Calcium Channels in Rat Sensory Neurons and a Novel Antinociceptive Agent. *Mol Pharmacol* **80,** 900-910.

Christensen MS (1974). Acid-base changes in cerebrospinal fluid and blood, and blood volume changes following prolonged hyperventilation in man. *Br J Anaesth* **46,** 348–357.

Corns LF, Atkinson L, Daniel J, Edwards IJ, New L, Deuchars J & Deuchars SA (2015). Cholinergic Enhancement of Cell Proliferation in the Postnatal Neurogenic Niche of the Mammalian Spinal Cord. *Stem Cells Dayt Ohio* **33,** 2864–2876.

Corns LF, Deuchars J & Deuchars SA (2013). GABAergic responses of mammalian ependymal cells in the central canal neurogenic niche of the postnatal spinal cord. *Neurosci Lett* **553,** 57–62.

Currie KP & Fox AP (1997). Comparison of N- and P/Q-type voltage-gated calcium channel current inhibition. *J Neurosci Off J Soc Neurosci* **17,** 4570–4579.

Dai S, Hall DD & Hell JW (2009). Supramolecular Assemblies and Localized Regulation of Voltage-Gated Ion Channels. *Physiol Rev* **89,** 411–452.

Dale N, Roberts A, Ottersen OP & Storm-Mathisen J (1987). The morphology and distribution of "Kolmer-Agduhr cells", a class of cerebrospinal-fluid-contacting neurons revealed in the frog embryo spinal cord by GABA immunocytochemistry. *Proc R Soc Lond Ser B Contain Pap Biol Character R Soc G B* **232,** 193–203.

Damkier HH, Brown PD & Praetorius J (2013). Cerebrospinal Fluid Secretion by the Choroid Plexus. *Physiol Rev* **93,** 1847–1892.

David F, Schmiedt JT, Taylor HL, Orban G, Di Giovanni G, Uebele VN, Renger JJ, Lambert RC, Leresche N & Crunelli V (2013). Essential Thalamic Contribution to Slow Waves of Natural Sleep. *J Neurosci* **33**, 19599-19610.

Davies A, Hendrich J, Van Minh AT, Wratten J, Douglas L & Dolphin AC (2007). Functional biology of the α2δ subunits of voltage-gated calcium channels. *Trends Pharmacol Sci* **28,** 220–228.

Davies A, Kadurin I, Alvarez-Laviada A, Douglas L, Nieto-Rostro M, Bauer CS, Pratt WS & Dolphin AC (2010). The α2δ subunits of voltage-gated calcium channels form GPI-anchored proteins, a posttranslational modification essential for function. *Proc Natl Acad Sci* **107,** 1654–1659.

Davson H, Welch K & Sagal MB (1988). The physiology and pathophysiology of the cerebrospinal fluid by Hugh Davson, Keasley Welch, and Malcolm B. Segal New York. Livingstone, I987. *Ann Neurol* **24,** 106–106.

DeCaen PG, Liu X, Abiria S & Clapham DE (2016). Atypical calcium regulation of the PKD2-L1 polycystin ion channel. *eLife*; DOI: 10.7554/eLife.13413.

Delmas P, Abogadie FC, Dayrell M, Haley JE, Milligan G, Caulfield MP, Brown DA & Buckley NJ (1998). G-proteins and G-protein subunits mediating cholinergic inhibition of N-type calcium currents in sympathetic neurons: G-protein mechanisms in cholinergic inhibition of $I_{Ca}$. *Eur J Neurosci* **10,** 1654–1666.

Di Terlizzi R & Platt S (2006). The function, composition and analysis of cerebrospinal fluid in companion animals: Part I – Function and composition. *Vet J* **172,** 422–431.

Dietrich D, Kirschstein T, Kukley M, Pereverzev A, von der Brelie C, Schneider T & Beck H (2003). Functional Specialization of Presynaptic $Ca_v2.3$ $Ca^{2+}$ Channels. *Neuron* **39,** 483–496.

Djenoune L, Desban L, Gomez J, Sternberg JR, Prendergast A, Langui D, Quan FB, Marnas H, Auer TO, Rio J-P, Del Bene F, Bardet P-L & Wyart C (2017). The dual developmental origin of spinal cerebrospinal fluid-contacting neurons gives rise to distinct functional subtypes. *Sci Rep* **7,** 719.

Djenoune L, Khabou H, Joubert F, Quan FB, Nunes Figueiredo S, Bodineau L, Del Bene F, Burcklé C, Tostivint H & Wyart C (2014). Investigation of spinal cerebrospinal fluid-contacting neurons expressing PKD2L1: evidence for a conserved system from fish to primates. *Front Neuroanat* **8,** 26.

Doering CJ, Hamid J, Simms B, McRory JE & Zamponi GW (2005). $Ca_v1.4$ Encodes a Calcium Channel with Low Open Probability and Unitary Conductance. *Biophys J* **89,** 3042–3048.

Dolphin AC (1995). The G.L. Brown Prize Lecture. Voltage-dependent calcium channels and their modulation by neurotransmitters and G proteins. *Exp Physiol* **80,** 1–36.

Dolphin AC (2003). G protein modulation of voltage-gated calcium channels. *Pharmacol Rev* **55,** 607–627.

Dolphin AC (2009). A short history of voltage-gated calcium channels: Voltage-gated calcium channels. *Br J Pharmacol* **147,** S56–S62.

Dolphin AC (2012). Calcium channel auxiliary α2δ and β subunits: trafficking and one step beyond. *Nat Rev Neurosci* **13,** 542–555.

Dreyfus FM, Tscherter A, Errington AC, Renger JJ, Shin H-S, Uebele VN, Crunelli V, Lambert RC & Leresche N (2010). Selective T-Type Calcium Channel Block in

Thalamic Neurons Reveals Channel Redundancy and Physiological Impact on $I_{Twindow}$. *J Neurosci* **30,** 99-109.

Fatt P & Ginsborg BL (1958). The ionic requirements for the production of action potentials in crustacean muscle fibres. *J Physiol* **142,** 516–543.

Fatt P & Katz B (1953). The electrical properties of crustacean muscle fibres. *J Physiol* **120,** 171–204.

Fernandez-Fernandez JM, Wanaverbecq N, Halley P, Caulfield MP & Brown DA (1999). Selective activation of heterologously expressed G protein-gated $K^+$ channels by $M_2$ muscarinic receptors in rat sympathetic neurones. *J Physiol* **515 ( Pt 3),** 631–637.

Fidelin K, Djenoune L, Stokes C, Gomez J, Baradel A, Del Bene F & Wyart C (2015). State-Dependent Modulation of Locomotion by GABAergic Spinal Sensory Neurons. *Curr Biol* **25,** 1–13.

Fill M & Copello JA (2002). Ryanodine Receptor Calcium Release Channels. *Physiol Rev* **82,** 893–922.

Finch E a. & Turner T j. (1991). Calcium as a coagonist of inositol 1,4,5-trisphosphate-induced calcium release. *Science* **252,** 443.

Fox AP, Nowycky MC & Tsien RW (1987). Kinetic and pharmacological properties distinguishing three types of calcium currents in chick sensory neurones. *J Physiol* **394,** 149–172.

Fujita T, Kanno T & Kobayashi S (2012). *The Paraneuron*. Springer Science & Business Media.

Galvez T (2001). Allosteric interactions between $G_{B1}$ and$G_{B2}$ subunits are required for optimal$GABA_B$ receptor function. *EMBO J* **20,** 2152–2159.

Galvez T, Parmentier M-L, Joly C, Malitschek B, Kaupmann K, Kuhn R, Bittiger H, Froestl W, Bettler B & Pin J-P (1999). Mutagenesis and Modeling of the $GABA_B$ Receptor Extracellular Domain Support a Venus Flytrap Mechanism for Ligand Binding. *J Biol Chem* **274,** 13362–13369.

Gees M, Colsoul B & Nilius B (2010). The role of transient receptor potential cation channels in $Ca^{2+}$ signaling. *Cold Spring Harb Perspect Biol* **2,** a003962.

Giamarchi A, Feng S, Rodat-Despoix L, Xu Y, Bubenshchikova E, Newby LJ, Hao J, Gaudioso C, Crest M, Lupas AN, Honoré E, Williamson MP, Obara T, Ong ACM & Delmas P (2010). A polycystin-2 (TRPP2) dimerization domain essential for the function of heteromeric polycystin complexes. *EMBO J* **29,** 1176–1191.

Goldberg NB, Sawinski VJ & Goldberg AF (1965). Human cerebrospinal fluid osmolality at 37°C. *Anesthesiology* **26,** 829.

Gosgnach S, Bikoff JB, Dougherty KJ, El Manira A, Lanuza GM & Zhang Y (2017). Delineating the Diversity of Spinal Interneurons in Locomotor Circuits. *J Neurosci* **37,** 10835–10841.

Grafton G & Thwaite L (2001). Calcium channels in lymphocytes. *Immunology* **104,** 119–126.

Grassi F & Lux HD (1989). Voltage-dependent GABA-induced modulation of calcium currents in chick sensory neurons. *Neurosci Lett* **105,** 113–119.

Grienberger C & Konnerth A (2012). Imaging Calcium in Neurons. *Neuron* **73,** 862–885.

Groth RD, Dunbar RL & Mermelstein PG (2003). Calcineurin regulation of neuronal plasticity. *Biochem Biophys Res Commun* **311,** 1159–1171.

Guerrero-Hernandez A, Dagnino-Acosta A & Verkhratsky A (2010). An intelligent sarco-endoplasmic reticulum $Ca^{2+}$ store: Release and leak channels have differential access to a concealed $Ca^{2+}$ pool. *Cell Calcium* **48,** 143–149.

Gurnett CA, Waard MD & Campbell KP (1996). Dual Function of the Voltage-Dependent $Ca^{2+}$ Channel Subunit in Current Stimulation and Subunit Interaction. 10.

Haemmerle CA dos S, Nogueira MI & Watanabe I (2015). The neural elements in the lining of the ventricular-subventricular zone: making an old story new by high-resolution scanning electron microscopy. *Front Neuroanat*; DOI: 10.3389/fnana.2015.00134.

Hagiwara S (1975). Voltage clamp analysis of two inward current mechanisms in the egg cell membrane of a starfish. *J Gen Physiol* **65,** 617–644.

Hamilton LK, Truong MKV, Bednarczyk MR, Aumont A & Fernandes KJL (2009). Cellular organization of the central canal ependymal zone, a niche of latent neural stem cells in the adult mammalian spinal cord. *Neuroscience* **164,** 1044–1056.

Harayama N, Shibuya I, Tanaka K, Kabashima N, Ueta Y & Yamashita H (1998). Inhibition of N- and P/Q-type calcium channels by postsynaptic $GABA_B$ receptor activation in rat supraoptic neurones. *J Physiol* **509,** 371–383.

Hashimoto K, Engberg G, Shimizu E, Nordin C, Lindström LH & Iyo M (2005). Elevated glutamine/glutamate ratio in cerebrospinal fluid of first episode and drug naive schizophrenic patients. *BMC Psychiatry* **5,** 6.

He R, Zhang J, Yu Y, Jizi L, Wang W & Li M (2018). New Insights Into Interactions of Presynaptic Calcium Channel Subtypes and SNARE Proteins in Neurotransmitter Release. *Front Mol Neurosci*; DOI: 10.3389/fnmol.2018.00213.

van Heijst ANP, Maas AHJ & Visser BF (1966). Comparison of the acid-base balance in cisternal and lumbar cerebrospinal fluid. *Pflüg Arch Für Gesamte Physiol Menschen Tiere* **287,** 242–246.

Heilig M, Zachrisson O, Thorsell A, Ehnvall A, Mottagni-Tabar S, Sjögren M, Åsberg M, Ekman R, Wahlestedt C & Ågren H (2004). Decreased cerebrospinal fluid neuropeptide Y (NPY) in patients with treatment refractory unipolar major depression: preliminary evidence for association with perproNPY gene polymorphism. *J Psychiatr Res* **38,** 113-121.

Helton TD (2005). Neuronal L-Type Calcium Channels Open Quickly and Are Inhibited Slowly. *J Neurosci* **25,** 10247–10251.

Hendry EB (1961). Osmolarity of human serum and of chemical solutions of biologic importance. *Clin Chem* **7,** 154–164.

Herlitze S, Garcia DE, Mackie K, Hille B, Scheuer T & Catterall WA (1996). Modulation of $Ca^{2+}$ channels by G-protein beta gamma subunits. *Nature* **380,** 258–262.

Hernández-Ochoa EO & Schneider MF (2018). Voltage sensing mechanism in skeletal muscle excitation-contraction coupling: coming of age or midlife crisis? *Skelet Muscle*; DOI: 10.1186/s13395-018-0167-9.

Higashida H, Hashii M, Fukuda K, Caulfield MP, Numa S & Brown DA (1990). Selective coupling of different muscarinic acetylcholine receptors to neuronal calcium currents in DNA-transfected cells. *Proc R Soc Lond B Biol Sci* **242,** 68–74.

Higuchi T, Shimizu T, Fujii T, Nilius B & Sakai H (2014). Gating modulation by heat of the polycystin transient receptor potential channel PKD2L1 (TRPP3). *Pflugers Arch*; DOI: 10.1007/s00424-013-1439-1.

Hockerman GH, Peterson BZ, Johnson, and BD & Catterall WA (1997). Molecular determinants of drug binding and action on L-type calcium channels. *Annu Rev Pharmacol Toxicol* **37,** 361–396.

Huang AL, Chen X, Hoon MA, Chandrashekar J, Guo W, Tränkner D, Ryba NJP & Zuker CS (2006). The cells and logic for mammalian sour taste detection. *Nature* **442,** 934–938.

Huang D, Huang S, Peers C, Du X, Zhang H & Gamper N (2015). $GABA_B$ receptors inhibit low-voltage activated and high-voltage activated $Ca^{2+}$ channels in sensory neurons via distinct mechanisms. *Biochem Biophys Res Commun* **465,** 188–193.

Hugnot JP & Franzen R (2011). The spinal cord ependymal region: a stem cell niche in the caudal central nervous system. *Front Biosci J Virtual Libr* **16,** 1044–1059.

Ikeda SR (1991). Double-pulse calcium channel current facilitation in adult rat sympathetic neurones. *J Physiol* **439,** 181–214.

Ikeda SR (1996). Voltage-dependent modulation of N-type calcium channels by G-protein beta gamma subunits. *Nature* **380,** 255–258.

Iliff JJ, Wang M, Liao Y, Plogg BA, Peng W, Gundersen GA, Benveniste H, Vates GE, Deane R, Goldman SA, Nagelhus EA & Nedergaard M (2012). A paravascular pathway facilitates CSF flow through the brain parenchyma and the clearance of interstitial solutes, including amyloid β. *Sci Transl Med* **4,** 147ra111.

Ishikawa T, Kaneko M, Shin H-S & Takahashi T (2005). Presynaptic N-type and P/Q-type Ca2+ channels mediating synaptic transmission at the calyx of Held of mice: Presynaptic N- and P/Q-type $Ca^{2+}$ currents. *J Physiol* **568,** 199–209.

Ivannikov MV, Sugimori M & Llinás RR (2010). Calcium clearance and its energy requirements in cerebellar neurons. *Cell Calcium* **47,** 507–513.

Jalalvand E, Robertson B, Tostivint H, Löw P, Wallén P & Grillner S (2018). Cerebrospinal Fluid-Contacting Neurons Sense pH Changes and Motion in the Hypothalamus. *J Neurosci* **38,** 7713–7724.

Jalalvand E, Robertson B, Tostivint H, Wallén P & Grillner S (2016*a*). The Spinal Cord Has an Intrinsic System for the Control of pH. *Curr Biol CB* **26,** 1346–1351.

Jalalvand E, Robertson B, Wallén P & Grillner S (2016*b*). Ciliated neurons lining the central canal sense both fluid movement and pH through ASIC3. *Nat Commun* **7,** 10002.

Jalalvand E, Robertson B, Wallén P, Hill RH & Grillner S (2014). Laterally projecting cerebrospinal fluid-contacting cells in the lamprey spinal cord are of two distinct types. *J Comp Neurol* **522,** 1753–1768.

Jay M & McDearmid JR (2015). Motor Control: The Curious Case of Cerebrospinal-Fluid-Contacting Neurons. *Curr Biol* **25,** R1138–R1140.

Jay SD, Ellis SB, Mccue AF, Willlams ME, Vedvick TS, Harpold MM & Campbell KP (1990). Primary Structure of the y Subunit of the DHP- Sensitive Calcium Channel from Skeletal Muscle.

Jessen NA, Munk ASF, Lundgaard I & Nedergaard M (2015). The Glymphatic System: A Beginner's Guide. *Neurochem Res* **40,** 2583–2599.

Johanson CE, Donahue JE, Spangenberger A, Stopa EG, Duncan JA & Sharma HS (2006). Atrial natriuretic peptide: its putative role in modulating the choroid plexus-CSF system for intracranial pressure regulation. *Acta Neurochir Suppl* **96,** 451–456.

Johanson CE, Duncan JA 3rd, Klinge PM, Brinker T, Stopa EG & Silverberg GD (2008). Multiplicity of cerebrospinal fluid functions: New challenges in health and disease. *Cerebrospinal Fluid Res* **5,** 10.

Jones LP, Patil PG, Snutch TP & Yue DT (1997). G-protein modulation of N-type calcium channel gating current in human embryonic kidney cells (HEK 293). *J Physiol* **498,** 601–610.

Jurčić N, Er-Raoui G, Airault C, Trouslard J, Wanaverbecq N & Seddik R (2019). $GABA_B$ receptors modulate $Ca^{2+}$ but not G protein-gated inwardly rectifying $K^+$ channels in cerebrospinal-fluid contacting neurones of mouse brainstem. *J Physiol* **597,** 631–651.

Juul R, Hara H, Gisvold SE, Brubakk AO, Fredriksen TA, Waldemar G, Schmidt JF, Ekman R & Edvinsson L (1995). Alterations in perivascular dilatory neuropeptides (CGRP, SP, VIP) in the external jugular vein and in the cerebrospinal fluid following subarachnoid haemorrhage in man. *Acta Neurochir (Wien)* **132,** 32–41.

Kaja S, Hilgenberg JD, Rybalchenko V, Medina-Ortiz WE, Gregg EV & Koulen P (2011). Polycystin-2 expression and function in adult mouse lacrimal acinar cells. *Invest Ophthalmol Vis Sci* **52,** 5605–5611.

Kammermeier PJ, Ruiz-Velasco V & Ikeda SR (2000). A Voltage-Independent Calcium Current Inhibitory Pathway Activated by Muscarinic Agonists in Rat Sympathetic Neurons Requires Both $G\alpha_{q/11}$ and $G\beta\gamma$. *J Neurosci* **20,** 5623–5629.

Khasawneh AH, Garling RJ & Harris CA (2018). Cerebrospinal fluid circulation: What do we know and how do we know it? *Brain Circ* **4,** 14–18.

Kirischuk S, Voitenko N, Kostyuk P & Verkhratsky A (1996). Calcium signalling in granule neurones studied in cerebellar slices. *Cell Calcium* **19,** 59–71.

Klugbauer N, Marais E & Hofmann F (2003). Calcium Channel α2δ Subunits: Differential Expression, Function, and Drug Binding. *J Bioenerg Biomembr*639–647.

van der Knaap MS, Wevers RA, Kure S, Gabreëls FJM, Verhoeven NM, van Raaij-Selten B & Jaeken J (1999). Increased Cerebrospinal Fluid Glycine: A Biochemical Marker for a Leukoencephalopathy With Vanishing White Matter. *J Child Neurol* **14,** 728–731.

Koschak A, Reimer D, Huber I, Grabner M, Glossmann H, Engel J & Striessnig J (2001). α1D (Cav1.3) Subunits Can Form L-type $Ca^{2+}$ Channels Activating at Negative Voltages. *J Biol Chem* **276,** 22100–22106.

Koschak A, Reimer D, Walter D, Hoda J-C, Heinzle T, Grabner M & Striessnig J (2003). $Ca_v1.4α1$ Subunits Can Form Slowly Inactivating Dihydropyridine-Sensitive L-Type $Ca^{2+}$ Channels Lacking Ca2+-Dependent Inactivation. *J Neurosci* **23,** 6041–6049.

Krashes MJ, Koda S, Ye C, Rogan SC, Adams AC, Cusher DS, Maratos-Flier E, Roth BL & Lowell BB (2011). Rapid, reversible activation of AgRP neurons drives feeding behavior in mice. *J Clin Invest* **121,** 1424–1428.

Krjukova J, Holmqvist T, Danis AS, Åkerman KEO & Kukkonen JP (2004). Phospholipase C activator m-3M3FBS affects $Ca^{2+}$ homeostasis independently of phospholipase C activation. *Br J Pharmacol* **143,** 3–7.

Kuo IY & Ehrlich BE (2015). Signaling in Muscle Contraction. *Cold Spring Harb Perspect Biol* **7,** a006023.

Kuroda H, Ogawa N, Yamawaki Y, Nukina I, Ofuji T, Yamamoto M & Otsuki S (1982). Cerebrospinal fluid GABA levels in various neurological and psychiatric diseases. *J Neurol Neurosurg Psychiatry* **45,** 257–260.

Kútna V, Sevc J, Gombalová Z, Matiašová A & Daxnerová Z (2013). Enigmatic cerebrospinal fluid-contacting neurons arise even after the termination of neurogenesis in the rat spinal cord during embryonic development and retain their immature-like characteristics until adulthood. *Acta Histochem*; DOI: 10.1016/j.acthis.2013.08.004.

Kvamme E (1988). Glutamine and glutamate in mammals vol II. Available at: http://b-ok.cc/book/3495849/b47710.

Lambert NA & Wilson WA (1996). High-threshold $Ca^{2+}$ currents in rat hippocampal interneurones and their selective inhibition by activation of GABA(B) receptors. *J Physiol* **492,** 115–127.

LaMotte CC (1987). Vasoactive intestinal polypeptide cerebrospinal fluid-contacting neurons of the monkey and cat spinal central canal. *J Comp Neurol* **258,** 527–541.

LaMotte CC & de Lanerolle NC (1986). VIP terminals, axons, and neurons: distribution throughout the length of monkey and cat spinal cord. *J Comp Neurol* **249,** 133–145.

Lanner JT, Georgiou DK, Joshi AD & Hamilton SL (2010). Ryanodine Receptors: Structure, Expression, Molecular Details, and Function in Calcium Release. *Cold Spring Harb Perspect Biol* **2,** a003996–a003996.

Lee A, Wang S, Williams B, Hagen J, Scheetz TE & Haeseleer F (2015). Characterization of $Ca_v1.4$ Complexes (α11.4, β2, and α2δ4) in HEK293T Cells and in the Retina. *J Biol Chem* **290,** 1505–1521.

Lee A, Westenbroek RE, Haeseleer F, Palczewski K, Scheuer T & Catterall WA (2002). Differential modulation of $Ca_v2.1$ channels by calmodulin and $Ca^{2+}$-binding protein 1. *Nat Neurosci* **5,** 210–217.

Lee A, Wong ST, Gallagher D, Li B, Storm DR, Scheuer T & Catterall WA (1999*a*). $Ca^{2+}$/calmodulin binds to and modulates P/Q-type calcium channels. *Nature* **399,** 155–159.

Lee J, Kim D & Shin H-S (2004). Lack of delta waves and sleep disturbances during non-rapid eye movement sleep in mice lacking $\alpha 1_G$-subunit of T-type calcium channels. *Proc Natl Acad Sci* **101,** 18195–18199.

Lee J-H, Gomora JC, Cribbs LL & Perez-Reyes E (1999*b*). Nickel Block of Three Cloned T-Type Calcium Channels: Low Concentrations Selectively Block α1H. *Biophys J* **77,** 9.

Li W-G & Xu T-L (2011). ASIC3 Channels in Multimodal Sensory Perception. *ACS Chem Neurosci* **2,** 26–37.

Lipscombe D, Helton TD & Xu W (2004). L-Type Calcium Channels: The Low Down. *J Neurophysiol* **92,** 2633–2641.

Llinás RR, Sugimori M & Cherksey B (1989). Voltage-Dependent Calcium Conductances in Mammalian Neurons. *Ann N Y Acad Sci* **560,** 103–111.

Luebke JI & Dunlap K (1994). Sensory neuron N-type calcium currents are inhibited by both voltage-dependent and -independent mechanisms. *Pflüg Arch Eur J Physiol* **428,** 499–507.

MacLennan DH, Rice WJ & Green NM (1997). The Mechanism of $Ca^{2+}$ Transport by Sarco(Endo)plasmic Reticulum $Ca^{2+}$-ATPases. *J Biol Chem* **272,** 28815–28818.

Madisen L et al. (2012). A toolbox of Cre-dependent optogenetic transgenic mice for light-induced activation and silencing. *Nat Neurosci* **15,** 793–802.

Mangoni ME, Couette B, Bourinet E, Platzer J, Reimer D, Striessnig J & Nargeot J (2003). Functional role of L-type $Ca_v1.3$ $Ca^{2+}$ channels in cardiac pacemaker activity. *Proc Natl Acad Sci* **100,** 5543–5548.

Marder E & Bucher D (2001). Central pattern generators and the control of rhythmic movements. *Curr Biol CB* **11,** R986-996.

Margeta-Mitrovic M, Jan YN & Jan LY (2001). Function of $G_{B1}$ and $G_{B2}$ subunits in G protein coupling of $GABA_{(B)}$ receptors. *Proc Natl Acad Sci U S A* **98,** 14649–14654.

Margeta-Mitrovic M, Mitrovic I, Riley RC, Jan LY & Basbaum AI (1999). Immunohistochemical localization of $GABA_{(B)}$ receptors in the rat central nervous system. *J Comp Neurol* **405,** 299–321.

Marichal N, García G, Radmilovich M, Trujillo-Cenóz O & Russo RE (2009). Enigmatic central canal contacting cells: immature neurons in "standby mode"? *J Neurosci Off J Soc Neurosci* **29,** 10010–10024.

McCafferty C, David F, Venzi M, Lőrincz ML, Delicata F, Atherton Z, Recchia G, Orban G, Lambert RC, Di Giovanni G, Leresche N & Crunelli V (2018). Cortical drive and thalamic feed-forward inhibition control thalamic output synchrony during absence seizures. Nat Neurosci 21, 744-756.

McCleskey EW, Foxt AP, Feldman DH, Cruz LJ, Olivera BM & Tsien RW (1987). ω-Conotoxin: Direct and persistent blockade of specific types of calcium channels in neurons but not muscle. *Proc Natl Acad Sci*5.

McDonough SI, Mintz IM & Bean BP (1997). Alteration of P-Type Calcium Channel Gating by the Spider Toxin ω-Aga-IVA. *Biophys J* **72,** 12.

Meissner G (2017). The structural basis of ryanodine receptor ion channel function. *J Gen Physiol* **149,** 1065–1089.

Mermelstein PG, Foehring RC, Tkatch T, Song W-J, Baranauskas G & Surmeier DJ (1999). Properties of Q-Type Calcium Channels in Neostriatal and Cortical Neurons are Correlated with β Subunit Expression. *J Neurosci* **19,** 7268–7277.

Messeter K & Siesjö BK (1971). Regulation of the CSF pH in Acute and Sustained Respiratory Acidosis. *Acta Physiol Scand* **83,** 21–30.

Meuth S, Pape H-C & Budde T (2002). Modulation of $Ca^{2+}$ currents in rat thalamocortical relay neurons by activity and phosphorylation: $Ca^{2+}$ current inactivation in thalamocortical neurons. *Eur J Neurosci* **15,** 1603–1614.

Miles GB, Hartley R, Todd AJ & Brownstone RM (2007). Spinal cholinergic interneurons regulate the excitability of motoneurons during locomotion. *Proc Natl Acad Sci U S A* **104,** 2448–2453.

Millar ID & Brown PD (2008). NBCe2 exhibits a 3 $HCO_3^-$:1 $Na^+$ stoichiometry in mouse choroid plexus epithelial cells. *Biochem Biophys Res Commun* **373,** 550–554.

Mintz IM, Adams ME & Bean BP (1992*a*). P-type calcium channels in rat central and peripheral neurons. *Neuron* **9,** 85–95.

Mintz IM & Bean BP (1993). GABAB Receptor Inhibition of P-type $Ca^{2+}$ Channels in Central Neurons. *Neuron* **10,** 889–898.

Mintz IM, Swiderek KM, Lee TD, Bean BP & Adamst ME (1992*b*). P-type calcium channels blocked by the spider toxin ω-Aga.IV A. 3.

Moore SA (2016). The Spinal Ependymal Layer in Health and Disease. *Vet Pathol* **53,** 746–753.

Moosmang S (2003). Dominant role of smooth muscle L-type calcium channel $Ca_v1.2$ for blood pressure regulation. *EMBO J* **22,** 6027–6034.

Nagatsu I, Sakai M, Yoshida M & Nagatsu T (1988). Aromatic L-amino acid decarboxylase-immunoreactive neurons in and around the cerebrospinal fluid-contacting neurons of the central canal do not contain dopamine or serotonin in the mouse and rat spinal cord. *Brain Res* **475,** 91–102.

Nelson M, Todorovic S & Perez-Reyes E (2006). The Role of T-Type Calcium Channels in Epilepsy and Pain. *Curr Pharm Des* **12,** 2189–2197.

Newcomb R, Szoke B, Palma A, Wang G, Chen X, Hopkins W, Cong R, Miller J, Urge L, Tarczy-Hornoch K, Loo JA, Dooley DJ, Nadasdi L, Tsien RW, Lemos J & Miljanich G (1998). Selective Peptide Antagonist of the Class E Calcium Channel from the Venom of the Tarantula *Hysterocrates gigas*. *Biochemistry* **37,** 15353–15362.

Nilius B & Owsianik G (2011). The transient receptor potential family of ion channels. *Genome Biol* **12,** 218.

Nimmrich V & Gross G (2012). P/Q-type calcium channel modulators: P/Q-type calcium channel blockers. *Br J Pharmacol* **167,** 741–759.

Noda M & Sakuta H (2013). Central regulation of body-fluid homeostasis. *Trends Neurosci* **36,** 661–673.

Nowycky MC, Fox AP & Tsien RW (1985). Three types of neuronal calcium channel with different calcium agonist sensitivity. *Nature* **316,** 440–443.

Oreskovi ć D & Klarica M (2010). The formation of cerebrospinal fluid: nearly a hundred years of interpretations and misinterpretations. *Brain Res Rev* **64,** 241–262.

Orhan F, Fatouros-Bergman H, Goiny M, Malmqvist A, Piehl F, Cervenka S, Collste K, Victorsson P, Sellgren CM, Flyckt L, Erhardt S & Engberg G (2018). CSF GABA is reduced in first-episode psychosis and associates to symptom severity. *Mol Psychiatry* **23,** 1244–1250.

Orts Del'Immagine A, Seddik R, Tell F, Airault C, Er-Raoui G, Najimi M, Trouslard J & Wanaverbecq N (2015). A single polycystic kidney disease 2-like 1 channel opening acts as a spike generator in cerebrospinal fluid-contacting neurons of adult mouse brainstem. *Neuropharmacology*; DOI: 10.1016/j.neuropharm.2015.07.030.

Orts-Del'Immagine A, Kastner A, Tillement V, Tardivel C, Trouslard J & Wanaverbecq N (2014). Morphology, distribution and phenotype of polycystin kidney disease 2-like 1-positive cerebrospinal fluid contacting neurons in the brainstem of adult mice. *PloS One* **9,** e87748.

Orts-Del'Immagine A, Trouslard J, Airault C, Hugnot J-P, Cordier B, Doan T, Kastner A & Wanaverbecq N (2017). Postnatal maturation of mouse medullo-spinal cerebrospinal fluid-contacting neurons. *Neuroscience* **343,** 39–54.

Orts-Del'Immagine A, Wanaverbecq N, Tardivel C, Tillement V, Dallaporta M & Trouslard J (2012). Properties of subependymal cerebrospinal fluid contacting neurones in the dorsal vagal complex of the mouse brainstem. *J Physiol* **590,** 3719–3741.

Oshio K, Watanabe H, Song Y, Verkman AS & Manley GT (2005). Reduced cerebrospinal fluid production and intracranial pressure in mice lacking choroid plexus water channel Aquaporin-1. *FASEB J Off Publ Fed Am Soc Exp Biol* **19,** 76–78.

Padgett CL & Slesinger PA (2010). $GABA_B$ receptor coupling to G-proteins and ion channels. *Adv Pharmacol San Diego Calif* **58,** 123–147.

Park H-C, Shin J & Appel B (2004). Spatial and temporal regulation of ventral spinal cord precursor specification by Hedgehog signaling. *Dev Camb Engl* **131,** 5959–5969.

Paterson CR, Griffiths PD & Craig JA (1971). Diagnostic Value of Estimations of the Cerebrospinal Fluid *Gamma* - Globulin. *Ann Clin Biochem Int J Biochem Lab Med* **8,** 163–167.

Peng W, Shen H, Wu J, Guo W, Pan X, Wang R, Chen SRW & Yan N (2016). Structural basis for the gating mechanism of the type 2 ryanodine receptor RyR2. *Science* **354,** aah5324.

Pérez-Garci E, Larkum ME & Nevian T (2013). Inhibition of dendritic $Ca^{2+}$ spikes by $GABA_B$ receptors in cortical pyramidal neurons is mediated by a direct Gi/o-βγ-subunit interaction with Cav1 channels. *J Physiol* **591,** 1599–1612.

Perez-Reyes E (2003). Molecular Physiology of Low-Voltage-Activated T-type Calcium Channels. *Physiol Rev* **83,** 117–161.

Perez-Reyes E, Cribbs LL, Daud A, Lacerda AE, Barclay J, Williamson MP, Fox M, Rees M & Lee J-H (1998). Molecular characterization of a neuronal low-voltage-activated T-type calcium channel. *Nature* **391,** 896–900.

Perez-Reyes E, Kimt HS, Lacerda AE, Horne W, Wei X, Rampe D, Campbell KP & Brown AM (1989). Induction of calcium currents by the expression of the a 1-subunit of the dihydropyridine receptor from skeletal muscle. **340,** 4.

Peterson BZ, Tanada TN & Catterall WA (1996). Molecular Determinants of High Affinity Dihydropyridine Binding in L-type Calcium Channels. *J Biol Chem* **271,** 5293–5296.

Petracca YL, Sartoretti MM, Di Bella DJ, Marin-Burgin A, Carcagno AL, Schinder AF & Lanuza GM (2016). The late and dual origin of cerebrospinal fluid-contacting neurons in the mouse spinal cord. *Dev Camb Engl* **143,** 880–891.

Pierani A, Moran-Rivard L, Sunshine MJ, Littman DR, Goulding M & Jessell TM (2001). Control of interneuron fate in the developing spinal cord by the progenitor homeodomain protein Dbx1. *Neuron* **29,** 367–384.

Pin JP, Joly C, Heinemann SF & Bockaert J (1994). Domains involved in the specificity of G protein activation in phospholipase C-coupled metabotropic glutamate receptors. *EMBO J* **13,** 342–348.

Pinheiro J, DebRoy S, Sarkar D & R Core Team (2016). nlme: Linear and nonlinear mixed effects models. Availabe at: https://cran.r-project.org/web/packages/nlme/citation.html [Accessed October 4, 2016].

Platzer J, Engel J, Schrott-Fischer A, Stephan K, Bova S, Chen H, Zheng H & Striessnig J (2000). Congenital Deafness and Sinoatrial Node Dysfunction in Mice Lacking Class D L-Type $Ca^{2+}$ Channels. *Cell* **102,** 89–97.

Randall A & Tsien R (1995). Pharmacological dissection of multiple types of $Ca^{2+}$ channel currents in rat cerebellar granule neurons. *J Neurosci* **15,** 2995–3012.

Redzic ZB & Segal MB (2004). The structure of the choroid plexus and the physiology of the choroid plexus epithelium. *Adv Drug Deliv Rev* **56,** 1695–1716.

Reiber H (2001). Dynamics of brain-derived proteins in cerebrospinal fluid. *Clin Chim Acta Int J Clin Chem* **310,** 173–186.

Reiber H (2003). Proteins in cerebrospinal fluid and blood: barriers, CSF flow rate and source-related dynamics. *Restor Neurol Neurosci* **21,** 79–96.

Romaus-Sanjurjo D, Fernández-López B, Sobrido-Cameán D, Barreiro-Iglesias A & Rodicio MC (2016). Cloning of the $GABA_B$ Receptor Subunits B1 and B2 and their Expression in the Central Nervous System of the Adult Sea Lamprey. *Front Neuroanat*; DOI: 10.3389/fnana.2016.00118.

Rossier MF, Python CP, Burnay MM, Schlegel W, Vallotton MB & Capponi AM (1993). Thapsigargin inhibits voltage-activated calcium channels in adrenal glomerulosa cells. *Biochem J* **296,** 309–312.

Rudick RA, Zirretta DK & Herndon RM (1982). Clearance of albumin from mouse subarachnoid space: a measure of CSF bulk flow. *J Neurosci Methods* **6,** 253–259.

Rusakov DA (2006). $Ca^{2+}$-Dependent Mechanisms of Presynaptic Control at Central Synapses. *The Neuroscientist* **12,** 317–326.

Russo RE, Fernández A, Reali C, Radmilovich M & Trujillo-Cenóz O (2004). Functional and molecular clues reveal precursor-like cells and immature neurones in the turtle spinal cord. *J Physiol* **560,** 831–838.

Sakka L, Coll G & Chazal J (2011). Anatomy and physiology of cerebrospinal fluid. *Eur Ann Otorhinolaryngol Head Neck Dis* **128,** 309–316.

Saloman JL, Scheff NN, Snyder LM, Ross SE, Davis BM & Gold MS (2016). Gi-DREADD Expression in Peripheral Nerves Produces Ligand-Dependent Analgesia, as well as Ligand-Independent Functional Changes in Sensory Neurons. *J Neurosci* **36,** 10769–10781.

Santulli G, Nakashima R, Yuan Q & Marks AR (2017). Intracellular calcium release channels: an update: RyRs vs IP3Rs. *J Physiol* **595,** 3041–3051.

Sheng Z-H, Rettig J, Cook T & Catterall WA (1996). Calcium-dependent interaction of N-type calcium channels with the synaptic core complex. *Nature* **379,** 451–454.

Sheng Z-H, Rettig J, Takahashi M & Catterall WA (1994). Identification of a syntaxin-binding site on N-Type calcium channels. *Neuron* **13,** 1303–1313.

Shimizu T, Higuchi T, Fujii T, Nilius B & Sakai H (2011). Bimodal effect of alkalization on the polycystin transient receptor potential channel, PKD2L1. *Pflüg Arch Eur J Physiol* **461,** 507–513.

Shimizu T, Higuchi T, Toba T, Ohno C, Fujii T, Nilius B & Sakai H (2017). The asparagine 533 residue in the outer pore loop region of the mouse PKD2L1 channel is essential for its voltage-dependent inactivation. *FEBS Open Bio* **7,** 1392–1401.

Shimizu T, Janssens A, Voets T & Nilius B (2009). Regulation of the murine TRPP3 channel by voltage, pH, and changes in cell volume. *Pflüg Arch Eur J Physiol* **457,** 795–807.

Shimosegawa T, Koizumi M, Toyota T, Goto Y, Yanaihara C & Yanaihara N (1986). An immunohistochemical study of methionine-enkephalin-Arg6-Gly7-Leu8-like immunoreactivity-containing liquor-contacting neurons (LCNs) in the rat spinal cord. *Brain Res* **379,** 1–9.

Shmigol A, Kostyuk P & Verkhratsky A (1995). Dual action of thapsigargin on calcium mobilization in sensory neurons: Inhibition of $Ca^{2+}$ uptake by caffeine-sensitive pools and blockade of plasmalemmal $Ca^{2+}$ channels. *Neuroscience* **65,** 1109–1118.

Shmigol A, Svichar N, Kostyuk P & Verkhratsky A (1996). Gradual caffeine-induced $Ca^{2+}$ release in mouse dorsal root ganglion neurons is controlled by cytoplasmic and luminal $Ca^{2+}$. *Neuroscience* **73,** 1061–1067.

Siesjö BK (1972). The regulation of cerebrospinal fluid pH. *Kidney Int* **1,** 360–374.

Simms BA & Zamponi GW (2014). Neuronal Voltage-Gated Calcium Channels: Structure, Function, and Dysfunction. *Neuron* **82,** 24–45.

Simon MJ & Iliff JJ (2016). Regulation of cerebrospinal fluid (CSF) flow in neurodegenerative, neurovascular and neuroinflammatory disease. *Biochim Biophys Acta BBA - Mol Basis Dis* **1862,** 442–451.

Singh A, Hamedinger D, Hoda J-C, Gebhart M, Koschak A, Romanin C & Striessnig J (2006). C-terminal modulator controls $Ca^{2+}$-dependent gating of $Ca_v1.4$ L-type $Ca^{2+}$ channels. *Nat Neurosci* **9,** 1108–1116.

Sochivko D, Pereverzev A, Smyth N, Gissel C, Schneider T & Beck H (2002). The $Ca_V2.3$ $Ca^{2+}$ channel subunit contributes to R-Type $Ca^{2+}$ currents in murine hippocampal and neocortical neurones. *J Physiol* **542,** 699–710.

Speake T, Whitwell C, Kajita H, Majid A & Brown PD (2001). Mechanisms of CSF secretion by the choroid plexus. *Microsc Res Tech* **52,** 49–59.

Spector R, Robert Snodgrass S & Johanson CE (2015). A balanced view of the cerebrospinal fluid composition and functions: Focus on adult humans. *Exp Neurol* **273,** 57–68.

Stea A, Tomlinson WJ, Soong TW, Bourinet E, Dubel SJ, Vincent SR & Snutch TP (1994). Localization and functional properties of a rat brain alA calcium channel reflect similarities to neuronal Q- and P-type channels. *Proc Natl Acad Sci USA*5.

Sternberg JR, Prendergast AE, Brosse L, Cantaut-Belarif Y, Thouvenin O, Orts-Del'Immagine A, Castillo L, Djenoune L, Kurisu S, McDearmid JR, Bardet P-L, Boccara C, Okamoto H, Delmas P & Wyart C (2018). Pkd2l1 is required for mechanoception in cerebrospinal fluid-contacting neurons and maintenance of spine curvature. *Nat Commun* **9,** 3804.

Stoeckel M-E, Uhl-Bronner S, Hugel S, Veinante P, Klein M-J, Mutterer J, Freund-Mercier M-J & Schlichter R (2003). Cerebrospinal fluid-contacting neurons in the rat spinal cord, a gamma-aminobutyric acidergic system expressing the P2X2 subunit of purinergic receptors, PSA-NCAM, and GAP-43 immunoreactivities: light and electron microscopic study. *J Comp Neurol* **457,** 159–174.

Strittmatter M, Grauer M, Isenberg E, Hamann G, Fischer C, Hoffmann K-H, Biaes F & Schimrigk K (1997). Cerebrospinal Fluid Neuropeptides and Monoaminergic Transmitters in Patients With Trigeminal Neuralgia. *Headache J Head Face Pain* **37,** 211–216.

Südhof TC (2012). Calcium Control of Neurotransmitter Release. *Cold Spring Harb Perspect Biol*; DOI: 10.1101/cshperspect.a011353.

Swandulla D & Armstrong CM (1989). Calcium channel block by cadmium in chicken sensory neurons. *Proc Natl Acad Sci U S A* **86,** 1736–1740.

Szebenyi SA, Ogura T, Sathyanesan A, AlMatrouk AK, Chang J & Lin W (2014). Increases in intracellular calcium via activation of potentially multiple phospholipase C isozymes in mouse olfactory neurons. *Front Cell Neurosci*; DOI: 10.3389/fncel.2014.00336.

Takahashi M, Seagar MJ, Jones JF, Reber BF & Catterall WA (1987). Subunit structure of dihydropyridine-sensitive calcium channels from skeletal muscle. *Proc Natl Acad Sci* **84,** 5478–5482.

Takahashi T & Momiyama A (1993). Different types of calcium channels mediate central synaptic transmission. *Nature* **366,** 156–158.

Tatebayashi H & Ogata N (1992). Kinetic analysis of the $GABA_B$-mediated inhibition of the high-threshold $Ca^{2+}$ current in cultured rat sensory neurones. *J Physiol* **447,** 391–407.

Taylor CW (1998). Inositol trisphosphate receptors: $Ca^{2+}$-modulated intracellular $Ca^{2+}$ channels. *Biochim Biophys Acta BBA - Mol Cell Biol Lipids* **1436,** 19–33.

Taylor CW & Konieczny V (2016). $IP_3$ receptors: take four $IP_3$ to open. *Sci Signal* **9,** pe1.

Taylor CW & Tovey SC (2010). $IP_3$ Receptors: Toward Understanding Their Activation. *Cold Spring Harb Perspect Biol*; DOI: 10.1101/cshperspect.a004010.

Tedford HW & Zamponi GW (2006). Direct G Protein Modulation of $Ca_v2$ Calcium Channels. *Pharmacol Rev* **58,** 837–862.

Telano LN & Baker S (2019). Physiology, Cerebral Spinal Fluid (CSF). In *StatPearls*. StatPearls Publishing, Treasure Island (FL). Available at: http://www.ncbi.nlm.nih.gov/books/NBK519007/.

Thomas NL & Williams AJ (2012). Pharmacology of ryanodine receptors and $Ca^{2+}$-induced $Ca^{2+}$ release. *Wiley Interdiscip Rev Membr Transp Signal* **1,** 383–397.

Toyoshima C, Nakasako M, Nomura H & Ogawa H (2000). Crystal structure of the calcium pump of sarcoplasmic reticulum at 2.6 Å resolution. **405,** 11.

Treiman M, Caspersen C & Christensen SB (1998). A tool coming of age: thapsigargin as an inhibitor of sarco-endoplasmic reticulum $Ca^{2+}$-ATPases. *Trends Pharmacol Sci* **19,** 131–135.

Urban DJ & Roth BL (2015). DREADDs (Designer Receptors Exclusively Activated by Designer Drugs): Chemogenetic Tools with Therapeutic Utility. *Annu Rev Pharmacol Toxicol* **55,** 399–417.

Usachev Y, Shmigol A, Pronchuk N, Kostyuk P & Verkhratsky A (1993). Caffeine-induced calcium release from internal stores in cultured rat sensory neurons. *Neuroscience* **57,** 845–859.

Vandecaetsbeek I, Vangheluwe P, Raeymaekers L, Wuytack F & Vanoevelen J (2011). The $Ca^{2+}$ Pumps of the Endoplasmic Reticulum and Golgi Apparatus. *Cold Spring Harb Perspect Biol*; DOI: 10.1101/cshperspect.a004184.

Venkatachalam K & Montell C (2007). TRP channels. *Annu Rev Biochem* **76,** 387–417.

Verkhratsky A (2005). Physiology and Pathophysiology of the Calcium Store in the Endoplasmic Reticulum of Neurons. *Physiol Rev* **85,** 201–279.

Verkhratsky A & Shmigol A (1996). Calcium-induced calcium release in neurones. *Cell Calcium* **19,** 1–14.

Vígh B, Manzano e Silva MJ, Frank CL, Vincze C, Czirok SJ, Szabó A, Lukáts A & Szél A (2004). The system of cerebrospinal fluid-contacting neurons. Its supposed role in the nonsynaptic signal transmission of the brain. *Histol Histopathol* **19,** 607–628.

Vigh B & Vigh-Teichmann I (1998). Actual problems of the cerebrospinal fluid-contacting neurons. *Microsc Res Tech* **41,** 57–83.

Vigh B, Vigh-Teichmann I & Aros B (1977). Special dendritic and axonal endings formed by the cerebrospinal fluid contacting neurons of the spinal cord. *Cell Tissue Res* **183,** 541–552.

Vigh B, Vigh-Teichmann I, Röhlich P & Oksche A (1983). Cerebrospinal fluid-contacting neurons, sensory pinealocytes and Landolt's clubs of the retina as revealed by means of an electron-microscopic immunoreaction against opsin. *Cell Tissue Res* **233,** 539–548.

Vigh-Teichmann I & Vigh B (1989). The cerebrospinal fluid-contacting neuron: a peculiar cell type of the central nervous system. Immunocytochemical aspects. *Arch Histol Cytol* **52 Suppl,** 195–207.

Wanaverbecq N, Marsh SJ, Al-Qatari M & Brown DA (2003). The plasma membrane calcium-ATPase as a major mechanism for intracellular calcium regulation in neurones from the rat superior cervical ganglion. *J Physiol* **550,** 83–101.

Watanabe H, Yamashita T, Saitoh N, Kiyonaka S, Iwamatsu A, Campbell KP, Mori Y & Takahashi T (2010). Involvement of $Ca^{2+}$ Channel Synprint Site in Synaptic Vesicle Endocytosis. *J Neurosci* **30,** 655–660.

Welch MJ, Markham CH & Jenden DJ (1976). Acetylcholine and choline in cerebrospinal fluid of patients with Parkinson's disease and Huntington's chorea. *J Neurol Neurosurg Psychiatry* **39,** 367–374.

Wettschureck N & Offermanns S (2005). Mammalian G Proteins and Their Cell Type Specific Functions. *Physiol Rev* **85,** 1159–1204.

Witts EC, Zagoraiou L & Miles GB (2014). Anatomy and function of cholinergic C bouton inputs to motor neurons. *J Anat* **224,** 52–60.

Wood JH (2013). Neurobiology of Cerebrospinal Fluid 1. Springer Science & Business Media.

Wright EM (1978). Transport processes in the formation of the cerebrospinal fluid. *Rev Physiol Biochem Pharmacol* **83,** 3–34.

Wright R (2009). The Necessity of NKCC1: Loss of the Chloride Cotransporter in a Knock-Out Model and Potential Compensatory Mechanisms. *J Neurosci* **29,** 13094–13096.

Wu D, Katz A, Lee CH & Simon MI (1992). Activation of phospholipase C by alpha 1-adrenergic receptors is mediated by the alpha subunits of Gq family. *J Biol Chem* **267,** 25798–25802.

Wu G, Hayashi T, Park JH, Dixit M, Reynolds DM, Li L, Maeda Y, Cai Y, Coca-Prados M & Somlo S (1998*a*). Identification of PKD2L, a human PKD2-related gene: tissue-specific expression and mapping to chromosome 10q25. *Genomics* **54,** 564–568.

Wu L-G, Borst JGG & Sakmann B (1998*b*). R-type $Ca^{2+}$ currents evoke transmitter release at a rat central synapse. *Proc Natl Acad Sci* **95,** 4720–4725.

Wyart C, Del Bene F, Warp E, Scott EK, Trauner D, Baier H & Isacoff EY (2009). Optogenetic dissection of a behavioural module in the vertebrate spinal cord. *Nature* **461,** 407–410.

Xu W & Lipscombe D (2001). Neuronal $Ca_V1.3\alpha$ L-Type Channels Activate at Relatively Hyperpolarized Membrane Potentials and Are Incompletely Inhibited by Dihydropyridines. *J Neurosci* **21,** 5944–5951.

Yamasaki H, Sugino M & Ohsawa N (1997). Possible Regulation of Intracranial Pressure by Human Atrial Natriuretic Peptide in Cerebrospinal Fluid. *Eur Neurol* **38,** 88–93.

Yan Z & Surmeier D (1996). Muscarinic (m2/m4) receptors reduce N- and P-type $Ca^{2+}$ currents in rat neostriatal cholinergic interneurons through a fast, membrane-delimited, G-protein pathway. *J Neurosci* **16,** 2592–2604.

Zagoraiou L, Akay T, Martin JF, Brownstone RM, Jessell TM & Miles GB (2009). A cluster of cholinergic premotor interneurons modulates mouse locomotor activity. *Neuron* **64,** 645–662.

Zalk R, Clarke OB, des Georges A, Grassucci RA, Reiken S, Mancia F, Hendrickson WA, Frank J & Marks AR (2015). Structure of a mammalian ryanodine receptor. *Nature* **517,** 44–49.

Zamponi GW (1997). Antagonist binding sites of voltage-dependent calcium channels. *Drug Dev Res* **42,** 131–143.

Zamponi GW & Currie KPM (2013). Regulation of $Ca_V2$ calcium channels by G protein coupled receptors. *Biochim Biophys Acta* **1828,** 1629–1643.

Zhang J-F, Randall AD, Ellinor PT, Horne WA, Sather WA, Tanabe T, Schwarz TL & Tsien RW (1993). Distinctive pharmacology and kinetics of cloned neuronal $Ca^{2+}$ channels and their possible counterparts in mammalian CNS neurons. *Neuropharmacology* **32,** 1075–1088.

Zheng J (2013). Molecular Mechanism of TRP Channels. In *Comprehensive Physiology*, ed. Terjung R. John Wiley & Sons, Inc., Hoboken, NJ, USA. Available at: http://doi.wiley.com/10.1002/cphy.c120001 [Accessed March 8, 2019].

# VII. SUPPLEMENTS

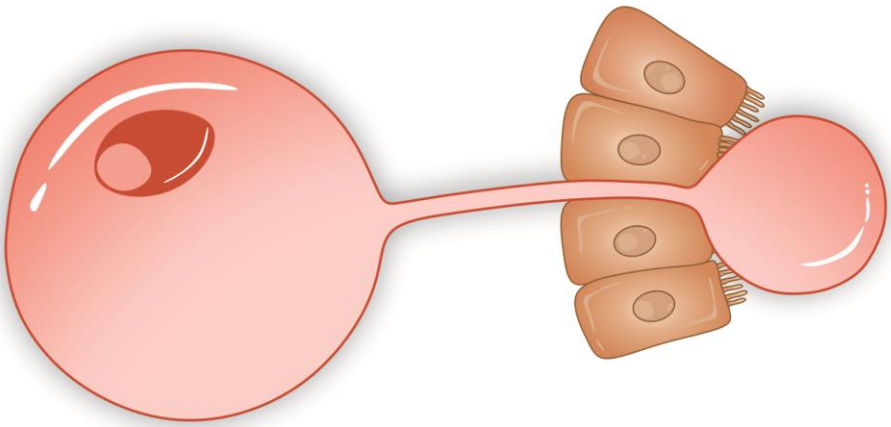

*J Physiol* 597.2 (2019) pp 631–651



The Journal of Physiology

# $GABA_B$ receptors modulate $Ca^{2+}$ but not G protein-gated inwardly rectifying $K^+$ channels in cerebrospinal-fluid contacting neurones of mouse brainstem

Nina Jurčić[1,*], Ghizlane Er-Raoui[1,3,*], Coraline Airault[2], Jérôme Trouslard[1], Nicolas Wanaverbecq[1,†] and Riad Seddik[1,†]

[1] *Aix Marseille Univ, CNRS, INT, Inst Neurosci Timone, Marseille, France*
[2] *Aix Marseille Univ, CNRS, LNC, Marseille, France*
[3] *Université Sultan Moulay Slimane, Laboratoire de Génie Biologique, Béni Mellal, Morocco*

Edited by: David Wyllie & Tadashi Isa

**Key points**

- Medullo-spinal CSF contacting neurones (CSF-cNs) located around the central canal are conserved in all vertebrates and suggested to be a novel sensory system intrinsic to the CNS.
- CSF-cNs receive GABAergic inhibitory synaptic inputs involving ionotropic $GABA_A$ receptors, but the contribution of metabotropic $GABA_B$ receptors ($GABA_B$-Rs) has not yet been studied.
- Here, we indicate that CSF-cNs express functional $GABA_B$-Rs that inhibit postsynaptic calcium channels but fail to activate inhibitory potassium channel of the Kir3-type.
- We further show that $GABA_B$-Rs localise presynaptically on GABAergic and glutamatergic synaptic inputs contacting CSF-cNs, where they inhibit the release of GABA and glutamate.
- Our data are the first to address the function of $GABA_B$-Rs in CSF-cNs and show that on the presynaptic side they exert a classical synaptic modulation whereas at the post-synaptic level they have an atypical action by modulating calcium signalling without inducing potassium-dependent inhibition.

**Abstract** Medullo-spinal neurones that contact the cerebrospinal fluid (CSF-cNs) are a population of evolutionary conserved cells located around the central canal. CSF-cN activity has been shown to be regulated by inhibitory synaptic inputs involving ionotropic $GABA_A$ receptors, but the contribution of the G-protein coupled $GABA_B$ receptors has not yet been studied. Here, we used a combination of immunofluorescence, electrophysiology and calcium imaging to investigate the expression and function of $GABA_B$-Rs in CSF-cNs of the mouse brainstem. We found that CSF-cNs express $GABA_B$-Rs, but their selective activation failed to induce G protein-coupled inwardly rectifying potassium (GIRK) currents. Instead, CSF-cNs express primarily N-type voltage-gated calcium ($Ca_V2.2$) channels, and $GABA_B$-Rs recruit $G\beta\gamma$

**Nina Jurčić** received her Master's degree in Biotechnology in Medicine at the University of Rijeka (Croatia). Currently, she is a PhD student at the Institute of Neuroscience (INT) at "La Timone", Aix-Marseille University, where she works under the supervision of Professor Jérôme Trouslard and Dr Nicolas Wanaverbecq. Her study aims at describing the physiological and functional properties of mammalian CSF-cNs using electrophysiological approaches together with calcium imaging. **Ghizlane Er-Raoui** is a graduate student from Sultan Mouly Sliman University (SMSU, Morocco), where she completed her Master's degree in Bioengineering. She has prepared her thesis on $GABA_B$ receptor regulation in murine CSF-cNs under the supervision of Professor Mohamed Najimi (SMSU) and Professor Jérôme Trouslard (AMU).

*N. Jurčić and G. Er-Raoui contributed equally to this work.
†R. Seddik and N. Wanaverbecq contributed equally to this work as Principal Investigators (PIs).



DOI: 10.1113/JP277172

subunits to inhibit $Ca_V$ channel activity induced by membrane voltage steps or under physiological conditions by action potentials. Moreover, using electrical stimulation, we indicate that GABAergic inhibitory (IPSCs) and excitatory glutamatergic (EPSCs) synaptic currents can be evoked in CSF-cNs showing that mammalian CSF-cNs are also under excitatory control by glutamatergic synaptic inputs. We further demonstrate that baclofen reversibly reduced the amplitudes of both IPSCs and EPSCs evoked in CSF-cNs through a presynaptic mechanism of regulation. In summary, these results are the first to demonstrate the existence of functional postsynaptic $GABA_B$-Rs in medullar CSF-cNs, as well as presynaptic $GABA_B$ auto- and heteroreceptors regulating the release of GABA and glutamate. Remarkably, postsynaptic $GABA_B$-Rs associate with $Ca_V$ but not GIRK channels, indicating that $GABA_B$-Rs function as a calcium signalling modulator without GIRK-dependent inhibition in CSF-cNs.

(Received 28 September 2018; accepted after revision 8 November 2018; first published online 12 November 2018)
**Corresponding authors** R. Seddik: Aix-Marseille Université, CNRS, INT, Institut de Neurosciences de la Timone, Marseille, France. Email: riad.seddik@univ-amu.fr;
N. Wanaverbecq: Aix-Marseille Université, CNRS, INT, Inst Neurosci Timone, Marseille, France.
Email: nicolas.wanaverbecq@univ-amu.fr

## Introduction

$GABA_B$ receptors ($GABA_B$-Rs) belong to family 3 (or family C) G-protein coupled receptors and mediate the slow inhibitory response to GABA by activating $G_{i/o}$ protein-dependent signalling pathways (Padgett & Slesinger, 2010; Pinard *et al.* 2010). The core structure of $GABA_B$-Rs consists of two principal subunits, $GABA_{B1}$ and $GABA_{B2}$ that assemble into heteromeric functional receptors at pre- and postsynaptic sites of the synapse (Möhler & Fritschy, 1999; Bettler *et al.* 2004; Pin & Bettler, 2016). Presynaptic $GABA_B$-Rs are positioned at axon terminals of both excitatory (heteroreceptors) and inhibitory (autoreceptors) neurones, where their activation suppresses neurotransmitter release through inhibition of voltage-dependent calcium channels ($Ca_V$), although other mechanisms have been implicated (Scanziani *et al.* 1992; Chen & van den Pol, 1998; Barral *et al.* 2000; Sakaba & Neher, 2003). Postsynaptic $GABA_B$-Rs are expressed in somatodendritic compartments of neurones and evoke a slow inhibitory postsynaptic current by gating G protein-coupled inwardly rectifying potassium (GIRK) channels, which hyperpolarises the membrane and inhibits neuronal excitability (De Koninck & Mody, 1997; Lüscher *et al.* 1997). Postsynaptic $GABA_B$-Rs additionally down-regulate $Ca_V$ channels, thus controlling calcium-dependent neuronal processes such as dendritic $Ca^{2+}$-spike propagation and synaptic plasticity (Pérez-Garci *et al.* 2006; Booker *et al.* 2018). Finally, $GABA_B$-Rs can influence pre- and postsynaptic functions by inhibiting adenylyl cyclase, though the physiological consequences of this modulation are poorly understood (Padgett & Slesinger, 2010). In addition to their diverse signalling pathways, $GABA_B$-Rs are widely expressed throughout the central nervous system including the hindbrain and the spinal cord, thereby playing pivotal roles in numerous physiological processes (Margeta-Mitrovic *et al.* 1999; Bettler *et al.* 2004).

Medullo-spinal neurones that contact the cerebrospinal fluid (CSF-cNs) constitute a peculiar neuronal population located around the central canal (CC) of all vertebrates (Vígh *et al.* 2004; Djenoune *et al.* 2014). They feature a bipolar morphology with a short dendritic process projecting toward the CC and ending in its lumen with a terminal protrusion or 'bud', suggesting a role in sensing CSF flow or composition (Stoeckel *et al.* 2003; Marichal *et al.* 2009; Orts-Del'Immagine *et al.* 2012, 2014). Consistent with this hypothesis, CSF-cNs express selectively the polycystic kidney disease 2-like 1 (PKD2L1) channel, a sensory transduction protein sensitive to extracellular variation of pH and osmolarity and sensing CSF flow and spinal cord torsion (Huang *et al.* 2006; Orts-Del'Immagine *et al.* 2012, 2016; Böhm *et al.* 2016; Jalalvand *et al.* 2016). PKD2L1 channels are non-selective cationic channels that produce enough depolarisation to trigger action potentials and therefore they contribute to setting the excitability of CSF-cNs (Orts-Del'Immagine *et al.* 2012, 2016). Moreover, CSF-cNs are embedded in a neuronal network, receiving primarily inhibitory synaptic inputs from yet-unidentified presynaptic partners (Orts-Del'Immagine *et al.* 2012). Inhibition of CSF-cNs was shown to be mediated by the amino acids GABA and glycine, which activate ionotropic $GABA_A$ and glycine receptors, respectively (Marichal *et al.* 2009; Orts-Del'Immagine *et al.* 2012). In addition, previous immunohistochemical studies revealed the presence of $GABA_B$-Rs in neurones of rat spinal cord surrounding the central canal and with morphological properties of CSF-cNs (Margeta-Mitrovic *et al.* 1999). However, their function, as well as their signalling effectors in CSF-cNs, remain unknown.

In the present study, we assessed the expression and functional properties of GABA$_B$-Rs in CSF-cNs of the mouse brainstem. Double immunohistofluorescence staining with the selective marker PKD2L1 for CSF-cNs show that the GABA$_{B1}$ subunit localises in the soma and the dendrite of medullar CSF-cNs. Using patch-clamp recordings and calcium imaging we demonstrate that post-synaptic GABA$_B$-Rs in CSF-cNs function by inhibiting $Ca_V$ channels through recruitment of G$\beta\gamma$ but surprisingly they do not activate GIRK channels in these neurones. CSF-cNs in the mouse brainstem were initially thought to be under the sole control of inhibitory synaptic inputs, but here, using an electrical stimulation protocol, we demonstrate that CSF-cNs also receive glutamatergic excitatory inputs involving AMPA/kainate receptors. Finally, we show that GABA$_B$-Rs, presumably localised on both GABAergic and glutamatergic terminals, have an inhibitory action on GABA and glutamate release onto CSF-cNs.

## Methods

### Animal ethics

All experiments were conducted in conformity with the rules set by the EC Council Directive (2010/63/UE) and the French 'Direction Départementale de la Protection des Populations des Bouches-du-Rhône (DDPP13)' (Licence No. 13.435 held by J.T. and No. 13.430 by N.W.). Experiments were performed using 98 C57BL/6J mice (*Mus musculus*) of both sexes aged 8–18 weeks old (25–30 g, obtained from Envigo, Gannat, France). All animals were housed at constant temperature (21°C), in an enriched environment, under a standard 12 h light–12 h dark cycle, with food (pellet AO4, UAR, Villemoisson-sur-Orge, France) and water provided *ad libitum*. Every precaution was taken to reduce to the minimum the number of animals used and to minimise animal stress during housing and prior to experiments. We understand the ethical principles under which *The Journal of Physiology* operates, and our work complies with the journal's animal ethics checklist.

### Histological procedures and confocal imaging

Adult mice were anaesthetised intraperitoneally with a combination of 100 mg kg$^{-1}$ ketamine (Carros, France) and 15 mg kg$^{-1}$ xylazine (Puteau, France). Animals were then transcardially perfused first with 0.1 M PBS and then by 4% paraformaldehyde in PBS (PFA; Sigma-Aldrich). Tissues were immediately removed, post-fixed for 30 min to 1 h in PFA at room temperature followed by overnight washing in PBS at 4°C. Tissues were finally cryoprotected for 24–48 h in 30% sucrose in PBS at 4°C and frozen in isopentane (−40°C). Coronal brainstem thin sections (40 $\mu$m) were obtained using a cryostat (Leica CM3050, Wetzlar, Germany) and collected serially in twelve-well plates containing 0.1 M PBS. Sections were then incubated for 1 h in PBS containing 0.3% Triton X100 (Sigma-Aldrich) and 2% donkey serum with 1% bovine serum albumin (BSA), followed by an overnight incubation at 4°C with rabbit anti-PKD2L1 IgG (1:700; AB9086, Millipore-Chemicon, Fontenay-sous-Bois, France) and then a 24 h incubation at room temperature with mouse anti-GABA$_{B1}$ IgG (1:100, AB55051, Abcam Biomedicals, Paris, France). Sections were then washed in PBS and incubated for 2 h with secondary antibodies conjugated to either AlexaFluor 488 (PKD2L1: 1:400; Millipore-Chemicon) or 594 (GABA$_{B1}$: 1:1000; Millipore-Chemicon). Sections were mounted on gelatine-coated slides and coverslipped with home-made mowiol mounting medium for fluorescence microscope examination. Confocal images were captured with a Zeiss LSM 700 laser scanning microscope before processing with ZEN 2009 light Edition (Zeiss, Iena, Germany) and ImageJ 1.8.0 software (NIH).

### Acute brainstem slice preparation

Coronal brainstem slices (from the caudal part up to the 4th ventricle) were prepared as previously described by (Orts-Del'Immagine *et al.* 2012). Briefly, 8- to 12-week-old mice were anaesthetised with the ketamine-xylazine solution, decapitated, and the brain rapidly removed and submerged in ice-cold (0–4°C), oxygenated (95% $O_2$-5% $CO_2$) and low calcium-high magnesium cutting solution containing (in mM): NaCl 75, $NaHCO_3$ 33, $NaH_2PO_4$ 1.25, KCl 3, $CaCl_2$ 0.5, $MgCl_2$ 7, glucose 15, sucrose 58, ascorbic acid 2, sodium pyruvate 2, *myo*-inositol 3 (pH 7.3–7.4; osmolality 300–310 mosmol kg$^{-1}$). Coronal brainstem slices (250 $\mu$m thick) were cut with a vibratome (Leica VT1000S) and incubated for 15–20 min at 35°C in a submerged chamber filled with oxygenated artificial CSF (aCSF) containing (in mM): NaCl 115, $NaHCO_3$ 23, $NaH_2PO_4$ 1.25, KCl 3, $CaCl_2$ 2, $MgCl_2$ 2, glucose 15, ascorbic acid 2, sodium pyruvate 2, *myo*-inositol 3 (pH 7.3–7.4; osmolality 300–310 mosmol kg$^{-1}$). Slices were then maintained in oxygenated aCSF at room temperature prior to recording. After a recovery period of at least 1 h, slices were transferred to the recording chamber superfused with aCSF at 1.5–2.5 ml min$^{-1}$.

### Electrophysiology

Neurones around the central canal were visualised under infrared illumination using oblique or DIC optics mounted on a Scientifica SliceScope Pro 1000 or Zeiss Axioscope S1 microscope, respectively. Whole-cell patch-clamp recordings were performed at room temperature (~20°C) in current- and/or voltage-clamp

mode using a Multiclamp 700B or Axopatch 200A patch-clamp amplifier (Molecular Devices, San Jose, CA, USA). Patch pipettes (4–6 MΩ) were pulled from borosilicate glass capillaries (Harvard Apparatus, Holliston, MA, USA) using a P-97 Flaming/Brown type micropipette puller (Sutter Instrument Co, Novato, CA, USA). In all experiments, 10 $\mu$M Alexa Fluor 594 (Invitrogen) was included in the patch pipettes for identifying the typical morphology of neurones in contact with the cerebrospinal fluid (CSF-cNs) during the whole-cell recording (Orts-Del'Immagine *et al.* 2012, 2016). Series resistance (10–20 MΩ) was monitored throughout each experiment and unstable recordings were discontinued. For voltage-gated calcium currents recordings, series resistance was compensated by 70–80%. Data were filtered at 2–2.4 kHz and digitised at 10 kHz using a Digidata 1322A or 1440A interface (Molecular Device) driven by pClamp 9.2 or 10.7, respectively (Molecular Device). The liquid junction potential was left uncorrected.

**Recording of voltage-gated calcium currents.** For the characterisation of postsynaptic voltage-gated calcium ($Ca^{2+}$) channels ($Ca_V$) and the study of their modulation by $GABA_B$-Rs, electrodes were filled with a solution containing (in mM): CsCl 3, caesium acetate 100, NaCl 5, $MgCl_2$ 1, $CaCl_2$ 1, TEA-Cl 20, EGTA 10, HEPES 10, disodium phosphocreatine 10, Mg-ATP 4, $Na_3GTP$ 0.2 (adjusted to pH 7.36 with CsOH; osmolality of 290–295 mosmol $kg^{-1}$). Calcium currents were elicited by 100–200 ms voltage steps ($V_{Step}$, 10 mV increments) from a holding potential of −70 mV while the neurone was perfused with oxygenated aCSF supplemented with 10 $\mu$M gabazine ($GABA_A$ receptor antagonist), 1 $\mu$M strychnine (glycine receptor antagonist), 0.5 $\mu$M tetrodotoxin (TTX, inhibitor of sodium channels) and 20 mM tetraethylammonium chloride (TEA-Cl, blocker of potassium channels). The current-voltage relationship was constructed for each cell by plotting the $Ca^{2+}$ peak current recorded for a given $V_{Step}$ and the properties and voltage-dependence of $Ca^{2+}$ current were analysed with a Boltzmann fit using the following equation: $I(V) = g_{max}\,(V - V_{rev})/[1 + \exp(V_{50} - V)/k]$; where I represents the current amplitude as a function of voltage ($V$), $g_{max}$ is the maximum whole-cell channel conductance, $V_{rev}$ is the current reversal potential, $V_{50}$ is the voltage for half-maximal channel activation and $k$ (the slope) is equal to $RT/z_gF$ where $z_g$ is the valency of the voltage sensor of the calcium channel.

Calcium current inhibition by postsynaptic $GABA_B$-Rs was assessed on $Ca^{2+}$ peak current (elicited with a 100 ms $V_{Step}$ to +10 mV every 30 s over a 10 min period) by application of baclofen (100 $\mu$M, 30 s), a selective agonist for $GABA_B$-Rs, using a pressure application pipette (~1 $\mu$m tip diameter) positioned at ~50 $\mu$m from the recorded cells and connected to a pressure application system (Toohey Company, Hollis, NH, USA). The molecular mechanism by which $GABA_B$-R activation modulates $Ca^{2+}$ currents was studied with a triple-pulse voltage protocol (recorded every 30 s for 10 min) consisting of two 50 ms test pulses to +10 mV from a holding potential of −70 mV, separated by a 50 ms conditioning pulse to +100 mV. The inhibition of calcium currents induced by application of baclofen was then compared before (prepulse) and after (postpulse) the large depolarising conditioning pulse (Herlitze *et al.* 1996; Ikeda, 1996).

**Recording of inwardly rectifying (GIRK/Kir3) potassium currents.** To record postsynaptic $GABA_B$-mediated Kir3-type $K^+$ currents (GIRK), patch pipettes were filled with a solution containing (in mM): potassium gluconate 140, NaCl 4, HEPES 5, $MgCl_2$ 2, EGTA 1.1, $Na_2ATP$ 2, disodium phosphocreatine 5, $Na_3GTP$ 0.6 (adjusted to pH 7.35 with KOH; osmolality 285 mosmol $kg^{-1}$). Kir3-type $K^+$ currents were evoked by pressure application of baclofen (100 $\mu$M, 40 s) at −50 mV in the presence of 10 $\mu$M gabazine, 1 $\mu$M strychnine and 20 $\mu$M DNQX (AMPA/kainate receptor antagonist).

**Recording of synaptic currents.** Electrically evoked inhibitory (IPSCs) and excitatory (EPSCs) postsynaptic currents were recorded with patch electrodes filled with (in mM): CsCl 130, NaCl 4, $MgCl_2$ 2, EGTA 1.1, HEPES 1.1, disodium phosphocreatine 5, $Na_2ATP$ 2, $Na_3GTP$ 0.6, lidocaine *N*-ethyl chloride 5 (adjusted to pH 7.35 with CsOH; osmolality 285 mosmol $kg^{-1}$). IPSCs and EPSCs were elicited at 0.1 Hz by voltage pulses with a stimulus isolator (100 $\mu$s, 50–60 V stimuli; ISO-Flex, A.M.P.I, Jerusalem, Israel) through a stimulating electrode filled with aCSF and positioned at 50–100 $\mu$m from the soma of the recorded cell. $GABA_A$ receptor-mediated IPSCs were recorded at −60 mV and were isolated by including 1 $\mu$M strychnine and 20 $\mu$M DNQX to the external solution. To record glutamatergic receptor-mediated EPSCs, the external solution was supplemented with 1 $\mu$M strychnine and 10 $\mu$M gabazine. EPSCs were recorded at holding potential of −60 mV. $GABA_B$-R-mediated inhibition of IPSCs and EPSCs was assessed by bath application of baclofen (20 or 100 $\mu$M, see Results). For paired-pulse ratio analysis, stimuli were delivered in pairs with 70 ms interpulse intervals and a frequency of 0.1 Hz.

## Calcium imaging

Calcium imaging experiments were performed in CSF-cNs patched with electrodes containing (in mM): KCl 3, potassium gluconate 120, NaCl 5, $MgCl_2$ 1, $CaCl_2$ 0.25, EGTA 2, HEPES 10, disodium phosphocreatine 10, Mg-ATP 4, $Na_3GTP$ 0.2 (adjusted to pH 7.33 with KOH;

osmolality 290–295 mosmol kg$^{-1}$). Cells were loaded with the fluorescent $Ca^{2+}$ probe Fluo-4 (50 $\mu$M, Invitrogen, Carlsbad, CA, USA) through the patch pipette and the preparation was illuminated (490 nm, excitation bandpass filter: 490 ± 30 nm; Chroma, Bellows Falls, VT, USA) using the CoolLED epifluorescence system (p1 PrecisExcite, Andover, UK), The emitted light (520 nm, emission bandpass filter: 535 ± 30 nm and a dichroic mirror set at 515 nm; Chroma) was collected with a HQ2 CoolSnap CCD camera (Standard mode at 10 MHz and Gain 1, Photometrics) connected to a PC through a frame grabber (CoolSNAP LVDS interface card, Photometrics, Tucson, AZ, USA) and controlled by MetaView software (Molecular Devices). To optimise imaging conditions and reduce fluorescence quenching, a square region of interest (ROI) was drawn around the recorded neurones, the illumination intensity was set at 25% of the maximum power. Images were acquired in time laps mode with 2 × 2 binning for 100 ms every 0.2 s over a 1 min period (151 images). CSF-cNs were recorded in current-clamp mode from the resting membrane potential (RMP) and after a period of baseline recording, 5 consecutive trains of action potentials (APs) (0.5 Hz) were triggered with a 500 ms DC current pulse (+20 pA) to induce $Ca^{2+}$ influx following membrane depolarisation and monitor the elicited elevation in intracellular $Ca^{2+}$. To test whether the $Ca^{2+}$ elevations were effectively mediated through $Ca_V$ activation, recordings were also carried out in voltage-clamp mode with an intracellular solution containing (mM): CsCl 3, caesium acetate 100, NaCl 5, $MgCl_2$ 1, $CaCl_2$ 1 TEA-Cl, 20, EGTA 2, HEPES 10, disodium phosphocreatine 10, Mg-ATP 4, $Na_3GTP$ 0.2, with 50 $\mu$M Fluo-4 (adjusted to pH 7.36 with CsOH; osmolality 290–295 mosmol kg$^{-1}$). CSF-cNs were depolarised to +10 mV for 100 ms from a holding potential set at −70 mV and the increase in fluorescence simultaneously recorded.

## Reagents

All reagents were purchased from Sigma-Aldrich except: Tetrodotoxin (TTX) from Latoxan (Portes-lés-Valence, France). 6,7-dinitroquinoxaline-2,3-dione disodium salt (DNQX) from Abcam Biochemicals. (R)-baclofen and gabazine (SR 95531) from Tocris Bioscience (Bristol, UK). $\omega$-conotoxin GVIA, $\omega$-agatoxin IVA and nifedipine from Alomone labs (Jerusalem, Israel). CGP54626A (CGP) was a gift from Bernhard Bettler (University of Basel, Switzerland) and was initially produced by Novartis Pharma AG (Basel, Switzerland).

## Data analysis and statistics

**Data analysis.** Current and potential responses were analysed using the Clampfit 10 suite (Molecular Devices Inc.) and Excel 2016 (Microsoft). In our analysis, the peak and the mean amplitudes were considered for current and voltage responses, respectively (see below). The RMP was determined in current-clamp mode at $I = 0$ just after the whole-cell configuration was achieved as well as by averaging in the current-clamp recordings a ∼1 s period in the absence of action potentials (APs) and of current injection ($I_{injection} = 0$ pA). AP properties were analysed either from recordings of the spontaneous discharge activity (10—30 s periods) or from trains of APs elicited by the injection of a +20 pA DC current pulse for 500 ms using the 'threshold detection' routine from Clampfit 10 with a threshold set at 0 mV. In each condition, the principal parameters of APs (amplitude, overshoot, 10–90% rise time and level of after hyperpolarisation) were determined, as well as AP frequency.

Over the period used to record $Ca^{2+}$ current (∼10 min) we consistently observed a decrease in the $Ca^{2+}$ current amplitude, known as rundown (see Discussion). Therefore, to account for this phenomenon when comparing $Ca^{2+}$ current amplitude over time, we fitted the baseline data points (control) before drug application ($Ca^{2+}$ channel blockers, toxins or baclofen) recorded for each cell with a linear regression function ($y = ax + b$; where $y$ and $x$ are the recorded peak current and time, respectively, and $a$ and $b$ are constants). The current amplitude in the presence of the drug was measured from the raw data and compared to the value in control calculated at the same time points from the linear regression; this procedure avoided an overestimation for the degree of inhibition.

To measure changes in fluorescence, i.e. intracellular calcium concentrations ($[Ca^{2+}]_i$), regions of interest (ROI) were drawn over the CSF-cN soma (ROI Cell, Fig. 5*A*) and the background (ROI Bkg, Fig. 5*A*) on the recorded images. The average fluorescence intensity was measured over time from these two ROIs and subsequently, the background fluorescence intensity was subtracted from the somatic data to compute the net fluorescence ($F$). The average fluorescence intensity before stimulus application ($Ca_V$ activation or train of APs), the so-called basal intensity or $F_0$, was then calculated over 30–40 images. Finally, the net rise from baseline in cell fluorescence was calculated as the $(F - F_0)/F_0$ or $\Delta F/F_0$ ratio and expressed as a percentage. The average fluorescence intensity was then plotted over time to illustrate $Ca^{2+}$ transients and the peak amplitude of the fluorescence rise measured and compared between the control and the test situations. Fluorescence signal when using imaging with epifluorescence and diffusion of Fluo-4 into the cell through the patch pipette exhibits a progressive decrease in intensity over time, a phenomenon known as fluorescence bleaching or quenching. We therefore computed the amount of quenching over time by fitting the baseline data with a linear regression function ($y = ax + b$; where $y$ and $x$ are the $\Delta F/F_0$ value and

time, respectively, and *a* and *b* are constants) and subtracted these data from the raw data points in a point to point manner. To compare the amplitude of the rise in fluorescence, in control *vs.* baclofen, the maximum amplitude recorded after the 5$^{th}$ train of APs was normalised against that of the 1st train for each recording.

The inhibitory effect of $GABA_B$-R activation on IPSCs and EPSCs was determined by comparing current amplitudes of 30 averaged traces including failures before and during application of baclofen or CGP. The paired-pulse ratio (PPR) was calculated as the ratio of the second postsynaptic current (PSC) over the first PSC. The decay times of EPSCs and IPSCs were obtained by fitting the decay phase of the current with a single exponential equation using Clampfit 10. Rise times (10–90%) of synaptic currents were calculated using the statistics tool of Clampfit 10. In all figures showing EPSCs and IPSCs, stimulus artifacts were blanked for clarity.

**Statistical analysis.** Data were expressed as means ± SD in text and represented as box-whisker plot using Tukey's method with Prism 6 (GraphPad) software or RStudio 1.1.456 (R Studio Team, 2018), as previously described (Orts-Del'Immagine *et al.* 2017). Briefly, for each data set, the median and the 25$^{th}$ to the 75$^{th}$ percentiles (lower and upper limits of each bar, respectively) are calculated. Next, the interquartile distance (IQR) is determined as the difference between the 25$^{th}$ and 75$^{th}$ percentiles and the whiskers limits or 'inner fences' calculated as the 75$^{th}$ percentile plus 1.5 times IQR and the 25$^{th}$ percentile minus 1.5 times IQR. All data with values either higher or lower than the inner fences are represented as individual data points and considered as outliers. In all the figures where data are presented with box-and-whiskers plots, the thick horizontal line represents the median. For all electrophysiological data and histological experiments, *n* refers to the number of recorded cells and to the number of mice exanimated, respectively. All data were tested for normal distribution using the Shapiro-Wilk test with Prism 6 software or R statistics. Data with normal distributions were analysed with a one-way ANOVA followed by Tukey's multiple comparison *post hoc* test for the statistical comparison of multiple groups or with a Student's two-tailed paired *t* test for the comparison of two groups (Prism 6, GraphPad, La Jolla, CA, USA). Data without normal distributions were analysed with a Friedman or Kruskal-Wallis test followed by a *post hoc* Dunn's multiple comparisons test when comparing multiple groups; Mann-Whitney or Wilcoxon matched-pairs signed rank test when comparing two groups (Prism 6, GraphPad or R statistics).

For the statistical analysis of $Ca^{2+}$ current blockade (use of blockers or toxins) and modulation by baclofen, as well as the reduction in the level of intracellular calcium elevation following activation of $GABA_B$-Rs, we had to consider dependent (data within a group) and independent (data between groups) variables. For a given cell, the measured parameter or variable (current amplitude or $Ca^{2+}$ elevation) and its inhibition/modulation by a drug is considered as a variable dependent on the condition (baseline or drug) within a given group while the same variable represents an independent factor when considered between different groups (control and drug of different types). Therefore, the statistical analyses require the use of a mixed effect model considering in a hierarchical way both dependent and independent variables. The drug effects within a group and between different groups on the analysed variable represent fixed factors (Condition and Group). Finally, because the choice of the cell recorded for this study was done randomly among all those available, it was necessary to implement a statistical model with a factor corresponding to this random effect. The statistical analyses were carried out using the 'linear mixed effect' (lme version 3.1-128) routine (Pinheiro *et al.* 2016). The lme model was subsequently tested using an ANOVA (ANOVA.lme) followed by a *post hoc* Dunn's multiple comparisons test. Wherever an interaction between the variables and the conditions was statistically significant we reported the *P* value. In the statistical analysis, the differences were considered significant when $P < 0.05$. Figures were prepared and finalised using CorelDraw 2018 (Corel Corporation, Ottawa, ON, Canada).

## Results

### CSF-cNs express the $B_1$ subunit of the $GABA_B$ receptor

A previous publication has shown a strong labelling for $GABA_{B1}$ subunits in cells of rat spinal cord with morphological hallmarks of CSF-cNs, that is a small round cell body with a single process extending toward the CC (Margeta-Mitrovic *et al.* 1999). To confirm that $GABA_{B1}$ is expressed in CSF-cNs, we performed in the hindbrain dorsal vagal complex double immunofluorescence labelling against $GABA_{B1}$ and PKD2L1 channel, a specific marker for medullospinal CSF-cNs of mouse (Orts-Del'Immagine *et al.* 2012, 2014). As described previously (McDermott *et al.* 2001; Liu & Wong-Riley, 2005), cell bodies with a marked immunostaining for $GABA_{B1}$ subunits were observed in the dorsal motor nucleus of the vagus nerve (DMNX) and the hypoglossal nucleus (XII, Fig. 1*A*; $n = 3$). In addition, an observation at higher magnification revealed the presence of immunoreactivity against $GABA_{B1}$ subunits (arrows) in the soma of small round cells present around the CC and presenting a projection towards the CC (open arrowhead, Fig. 1*B*; $n = 3$). These cells around the CC were positively immunolabelled by antibodies against the PKD2L1 channel, a selective marker of medullo-spinal CSF-cNs (Fig. 1*C*; $n = 3$). Therefore, our results indicate that medullar

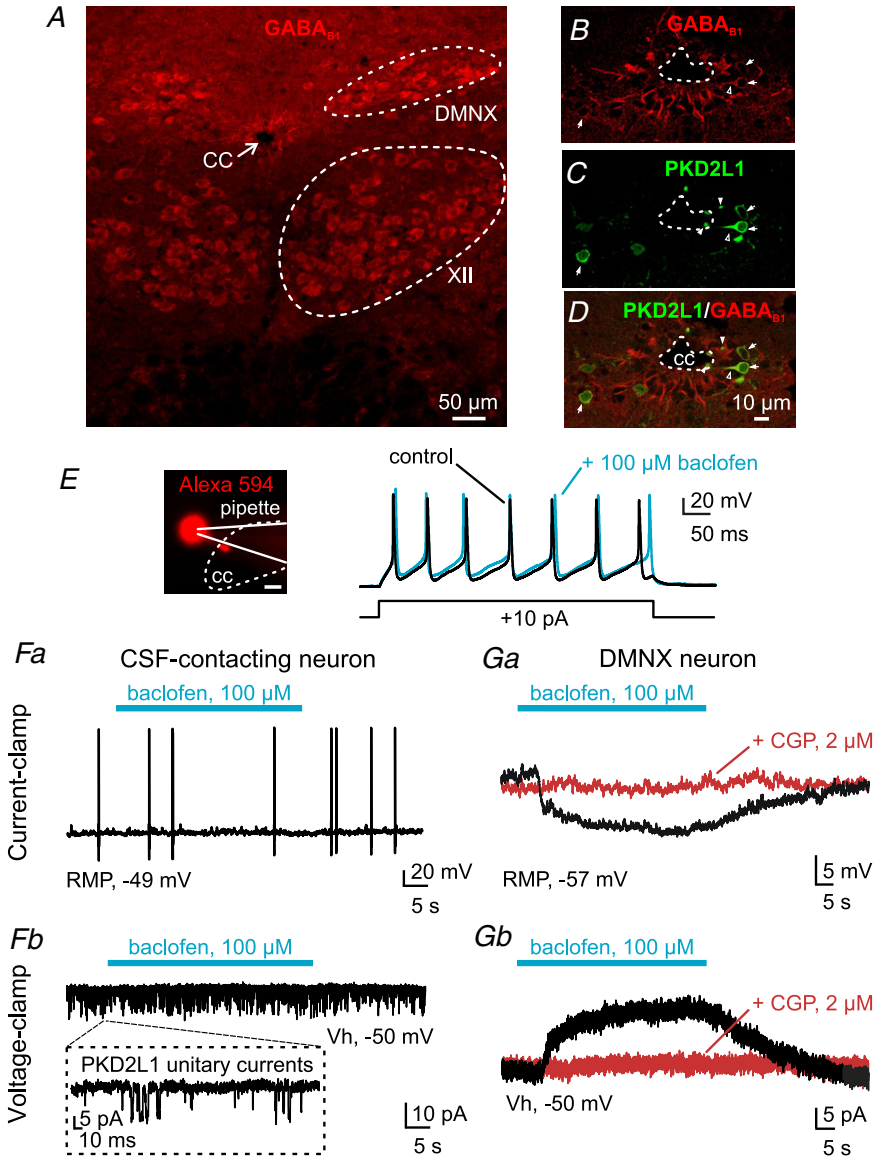


**Figure 1. $GABA_B$ receptors are expressed in CSF-cNs but their activation does not mediate Kir3-type potassium currents**
*A*, image of the mouse brainstem showing immunoreactivity for $GABA_{B1}$ subunit in the dorsal motor nucleus of the vagus (DMNX), the hypoglossal nucleus (XII) and around the central canal (CC). *B–D*, colocalisation of $GABA_{B1}$ subunit (red, panel *B*) with PKD2L1 channel (green, panel *C*; merged image in panel *D*) in neurones in contact with the cerebrospinal fluid (CSF-cNs). $GABA_{B1}$ staining was visualised in soma (arrows) and dendrites (open arrowheads) of CSF-cNs, but at low levels in their terminal dendritic protrusion or bud (closed arrowheads). *E*, left: micrograph showing the typical morphology of CSF-cNs after whole-cell dialysis with Alexa 594 (10 $\mu$M). CSF-cNs have a round cell body and extend a dendrite ending with a bud in proximity to the CC. Scale bar, 10 $\mu$m. *E*, right: action potentials evoked by a 500 ms depolarising current pulse (+10 pA) in identified CSF-cNs had the same properties in controls (black trace) and in the presence of 100 $\mu$M baclofen (blue trace). *F*, in CSF-cNs, pressure application of 100 $\mu$M baclofen for 40 s did not induce either a hyperpolarisation under current-clamp recording (*a*), or an increase in the holding current under voltage-clamp mode (*b*). Note the single-channel activity (inset in *Fb*) mediated by the PKD2L1 channel, as previously described in CSF-cNs. *G*, in DMNX neurones, application of baclofen (100 $\mu$M, 40 s) evoked a hyperpolarisation under current-clamp recording (*a*), or an outward current when the cell was recorded in voltage-clamp mode (*b*). Current and voltage responses were abolished by bath application of the selective $GABA_B$ receptor antagonist CGP (2 $\mu$M; red traces). [Colour figure can be viewed at wileyonlinelibrary.com]

**Table 1. Electrophysiological properties of CSF-cNs before and after the activation of $GABA_B$ receptors with baclofen**

| | Control | Baclofen | *P* value |
|---|---|---|---|
| Resting potential (mV) | −57.08 ± 7.39 ($n = 12$) | −53.08 ± 6.70 ($n = 11$) | 0.1079 |
| Threshold potential (mV) | −37.41 ± 4.37 ($n = 8$) | −35.54 ± 4.92 ($n = 7$) | 0.4290 |
| AP amplitude (mV) | 102.30 ± 7.74 ($n = 8$) | 98.73 ± 8.58 ($n = 7$) | 0.2183 |
| AP frequency (Hz) | 17.68 ± 5.89 ($n = 8$) | 19.67 ± 5.80 ($n = 7$) | 0.7345 |
| AP half-width (ms) | 3.78 ± 0.67 ($n = 8$) | 3.83 ± 0.66 ($n = 7$) | 0.8245 |

In the presence of 100 $\mu$M baclofen, the resting membrane and threshold potential as well as action potentials (APs) parameters are not significantly different from control (two-tailed paired Student's t-test for all comparisons). APs were evoked by +10 pA current pulses of 500 ms duration.

CSF-cNs express $GABA_{B1}$ subunits (Fig. 1*D*; $n = 3$). $GABA_{B1}$ coexpressed with PKD2L1 in the somatodendritic compartment of CSF-cNs (arrows and open arrowheads; Fig. 1*C* and *D*; $n = 3$) but a clear labelling for $GABA_{B1}$ was difficult to observe in the bud (closed arrowheads; Fig. 1*C* and *D*), suggesting a low expression of the protein in the dendritic terminal protrusion. Altogether, these data suggest that medullar CSF-cNs possess $GABA_B$-Rs.

## $GABA_B$ receptors do not mediate Kir3-type potassium currents in CSF-cNs

We next investigated the functional properties of $GABA_B$-Rs in CSF-cNs. In different neuronal models, including the hindbrain, activation of $GABA_B$-Rs was shown to elicit Kir3-type potassium currents (GIRK). We therefore assessed whether a similar response is generated in medullar CSF-cNs. Using whole-cell patch-clamp recordings in current-clamp conditions, we showed that local application of baclofen (100 $\mu$M, for 30–40 s), a selective agonist for $GABA_B$-Rs, changed neither the properties of APs evoked by a depolarising current pulse (Fig. 1*E* and Table 1) nor the CSF-cN intrinsic properties (Table 1). Further, at a holding potential of −50 mV, in all CSF-cNs tested, baclofen activation of $GABA_B$ receptors failed to elicit either a hyperpolarisation of the resting membrane potential (RMP, current-clamp recording, Fig. 1*Fa*; $n = 10$) or an increase in the holding current (voltage-clamp recording, Fig. 1*Fb*; $n = 22$). Since DMNX neurones also express $GABA_B$-Rs (Fig. 1*A*) and were shown to have $GABA_B$-mediated potassium currents (Browning & Travagli, 2001), we tested, as an internal control in the same slice preparation, whether $GABA_B$-R-mediated response can be recorded. In all DMNX neurones, pressure application of baclofen (100 $\mu$M, 40 s) induced a hyperpolarisation of the membrane potential by 9.45 ± 4.12 mV in current-clamp mode (Fig. 1*Ga*; $n = 6$) or an outward potassium current under voltage-clamp mode with an average amplitude of 23.67 ± 25.21 pA (Fig. 1*Gb*; $n = 6$). Both responses were fully blocked in the presence of CGP54626A (CGP), a $GABA_B$-R selective antagonist (Fig. 1*Ga* and *Gb*; $n = 3$). These data show that $GABA_B$-Rs activate Kir3-type potassium channels in DMNX neurones but not in CSF-cNs.

## Characterisation of voltage-gated calcium channels in CSF-cNs

In juvenile rats, CSF-cNs were suggested to express calcium voltage-dependent channels ($Ca_V$) (Marichal *et al.* 2009) but so far, no functional data are available in adult mice and the type of $Ca_V$ expressed is unknown. To address this point in our model, we carried out voltage-clamp recordings in conditions enabling selective isolation of the $Ca^{2+}$ current (see Methods, Recording of voltage-gated calcium currents) and applied voltage steps ($V_{step}$ from −60 to +30 mV, 10 mV increments) for 100 ms from a holding potential of −70 mV to evoke inward currents of increasing amplitude (Fig. 2*A*). The evoked currents exhibit fast activation at the start of the voltage steps followed by a sustained current showing little inactivation and ending with a fast tail current. As illustrated from the average current–voltage relationship (*I–V* curve, Fig. 2*B*) and the fit of the experimental data using a Boltzmann function (red line in Fig. 2*B*), the current activates for membrane potentials more depolarised than −40 mV, reaches a peak amplitude of −129.72 ± 54.91 pA at a membrane potential of +11.60 ± 0.43 mV (Fig. 2*B*; $n = 13$). These properties of the recorded current are in agreement with those reported for high voltage activated $Ca^{2+}$ currents (Catterall, 2011) and this assumption is confirmed by the full block of the current observed in the presence of 200 $\mu$M cadmium ($Cd^{2+}$), a selective blocker of $Ca_V$ (peak current amplitudes: −177.00 ± 38.36 pA in control and +7.25 ± 21.32 pA in $Cd^{2+}$; Fig. 2*C*, $n = 12$; $P < 0.01$, Wilcoxon matched-pairs signed ranked test). Next, we characterised the nature of $Ca_V$ expressed by CSF-cNs and underlying the observed current using selective toxins or inhibitors for the principal $Ca_V$ subtypes. In the presence of 500 nM $\omega$-conotoxin GVIA ($\omega$-CnTx GVIA), a selective blocker for $Ca_V2.2$ (or N-type $Ca^{2+}$ channels), the amplitude of the recorded current was strongly reduced (peak current amplitudes: −141.71 ± 19.59 pA in control and -52.57 ± 28.14 pA in $\omega$-CnTx

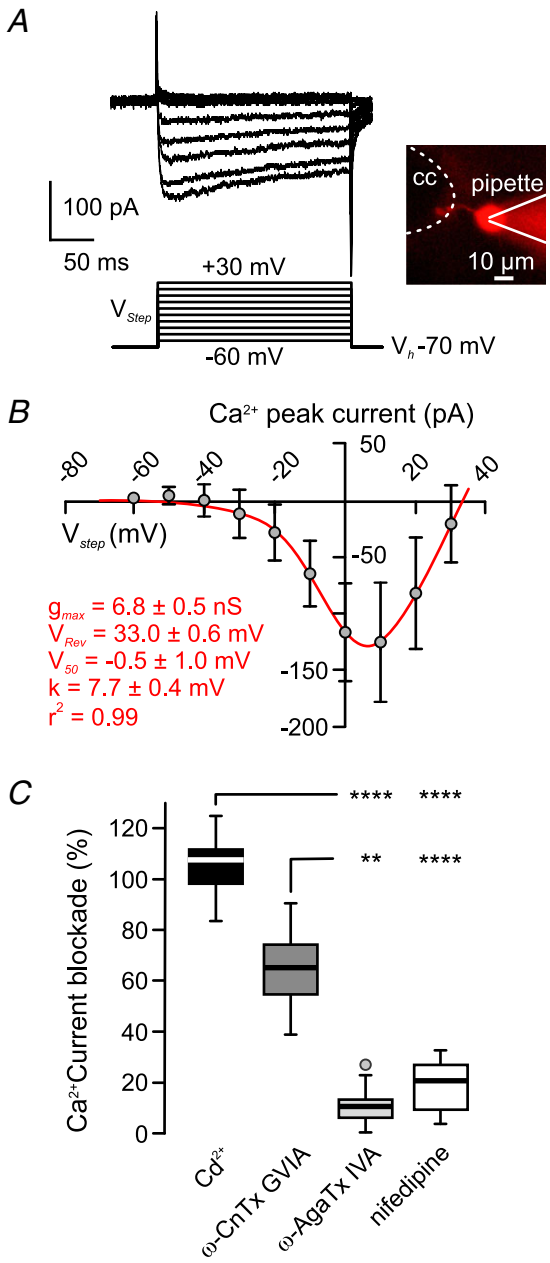


**Figure 2. CSF-cNs express N-type voltage-gated $Ca^{2+}$ channels**
*A*, representative whole-cell current traces recorded in response to voltage steps from −60 mV to +30 mV ($V_{Step}$, +10 mV increments, protocol illustrated under the current traces) from a holding potential of −70 mV ($V_h$) to elicit $Ca^{2+}$ current in a CSF-cN. The inset represents the recorded CSF-cN after cell dialysis with Alexa 594 (10 $\mu$M) to confirm the morphology. CC: central canal. *B*, average current-voltage relationship for the $Ca^{2+}$ currents recorded in CSF-cNs ($n = 13$). Data are fitted using a Boltzmann function (red trace, see Methods for more details). The inset in red gives the values defining the properties of the $Ca^{2+}$ current in CSF-cNs obtained from the Boltzmann fit of the average data (see text for details). *C*, summary box-and-whiskers plots of the averaged percentage of $Ca^{2+}$ current blockade in the presence of cadmium ($Cd^{2+}$; 105 ± 3%; black box, $n = 12$), $\omega$-conotoxin GVIA ($\omega$-CnTx GVIA; 64 ± 6%; grey box, $n = 7$), $\omega$-agatoxin IVA ($\omega$-AgaTx IVA; 11 ± 2%, light grey box, $n = 11$), and nifedipine (14 ± 3%; white box, $n = 9$). $Ca^{2+}$ current sensitivity to cadmium and $\omega$-CnTx GVIA is significantly higher compared to that observed in the presence of $\omega$-agatoxin IVA (****$P < 0.0001$, **$P < 0.01$; Kruskal-Wallis/Dunn's *post hoc* multiple comparison test). [Colour figure can be viewed at wileyonlinelibrary.com]

GVIA$^+$; Fig. 2*C*, $n = 12$; $P < 0.05$, Wilcoxon matched-pairs signed ranked test). In contrast, in the presence of 500 nM $\omega$-agatoxin IVA ($\omega$-AgaTx VIA), a blocker of $Ca_V2.1$ (P/Q type), or 1 $\mu$M nifedipine, a blocker of $Ca_V1.2$ and 1.3 (neuronal L type), there was only a small decrease in the $Ca^{2+}$ current amplitude (peak current amplitudes: −162.64 ± 75.60 pA in control and −144 ± 60.84 pA in $\omega$-AgaTx VIA, $n = 11$; −123.17 ± 49.39 pA in control and -97.33 ± 29.37 pA in nifedipine, $n = 6$; $P < 0.01$ and $P < 0.05$, respectively, Wilcoxon matched-pairs signed ranked test). Taken together, our results demonstrate that medullar CSF-cNs express functional voltage-dependent $Ca^{2+}$ channels that are primarily of the $Ca_V2.2$ type (N type).

## GABA$_B$ receptors are functional in CSF-cNs and modulate voltage-gated calcium channels

Classically GABA$_B$-R activation has been shown to inhibit $Ca_V$ both at pre- and postsynaptic levels and therefore to modulate cellular activity and synaptic transmission (see below), respectively. To assess whether GABA$_B$-Rs activation modulates $Ca_V$ in CSF-cNs, we elicited peak $Ca^{2+}$ currents (holding potential of −70 mV, voltage step to +10 mV) and tested the effect of baclofen on the current amplitude. Figure 3*A* and *B* illustrates representative traces showing the effect of baclofen on $Ca^{2+}$ current recorded in two CSF-cNs in the absence and presence of CGP. In all tested CSF-cNs, baclofen application (100 $\mu$M, for 30 s) induced a rapid and long-lasting inhibition of $Ca^{2+}$ currents (Fig. 3*C* and *D*; $n = 13$) that slowly reversed upon baclofen wash out. In the presence of CGP, the baclofen-mediated $Ca^{2+}$ current inhibition was strongly reduced (Fig. 3*A*–*D*; $n = 14$).

G protein coupled receptors (GPCR) of the $G\alpha_{i/o}$ type primarily inhibit $Ca^{2+}$ current through the direct binding of the $G\beta\gamma$ subunits to the channel. This inhibition is voltage dependent and can be removed by a strong depolarisation (Herlitze *et al.* 1996; Ikeda, 1996). To test whether the observed effect on $Ca^{2+}$ currents following GABA$_B$-R activation is mediated through a similar mechanism in CSF-cNs, we used the classical triple pulse protocol (see Methods, Recording of voltage-gated calcium currents). In controls, the $Ca^{2+}$ current elicited by the prepulse and the postpulse had similar average amplitudes of −176.83 ± 99.62 pA and −149.43 ± 65.48 pA, respectively (Fig. 4*Aa*; $n = 9$, $P = 0.3719$ pre- *vs.* postpulse amplitude in control, ANOVA.lme/*post hoc* Dunn's multiple comparison test) and the pre/postpulse

ratio was around 95% (Fig. 4*D*; $n = 9$). As illustrated for a representative recording (Fig. 4*Aa* and *Ba*), baclofen application strongly reduced the peak amplitude of the $Ca^{2+}$ current activated during the prepulse (average peak amplitude: $-61.76 \pm 44.41$ pA, $n = 9$; ANOVA.lme/*post hoc* Dunn's test, $P < 0.0001$ compared to control; see above; (1) in Fig. 4*Aa*, *Ba*, *C* and *D*). Note that the level of inhibition was similar to that reported in Fig. 3 (inhibition: $51 \pm 24\%$; $n = 13$, in Fig. 3*D* for single pulse protocol; $52 \pm 24\%$; $n = 9$, in Fig. 4*D* for triple pulse protocol; Mann-Whitney test, $P = 0.8409$). However, following the depolarisation to +100 mV, the current inhibition mediated by baclofen was strongly reduced for the postpulse compared to the prepulse in the same conditions and the average peak amplitude was similar to that observed for the postpulse recordings in controls (control postpulse: $-149.43 \pm 65.48$ pA; baclofen postpulse: $-114.66 \pm 63.99$ pA, $P = 0.078$ and prepulse *vs.* postpulse in baclofen, $P < 0.01$, ANOVA.lme/*post hoc* Dunn's multiple comparison test; $n = 9$; (2) in Fig. 4*Aa*, *Ba* and *C*; $n = 9$). Accordingly, the pre/postpulse ratio decreased by around 40% compared to the control situation (Fig. 4*D*; $n = 9$). In the presence of CGP, the inhibition of the $Ca^{2+}$ current by baclofen was strongly reduced for the current elicited by the pre- and postpulse (average peak amplitude: $-179.59 \pm 72.86$ pA and $-166.84 \pm 79.71$ pA for the prepulse ($P = 0.9591$) and $-154.22 \pm 60.94$ pA and $-144.32 \pm 59.82$ pA for the postpulse ($P = 0.9901$) in CGP in the absence or presence of baclofen, respectively, $n = 10$; $P = 0.0703$ and 0.9801 for the pre- and postpulse in baclofen in the absence ($n = 9$) or presence ($n = 10$) of CGP; ANOVA.lme/*post hoc* Dunn's multiple comparison test; see (2) in Fig. 4*Ab*, *Bb*, and *C*). In the presence of CGP alone and with baclofen, the pre/postpulse ratio was similar to that observed in control and close to 100% (Fig. 4*D*; $n = 10$). Altogether, these results show that $GABA_B$-Rs are functional in CSF-cNs and inhibit $Ca^{2+}$ current through a $G\beta\gamma$-mediated effect.

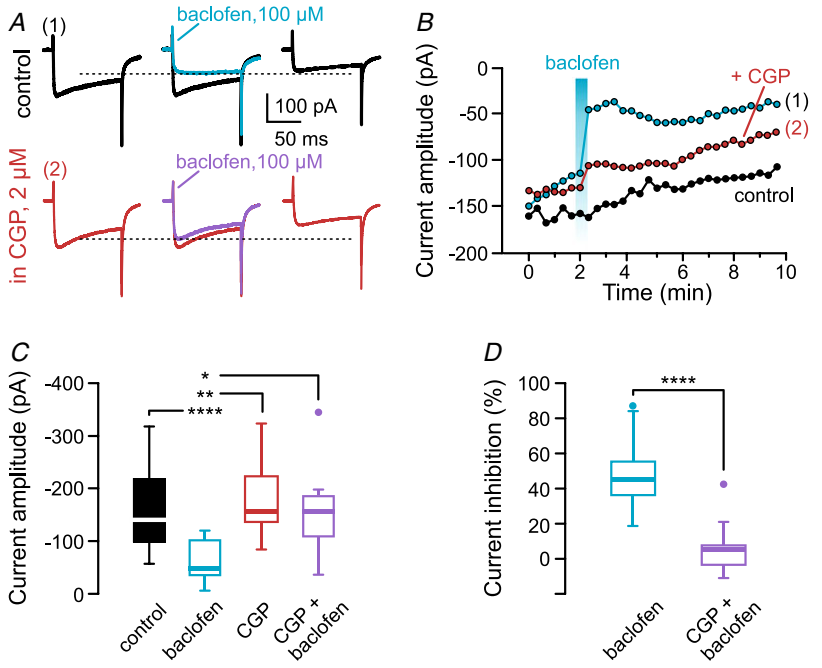


**Figure 3. Activation of $GABA_B$ receptors by baclofen inhibits $Ca^{2+}$ current**
*A*, representative peak $Ca^{2+}$ currents traces elicited with a voltage step to +10 mV from a holding potential of −70 mV and recorded in two different CSF-cNs in control (top, 1, black traces) or in the presence of 2 $\mu$M CGP (bottom, 2, red traces) and in the presence of 100 $\mu$M baclofen (top 1, blue trace) alone or with CGP (bottom, 2, violet trace). *B*, time course of the $Ca^{2+}$ current peak amplitude for one recording in control (black circles) and the recordings presented in *A* in the absence (1, blue circles) and presence (2, red circles) of 2 $\mu$M CGP. Baclofen was applied at 100 $\mu$M by pressure for 30 s, as indicated by the blue bar. *C*, summary box-and-whiskers plots for the average $Ca^{2+}$ current peak amplitude before and during baclofen application and in the absence or presence of CGP (control, black box: $-159.33 \pm 87.18$ pA, $n = 13$; baclofen, blue open box: $-60.63 \pm 39.44$ pA, $n = 13$; CGP, red open box: $-172.56 \pm 66.74$, $n = 14$ and baclofen in CGP, violet open box: $-154.65 \pm 72.62$, $n = 14$; $^{****}P < 0.0001$, $^{**}P < 0.01$, $^{*}P < 0.05$; ANOVA.lme/Dunn's *post hoc* multiple comparison test). *D*, summary box-and-whiskers plots for the $Ca^{2+}$ current inhibition induced by baclofen in the absence (blue open box) and presence (violet open box) of CGP. Baclofen produced a significant inhibition of the $Ca^{2+}$ current peak amplitude, while in the presence of CGP this inhibitory effect was abolished (baclofen: $49 \pm 6\%$, $n = 13$; baclofen in CGP: $7 \pm 4\%$, $n = 14$; $^{****}P < 0.0001$, Mann-Whitney test). [Colour figure can be viewed at wileyonlinelibrary.com]

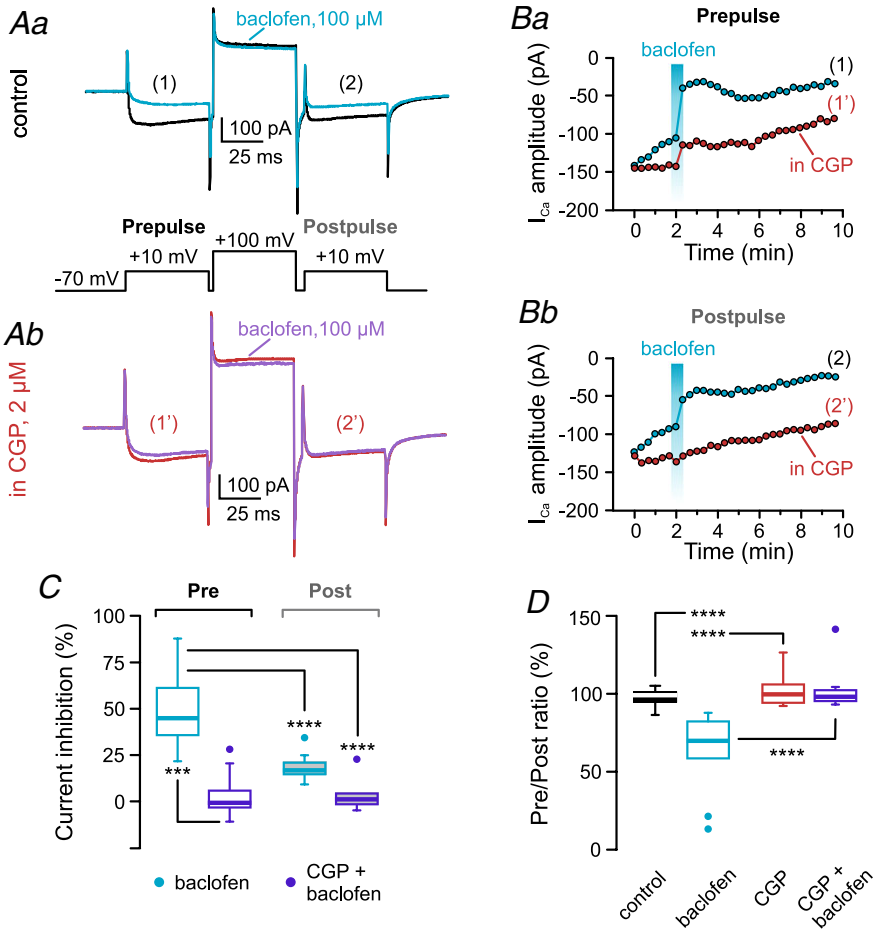


**Figure 4. GABA$_B$ receptors inhibit voltage-gated Ca$^{2+}$ channels through a G$\beta\gamma$-mediated mechanism**
*A*, representative traces illustrating the peak Ca$^{2+}$ current recorded in two CSF-cNs in control (*a*) or in the presence of 2 $\mu$M CGP (*b*) using a triple pulse protocol where 2 voltage steps to +10 mV (50 ms) from a holding potential of −70 mV are applied and separated by a depolarising step to +100 mV for 50 ms. The recording protocol is illustrated below the traces in panel *a* and the pulses before and after the depolarisation to +100 mV represent the prepulse (black font) and postpulse (grey font), respectively. *Aa*, current traces recorded in control (black trace) in the presence of baclofen (blue trace) and elicited by the prepulse (1) and the postpulse (2). *Ab*, recordings in the presence of 2 $\mu$M CGP before (red trace) and during baclofen application (violet trace) for the prepulse (1′) and the postpulse (2′). *B*, time course of the Ca$^{2+}$ current peak amplitude for the neurones illustrated in *Aa* and *Ab* and illustrating the baclofen effect on the amplitude of the Ca$^{2+}$ current elicited by the prepulse (*a*) and the postpulse (*b*) in the absence (1 and 2, blue circles) and the presence of 2 $\mu$M CGP (1′ and 2′, red circles). Baclofen was pressure applied at 100 $\mu$M for 30 s as indicated by the blue bars. *C*, summary box-and-whiskers plots for the Ca$^{2+}$ current inhibition induced by baclofen in the absence (blue box) and presence (violet box) of 2 $\mu$M CGP for the prepulse (open box) and the postpulse (grey box) as indicated above the graph. Baclofen produced a significant inhibition of the peak Ca$^{2+}$ current amplitude elicited by the prepulse that was larger than that observed for the postpulse Ca$^{2+}$ current (baclofen: 52 ± 24% for the prepulse and 19 ± 8% for the postpulse, $n = 9$). In the presence of CGP, the baclofen inhibitory effect was strongly and significantly reduced and there was no significant difference between the inhibition observed for the pre- and postpulse currents (baclofen in CGP: 4 ± 12% for the prepulse and 3 ± 7% for the postpulse, $n = 10$). *D*, summary box-and-whiskers plots for the prepulse/postpulse ratio recorded in control (black box), in baclofen (blue open box), in CGP (red open box) and in baclofen with CGP (violet open box). In the presence of baclofen alone, the prepulse/postpulse ratio was strongly reduced (control: 98 ± 6%, baclofen: 62 ± 27%, $n = 9$). In the presence of CGP, baclofen failed to reduce the prepulse/postpulse ratio (CGP: 102 ± 11%, baclofen in CGP: 103 ± 14%, $n = 10$; $P = 0.9998$). The prepulse/postpulse ratios calculated in the presence of CGP and baclofen with CGP were both significantly higher than that calculated for baclofen alone (see above; ****$P < 0.0001$ for the ratio with baclofen alone compared to CGP alone and CGP with baclofen, respectively). Statiscal test: ANOVA.lme/Dunn's *post hoc* multiple comparison test; ****$P < 0.001$, ****$P < 0.0001$. [Colour figure can be viewed at wileyonlinelibrary.com]

### $GABA_B$ receptor activation reduces action potential evoked intracellular calcium rises

Following activation of $Ca_V$, the $Ca^{2+}$ influx will induce an elevation in the intracellular $Ca^{2+}$ concentration ($[Ca^{2+}]_i$). Using combined electrophysiology and $Ca^{2+}$ imaging with Fluo-4, we tested the consequence of $GABA_B$-R activation on $[Ca^{2+}]_i$ increase induced by a short depolarisation. First, when $Ca^{2+}$ currents are elicited in voltage-clamp mode (from −70 mV to +10 mV for 100 ms), the Fluo-4 fluorescence, i.e. $[Ca^{2+}]_i$ in CSF-cN soma increased by 560 ± 313% (n = 5; data not shown) from baseline. This result confirms that activation of $Ca_V$ elicits a large elevation in $[Ca^{2+}]_i$. Next, to reproduce a more physiological condition, we elicited $[Ca^{2+}]_i$ elevation using 5 consecutive trains of APs by injecting in current-clamp mode +20 pA DC current from the CSF-cN RMP (Fig. 5*A* and *B*; see Methods, Calcium imaging). As expected, $[Ca^{2+}]_i$ increased by 14 ± 14% ($\Delta F/F_0$; $n = 12$) from baseline on the first AP train and subsequent trains of APs induced a cumulative rise in $[Ca^{2+}]_i$ to reach on average an amplitude of 38 ± 43%

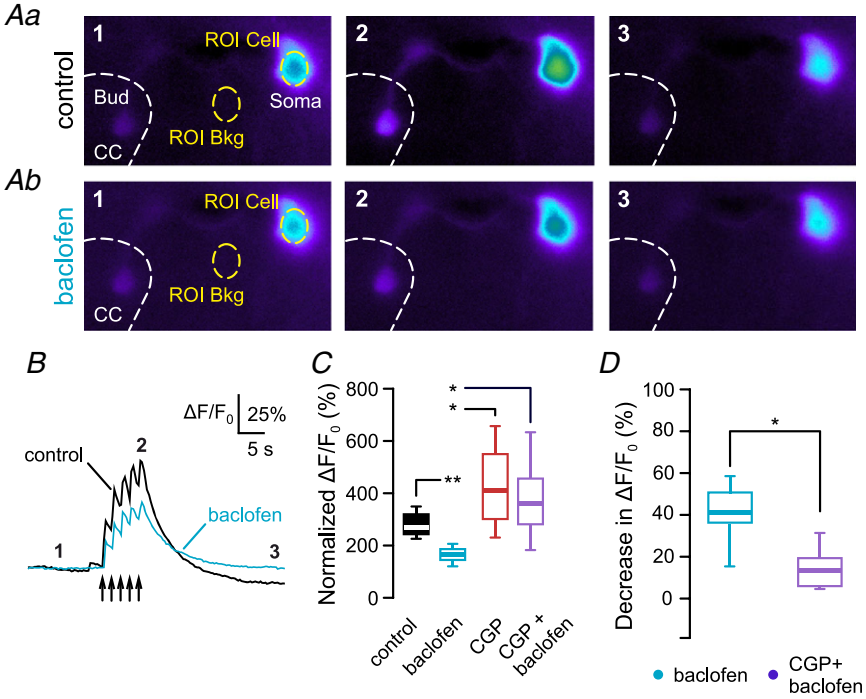


**Figure 5. $GABA_B$ receptor activation inhibits intracellular $Ca^{2+}$ increase induced by $Ca_V$ activation**
*A*, representative average images illustrating in control (*a*) and in the presence of baclofen (*b*, 100 $\mu$M) the baseline fluorescence (1) acquired in one CSF-cN recorded in current-clamp mode at the resting membrane potential (RMP: −56 mV) and dialysed (whole-cell configuration) with 50 $\mu$M Fluo-4, a $Ca^{2+}$-sensitive fluorescent probe, (2) the maximum fluorescence increase after 5 consecutive trains of action potentials (APs) and (3) the fluorescence at the end of the recovery period (see also control and baclofen in panel *B*, black and blue lines respectively). Images are presented in pseudocolour (black: low fluorescence; red: high fluorescence) and each average was obtained from 5 consecutive images (~1 s) in the different conditions. Dashed white line delineates the central canal (CC) and yellow dashed lines represent the regions of interest (ROI) drawn in the background (ROI Bkg) and on the CSF-cN soma (ROI Cell). These two ROIs were used to calculate the net average fluorescence intensity ($\Delta F/F_0$; see Methods) and generate the fluorescence time course, i.e. the calcium transient. The 5 trains of APs were triggered with a DC current injection pulse of +20 pA for 500 ms delivered at 0.5 Hz. *B*, time course of the net fluorescence changes acquired in control (black trace) and in the presence of 100 $\mu$M baclofen applied during the AP train (blue trace) from the cell illustrated in *A*. The arrows under the traces represent the time point when each train of APs was triggered. Trace was corrected for fluorescence quenching. *C*, summary box-and-whiskers plots for the normalised fluorescence increase recorded after the 5th train of APs in control (black box), in baclofen (blue open box), in CGP (red open box) and in baclofen with CGP (violet open box). In the presence of baclofen alone, the net increase in fluorescence was significantly reduced while that effect was abolished when CGP was bath applied (control: 282 ± 51% and baclofen: 166 ± 35%, $n = 6$; CGP: 429 ± 170% and baclofen in CGP: 379 ± 158%, $n = 7$; $^{**}P < 0.01$, $^{*}P < 0.05$, ANOVA.lme/Dunn's *post hoc* multiple comparison test). *D*, summary box-and-whiskers plots for the decrease in the normalised fluorescence rise recorded after the 5th train of APs in the presence of baclofen alone (open blue box, $n = 6$) and in the presence of baclofen with CGP (open violet box, $n = 7$). In the presence of CGP, the decrease in the recorded fluorescence rise was significantly reduced (baclofen alone: 40 ± 15%, $n = 6$; baclofen in CGP: 9 ± 18%, $n = 7$; $^{*}P < 0.05$, Mann-Whitney test). [Colour figure can be viewed at wileyonlinelibrary.com]

from baseline on the 5$^{th}$ train (Fig. 5*Aa* and *B*; $n = 12$). This $[Ca^{2+}]_i$ elevation corresponded to 292 ± 70% when normalised to the increase recorded for the 1st AP train (Fig. 5*C*; $n = 12$). At the end of the 5$^{th}$ train of APs, the $[Ca^{2+}]_i$ slowly decreased in an exponential manner to return after several seconds to a value similar to the baseline value (3 in Fig. 5*A* and *B*). As illustrated in Fig. 5*Ab* and *B* for a representative recording, in the presence of baclofen, the amplitude of the $[Ca^{2+}]_i$ elevation, recorded on the 5$^{th}$ train of APs, was reduced by nearly half (Fig. 5*C* and *D*; $n = 6$). We reproduced the same protocol in the presence of CGP and, in 7 out of 9 cells recorded, baclofen application failed to reduce the $[Ca^{2+}]_i$ elevation (Fig. 5C and *D*; $n = 7$). Our results, therefore, indicate that CSF-cN depolarisation following a train of APs induces an elevation of $[Ca^{2+}]_i$ through activation of $Ca_V2.2$ and that GABA$_B$-R activation leads to a reduction in this rise.

## Inhibitory synaptic transmission is modulated by GABA$_B$ receptors in CSF-cNs

Activation of GABA$_B$-Rs inhibits synaptic transmission by acting on voltage-gated calcium channels at a variety of central synapses. Therefore, we studied in CSF-cNs the effect of baclofen on postsynaptic inhibitory (IPSCs) and excitatory synaptic currents (EPSCs) evoked by local electrical stimulation. Our previous work has demonstrated the presence of spontaneous inhibitory synaptic transmission (Orts-Del'Immagine *et al.* 2012) but electrically evoked IPSCs have never been recorded in CSF-cNs. Thus, we first characterised evoked IPSCs in medullar CSF-cNs. In the presence of DNQX (20 $\mu$M) and strychnine (1 $\mu$M) to block respectively glutamatergic and glycinergic receptors, electrical stimulation (50−60 V, 100 $\mu$s) at a frequency of 0.1 Hz elicited postsynaptic inward currents in CSF-cNs voltage-clamped at −60 mV (Fig. 6*Aa* and *b*). Postsynaptic inward currents were reversibly reduced by bath application of gabazine, (GBZ, 10 $\mu$M), a selective GABA$_A$ receptor antagonist, with a percentage of inhibition of 98 ± 6% (Fig. 6*Aa*, *Ab* and *B*; $n = 10$). In addition, the reversal potential of postsynaptic inward currents determined by measuring the current amplitudes at different holding potentials from −60 to +40 mV (with 20 mV increments) was −9.75 ± 3.15 mV (Fig. 6*C* and *D*; $n = 6$), which is close to the calculated equilibrium potential for chloride ions (+3.2 mV). These results show that evoked IPSCs recorded in CSF-cNs were mediated by GABA$_A$ receptors. We next checked whether baclofen has an inhibitory effect on evoked IPSCs. Bath application of the selective GABA$_B$ receptor agonist baclofen (100 $\mu$M) powerfully reduced the amplitudes of evoked IPSCs recorded in CSF-cNs at a holding potential of −60 mV, with a percentage inhibition of 82 ± 12% (Fig. 6*Ea*, *Eb* and *F*; $n = 6$). The inhibitory effect of baclofen was reversed by bath application of 2 $\mu$M CGP (Fig. 6*Ea*, *Eb* and *F*; $n = 6$). Therefore, our data show that GABA$_B$-R activation inhibits the GABA$_A$-dependent inhibitory synaptic transmission in CSF-cNs.

## GABA$_B$ receptors inhibit excitatory synaptic transmission in CSF-cNs

We previously reported that CSF-cNs express AMPA/kainate receptors but stimulation of neurotransmitter release with a hypertonic shock did not evoke EPSCs and therefore we suggested that CSF-cNs do not receive excitatory synaptic inputs (Orts-Del'Immagine *et al.* 2016). However, the mechanisms involved in the enhancement of the transmitter release by hypertonic shocks are not yet known and in neurones the enhancement is not dependent on calcium entry into presynaptic terminals (Rosenmund & Stevens, 1996; Mochida *et al.* 1998). In this study, we therefore tested whether EPSCs can be induced in CSF-cNs following presynaptic calcium influx induced by electrical stimulation. In the presence of gabazine and strychnine to block, respectively, GABA$_A$- and glycine receptor-dependent synaptic transmission, electrical stimulation (50−60 V, 100 $\mu$s) at a frequency of 0.1 Hz and from a holding potential of −60 mV induced fast postsynaptic inward currents in CSF-cNs that were reversibly inhibited by bath application of DNQX (20 $\mu$M), an AMPA/kainate receptor antagonist (Fig. 7*Aa*, *Ab* and *B*). The percentage of inhibition of EPSCs by DNQX was 95 ± 6% ($n = 7$). Moreover, the reversal potential determined by recording postsynaptic currents at a holding potential ranging from −60 to +40 mV (20 mV increments) was 0.60 ± 7.10 mV (Fig. 7*C* and *D*, $n = 5$), consistent with the multiple cationic permeability of AMPA/kainate receptors. These data show that electrical stimulation evoked EPSCs mediated by AMPA/kainate receptors in CSF-cNs. We further studied the effect of GABA$_B$-R activation on excitatory synaptic transmissions in CSF-cNs. At a holding potential of −60 mV, bath application of baclofen (100 $\mu$M) had a marked inhibitory effect on the amplitudes of EPSCs recorded in CSF-cNs, with a percentage of inhibition of 63 ± 16% (Fig. 7*Ea*, *Eb* and *F*; $n = 7$). Bath application of the antagonist CGP reversed the inhibitory effect of baclofen on EPSCs (Fig. 7*Ea*, *Eb* and *F*; $n = 7$). These results show for the first time that CSF-cNs receive excitatory glutamatergic inputs and that activation of GABA$_B$ receptors has an inhibitory effect on the excitatory synaptic transmission.

## Presynaptic action for GABA$_B$ receptor-mediated inhibition of inhibitory and excitatory synaptic transmission

We then examined whether the baclofen-mediated inhibition of EPSCs and IPSCs in CSF-cNs is caused by a pre- or postsynaptic mechanism. For this purpose, we first

evoked synaptic responses by paired-pulse stimulation and we compared the paired-pulse ratio (PPR: amplitude of the second postsynaptic current/amplitude of the first postsynaptic current) before and during application of baclofen and CGP. At a stimulus interval of 70 ms (50−60 V, 100 $\mu$s for each pulse) and from a holding potential of −60 mV, bath application of baclofen (20 $\mu$M) significantly increased the PPR of both IPSCs (Fig. 8*A* and *C*) and EPSCs (Fig. 8*B* and *D*) by, respectively, 65 ± 37% ($n = 7$) and 92 ± 70% ($n = 7$), largely due to a reduction in the amplitude of the first response (see lower traces in Fig. 8*A* and *B*). Bath application of CGP (2 $\mu$M) reversed the increase in PPR induced by baclofen of both IPSCs (Fig. 8*A* and *C*) and EPSCs (Fig. 8*B* and *D*). To confirm further the presynaptic locus of $GABA_B$ receptor-mediated inhibition, we next checked whether there is a postsynaptic

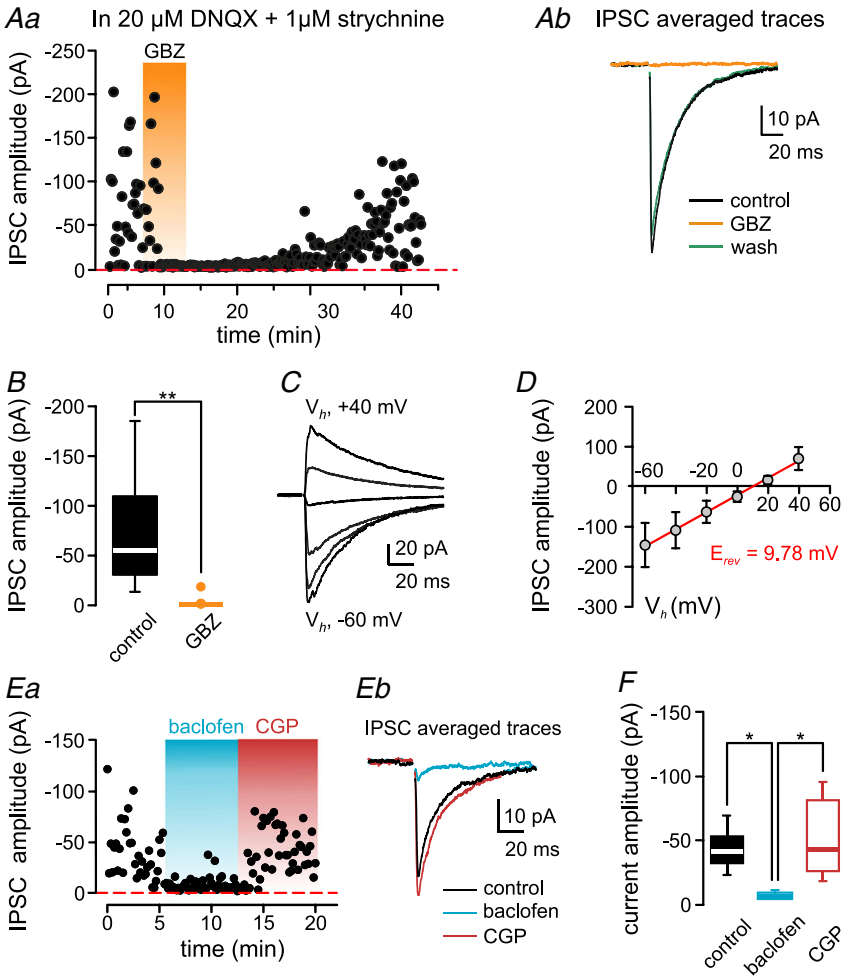


**Figure 6. Baclofen inhibits evoked inhibitory synaptic transmission in CSF-cNs**
*A*, IPSC peak amplitudes plotted *versus* time (*a*) and representative averaged traces (*b*) before (black trace), during (orange trace) and after (green trace) bath application of the selective $GABA_A$ receptor antagonist gabazine (GBZ, 10 $\mu$M). IPSCs were evoked every 10 s at a holding potential of −60 mV and in the presence of 20 $\mu$M DNQX (an AMPA/kainite antagonist) and 1 $\mu$M strychnine (a glycine receptor antagonist). *B*, box-and-whisker plots of IPSCs peak amplitudes in control and in the presence of gabazine. Gabazine had a significant inhibitory effect on IPSC amplitude (control: −71.39 ± 58.04 pA, $n = 10$; gabazine: −1.84 ± 5.60 pA, $n = 10$; $^{**}P < 0.01$, Wilcoxon matched-pairs signed rank test). *C*, averaged IPSCs traces in response to voltage-step applications from −60 mV to +40 mV using 20 mV increments. *D*, IPSC mean peak amplitudes plotted against the holding potential. The indicated reversal potential was determined from the linear regression of the current-potential relationship ($R^2 = 0.99$). *E*, time course of peak IPSCs amplitudes (*a*) and representative averaged traces (*b*) before (black trace) after bath application of 100 $\mu$M baclofen (selective agonist of $GABA_B$ receptors, blue trace) and 2 $\mu$M CGP (selective antagonist of $GABA_B$ receptors, red trace). IPSCs were evoked at 0.1 Hz and at −60 mV. *F*, box-and-whisker plots of IPSCs amplitudes in control and in the presence of baclofen and CGP. Baclofen significantly reduced the amplitude of IPSCs and the inhibitory effect was reversed with CGP (control: −42.82 ± 15.82 pA, $n = 6$; baclofen: −6.38 ± 1.97 pA, $n = 6$; CGP: −50.78 ± 30.12 pA, $n = 6$; $^{*}P < 0.05$, Friedman/Dunn *post hoc* multiple comparison test). [Colour figure can be viewed at wileyonlinelibrary.com]

interaction between GABA$_B$ receptors and GABA$_A$ or AMPA/kainate receptors by analysing the kinetics of evoked IPSCs and EPSCs, respectively. We found that application of baclofen (20 $\mu$M) did not affect either the decay time or the 10–90% rise time of IPSCs (Fig. 8*E* and *G*) and EPSCs (Fig. 8*F* and *H*). Therefore, these results suggest that inhibition of both inhibitory and excitatory synaptic transmission by baclofen is mediated by activation of presynaptic GABA$_B$ receptors.

## Discussion

Over the last few years, substantial advances have been made in identifying membrane proteins expressed in medullar CSF-cNs and involved in the control of their excitability. Excitation in CSF-cNs was shown to be mediated by pH sensitive PKD2L1 and ASICs channels whereas inhibition involves ionotropic GABA$_A$ and glycine receptors (Orts-Del'Immagine *et al.* 2012, 2016). In

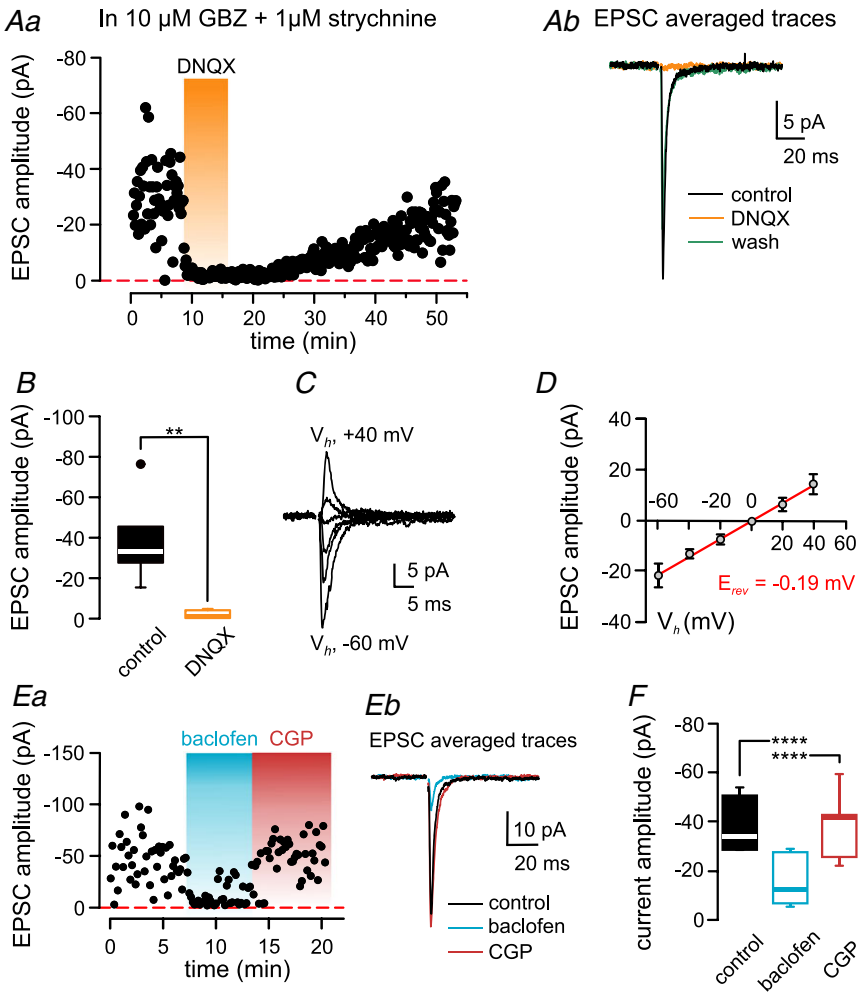


**Figure 7. Evoked excitatory synaptic transmission is inhibited by baclofen in CSF-cNs**
*A*, time course of peak EPSCs (*a*) and representative averaged traces (*b*) before (black trace), during (orange trace) and after (green trace) bath application of the selective antagonist of AMPA/kainate receptors DNQX (20 $\mu$M). EPSCs were recorded every 10 s at a holding potential of −60 mV and in the presence of gabazine (10 $\mu$M) and strychnine (1 $\mu$M). *B*, box-and-whisker plots of EPSCs amplitudes summarising the inhibitory effect of DNQX (control: −38.43 ± 19.51 pA, $n = 7$; DNQX: −1.57 ± 1.91 pA, $n = 7$; $^{**}P < 0.01$, Student's two-tailed paired *t* test). *C*, averaged EPSCs traces recorded at different holding potentials (from −60 to +40 mV). *D*, plot of the mean current amplitude of EPSC against the holding membrane potential. EPSCs had a linear relationship to holding membrane potential and linear regression analysis showed an extrapolated reversal potential close to 0 mV ($R^2 = 0.99$). *E*, EPSC peak amplitudes plotted *versus* time (*a*) and representative averaged traces (*b*) before (black trace) and after bath application of 100 $\mu$M baclofen (blue trace) and 2 $\mu$M CGP (red trace). EPSCs were evoked at 0.1 Hz and at −60 mV. *F*, summary box-and-whisker plots showing the effect of baclofen on EPSC amplitudes. Baclofen had a significant inhibitory effect on EPSC amplitudes that was reversed with CGP (control: −37.96 ± 10.64 pA, $n = 7$; baclofen: −14.86 ± 9.79 pA, $n = 7$; CGP: −37.59 ± 12.99 pA, $n = 7$; $^{****}P < 0.0001$, repeated measures ANOVA/Tukey *post hoc* multiple comparison test). [Colour figure can be viewed at wileyonlinelibrary.com]

the present study, we provide additional insights into the functional properties of CSF-cNs by analysing the contribution of metabotropic $GABA_B$-Rs in the control of CSF-cNs activity. We demonstrate that $GABA_B$-Rs are present in CSF-cNs, but they do not activate the canonical GIRK pathway. In contrast, CSF-cNs express primarily N-type voltage-gated $Ca^{2+}$ channels ($Ca_V2.2$). Activation of $GABA_B$ receptors recruits $G\beta\gamma$ subunits to inhibit $Ca_V2.2$ activity and reduces the increase in intracellular $Ca^{2+}$. Our study further shows, for the first time in rodents, that CSF-cNs have AMPA/kainate receptors that are engaged in a synaptic transmission, which demonstrates that CSF-cNs receive an additional excitatory control through glutamatergic inputs. Finally, we found that $GABA_B$ receptors are located presynaptically on both GABAergic and glutamatergic terminals and their activation inhibits the release of GABA and glutamate onto CSF-cNs. The schematic illustration in Figure 9 summarises the overall results.

## Absence of GIRK-dependent inhibition in CSF-cNs

The most intriguing result reported here is the lack of $GABA_B$-mediated GIRK response in CSF-cNs. Indeed, our data revealed that the application of baclofen, the selective agonist of $GABA_B$-Rs, had no effect in all cells tested,

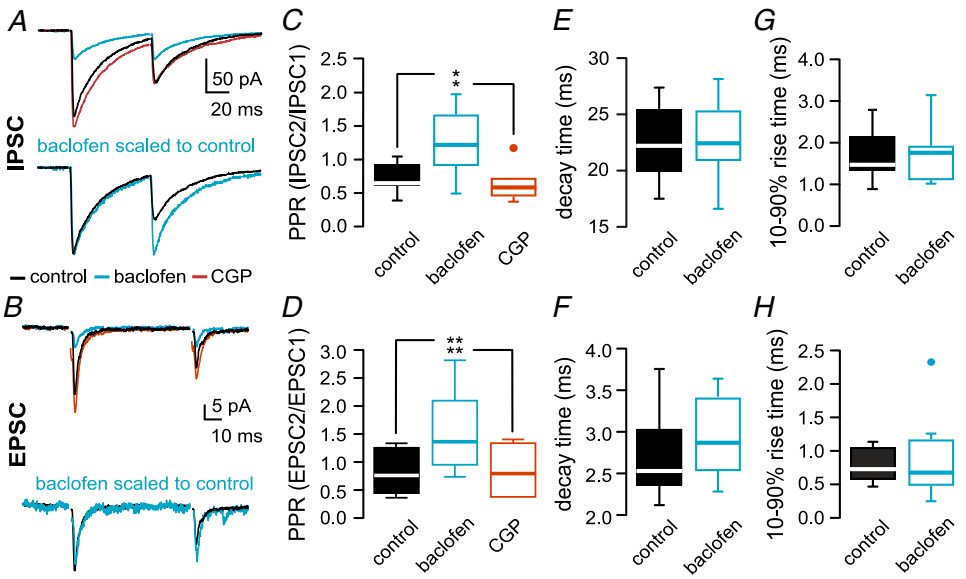


**Figure 8. Baclofen increases the paired-pulse ratio of both IPCSs and EPSCs but has no effect on their kinetics**
*A*, upper traces: representative averaged IPSCs recorded by a paired-pulse stimulation at an interstimulus interval of 70 ms before (black) and in the presence of 20 $\mu$M baclofen (blue) and 2 $\mu$M CGP (red). IPSCs were recorded at 0.1 Hz from CSF-cNs voltage-clamped at −60 mV in aCSF containing DNQX (20 $\mu$M) and strychnine (1 $\mu$M). *A*, lower traces: IPSCs recorded without (black) or in the presence of baclofen (blue) were scaled to the first response. *B*, upper traces: representative paired-pulse EPSCs averaged traces evoked at an interstimulus interval of 70 ms before (black) and in the presence of 20 $\mu$M baclofen (blue) and 2 $\mu$M CGP (red). EPSCs were recorded every 10 s at −60 mV and with aCSF containing gabazine (10 $\mu$M) and strychnine (1 $\mu$M). *B*, lower traces: EPSCs recorded without (black) or in the presence of baclofen (blue) were scaled to the first response. *C*, summary box-and-whisker plots showing the effect of baclofen on the paired-pulse ratio of IPSCs (PPR: amplitude of the second IPSC/amplitude of the first IPSC). Baclofen significantly increased the PPR of IPSCs and its effect was reversed with CGP (control: 0.72 ± 0.23, $n = 7$; baclofen: 1.22 ± 0.50, $n = 5$; CGP: 0.65 ± 0.26, $n = 7$; $^*P < 0.05$, repeated measures ANOVA/Tukey *post hoc* multiple comparison test). *D*, summary box-and-whisker plots showing that baclofen significantly increased the paired-pulse ratio of EPSCs (PPR: amplitude of the second EPSC/amplitude of the first EPSC). The baclofen-mediated increase of the PPR was reversed with CGP (control: 0.85 ± 0.40, $n = 7$; baclofen: 1.52 ± 0.73, $n = 7$; CGP: 0.86 ± 0.43, $n = 7$: $^{**}P < 0.01$, repeated measures ANOVA/Tukey *post hoc* multiple comparison test). *E* and *F*, summary box-and-whisker plots showing that IPSCs (*E*) and EPSCs (*F*) had similar decay times between control (IPSC: 22.35 ± 3.01 ms, $n = 11$; EPSC: 2.71 ± 0.50 ms, $n = 9$) and 20 $\mu$M baclofen (IPSC: 23.07 ± 3.26 ms, $n = 11$; $P = 0.5305$, Student's two-tailed paired *t* test; EPSC: 2.82 ± 0.48 ms, $n = 9$; $P = 0.6106$, Student's two-tailed paired *t* test). For both IPSCs and EPSCs, decay time constants were obtained from a monoexponential fit to the decay phase of synaptic currents. *G* and *H*, box-and-whisker plots summarising the effect of baclofen (20 $\mu$M) on the 10–90% rise time of evoked IPSCs (*G*) and EPSCs (*H*). Baclofen had no significant effect on the 10–90% rise time of IPSCs (control: 1.68 ± 0.55 ms, $n = 11$; baclofen: 1.68 ± 0.63 ms, $n = 11$; $P = 0.9810$, Student's two-tailed paired *t* test) and EPSCs (control: 0.79 ± 0.25 ms, $n = 9$; baclofen: 0.89 ± 0.63 ms, $n = 9$; $P = 0.6065$, Student's two-tailed paired *t* test). [Colour figure can be viewed at wileyonlinelibrary.com]

neither on holding currents when CSF-cNs were recorded in voltage-clamp mode, nor on membrane potentials under current-clamp recordings. However, GABA$_B$-Rs had an inhibitory effect on Ca$_V$ channels mediated by G$\beta\gamma$ activation, indicating that GABA$_B$-Rs are functional at the membrane of CSF-cNs and able to activate the G protein-dependent signalling cascade. Furthermore, GABA$_B$-R activation induced classical outward $K^+$ currents in other neurones of the brainstem such as DMNX neurones, as previously shown (Browning & Travagli, 2001), which rules out eventual bias in our recording conditions of GIRK responses.

Postsynaptic GABA$_B$-Rs express after birth but they do not open GIRK channels in developing brain in the first days of life (Gaiarsa & Porcher, 2013). GABA$_B$-R-mediated GIRK currents establish in brain rodents after the first postnatal week (Luhmann & Prince, 1991; Gaiarsa *et al.* 1995) or at the latest between the third and the fifth postnatal week (Nurse & Lacaille, 1999; Lei & McBain, 2003). In our study, we recorded CSF-cNs in 8- to 12-week-old adult mice, therefore in a time window in which GABA$_B$-Rs are supposed to be fully mature and trigger GIRK currents. However, CSF-cNs were shown to retain some immature features in adulthood because they continue to exhibit immature markers such as the expression of doublecortin or Nkx6.1 proteins, as well as a high resting potential and input resistance (Orts-Del'Immagine *et al.* 2012, 2014, 2017). As GIRK inhibition has been shown to appear in mature neurones (Mongiat *et al.* 2009; Gonzalez *et al.* 2018), one could suggest that the lack of GABA$_B$-R-mediated GIRK inhibition in CSF-cNs is the consequence of their persistent immature state. The physiological conditions in which CSF-cNs terminate their development, as well as the underlying mechanisms, are still unknown, but the expression of GIRK inhibition concomitantly with the full maturation of CSF-cNs may strongly change their excitability properties (Mongiat *et al.* 2009). Interestingly, in developing brain regions where GABA$_B$-Rs do not control cell excitability by gating GIRK channels, it was shown that the receptor is coupled to signalling pathways involved in neuronal development (Bony *et al.* 2013; Gaiarsa & Porcher, 2013; Giachino *et al.* 2014). One could therefore hypothesise that GABA$_B$-Rs might be involved in maturation processes of CSF-cNs, but further studies will need to address this potential function for GABA$_B$-Rs in CSF-cNs.

## CSF-cNs express voltage-gated $Ca^+$ channels and they are inhibited by GABA$_B$ receptors

To date there is little information about the Ca$_V$ expression and function in medullo-spinal CSF-cNs, nor about the isoform(s) expressed. Classically, depending on the $\alpha$-subunit forming the channel, Ca$_V$ can be subdivided in high (Ca$_V$1 and 2) and low voltage-activated (Ca$_V$3) channel classes comprising different isoforms based on channel electrophysiological properties (Catterall, 2011). Here, using a selective pharmacological approach, we conducted the first characterisation of Ca$_V$ expression in CSF-cNs from adult mice. Our results indicate that CSF-cNs express primarily the N-type $Ca^{2+}$ channels (Ca$_V$2.2; around 80% of the total current) along with Ca$_V$2.1 (P/Q-type) and Ca$_V$1.2 and 1.3 (neuronal L-type), although at a lower level (<20% of the total current). All identified isoforms are the neuronal forms of high-voltage activated $Ca^{2+}$ channels (Catterall, 2011), a result consistent with the neuronal nature of CSF-cNs.

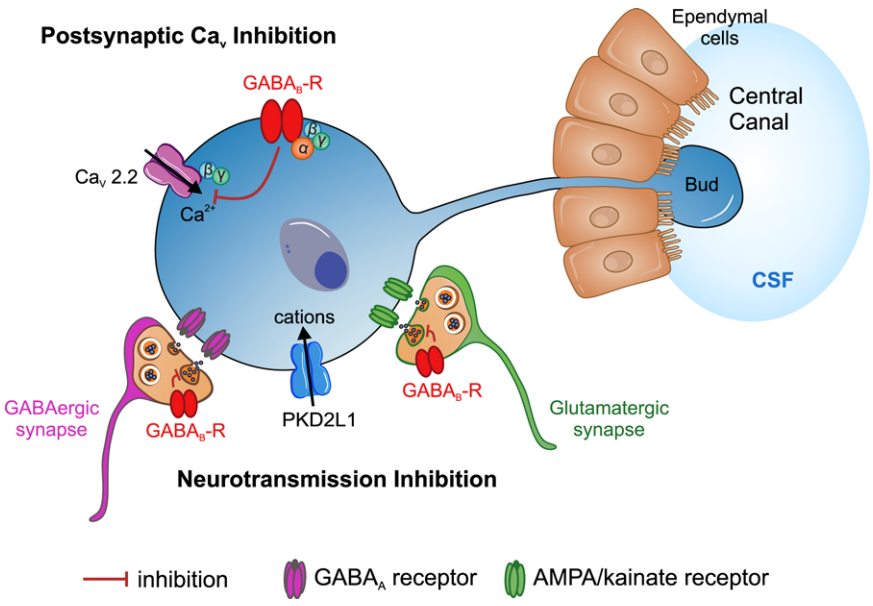


**Figure 9. Cartoon summarising the function of GABA$_B$-Rs in CSF-cNs**
CSF-cNs express GABA$_B$-Rs that inhibit voltage-gated calcium (Ca$_V$) channels through the recruitment of G$\beta\gamma$-subunits. Note that following GABA$_B$-R activation no G protein-activated inwardly rectifying $K^+$ (GIRK) response could be observed. GABA$_B$-Rs are also localised presynaptically on GABAergic and glutamatergic axon terminals forming synapses onto CSF-cNs, and their activation inhibits the release of GABA and glutamate, respectively. [Colour figure can be viewed at wileyonlinelibrary.com]

Marichal and colleagues (2009) indicated that CSF-cNs recorded from juvenile rats express T-type $Ca^{2+}$ channels ($Ca_V3$). This subtype is characterised by an activation around −60 mV (low-voltage) and a fast inactivation around −40 mV (Fox *et al.* 1987; Ikeda & Dunlap, 2007; Catterall, 2011). Our results suggest that CSF-cNs from adult mice do not express the $Ca_V3$ subtype. Indeed, in adult mouse CSF-cNs, $Ca^{2+}$ currents could only be activated for membrane potentials higher than -40 mV and we did not observe in the current-voltage relationships the characteristic shoulder (between −60 and -40 mV) underlying $Ca_V3$ activation.

The characterisation of $Ca_V$ subtypes expressed in CSF-cNs and the analysis of their modulation following $GABA_B$-R activation typically required 10 min long recordings, a period over which we observed a decrease in the $Ca^{2+}$ current amplitude by $35.8 \pm 9\%$ ($n = 13$), even in the presence of 10 mM intracellular EGTA as $Ca^{2+}$ buffer (slow kinetics), while the access resistance and the holding current remained unchanged over the same period of time (data not shown). Calcium currents have been reported to undergo rundown when recorded over long periods in the whole-cell configuration and this phenomenon is largely due to a $Ca^{2+}$-dependent mechanism (Belles *et al.* 1988). In the presence of 10 mM BAPTA, another type of $Ca^{2+}$ buffer with faster binding kinetics and higher buffering capacity, we observed a similar phenomenon (amplitude decreased by $24.2 \pm 4\%$, $n = 11$; $P = 0.706$ when compared to recordings with EGTA, Mann-Whitney test; data not shown). This result would suggest that the observed rundown is not $Ca^{2+}$ dependent and would involve some other regulatory processes. On the other hand, CSF-cNs are small neurones ($\sim 10\ \mu$m diameter) with little cytosolic space, and one could suggest that recordings performed under whole-cell configuration would lead to massive dialysis of intracellular compounds necessary for $Ca^{2+}$ channel activity. To characterise the molecular basis of the observed rundown, one would need to carry out a set of specific experiments but, since this is beyond the scope of the present study, it was not further addressed.

In the past decades, numerous studies have demonstrated that $Ca^{2+}$ channels, especially $Ca_V2.2$ in neurones, are inhibited by activation of metabotropic receptors primarily of the $G_{i/o}$ type (Pertussis toxin sensitive) (Ikeda & Dunlap, 1999, 2007; Dolphin, 2003) through the direct binding to the channel of the $G\beta\gamma$ dimers (Bean, 1989; Ruiz-Velasco & Ikeda, 2000; Dolphin, 2003; Zamponi & Currie, 2013). Medullar CSF-cNs receive GABAergic synaptic entries that would activate both synaptic ionotropic $GABA_A$ and metabotropic $GABA_B$ receptors. The latter GABAergic receptor subtype was shown in different neuronal populations to inhibit both pre- and postsynaptic $Ca^{2+}$ channels (Pérez-Garci *et al.* 2006; Booker *et al.* 2018). Consistent with the literature, we demonstrate in medullar CSF-cNs that $GABA_B$-Rs strongly and selectively inhibit $Ca_V2.2$ and we show that this inhibition is mediated by a voltage-dependent $G\beta\gamma$ mechanism. As a consequence, $GABA_B$-R-mediated $Ca_V$ inhibition leads to a decrease in the $Ca^{2+}$ influx and thus in the intracellular $Ca^{2+}$ concentration. Except for its role in triggering neurotransmission, $Ca^{2+}$ plays crucial functions in the regulation of neuronal physiology and activity. First, at the genomic level, $Ca^{2+}$ was shown to stimulate $Ca^{2+}$-regulated-kinase-cascades and phosphorylation of AMP-response element binding protein (CREB) and to play a role in gene transcription (Gallin & Greenberg, 1995; West *et al.* 2001). Thus, variation in intracellular $Ca^{2+}$ might recruit basal transcription machinery in CSF-cNs, leading to an activity-dependent protein expression. Second, several reports indicate that $Ca^{2+}$ is capable of activating or modulating sodium, potassium (Shah *et al.* 2006) and chloride (Frings *et al.* 2000) ionic conductance and/or of regulating postsynaptic receptors through $Ca^{2+}$-dependent phosphorylation processes (Booker *et al.* 2018). Similar mechanisms might exist in CSF-cNs to regulate their activity and excitability. Finally, PKD2L1 channels were shown to be regulated by intracellular $Ca^{2+}$ (Chen *et al.* 1999; DeCaen *et al.* 2016) and to act as a sensory receptor modulating CSF-cN excitability (Orts-Del'Immagine *et al.* 2016; Jalalvand *et al.* 2016). Thus, in CSF-cNs, variation in intracellular $Ca^{2+}$ would affect PKD2L1 activity and in turn CSF-cN excitability. Considering that $GABA_B$-R activation reduces $Ca^{2+}$ influx in CSF-cNs, one would expect a reduced activation or stimulation of the previously mentioned signalling cascades and, as a consequence, a modulation of CSF-cN activity and physiology. Similarly, bioactive compounds circulating in the CSF or released by synaptic partners might activate other GPCR subtypes expressed in CSF-cNs and targeting $Ca^{2+}$ signalling to regulate CSF-cN activity. The identification of such regulatory pathways represents one of the future challenges in the demonstration for the role and modulation of medullo-spinal CSF-cNs in the central nervous system.

## CSF-cNs receive synaptic glutamatergic inputs

As the spontaneous synaptic activity is very low in rodent CSF-cNs, we used in our previous works the application of a hypertonic solution to increase the synaptic release of neurotransmitters and found that hypertonic shocks induce in CSF-cNs inhibitory $GABA_A$ and glycinergic synaptic currents, but not excitatory glutamatergic synaptic currents (Orts-Del'Immagine *et al.* 2012, 2016). In neurones, the mechanisms underlying the increase of synaptic release following hypertonic shocks are not well known and more importantly they do not involve calcium entry into the presynaptic compartment (Rosenmund & Stevens, 1996; Mochida

*et al.* 1998). For a more accurate analysis of synaptic transmission, we therefore used in this study a physiologically relevant approach using electrical stimulations to evoke calcium-dependent synaptic transmission. We found that local electrical stimulations indeed evoked in CSF-cNs glutamatergic synaptic currents (EPSCs), showing that, in addition to GABAergic and glycinergic synaptic inputs, CSF-cNs receive also functional glutamatergic synaptic inputs. Evoked EPSCs were almost fully inhibited by DNQX, a selective antagonist of AMPA/kainate receptors, indicating that EPSCs in CSF-cNs do not have a NMDA receptor component. These results are consistent with our previous data showing that CSF-cNs express functional kainate and AMPA receptors but not NMDA receptors (Orts-Del'Immagine *et al.* 2016). Indeed, currents evoked by local application of glutamate in medullar CSF-cNs were inhibited by DNQX but not by the NMDA receptor antagonist AP-V and application of NMDA failed to induce any currents, even at more depolarised potentials to remove the magnesium block (Orts-Del'Immagine *et al.* 2016). Note that spinal CSF-cNs in lower vertebrates such as lampreys have been shown to exhibit glutamatergic transmission engaging both AMPA and NMDA receptors (Jalalvand *et al.* 2016). Whether this difference is the consequence of NMDA receptor loss of expression in mammalian CSF-cNs during evolution or more simply a different glutamatergic signalling between CSF-cNs localised in brainstem and spinal cord remains an open question.

### GABA$_B$ receptors inhibit both the release of GABA and glutamate onto CSF-cNs

We demonstrated that activation of GABA$_B$-Rs by baclofen inhibits the amplitude of evoked IPSCs and EPSCs recorded in CSF-cNs. The inhibitory effect of baclofen on the synaptic transmission in CSF-cNs is most likely mediated by the activation of GABA$_B$-Rs located presynaptically on terminals of GABAergic and glutamatergic inputs and by interfering with the neurotransmitter release machinery, as shown in many brain regions (Pinard *et al.* 2010). Two results in our study support this assumption. First, we show that baclofen enhanced the paired-pulse ratio of two consecutives IPSCs or EPSCs, an observation consistent with an alteration of the neurotransmitter release probability, as reported in a variety of different synapses (Manabe *et al.* 1993; Wilcox & Dichter, 1994; Fioravante & Regehr, 2011). Second, we show that baclofen had no effects on IPSC and EPSC kinetics (rise and decay times), therefore ruling out eventual interactions between postsynaptic GABA$_B$-Rs and postsynaptic GABA$_A$ or AMPA/kainate receptors. Studying the effect of baclofen on the frequency of miniature IPSCs and EPSCs would be a suitable approach to further confirm the presynaptic terminal localisation of GABA$_B$-Rs on GABAergic and glutamatergic inputs to CSF-cNs. However, such experiments would be difficult to achieve in CSF-cNs since the frequency of spontaneous synaptic events is very low in these neurones (Orts-Del'Immagine *et al.* 2012, 2016).

### Conclusion

In the present study, we characterise for the first time in mouse medullar CSF-cNs their synaptic connectivity and show that they receive both GABAergic and AMPA/kainate glutamatergic inputs. Further we indicate that GABA$_B$-Rs are functional and act as modulators of CSF-cN activity both at the pre- and postsynaptic level where they target $Ca^{2+}$ channels. These results add to the growing bulk of data on CSF-cN physiology and give the first insights into CSF-cN regulation through synaptic partners. In future studies, one will first need to identify the localisation of the GABAergic and glutamatergic neuronal partners connected to medullar CSF-cNs and to determine how they modulate their activity. It will then be necessary to identify whether they receive synaptic projections from other neuronal populations. Together, the expected results of these studies will form a basis for understanding the function of this unique neuronal population.

## References

Barral J, Toro S, Galarraga E & Bargas J (2000). GABAergic presynaptic inhibition of rat neostriatal afferents is mediated by Q-type $Ca^{2+}$ channels. *Neurosci Lett* **283**, 33–36.

Bean BP (1989). Neurotransmitter inhibition of neuronal calcium currents by changes in channel voltage dependence. *Nature* **340**, 153–156.

Belles B, Malécot CO, Hescheler J & Trautwein W (1988). "Run-down" of the Ca current during long whole-cell recordings in guinea pig heart cells: role of phosphorylation and intracellular calcium. *Pflugers Arch* **411**, 353–360.

Bettler B, Kaupmann K, Mosbacher J & Gassmann M (2004). Molecular structure and physiological functions of GABA$_B$ receptors. *Physiol Rev* **84**, 835–867.

Böhm UL, Prendergast A, Djenoune L, Nunes Figueiredo S, Gomez J, Stokes C, Kaiser S, Suster M, Kawakami K, Charpentier M, Concordet J-P, Rio J-P, Del Bene F & Wyart C (2016). CSF-contacting neurons regulate locomotion by relaying mechanical stimuli to spinal circuits. *Nat Commun* **7**, 10866.

Bony G, Szczurkowska J, Tamagno I, Shelly M, Contestabile A & Cancedda L (2013). Non-hyperpolarizing GABA$_B$ receptor activation regulates neuronal migration and neurite growth and specification by cAMP/LKB1. *Nat Commun* **4**, 1800.

Booker SA, Loreth D, Gee AL, Watanabe M, Kind PC, Wyllie DJA, Kulik Á & Vida I (2018). Postsynaptic GABA$_B$Rs inhibit L-type calcium channels and abolish long-term potentiation in hippocampal somatostatin interneurons. *Cell Rep* **22**, 36–43.

Browning KN & Travagli RA (2001). Mechanism of action of baclofen in rat dorsal motor nucleus of the vagus. *Am J Physiol Gastrointest Liver Physiol* **280**, G1106–G1113.

Catterall WA (2011). Voltage-gated calcium channels. *Cold Spring Harb Perspect Biol* **3**, a003947.

Chen G & van den Pol AN (1998). Presynaptic $GABA_B$ autoreceptor modulation of P/Q-type calcium channels and GABA release in rat suprachiasmatic nucleus neurons. *J Neurosci* **18**, 1913–1922.

Chen XZ, Vassilev PM, Basora N, Peng JB, Nomura H, Segal Y, Brown EM, Reeders ST, Hediger MA & Zhou J (1999). Polycystin-L is a calcium-regulated cation channel permeable to calcium ions. *Nature* **401**, 383–386.

DeCaen PG, Liu X, Abiria S & Clapham DE (2016). Atypical calcium regulation of the PKD2-L1 polycystin ion channel. *Elife* **5**, e13413.

De Koninck Y & Mody I (1997). Endogenous GABA activates small-conductance $K^+$ channels underlying slow IPSCs in rat hippocampal neurons. *J Neurophysiol* **77**, 2202–2208.

Djenoune L, Khabou H, Joubert F, Quan FB, Nunes Figueiredo S, Bodineau L, Del Bene F, Burcklé C, Tostivint H & Wyart C (2014). Investigation of spinal cerebrospinal fluid-contacting neurons expressing PKD2L1: evidence for a conserved system from fish to primates. *Front Neuroanat* **8**, 26.

Dolphin AC (2003). G protein modulation of voltage-gated calcium channels. *Pharmacol Rev* **55**, 607–627.

Fioravante D & Regehr WG (2011). Short-term forms of presynaptic plasticity. *Curr Opin Neurobiol* **21**, 269–274.

Fox AP, Nowycky MC & Tsien RW (1987). Kinetic and pharmacological properties distinguishing three types of calcium currents in chick sensory neurones. *J Physiol* **394**, 149–172.

Frings S, Reuter D & Kleene SJ (2000). Neuronal $Ca^{2+}$ -activated $Cl^-$ channels – homing in on an elusive channel species. *Prog Neurobiol* **60**, 247–289.

Gaiarsa J-L & Porcher C (2013). Emerging neurotrophic role of $GABA_B$ receptors in neuronal circuit development. *Front Cell Neurosci* **7**, 206.

Gaiarsa JL, Tseeb V & Ben-Ari Y (1995). Postnatal development of pre- and postsynaptic $GABA_B$-mediated inhibitions in the CA3 hippocampal region of the rat. *J Neurophysiol* **73**, 246–255.

Gallin WJ & Greenberg ME (1995). Calcium regulation of gene expression in neurons: the mode of entry matters. *Curr Opin Neurobiol* **5**, 367–374.

Giachino C, Barz M, Tchorz JS, Tome M, Gassmann M, Bischofberger J, Bettler B & Taylor V (2014). GABA suppresses neurogenesis in the adult hippocampus through $GABA_B$ receptors. *Development* **141**, 83–90.

Gonzalez JC, Epps SA, Markwardt SJ, Wadiche JI & Overstreet-Wadiche L (2018). Constitutive and synaptic activation of GIRK channels differentiates mature and newborn dentate granule cells. *J Neurosci* **38**, 6513–6526.

Herlitze S, Garcia DE, Mackie K, Hille B, Scheuer T & Catterall WA (1996). Modulation of $Ca^{2+}$ channels by G-protein beta gamma subunits. *Nature* **380**, 258–262.

Huang AL, Chen X, Hoon MA, Chandrashekar J, Guo W, Tränkner D, Ryba NJP & Zuker CS (2006). The cells and logic for mammalian sour taste detection. *Nature* **442**, 934–938.

Ikeda SR (1996). Voltage-dependent modulation of N-type calcium channels by G-protein beta gamma subunits. *Nature* **380**, 255–258.

Ikeda SR & Dunlap K (1999). Voltage-dependent modulation of N-type calcium channels: role of G protein subunits. *Adv Second Messenger Phosphoprotein Res* **33**, 131–151.

Ikeda SR & Dunlap K (2007). Calcium channels diversify their signaling portfolio. *Nat Neurosci* **10**, 269–271.

Jalalvand E, Robertson B, Wallén P & Grillner S (2016). Ciliated neurons lining the central canal sense both fluid movement and pH through ASIC3. *Nat Commun* **7**, 10002.

Lei S & McBain CJ (2003). $GABA_B$ receptor modulation of excitatory and inhibitory synaptic transmission onto rat CA3 hippocampal interneurons. *J Physiol* **546**, 439–453.

Liu Q & Wong-Riley MTT (2005). Postnatal developmental expressions of neurotransmitters and receptors in various brain stem nuclei of rats. *J Appl Physiol* **98**, 1442–1457.

Luhmann HJ & Prince DA (1991). Postnatal maturation of the GABAergic system in rat neocortex. *J Neurophysiol* **65**, 247–263.

Lüscher C, Jan LY, Stoffel M, Malenka RC & Nicoll RA (1997). G protein-coupled inwardly rectifying $K^+$ channels (GIRKs) mediate postsynaptic but not presynaptic transmitter actions in hippocampal neurons. *Neuron* **19**, 687–695.

McDermott CM, Abrahams TP, Partosoedarso E, Hyland N, Ekstrand J, Monroe M & Hornby PJ (2001). Site of action of $GABA_B$ receptor for vagal motor control of the lower esophageal sphincter in ferrets and rats. *Gastroenterology* **120**, 1749–1762.

Manabe T, Wyllie DJ, Perkel DJ & Nicoll RA (1993). Modulation of synaptic transmission and long-term potentiation: effects on paired pulse facilitation and EPSC variance in the CA1 region of the hippocampus. *J Neurophysiol* **70**, 1451–1459.

Margeta-Mitrovic M, Mitrovic I, Riley RC, Jan LY & Basbaum AI (1999). Immunohistochemical localization of $GABA_B$ receptors in the rat central nervous system. *J Comp Neurol* **405**, 299–321.

Marichal N, García G, Radmilovich M, Trujillo-Cenóz O & Russo RE (2009). Enigmatic central canal contacting cells: immature neurons in "standby mode"? *J Neurosci* **29**, 10010–10024.

Mochida S, Yokoyama CT, Kim DK, Itoh K & Catterall WA (1998). Evidence for a voltage-dependent enhancement of neurotransmitter release mediated via the synaptic protein interaction site of N-type $Ca^{2+}$ channels. *Proc Natl Acad Sci U S A* **95**, 14523–14528.

Möhler H & Fritschy JM (1999). $GABA_B$ receptors make it to the top – as dimers. *Trends Pharmacol Sci* **20**, 87–89.

Mongiat LA, Espósito MS, Lombardi G & Schinder AF (2009). Reliable activation of immature neurons in the adult hippocampus. *PLoS One* **4**, e5320.

Nurse S & Lacaille JC (1999). Late maturation of $GABA_B$ synaptic transmission in area CA1 of the rat hippocampus. *Neuropharmacology* **38**, 1733–1742.

Orts-Del'Immagine A, Kastner A, Tillement V, Tardivel C, Trouslard J & Wanaverbecq N (2014). Morphology, distribution and phenotype of polycystin kidney disease 2-like 1-positive cerebrospinal fluid contacting neurons in the brainstem of adult mice. *PLoS One* **9**, e87748.

Orts-Del'Immagine A, Seddik R, Tell F, Airault C, Er-Raoui G, Najimi M, Trouslard J & Wanaverbecq N (2016). A single polycystic kidney disease 2-like 1 channel opening acts as a spike generator in cerebrospinal fluid-contacting neurons of adult mouse brainstem. *Neuropharmacology* **101**, 549–565.

Orts-Del'Immagine A, Trouslard J, Airault C, Hugnot J-P, Cordier B, Doan T, Kastner A & Wanaverbecq N (2017). Postnatal maturation of mouse medullo-spinal cerebrospinal fluid-contacting neurons. *Neuroscience* **343**, 39–54.

Orts-Del'Immagine A, Wanaverbecq N, Tardivel C, Tillement V, Dallaporta M & Trouslard J (2012). Properties of subependymal cerebrospinal fluid contacting neurones in the dorsal vagal complex of the mouse brainstem. *J Physiol* **590**, 3719–3741.

Padgett CL & Slesinger PA (2010). $GABA_B$ receptor coupling to G-proteins and ion channels. *Adv Pharmacol* **58**, 123–147.

Pérez-Garci E, Gassmann M, Bettler B & Larkum ME (2006). The $GABA_{B1b}$ isoform mediates long-lasting inhibition of dendritic $Ca^{2+}$ spikes in layer 5 somatosensory pyramidal neurons. *Neuron* **50**, 603–616.

Pin J-P & Bettler B (2016). Organization and functions of mGlu and $GABA_B$ receptor complexes. *Nature* **540**, 60–68.

Pinard A, Seddik R & Bettler B (2010). $GABA_B$ receptors: physiological functions and mechanisms of diversity. *Adv Pharmacol* **58**, 231–255.

Pinheiro J, DebRoy S, Sarkar D & R Core Team (2016). nlme: Linear and nonlinear mixed effects models. Available at: https://cran.r-project.org/web/packages/nlme/citation.html [Accessed October 4, 2016].

Rosenmund C & Stevens CF (1996). Definition of the readily releasable pool of vesicles at hippocampal synapses. *Neuron* **16**, 1197–1207.

Ruiz-Velasco V & Ikeda SR (2000). Multiple G-protein $\beta\gamma$ combinations produce voltage-dependent inhibition of N-type calcium channels in rat superior cervical ganglion neurons. *J Neurosci* **20**, 2183–2191.

Sakaba T & Neher E (2003). Direct modulation of synaptic vesicle priming by $GABA_B$ receptor activation at a glutamatergic synapse. *Nature* **424**, 775–778.

Scanziani M, Capogna M, Gähwiler BH & Thompson SM (1992). Presynaptic inhibition of miniature excitatory synaptic currents by baclofen and adenosine in the hippocampus. *Neuron* **9**, 919–927.

Shah VN, Chagot B & Chazin WJ (2006). Calcium-dependent regulation of ion channels. *Calcium Bind Proteins* **1**, 203–212.

Stoeckel M-E, Uhl-Bronner S, Hugel S, Veinante P, Klein M-J, Mutterer J, Freund-Mercier M-J & Schlichter R (2003). Cerebrospinal fluid-contacting neurons in the rat spinal cord, a gamma-aminobutyric acidergic system expressing the P2X2 subunit of purinergic receptors, PSA-NCAM, and GAP-43 immunoreactivities: light and electron microscopic study. *J Comp Neurol* **457**, 159–174.

Vígh B, Manzano e Silva MJ, Frank CL, Vincze C, Czirok SJ, Szabó A, Lukáts A & Szél A (2004). The system of cerebrospinal fluid-contacting neurons. Its supposed role in the nonsynaptic signal transmission of the brain. *Histol Histopathol* **19**, 607–628.

West AE, Chen WG, Dalva MB, Dolmetsch RE, Kornhauser JM, Shaywitz AJ, Takasu MA, Tao X & Greenberg ME (2001). Calcium regulation of neuronal gene expression. *Proc Natl Acad Sci U S A* **98**, 11024–11031.

Wilcox KS & Dichter MA (1994). Paired pulse depression in cultured hippocampal neurons is due to a presynaptic mechanism independent of $GABA_B$ autoreceptor activation. *J Neurosci* **14**, 1775–1788.

Zamponi GW & Currie KPM (2013). Regulation of $Ca_v2$ calcium channels by G protein coupled receptors. *Biochim Biophys Acta* **1828**, 1629–1643.

## Additional information

### Competing interests

The authors declare no competing financial interests.

### Author contributions

All authors approved the final version of the manuscript and agreed to be accountable for all aspects of the work in ensuring that questions related to the accuracy or integrity of any part of the work are appropriately investigated and resolved. All persons designated as authors qualify for authorship, and all those who qualify for authorship are listed. Conception of the work (R.S., J.T. & N.W.); Acquisition, analysis and interpretation of data for the work (C.A., N.J., G.E.-R., R.S. & N.W.); Drafting the work and revising it for critically intellectual content (C.A., N.J., G.E.-R., R.S., J.T. & N.W).

### Funding

This research was supported by funding obtained from Aix-Marseille University, the "Région Provence-Alpes-Côte d'Azur" and the "Conseil Général des Bouches-du-Rhône" (PACA, CG13 - Neuracid, J.T.), PEPS 2010 from the CNRS INSB (Neuracil, N.W.), La Ville de Marseille (Nanocan, J.T.), l'Agence National pour la Recherche et la Deutsche Forschung Gemeinshaft (ANR-DFG PRCI- MOTAC80C/A134/AN16HRJ NMF, N.W.). G.E.-R. was supported by scholarship from a France-Morocco Neurosciences program. N.J. is recipient of an A*Midex AMU PhD scholarship from the '*Integrative and Clinical PhD international program*'.

### Acknowledgements

We thank the Aix Marseille University (AMU) Microscopy Centre (CP2M) for access to confocal microscopy and Kévin Poirot for his assistance in image acquisition.